TU Delft

Delft University of Technology

Document Version
Final published version

Licence
CC BY

Citation (APA)
Mulder, J. T. (2023). *Shaping the nanoworld: From precursors to functional nanocrystals*. [Dissertation (TU Delft), Delft University of Technology]. https://doi.org/10.4233/uuid:11a27e7d-8d43-47ed-91b5-99dc1b3264de

Important note
To cite this publication, please use the final published version (if applicable).
Please check the document version above.

Copyright
In case the licence states “Dutch Copyright Act (Article 25fa)”, this publication was made available Green Open Access via the TU Delft Institutional Repository pursuant to Dutch Copyright Act (Article 25fa, the Taverne amendment). This provision does not affect copyright ownership.
Unless copyright is transferred by contract or statute, it remains with the copyright holder.

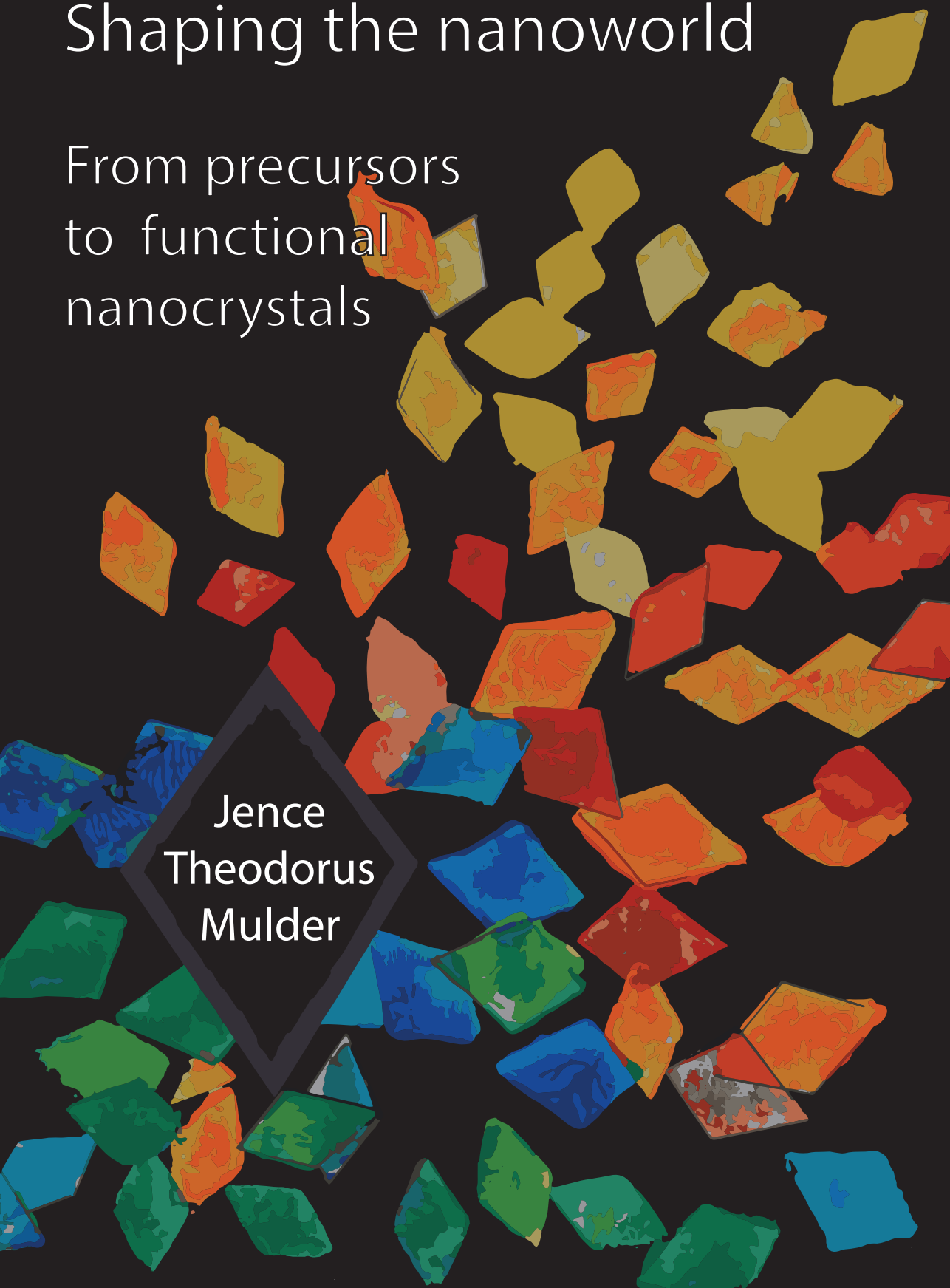
Sharing and reuse
Other than for strictly personal use, it is not permitted to download, forward or distribute the text or part of it, without the consent of the author(s) and/or copyright holder(s), unless the work is under an open content license such as Creative Commons.

Takedown policy
Please contact us and provide details if you believe this document breaches copyrights.
We will remove access to the work immediately and investigate your claim.

This work is downloaded from Delft University of Technology.

Shaping the nanoworld

From precursors to functional nanocrystals



Jence Theodorus Mulder

Shaping the nanoworld

From precursors to functional nanocrystals

Jence Theodorus Mulder

Shaping the nanoworld

From precursors to functional nanocrystals

Dissertation

for the purpose of obtaining the degree of doctor
at Delft University of Technology
by the authority of the Rector Magnificus Prof. dr. ir. T. H. J. J. van der Hagen
chair of the Board for Doctorates

to be defended publicly on
Tuesday 25 April 2023 at 12:30 o'clock

Jence Theodorus MULDER
Master of Science in Chemical Engineering
Delft University of Technology, the Netherlands
born in Zoetermeer, the Netherlands

This dissertation has been approved by the promotors.

Prof. dr. A. J. Houtepen	Delft University of Technology, promotor
Prof. dr. L. Manna	Italian Institute of Technology, promotor

Composition of the doctoral committee:

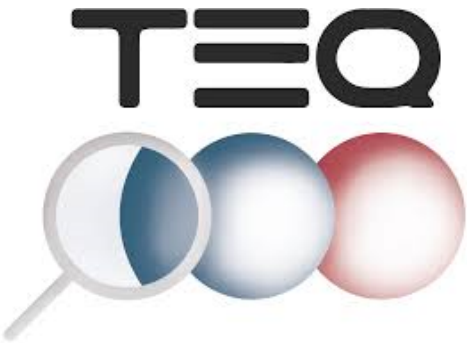
Rector Magnificus,	chairperson
Prof. dr. A. J. Houtepen	Delft University of Technology, promotor
Prof. dr. L. Manna	Italian Institute of Technology, promotor

Independent members:

Prof. dr. P. Schall	University of Amsterdam
Dr. F. T. Rabouw	Utrecht University
Prof. dr. ir. A. Urakawa	Delft Univeristy of Technology
Prof. dr. F. M. Mulder	Delft University of Technology
Dr. ir. T. J. Savenije	Delft University of Technology

This work received financial support from the European Commission – Horizon 2020
Grant Agreement No. 766900 – Testing the Large-Scale Limit of Quantum Mechanics





ISBN: 978-94-6473-084-5
Copyright © 2023 Jence Theodorus Mulder
Cover designed by Tilly Wils
Printed by Ipskamp printing, the Netherlands
An electronic version of this thesis is freely available at: https://repository.tudelft.nl

...Schrei nu niet meer, en ga nu slapen,
en als je niet slapen kan, zal ik je een sprookje vertellen,
een mooi verhaaltje van bloemen en edelsteenen en vogels,
van een jongen prins en een klein prinsesje...
Want meer is er niet in de wereld, dan een sprookje...

Metamorfoze

From: Psyche, Louis Couperus, 1898

For Daphne



03/06/1991 – 18/10/1997

Table of Contents

Chapter 1 1
Introduction

Chapter 2 23
Nucleation and Growth of Bipyramidal Yb:$LiYF_4$ Nanocrystals - Growing up in a Hot Environment

Chapter 3 59
Understanding and Preventing Photoluminescence Quenching to Achieve Unity Photoluminescence Quantum Yield in Yb:YLF Nanocrystals

Chapter 4 109
Developing Lattice Matched ZnMgSe Shells on InZnP Quantum Dots for Phosphor Applications

Chapter 5 137
Electrochemical p-Doping of $CsPbBr_3$ Perovskite Nanocrystals

Chapter 6 173
Orthogonal Electrochemical Stability of Bulk and Surface in Lead Halide Perovskite Nanocrystals

Summary 219

Samenvatting 223

Acknowledgements 229

Posters and Presentations 238

Supervised Thesis Projects 239

List of Publications 240

Curriculum Vitae 241

1

Chapter 1

Introduction

This thesis deals with various optically active nanocrystals (NCs). These are crystals in the nanometer range that absorb and emit photons, giving them properties that are useful for application in for example displays, biomedical imaging and optical refrigeration to name a few. In general, photoluminescent materials are called phosphors. They have been important for lighting and display applications for a long time. Making such phosphors in the form of small, nanometer sized particles has consequences for their synthesis and processing, but also for their physical properties. This presents large opportunities such as size tunable optical properties, solution processability and the possibility to administer luminescent NCs as biological probes, and equally large challenges like control over the size distribution and, most notably, photoluminescence quenching at the surface.
As an example, indium phosphide semiconductor quantum dots (InP QDs) are nowadays widely used in optically active products such display panels. These products were once based on cadmium selenide (CdSe) QDs,[1] however since CdSe has been limited in its application due to the toxicity of cadmium,[2] InP is currently the material of choice. Samsung's QLED-TVs are thus based on high quality InP QDs, resulting in a more color-pure depiction of the images compared to previously used, generally lanthanide point emitter-based phosphors.[3] The bandgap-tunability, a function of the particle size for QDs, can furthermore be used in the production of lamps with specific emission spectra (*e.g.* in order to mimic the solar spectrum).[4] QDs are further investigated for use in a range of optoelectronic devices, like LEDs, lasers, photodetectors and solar cells.[4–9]
This does not mean that lanthanide-based materials are being phased out by semiconductor QDs. Even more, also lanthanide-based materials can be synthesized as well-defined nanocrystals (NCs). These NCs find use as biological probes, photon upconverting materials and nanoscopic temperature sensors, and are furthermore investigated for their use in anti-cancer treatments and single particle studies.[10–15]

In this PhD thesis both of these material classes, semiconductor QDs and NCs, and lanthanide-based nanophosphors will be covered. To clearly explain the differences and similarities between these two classes of nanomaterials, we first have to dig into the difference between the two bulk material classes. Therefore, in this chapter, we first look into how materials are composed out of single atoms in order to form nano- and bulk-materials with in the cases described, specific optical properties.

1

1.1 Electronic Structure of Materials

All matter is composed of atoms that can bind together to form solids, if energetically favorable. The properties of atoms can be described by their atomic orbitals (AOs), mathematical representations of the wave-like behavior of an electron around the nucleus of an atom, for which the general shapes (defined by the angular momentum quantum number l) are shown in Figure 1.1.[16] For single atoms, AOs define all properties of the atoms and describe the probability density of finding a specific electron in a given position around the nucleus when multiplied by its complex conjugate AO*.

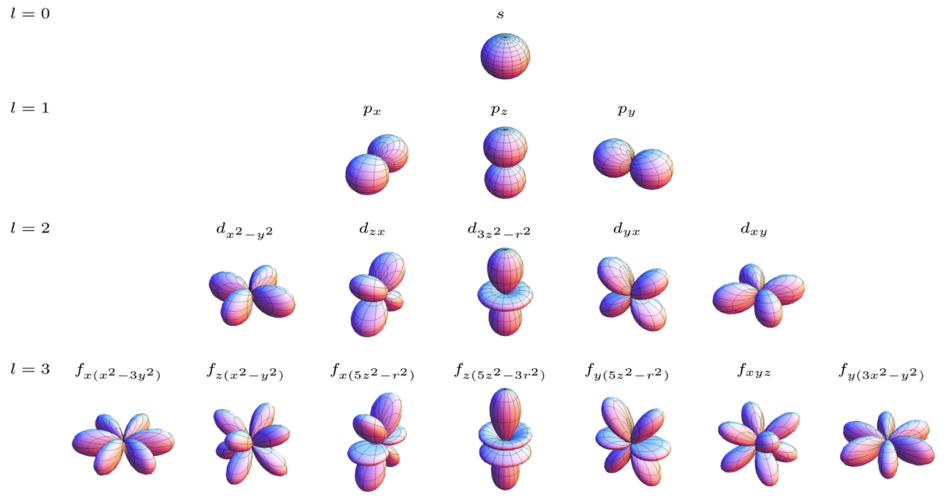


Figure 1.1. A schematic representation of atomic orbitals. The shape depends on the angular momentum quantum number (l) and gets more complex with higher atomic numbers. Figure originating from P. Marra.[16]

When bringing two atoms together, the AOs on individual atoms may overlap and form bonding and anti-bonding molecular orbitals (MOs), as shown in Figure 1.2. When this leads to an overall reduction of the energy this results in the formation of chemical bonds that make the atoms come closer and bind together. It is predominantly the valence orbitals (the highest occupied AOs on the individual atoms) that are responsible for this bond formation. The resulting MOs can again undergo bonding with other atoms, to form bulk materials, restructuring the initial AOs into a large bulk-like set of orbitals with an overall lower energy compared to their initial AOs.

As illustrated in Figure 1.2, the MOs are discrete energy states where electrons can reside. In bulk materials, the set of MOs is so large, that essentially bands are formed from all discrete states. From the separation between the highest occupied molecular orbital (HOMO), and the lowest unoccupied molecular orbital (LUMO), material classes are distinguished. If there is no energy difference between the HOMO and the LUMO, and hence the Fermi level (E_F) lays inside the band, electrons are free to move to any slightly higher state due to thermal energy, or in an electric field. Materials where electrons can freely move are better known as metals.

However, when the HOMO and LUMO do not overlap, an energy gap (or bandgap, E_g) is

created. Materials wherein an electron can be photo-excited from the HOMO to the LUMO by absorption of a visible photon are considered semiconductors. Materials with a larger bandgap are insulators. In these cases, the electron-containing band is referred to as the valence band, containing the valence electrons. The electron-poor band is the conduction band, as the presence of electrons in this band results in increased conductivity.

For luminescent materials, the class of metals is less interesting since optical excitation in a metal results in very fast, non-radiative dissipation of the energy through phonon emission, *i.e.* lattice vibrations or heat, as the excited electron and hole relax through the continuous density of states.
Semiconductors on the other hand may absorb and emit light of visible wavelengths, since their bandgap is in that range of the spectrum (roughly 400 to 700 nm). Upon photoexcitation, an electron and hole are created in the CB and VB respectively, as shown in Figure 1.2. Similar to carrier relaxation in metals the electron and hole will quickly relax, but only to the band edges. The large bandgap prevents further non-radiative recombination as the energy cannot be dissipated by single phonons, whose energy is typically in the 10 meV range.[17] Tens to hundreds of phonons would need to be emitted simultaneously, which is an unlikely and hence slow process. This means that carrier recombination can be *via* radiative transitions, resulting in light emission in the visible or near-infrared (NIR) range of the spectrum.

Insulators may absorb and emit photons, but since their bandgap is not in the visible range

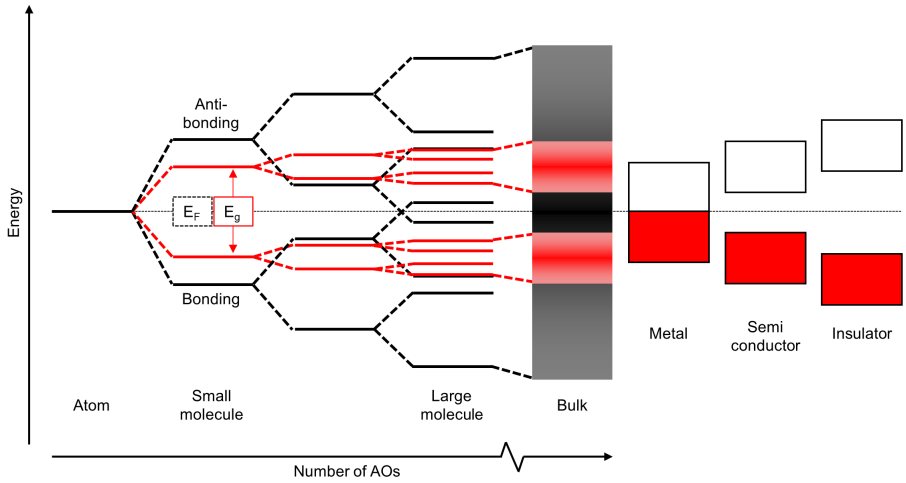


Figure 1.2. A schematic representation of the formation of MOs out of AOs. When atoms form a bond together, the AO-energy levels split into a lower and higher energy, the bonding and anti-bonding orbitals. Depending on the energy difference between the bonding and anti-bonding orbitals, these orbitals can overlap or remain separated by a band gap energy (E_g) in the bulk material. When the Fermi level (E_F) lays inside an orbital containing band, these materials act as metals. When the E_F lays inside the orbital-empty E_g, the material acts as either a semiconductor (when the E_g is small enough for optical excitation) or as an insulator (when the E_g is too large for optical excitation).

these photons are in the (deep) ultraviolet (UV). This can be changed, however, by doping insulators with luminescent ions, such as transition metal- or rare earth-ions, as explained in the coming section.

1.2 Insulators for Visible Optics

In the case of insulating materials, generally no electrons reside in the LUMO as exciting an electron to this level requires a large amount of energy. The lack of electrons in the LUMO, as well as a completely full HOMO, ensures that there is no possibility for electrons to move in such a material. This makes these materials poorly conducting, a property that can be used very well for optics. In this thesis, lithium yttrium fluoride, written as $LiYF_4$ or YLF, is used as an insulating material with a bandgap of 11.1 eV.[18] This is because the electron configuration of all three ions resembles a noble gas configuration, for Li^+: $1s^2$ = [He], for F^-: $1s^2\ 2s^2\ 2p^6$ = [Ne] and for Y^{3+}: $1s^2\ 2s^2\ 2p^6\ 3s^2\ 3p^6\ 3d^{10}\ 4s^2\ 4p^6$ = [Kr]. Therefore, there are no low-energetic transitions possible between the AOs of any of the ions in YLF. However, this changes if a part of the yttrium ions is substituted by (*i.e.* doped with) trivalent ytterbium ions (Yb^{3+}), which have an ionic configuration of $1s^2\ 2s^2\ 2p^6\ 3s^2\ 3p^6\ 3d^{10}\ 4s^2\ 4p^6\ 4d^{10}\ 5s^2\ 5p^6\ 4f^{13}$ = [Xe] $4f^{13}$. This allows one transition within the f-orbitals, making the Yb^{3+} ions optically active as illustrated in Figure 1.3. As the Yb^{3+} ions are incorporated in the non-conductive YLF-host, the excited state of the Yb^{3+} ions cannot leave the ion as long as no other Yb^{3+} ion, or another overlapping energy state, is near to accept the energy of the originally excited state. An optically excited and well-isolated Yb^{3+} ion can therefore, after a given amount of time (the photoluminescence-

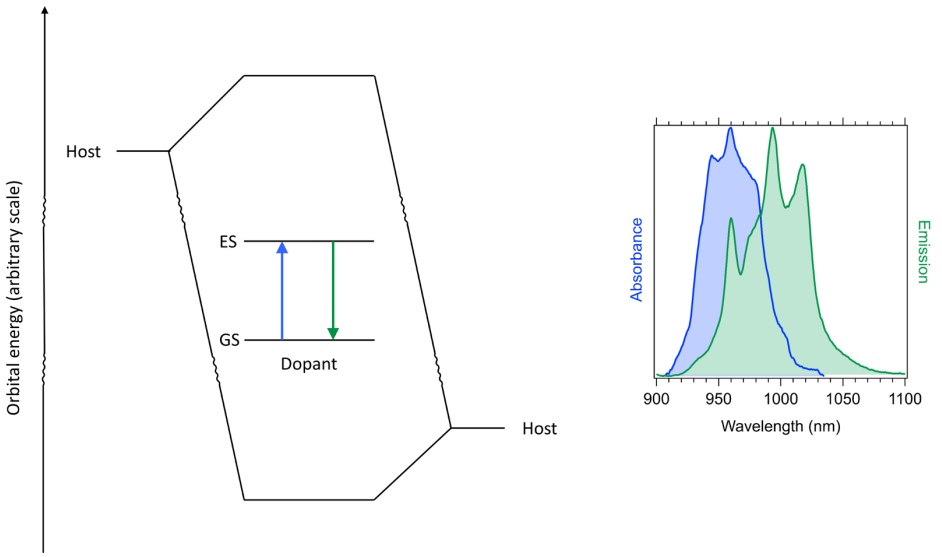


Figure 1.3. A schematic representation of transitions in an optically active ion (dopant) in a large bandgap, insulating host resulting in the emission of a photon. The lack of overlap between energy states of the host and the dopant protects the excited states well against non-radiative PL-quenching. The absorbance and emission spectra are determined by the possible transitions in the dopant.

or PL-lifetime), recombine to the ground state. When it does so, the excess energy is released in the form of a photon with an energy equal to the energy difference between the ground and the excited state (GS and ES respectively).

1.3 Quantum Confinement in Semiconductors

For semiconductor materials, electrons can optically be excited from occupied to unoccupied MO levels, generally referred to as valence band (VB) and conduction band (CB) respectively. Therefore, doping with optically active ions is not necessary for optical transitions although that is also possible. Additionally, when reducing the size of the material, the number of MOs reduces. The energy bands, built out of discrete energy states, therefore start to consist of fewer and fewer states when making the material smaller and smaller. Especially at the band edges, where the density of states is relatively low, the spacing between energy levels starts to increase and at a particular size becomes larger than kT, even at room temperature. At this point, optical spectra reveal discrete, quantized transitions, as well as an increase of the bandgap energy with reducing size. This effect is called quantum confinement and most notably results in a change in color of absorbed and emitted light. Note that this effect is generally only observed for semiconductor NCs, which are then referred to as QDs. For metals, wherein the density of states around the Fermi level is very high, NCs generally have to be smaller than one nanometer to show appreciable changes to the density of states due to quantum confinement.

This quantum confinement effect means that a single material (*e.g.* InP or CdSe) can appear to have different colors, depending solely on the size of the material. Although these materials can absorb all light with energies larger than the bandgap by exciting electrons from different occupied to different unoccupied levels, as shown in Figure 1.4a, any emission occurs solely from the band edges. The emitted light is therefore directly coupled to the bandgap energy of the material. This is because thermalization from the "hot" charge carriers to the band edges through phonon-emission is orders of magnitude faster (picosecond to nanosecond range[19]) than the emissive recombination of the generated electron and hole (Figure 1.4b and 1.4c respectively), similar to their bulk counterparts. A sample of QDs of identical size, therefore, has a very color pure emission with a broad absorbance (as shown in Figure 1.4d), making it excellent for use in for example high-quality optical displays and wavelength-specific lasers.

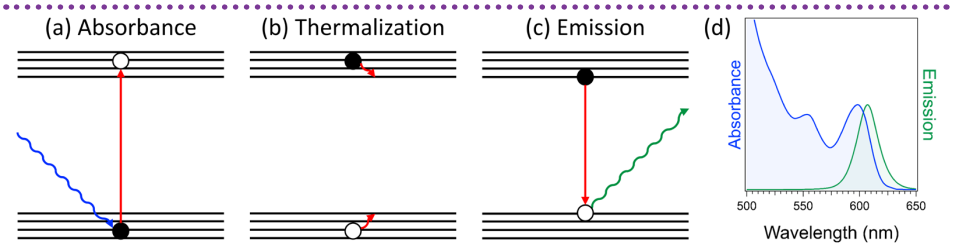


Figure 1.4. A schematic representation of transitions in a semiconductor material resulting in the emission of a photon. (a) The sequential processes of photon-absorption (or photo-excitation) from VB to CB, (b) thermal relaxation of the excited states to the band edge through phonon emission and (c) subsequent recombination resulting in the emission of a photon of the band edge energy. This results in a broad absorption spectrum and a sharp emission spectrum, as shown in (d).

1.4 Why is the Photoluminescence Quantum Yield of Phosphors Usually not Unity?

Apart from radiative recombination, non-radiative processes can also take place, as shown schematically in Figure 1.5. This results in a lower than unity (*i.e.* 100%) efficiency, generally denoted as the photoluminescence quantum yield (PLQY). As indicated in Process 1 of Figure 1.5, excited states can lose their energy by transferring it non-radiatively to other (parasitic) dopants (generally metal impurities) or states inside of the bandgap (caused by *e.g.* undercoordinated surface atoms or bulk defects). All these types of energy loss mechanisms are possible, as long as there is an overlap between the excited state and the acceptor.

Furthermore, excited states can be lost through Auger recombination, Process 2 of Figure 1.5. In this process, the energy of one excited state is transferred to a second excited state that is close by, followed by non-radiative thermalization. This process occurs especially at high excitation density, as Auger recombination requires overlap of the two excited states.

Process 3, parasitic absorption, relates to the absorbance of photons by impurities themselves, generally resulting in phonon-emission, thus resulting in a reduction of the PLQY. Although radiative emission from these states is possible, and hence this process does not necessarily result in a reduction of the PLQY, the emitted photon is then of a different energy than the band-to-band recombination, resulting in broadening of the emission spectrum or the presence of a lower-energy emission peak.

In yet another process, multi-phonon relaxation, the energy of a single excited state dissipates as lattice vibrations or heat, generally referred to as phonons, depicted in Process 4. This process is practically unavoidable, but reduces significantly in efficiency when the number of phonons that need to be emitted per excited state increases, as depicted by the difference between Processes 4 and 5. Materials with very low phonon energies, such as fluoride-based glasses, are therefore logical choices for keeping high PL efficiencies. Well-passivated optically active ions in a low-phonon energy host can therefore be very efficient emitters without further treatments.

Additionally, as depicted in Process 6, energy can be transferred through dipole-dipole interactions when there is electromagnetically resonant overlap between the excited state and any acceptor state. As this process does not require two electrons to be in very close proximity, this process allows non-radiative energy transfer over longer distances. This process, which is generally referred to as Förster resonance energy transfer or FRET, thus mostly causes surface-related PL-quenching. Once an excited state is at or near the material surface, the energy can resonantly be transferred to surface ligands, unintentionally present surface moieties (*e.g.* OH^- ions, as shown in Process 6) and solvent molecules.

In semiconductor NCs, electrons can optically be excited from the HOMO to the LUMO of the "host" material, leaving a hole behind in the HOMO. As the HOMO and LUMO are wavefunctions delocalized over most of the NC, they also overlap significantly with the NC surface. If trap states are present on the surface, the rate of electron or hole trapping is thus usually high. This causes a problem, because if any of these charge carriers reach a surface atom, which is undercoordinated and hence may have different energy levels than the bulk material, they can get localized (*i.e.* trapped) in such a state. This generally results in non-radiative recombination, where the energy is again dissipated in the form

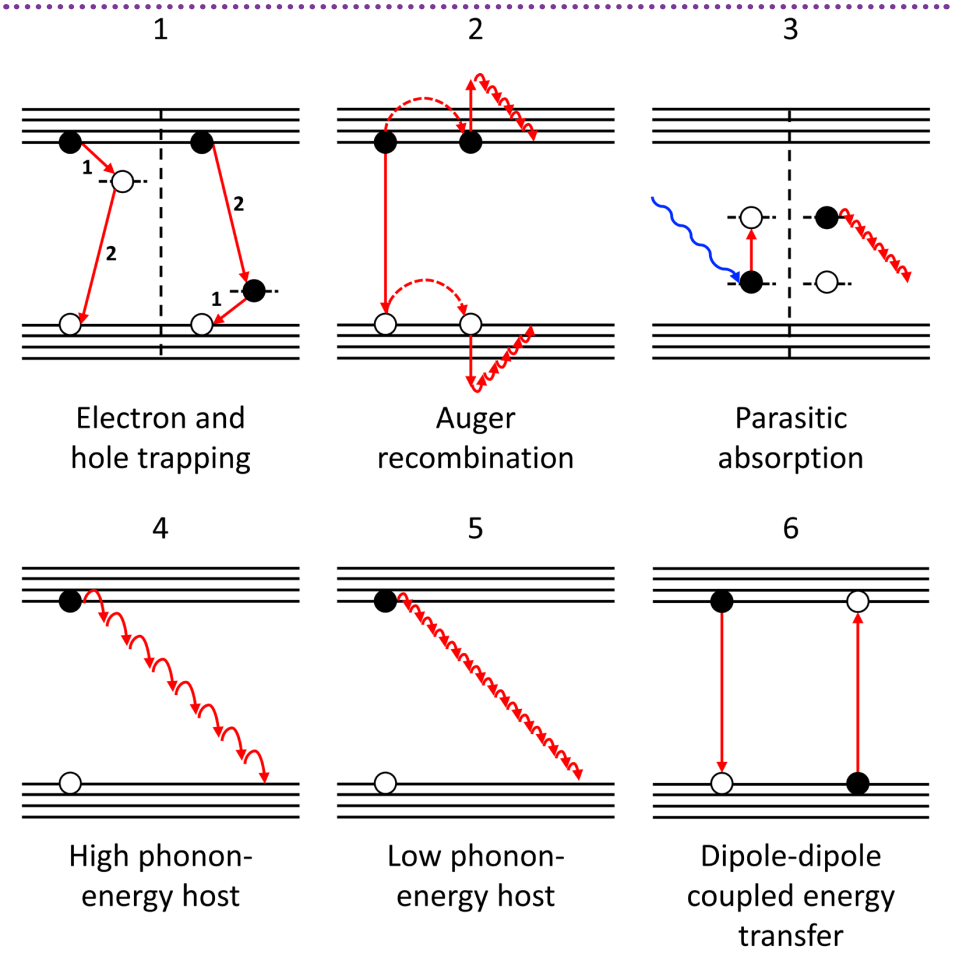


Figure 1.5. A schematic representation of different PL quenching pathways. Excited states can get trapped in so-called trap-states (Process 1) or lost by exciting another excited state to a higher energy level (Auger recombination, Process 2). Parasitically absorbing impurities can not only act as a trap state, but also absorb photons themselves (Process 3), generally reducing the PLQY and broadening the emission spectrum. Multi-phonon-relaxation (Process 4) is a process that is practically unavoidable, but can be reduced significantly by using a low-phonon energy host that is free of any impurities, as indicated in Process 5. Dipole-dipole coupled energy transfer allows more distant quenching of excited states by resonantly coupling to any energetically overlapping vibrations in surface ligands, unintentional surface moieties or solvent molecules, as shown in Process 6.

of several phonons. When trap states do take part in radiative recombination, the emitted photon is generally of lower energy broadening the emission spectrum. For unprotected QDs, this results in a reduction of the PLQY and a broadening of the emission spectrum, *i.e.* less efficient emission with a lower color purity.

The effect of surface-related PL quenching is one of the main fields of study for nanomaterials for optical applications, because a large fraction of atoms is part of, or near the surface.[20–24] Therefore, for both semiconductor- and insulator-based NCs (as even

dopants are generally still close to the surface from any point in the NC), all excited states have to be isolated from the NC surface in order to stay color pure (for semiconducting NCs) and keep a high PLQY. To do this, several methods are used during and after the synthesis of these nanomaterials, as will be explained in Section 1.5.

1.5 Synthesizing Well-Passivated Nanocrystals

Both semiconductor- and insulator-based NCs are synthesized following the same principles. Generally, at a high temperature, the different precursors are swiftly added or released far over the supersaturation to initiate rapid nucleation of the NCs. If secondary nucleation, prolonged nucleation or Ostwald ripening occurs, the sample loses its monodispersity. Therefore, ligands are added to control the nucleation and growth, and at the same time passivate the undercoordinated atoms on the NC surface. Once the NC cores are grown, the synthesis solution is cooled down stopping any NC growth that was still ongoing. As most NCs that are not based on oxides or hydroxides are oxophilic and tend to hydrolyze when coming into contact with water, NC syntheses are generally performed under an inert atmosphere (nitrogen or argon). The samples are subsequently washed and stored under an inert atmosphere in anhydrous and degassed solvents. Any contact between the synthesized NCs and air can result in oxidation of the NC surface, introducing unwanted surface trap states that are difficult, if not impossible to remove.

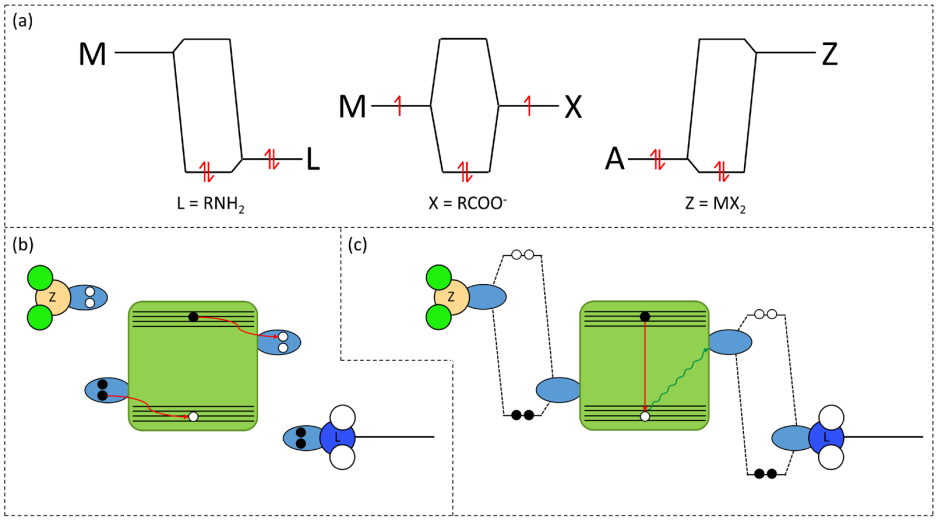


Figure 1.6. Surface passivation using ligands. (a) Ligand binding of L-, X- and Z-type ligands explained using MO diagrams, with a general example per ligand type. Here, M indicates a cation and A an anion. (b) Schematic representations of electron and hole trapping on unpassivated surface states and (c) emissive recombination after passivation of the trap states by the binding of ligands, resulting in MOs that lay outside of the bandgap.

In principle, the native synthesis ligands protect the NC surface by binding to undercoordinated surface atoms depending on the nature of the surface atom and the type of ligand (Figure 1.6a). These surface atoms are coordinated by fewer atoms and are therefore of higher energy than a bulk atom. Depending on the energy of the AO

of this surface atom, it can result in an energy state inside the bandgap, as indicated in Figure 1.6b. Such a state can trap electrons or holes (following Process 1 in Figure 1.5) and thereby lower the PLQY. Binding ligands to these surface atoms results in the formation of new bonding and antibonding orbitals, which may then reside inside the VB and CB if the bonding is strong enough (Figure 1.6c). In that case, the trap state can be removed. However, as the native ligands are generally long carboxylate ions that only have moderate binding energy, in general, not all trap states can be moved inside of the CB and VB. The ligand binding is furthermore dynamic, implying that at points in time ligands detach from the NC surface, hence surface trap states are continuously reintroduced. To counter this, apart from adding more ligands into the solution to move the equilibrium more towards ligands on the surface, ligand exchange- and shelling-methods are generally applied to improve the surface passivation, thereby increasing the PLQY. For the first method, a ligand exchange, generally stronger binding ligands are added to the NC dispersion to replace the native ligands. This is often performed with a large excess of the preferred ligands, using a concentration difference as the driving force for the ligand exchange. Depending on the nature of the surface ions, different ligand types are chosen.

Surface anions have an excess of electrons to bind with atoms, and hence neutral ligands are chosen that can bind with these electrons. These ligands are generally referred to as Z-type ligands. An example is $CdCl_2$, where the Cd^{2+} ion acts as the electron acceptor. The two chloride ions remain on the Cd^{2+}, keeping the entire NC system charge neutral. Similarly, for surface cations which are electron deficient, electron-rich neutral L-type ligands with a lone pair of electrons, such as amines, are chosen. If the overall nanomaterial is charged, generally due to an excess of surface cations, charged anions such as carboxylates are used to keep the system overall charge balanced. These charged anionic ligands are referred to as X-type ligands. Whereas ligand exchange methods have shown to significantly increase the PLQY of certain types of NCs, there is still a dynamic equilibrium and hence from time to time ligands will detach.

In this thesis, ligand exchanges are also performed to change the dispersibility of the NCs in different solvents. Ligands namely do not only act as surface passivating molecules, they also determine the dispersibility of the NCs in polar and nonpolar solvents. For Yb:YLF NCs, the native carboxylate X-type ligands that disperse NCs well in nonpolar solvents (*e.g.* hexane or toluene), are completely replaced by charge-balancing surface anions

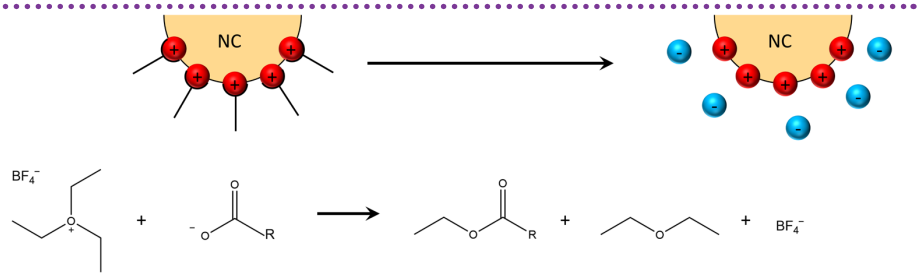


Figure 1.7. A method to completely change the dispersability of NCs from nonpolar to polar solvents by means of a ligand exchange. In this figure, native carboxylate ligands react with triethyloxonium ions, to form diethyl ether and the ethyl-carboxylate ester. Here, the ligands are replaced by BF_4^- anions, which were introduced together with the triethyloxonium cations as $[Et_3O]^+[BF_4]^-$.

which help disperse the NCs in polar solvents *e.g.* water or methanol). A complete ligand exchange in this case is performed by chemically reacting away all oleate ligands following the reaction shown in Figure 1.7.

The second method of NC surface passivation is the growth of an inert shell around the core NC that passivates all surface atoms, therefore removing any surface traps entirely. The downside of this method is that not for every core-material a proper shell material can (easily) be grown. In the case of doped insulating NCs, this method is straightforward, as in principle the undoped host material can be used to synthesize the shell, preventing excited states on dopants in the core from reaching the surface.
For QDs such as InP or CdSe, a different material needs to be selected as shell material. If the core material is chosen in these cases, then the HOMO and LUMO delocalize again over the entire QD, thus not resulting in the surface passivation of the core. This complicates shell growth on semiconductor NCs significantly, as the shell material should be able to be grown in the right crystal structure (or at least with matching crystal facets) and with a matching lattice parameter, otherwise not all quenching sites (*i.e.* surface states) can be passivated, as illustrated in Figure 1.8. Additionally, the bandgap of the shell should be (significantly) larger, and also have a type I band structure to keep both the

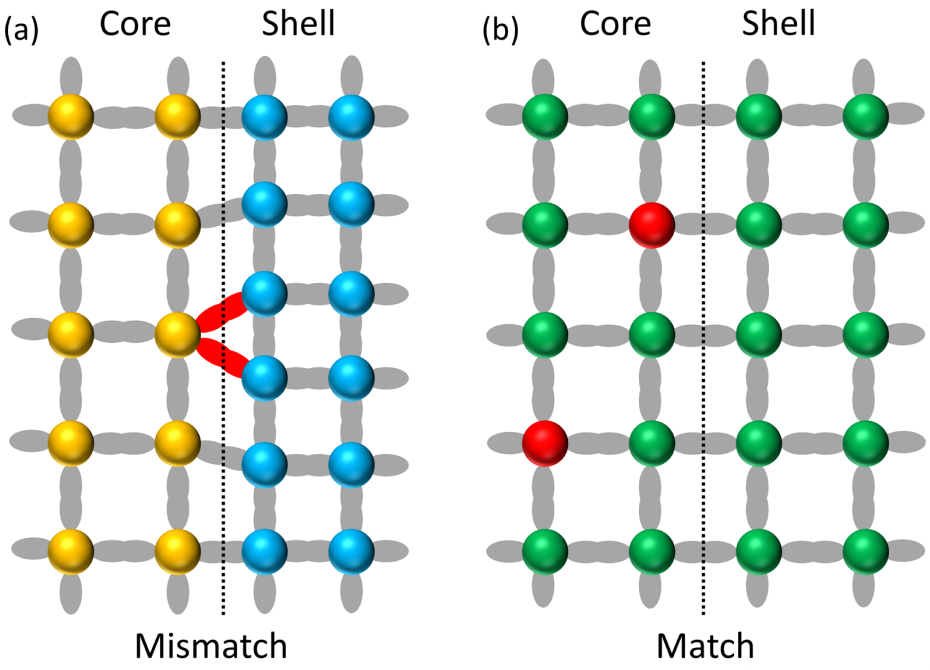


Figure 1.8 A schematic representation of two cases of NC shell growth. When growing a shell material around a NC core, the lattice mismatch between the two materials should be kept as small as possible. If there is a lattice mismatch in-between the core and shell (a), an irremovable (potential) trap state in the form of an undercoordinated ion, bonds depicted in red, is generated. If a proper matching shell material is grown, *e.g.* an undoped shell on a doped insulated NC (b), no lattice mismatch should be introduced.

excited electron and hole confined in the QD core. Any delocalization of the wavefunction of the excited electron or hole over the shell may still result in surface quenching. As shells providing electronic passivation are not necessarily stable under ambient conditions and illumination, QD cores are often passivated by not one, but two shell materials. The second shell thus acts as a protection layer for the first shell.

For some semiconductor NCs, no suitable shell materials have been found yet. Most notable are the cesium lead halide-based perovskite NCs ($CsPbX_3$, X = Cl, Br, I), which can be considered the next generation of NCs for most optical applications. In contrast to QDs, these NCs are often not quantum confined. Still, the bandgap can be tuned such that emission in the entire visible spectrum is obtained. In this case, it is solely an effect of the bulk bandgap. An additional benefit of perovskite NCs is that these NCs are considered "defect tolerant". The origin of this effect is still debated, but the practical implication is that even with a poorly passivated surface these NCs generally have a high PLQY. The main downside, and hence the reason a shell for these NCs is still preferred, is their overall stability. Due to their highly ionic character, in contrast to general semiconductor QDs, these NCs tend to degrade rapidly when manipulated.

If the NC surface is perfectly passivated generally the PLQY gets close to unity, a highly sought-after property. As stated in the introductory sentences, NCs are already used for certain common applications. And with improved efficiencies, these nanomaterials will become interesting for an increasing number of applications. Where some of the NCs discussed in this thesis have already appeared in consumer products, others still need to be improved to become widely useful.

1.6 Studying a Single Nanocrystal

Next to applications where ensembles of near-unity PLQY NCs are used (such as QLEDs), single nanoparticles can also be used, for example in scientific studies. In January 2017 a project proposal was submitted to the European Commission's Horizon 2020 – Future and Emerging Technologies (FET-Open) program with the title "TEsting the large-scale limit of Quantum mechanics", or TEQ for short, which got granted for approximately €4.4 million in June 2017. The aim of this consortium, of which this thesis is also a part, is to study at what size of a molecule or particle, observations can no longer be described by a quantum mechanical wavefunction, but due to a spontaneous collapse of this wavefunction needs to be described using general, macroscopic physics. The Yb:YLF NCs discussed in parts of this thesis were designed as objects to test this.

At TEQ-partner University College London (UCL) a set-up was designed to capture and subsequently study a single NC using optical tweezers (Figure 1.9). These tweezers are focused laser beams in which a single particle can be trapped. The motion of the particle in the optical field is monitored by detecting probe light scattered in different directions. The information obtained from these measurements can be used as an indication of quantum mechanical behavior. However, to study the quantum mechanical behavior of this NC, all external perturbations have to be removed to ensure any observed quantum collapse is not related to external influences, but spontaneous and induced by the size of the NC itself. The originally designed set-up is therefore operated in an ultra-high vacuum environment

at ultra-low temperatures. This environment ensures that as few external perturbations as possible could disturb the measurements by removing thermal motion as well as any gas molecules the NC could interact with. This however results in one critical problem; the NC itself cannot lose any absorbed energy from the optical tweezers through conduction or convection. Any background absorbance thus results in internal thermal heating of the NC, eventually resulting in evaporation and hence loss of the particle.

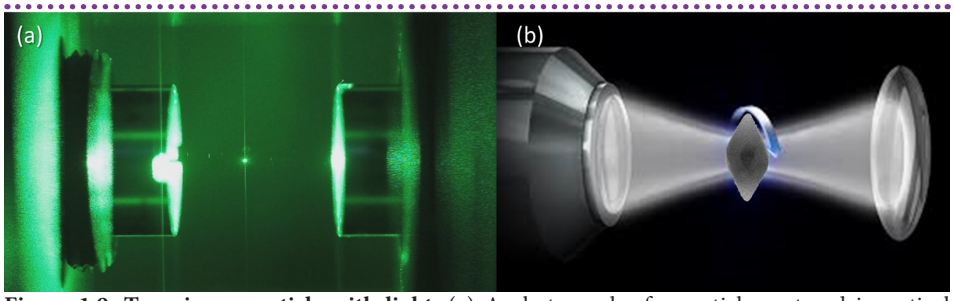


Figure 1.9. Trapping a particle with light. (a) A photograph of a particle captured in optical tweezers (photo made by James Millen, UCL). (b) The aim of TEQ is to capture a well-defined, optically refrigerating NC in an ultra-high vacuum environment, as illustrated in the image (adapted from Rahman *et al.*[25]).

1.7 Cooling a Captured Nanocrystal with Light

To keep the particles stable during the TEQ measurements, a cooling mechanism for the NC is needed that is independent of heat convection and conduction. The only remaining option, radiative heat loss, is conceptually not the most straightforward for an isolated, levitating NC. However, stimulated radiative cooling, also known as laser cooling or optical refrigeration, has been shown in bulk YLF that is heavily doped with Yb ions, and cooling to as low as 91K has been reported.[26] Furthermore, YLF NCs, co-doped with Yb^{3+} and other lanthanide ions (generally Tb^{3+}, Er^{3+} or Tm^{3+}) already exist, and are commonly synthesized for multi-photon-upconversion. These NCs are relatively large (20 nm up to a few microns), and do not absorb at the wavelengths of the optical tweezers (λ = 1064 nm) when solely doped with Yb^{3+} and are non-spherical, allowing a more detailed study of their rotational motion. Yb:YLF NCs are therefore the perfect candidate for the TEQ studies.

Optical refrigeration in Yb:YLF is possible due to a combination of physical phenomena and material properties. A free Yb^{3+} ion has only one optical transition ($^2F_{7/2} \rightarrow {}^2F_{5/2}$) at approximately 980 nm. When introduced in the YLF host, however, the ground state level splits in 4, and the excited state level in 3 levels due to crystal field splitting,[27] where most of the intra-state levels have an energy difference of approximately 1 phonon (Figure 1.10). When exciting an electron in the highest of the ground state levels (E_4) to the lowest of the excited state levels (E_5), and giving the system sufficient time to interact with phonons, the excited state can effectively absorb the phonons. When the excited state returns to the ground state, it then on average leads to the emission of a photon with higher energy than the absorbed photon. The absorbed phonon-energy is lost from the Yb:YLF, cooling down the lattice. Because the $^2F_{7/2} \rightarrow {}^2F_{5/2}$ transition is parity forbidden, the photoluminescence (PL) lifetime of the Yb^{3+} ion exceeds 2 ms in the YLF host. Therefore, there is ample time for thermalization, resulting in a Boltzmann distribution over the different states.

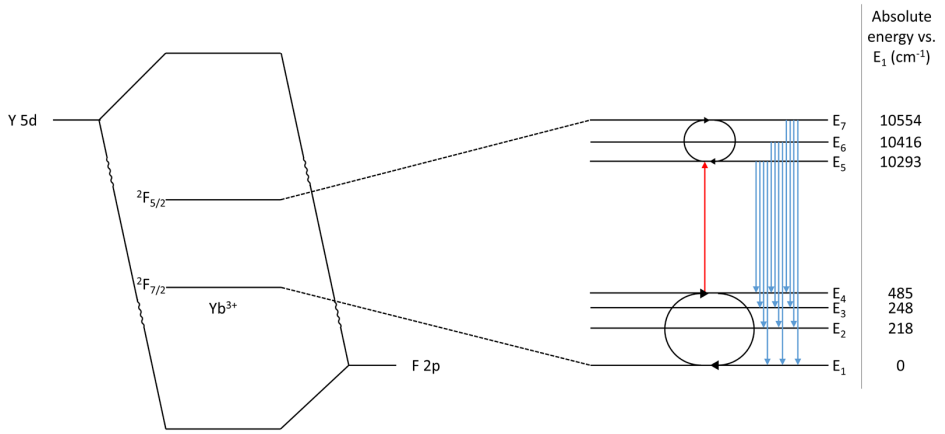


Figure 1.10. A schematic representation of an Yb^{3+} ion located far inside the bandgap of the YLF host, composed of the 5d-orbitals of the Y^{3+} ions and the 2p-orbitals of the F^- ions. Due to a very long PL-lifetime of the Yb^{3+} transition, and solely one ground state and one excited state which are split in multiple Stark-levels of roughly a phonon in energy due to crystal field splitting,[27] exciting the lowest possible transition ($E_4 \rightarrow E_5$) results in a Boltzmann distribution over all possible states, leading to an overall higher energy of the emitted photon due to phonon-absorption. Absolute energy values obtained from Demirbas *et al.*[28]

To exhibit optical refrigeration, however, the NCs need to have a near-unity PLQY as the effective loss of energy from the system (*i.e.* cooling through phonon-absorption) is relatively small compared to the energy of the photon required. Any non-radiative PL-decay results in the emission of phonons back into the NC, effectively heating the NCs further. For the TEQ project it is sufficient if there is no heating, as that implies the particles will not evaporate. The PLQY φ required to avoid heating can be calculated from the steady state temperature condition:

$$\begin{aligned} \text{Heating} &= \text{Cooling} \\ (1-\varphi)\, E_{ex} &= \varphi(\overline{E_{em}} - E_{ex}) \\ E_{ex} - \varphi \cdot E_{ex} &= \varphi(\overline{E_{em}} - E_{ex}) \\ \varphi &\geq E_{ex}/\overline{E_{em}} \end{aligned}$$

When exciting at 1030 nm (E_{ex} = 1.204 eV), the weighted average energy of the emission, obtained from the emission spectrum, $\overline{\lambda_{em}}$ = 992 nm ($\overline{E_{em}}$ = 1.250 eV) and hence $\varphi \geq 96.3\%$ is required to avoid heating of the NCs.

The main purpose of this thesis for the TEQ project is to understand all factors that limit the PLQY and hence result in heating of the optically captured Yb:YLF NC. By identifying and removing all factors that lead to non-radiative decay, the goal is to synthesize as highly Yb-doped NCs as possible, while retaining a PLQY of at least 96.3%.

1

1.8 General Overview of the Materials Studied

In this thesis, three types of optically active nanomaterials are studied, namely quantum confined InP QDs, non-quantum confined $CsPbBr_3$ semiconductor NCs and YLF insulator NCs with optically active Yb^{3+} dopants. To facilitate the understanding of the similarities and differences between these materials, specific material properties are shown in this section.

Indium phosphide (InP)

Bandgap	1.34 eV (bulk)[29] 2.8 eV (core NCs used in this thesis)
Crystal structure	Zinc blende (ZnS)
VB orbital composition	σ of P 3p and In 5p [30]
CB orbital composition	σ* of P 3p, In 5s and In 5p [30]
NC size range	4 – 6 nm (in this thesis)
Color tunability	By changing NC size

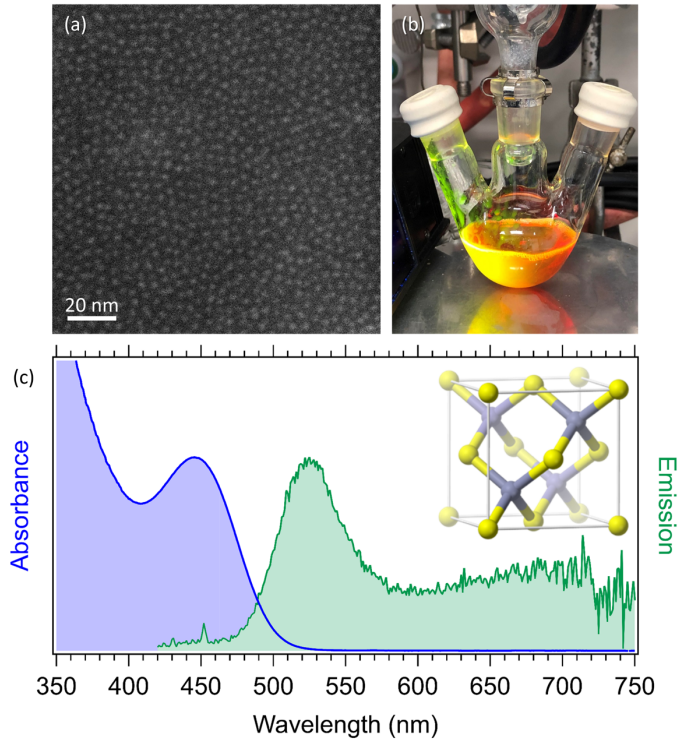


Figure 1.11. Overview of indium phodsphide (InP) (a) TEM image of In(Zn)P QD cores. (b) A photograph showcasing the bright photoluminescence of In(Zn)P cores after the growth of a passivating shell (as worked out in Chapter 4). (c) Absorbance and emission spectra of In(Zn)P core QDs, showcasing a large Stokes shift and a significant fraction of sub-bandgap emission. Added to the figure is an InP unit cell.

Cesium lead bromide ($CsPbBr_3$)

Bandgap	2.4 eV (bulk)[29]
Crystal structure	Perovskite ($CaTiO_3$)
VB orbital composition	σ^* of Br 4p and Pb 6s [31]
CB orbital composition	σ^* of Br 4p and Pb 6p [31]
NC size range	8 – 12 nm (in this thesis)
Color tunability	By changing halide composition or reduction of the NC size

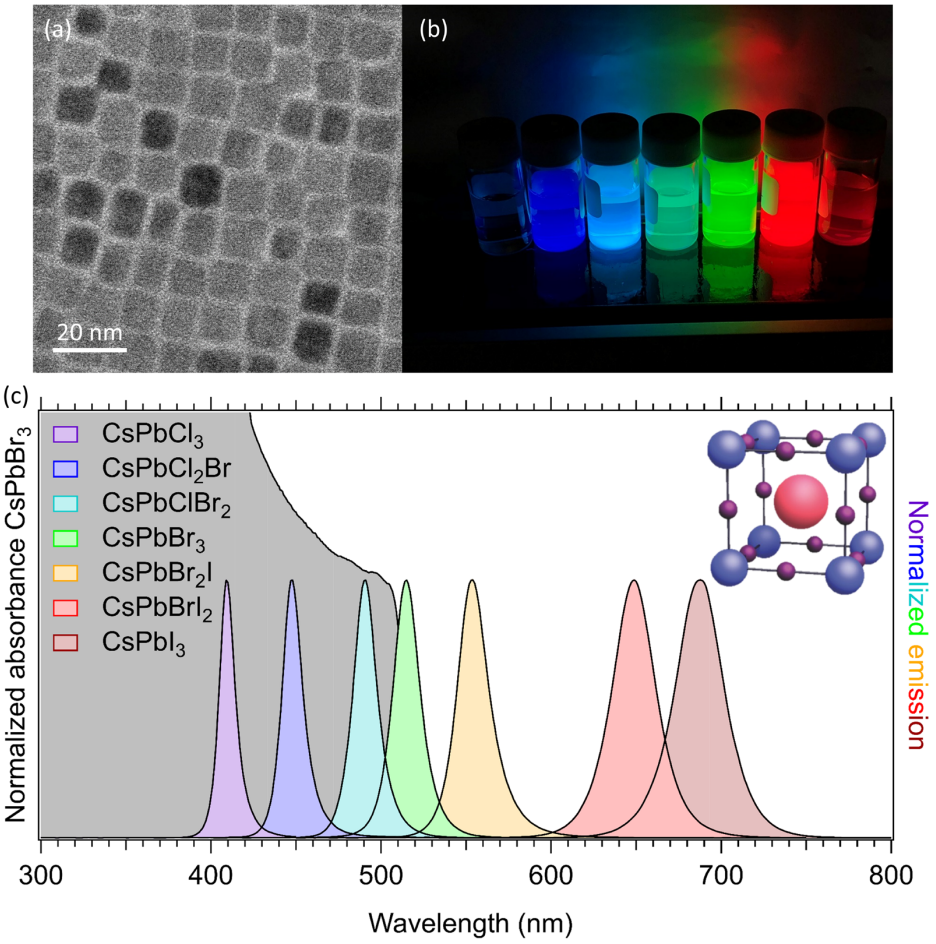


Figure 1.12. Overview of cesium lead bromide ($CsPbBr_3$) (a) A TEM image of $CsPbBr_3$ NCs. (b) A range of cesium lead halide based NC samples, from a full chloride-based sample (left) to a full bromide-based sample (middle) to a full iodide-based sample (right), and mixtures thereof. (c) The emission spectra of the samples shown in (b), together with the absorbance spectrum of $CsPbBr_3$, the NCs used in this thesis. Added to the figure is the perovskite unit cell, adapted from Zhou *et al.*[7]

1

Ytterbium doped lithium yttrium fluoride ($Yb:LiYF_4$ or Yb:YLF)

Bandgap	11.1 eV ($LiYF_4$ host)[32], 1.2 eV (Yb^{3+} dopant)
Crystal structure	Scheelite ($CaWO_4$)
VB orbital composition	σ of F 2p and Y 5d (host)[32]
CB orbital composition	σ* of F 2p and Y 5d (host)[32]
NC size range	50 – 250 nm (in this thesis)
Color tunability	By changing or adding dopant ions

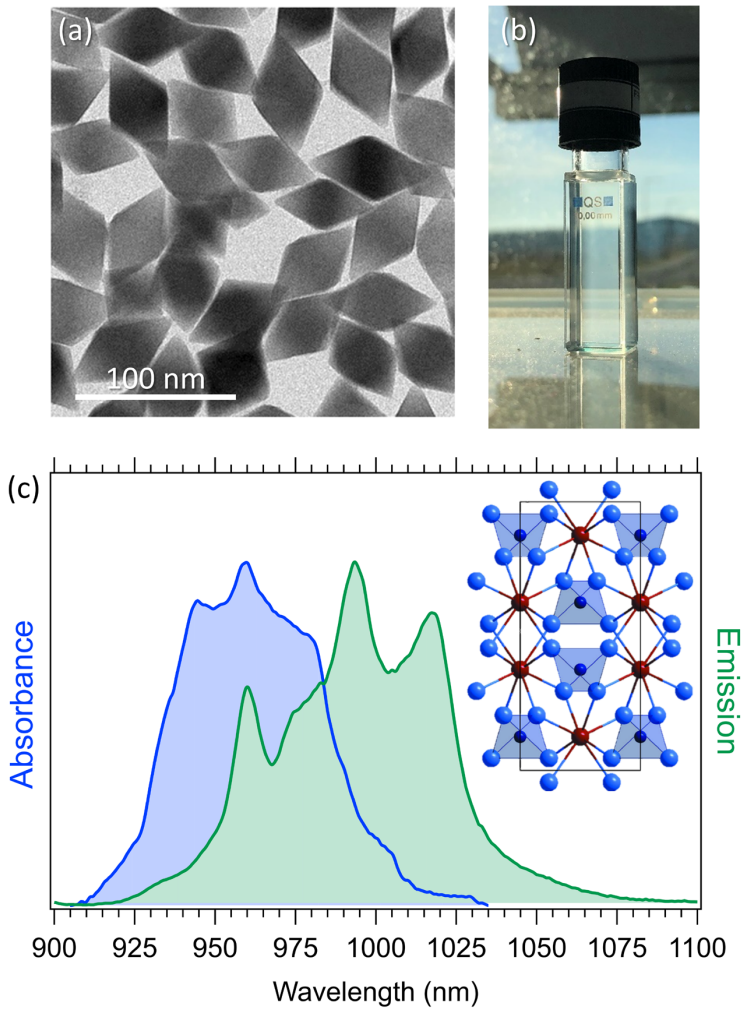


Figure 1.13. Overview of ytterbium doped lithium yttrium fluoride ($Yb:LiYF_4$) (a) TEM images of $LiYbF_4$ NC cores. (b) A photograph of a typical YLF NC dispersion in methanol, showcasing the scattering of light. (c) An absorption and emission spectrum of Yb:YLF NCs with in the top right corner the Scheelite unit cell of YLF, adapted from Schustereit *et al.*[33]

1.9 Outline of this Thesis and Motivation for the Broad Pallet of Topics Covered in this PhD Thesis

Near the end of 2017, I was asked whether I would be interested in working on the TEQ project. After completing my master's thesis in Arjan Houtepen's group and a 3-month research visit at the Italian Institute of Technology (IIT) under the guidance of Liberato Manna, I started my PhD project at TU Delft in July 2018. At that time, we decided that the likelihood of performing PhD-worthy research on solely the TEQ particles (Yb:YLF) had its risks, as we were not sure that there were significant scientific challenges to tackle in this project. The decision was made that, apart from synthesizing and optimizing TEQ particles for the group of Peter Barker at UCL, we would also work on semiconductor NCs. In hindsight a "mistake" and an opportunity, that opened the possibility to diverge, understand and explore not only the synthesis of the materials required for TEQ but also the field of semiconductor NCs where both of my promotors, Arjan Houtepen and Liberato Manna, as well as the Optoelectronic Materials research group, have significantly more experience in. A mistake, as I have shown in this thesis that significant improvements in both the understanding and synthesis of Yb:YLF NCs are possible. But more so an opportunity, as working on these more complex "side projects" allowed me to broaden my scope with additional research topics, including the synthesis of core-shell InP QDs and electrochemical doping of perovskite NCs. Therefore, this thesis consists of five chapters describing three significantly different topics, but all based on optically active NCs with a broad variety of shapes and applications.

In Chapter 2, the nucleation and growth of Yb:YLF core NCs is explained, forming the foundation of the main project on Yb:YLF NCs for optical refrigeration. Here we investigate how YLF NCs form from their precursors, and show that the formation of YLF starts from a mostly amorphous nanomaterial, only showing short-range YF_3 order. Over time this material crystallizes as YLF. However, if not collected in time, the YLF NCs degrade and the formation of LiF is observed. If collected in time, these NCs showcase a high PLQY, necessary for optical refrigeration. As mentioned in Section 1.4, most PL-quenching occurs on the NC surface. For Yb:YLF, this effect is strong at higher doping concentrations due to increasingly efficient energy transfer between Yb^{3+} ions as will be shown in Chapter 3. However, Yb^{3+} ions can still relatively easily be isolated from the exterior by growing an undoped YLF-shell around the Yb-doped core, facilitated by the absence of a lattice mismatch. In this chapter we show that by removing all PL-quenching factors, unity PLQY can be obtained within the error of our measurements for YLF@Yb:YLF NCs for all Yb-doping fractions up a full $LiYF_4$@$LiYbF_4$ NC sample.

In Chapter 4, we have grown a new type of shell material on In(Zn)P QDs to improve the lattice match of the core-shell interface. As previously explained, shells on semiconductor-based QDs generally require more engineering than the insulating NCs doped with luminescent ions. For these In(Zn)P QDs, lattice matched $Zn_xMg_{1-x}Se$ was grown around In(Zn)P QDs. To prevent this very reactive shell material from reacting with its environment, an extra ZnS shell was grown. We show an improved color purity for samples with higher Mg-fractions in the shell, and explain this as an effect of an improved core-shell lattice match.

1

Chapters 5 and 6 are devoted to understanding the electrochemical (in)stability and the (im)possibility to dope $CsPbBr_3$ NCs with supplied electrons or holes. In Chapter 5, we show electrochemical p-doping of $CsPbBr_3$ NC thin films by a continuous supply of holes, indicating that p-doping of $CsPbBr_3$ is possible but unstable in the long term. These stability problems are worse when supplying electrons instead of holes to the system, as we show in Chapter 6. In this chapter we systematically study what limits the stability of electrochemical n-doping, resulting in the cathodic decomposition of the NCs. We show that the electrochemical reduction of lead species in solution is the culprit, and explain that using electrolyte solvents with the lowest solubility for any lead species results in the most stable measurements.

References

1. Bechu, A.; Liao, J.; Huang, C.; Ahn, C.; McKeague, M.; Ghoshal, S.; Moores, A. Cadmium-Containing Quantum Dots Used in Electronic Displays: Implications for Toxicity and Environmental Transformations. ACS Appl. Nano Mater. 2021, 4 (8), 8417–8428.
2. European Union. Environment : EU Ban on Hazardous Substances in Electrical and Electronic Products Takes Effect; 2006.
3. Won, Y.-H.; Cho, O.; Kim, T.; Chung, D.-Y.; Kim, T.; Chung, H.; Jang, H.; Lee, J.; Kim, D.; Jang, E. Highly Efficient and Stable InP/ZnSe/ZnS Quantum Dot
4. Light-Emitting Diodes. Nature 2019, 575 (7784), 634–638.
   Zhao, Y.; Xue, D.; Wang, J.; Lu, M.; Shen, X.; Gao, X.; Yu, W. W.; Bai, X. Smart Quantum Dot LEDs with Simulated Solar Spectrum for Intelligent Lighting. Nanotechnology 2020, 31 (50), 505207.
5. Shirasaki, Y.; Supran, G. J.; Bawendi, M. G.; Bulović, V. Emergence of Colloidal Quantum-Dot Light-Emitting Technologies. Nat. Photonics 2013, 7 (1), 13–23.
6. Geuchies, J. J.; Brynjarsson, B.; Grimaldi, G.; Gudjonsdottir, S.; Van Der Stam, W.; Evers, W. H.; Houtepen, A. J. Quantitative Electrochemical Control over Optical Gain in Quantum-Dot Solids. ACS Nano 2021, 15 (1), 377–386.
7. Zhou, J.; Huang, J. Photodetectors Based on Organic-Inorganic Hybrid Lead Halide Perovskites. Adv. Sci. 2018, 5 (1), 1700256.
8. Crisp, R. W.; Kirkwood, N.; Grimaldi, G.; Kinge, S.; Siebbeles, L. D. A.; Houtepen, A. J. Highly Photoconductive InP Quantum Dots Films and Solar Cells. ACS Appl. Energy Mater. 2018, 1 (11), 6569–6576.
9. Yuan, J.; Hazarika, A.; Zhao, Q.; Ling, X.; Moot, T.; Ma, W.; Luther, J. M. Metal Halide Perovskites in Quantum Dot Solar Cells: Progress and Prospects. Joule 2020, 4 (6), 1160–1185.
10. Rademacher, M.; Gosling, J.; Pontin, A.; Toroš, M.; Mulder, J. T.; Houtepen, A. J.; Barker, P. F. Measurement of Single Nanoparticle Anisotropy by Laser Induced Optical Alignment and Rayleigh Scattering for Determining Particle Morphology. Appl. Phys. Lett. 2022, 121 (22), 221102.
11. Li, H.; Wang, X.; Li, X.; Zeng, S.; Chen, G. Clearable Shortwave-Infrared-Emitting $NaErF_4$ Nanoparticles for Noninvasive Dynamic Vascular Imaging. Chem. Mater. 2020, 32 (8), 3365–3375.
12. Skripka, A.; Benayas, A.; Marin, R.; Canton, P.; Hemmer, E.; Vetrone, F. Double

Rare-Earth Nanothermometer in Aqueous Media: Opening the Third Optical Transparency Window to Temperature Sensing. Nanoscale 2017, 9 (9), 3079–3085.

13. Panov, N.; Marin, R.; Hemmer, E. Microwave-Assisted Solvothermal Synthesis of Upconverting and Downshifting Rare-Earth-Doped $LiYF_4$ Microparticles. Inorg. Chem. 2018, 57 (23), 14920–14929.
14. Sandrock, T.; Heumann, E.; Huber, G.; Chai, B. H. T. Continuous-Wave Pr, Yb:$LiYF_4$ Upconversion Laser in the Red Spectral Range at Room Temperature. In Advanced Solid State Lasers; OSA: Washington, D.C., 1996; Vol. I, p PM1.
15. Tsang, M. Y.; Fałat, P.; Antoniak, M. A.; Ziniuk, R.; Zelewski, S. J.; Samoć, M.; Nyk, M.; Qu, J.; Ohulchanskyy, T. Y.; Wawrzyńczyk, D. Pr^{3+} Doped $NaYF_4$ and $LiYF_4$ Nanocrystals Combining Visible-to-UVC Upconversion and NIR-to-NIR-II Downconversion Luminescence Emissions for Biomedical Applications. Nanoscale 2022, 14 (39), 14770–14778.
16. Marra, P. Theoretical Approach to Direct Resonant Inelastic X-Ray Scattering on Magnets and Superconductors, Technical University Dresden, 2016.
17. Denning, E. V.; Iles-Smith, J.; Gregersen, N.; Mork, J. Phonon Effects in Quantum Dot Single-Photon Sources. Opt. Mater. Express 2020, 10 (1), 222.
18. Luong, M. V.; Empizo, M. J. F.; Gabayno, J. L. F.; Minami, Y.; Yamanoi, K.; Shimizu, T.; Sarukura, N.; Pham, M. H.; Nguyen, H. D.; Steenbergen, K. G.; Schwerdtfeger, P.; Cadatal-Raduban, M. Direct Band Gap Tunability of the $LiYF_4$ Crystal through High-Pressure Applications. Comput. Mater. Sci. 2018, 153 (July), 431–437.
19. Chung, S.; Wen, X.; Huang, S.; Gupta, N.; Conibeer, G.; Shrestha, S.; Harada, T.; Kee, T. W. Nanosecond Long Excited State Lifetimes Observed in Hafnium Nitride. Sol. Energy Mater. Sol. Cells 2017, 169 (March), 13–18.
20. Mei, S.; Zhou, J.; Sun, H. T.; Cai, Y.; Sun, L. D.; Jin, D.; Yan, C. H. Networking State of Ytterbium Ions Probing the Origin of Luminescence Quenching and Activation in Nanocrystals. Adv. Sci. 2021, 8 (6), 1–9.
21. Arppe, R.; Hyppänen, I.; Perälä, N.; Peltomaa, R.; Kaiser, M.; Würth, C.; Christ, S.; Resch-Genger, U.; Schäferling, M.; Soukka, T. Quenching of the Upconversion Luminescence of $NaYF_4$:Yb^{3+}, Er^{3+} and $NaYF_4$:Yb^{3+}, Tm^{3+} Nanophosphors by Water: The Role of the Sensitizer Yb^{3+} in Non-Radiative Relaxation. Nanoscale 2015, 7 (27), 11746–11757.
22. Van Der Stam, W.; Grimaldi, G.; Geuchies, J. J.; Gudjonsdottir, S.; Van Uffelen, P. T.; Van Overeem, M.; Brynjarsson, B.; Kirkwood, N.; Houtepen, A. J. Electrochemical Modulation of the Photophysics of Surface-Localized Trap States in Core/Shell/(Shell) Quantum Dot Films. Chem. Mater. 2019, 31 (20), 8484–8493.
23. Wang, F.; Wang, J.; Liu, X. Direct Evidence of a Surface Quenching Effect on Size-Dependent Luminescence of Upconversion Nanoparticles. Angew. Chemie Int. Ed. 2010, 49 (41), 7456–7460.
24. Zhao, J.; Lu, Z.; Yin, Y.; McRae, C.; Piper, J. A.; Dawes, J. M.; Jin, D.; Goldys, E. M. Upconversion Luminescence with Tunable Lifetime in $NaYF_4$:Yb,Er Nanocrystals: Role of Nanocrystal Size. Nanoscale 2013, 5 (3), 944–952.
25. Rahman, A. T. M. A.; Barker, P. F. Laser Refrigeration, Alignment and Rotation of Levitated Yb^{3+}:YLF Nanocrystals. Nat. Photonics 2017, 11 (10), 634–638.
26. Melgaard, S. D.; Albrecht, A. R.; Hehlen, M. P.; Sheik-Bahae, M. Solid-State Optical Refrigeration to Sub-100 Kelvin Regime. Sci. Rep. 2016, 6 (1), 20380.

27. Auzel, F. On the Maximum Splitting of the ($^2F_{7/2}$) Ground State in Yb^{3+}-Doped Solid State Laser Materials. J. Lumin. 2001, 93 (2), 129–135.
28. Demirbas, U.; Thesinga, J.; Kellert, M.; Kärtner, F. X.; Pergament, M. Detailed Investigation of Absorption, Emission and Gain in Yb:YLF in the 78–300 K Range. Opt. Mater. Express 2021, 11 (2), 250.
29. Mulder, J. T.; Kirkwood, N.; De Trizio, L.; Li, C.; Bals, S.; Manna, L.; Houtepen, A. J. Developing Lattice Matched ZnMgSe Shells on InZnP Quantum Dots for Phosphor Applications. ACS Appl. Nano Mater. 2020, 3 (4), 3859–3867.
30. García, G.; Sánchez-Palencia, P.; Palacios, P.; Wahnón, P. Transition Metal-Hyperdoped InP Semiconductors as Efficient Solar Absorber Materials. Nanomaterials 2020, 10 (2), 283.
31. Akkerman, Q. A.; Rainò, G.; Kovalenko, M. V.; Manna, L. Genesis, Challenges and Opportunities for Colloidal Lead Halide Perovskite Nanocrystals. Nat. Mater. 2018, 17 (5), 394–405.
32. Luong, M. V.; Empizo, M. J. F.; Gabayno, J. L. F.; Minami, Y.; Yamanoi, K.; Shimizu, T.; Sarukura, N.; Pham, M. H.; Nguyen, H. D.; Steenbergen, K. G.; Schwerdtfeger, P.; Cadatal-Raduban, M. Direct Band Gap Tunability of the $LiYF_4$ Crystal through High-Pressure Applications. Comput. Mater. Sci. 2018, 153 (April), 431–437.
33. Schustereit, T.; Schleid, T.; Hartenbach, I. The Defect Scheelite-Type Lanthanum(III) Ortho-Oxidomolybdate(VI) $La_{0.667}[MoO_4]$. Acta Crystallogr. Sect. E Struct. Reports Online 2013, 69 (2), i7–i7.

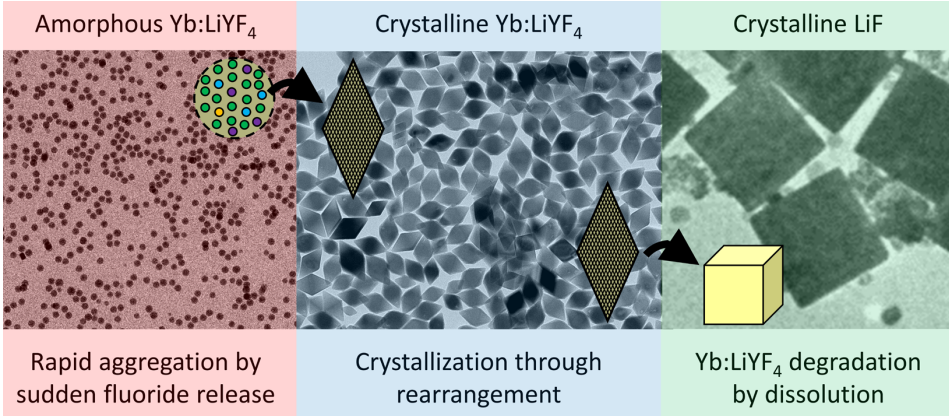
1

2

Chapter 2

Nucleation and Growth of Bipyramidal Yb:$LiYF_4$ Nanocrystals

Growing Up in a Hot Environment



Ytterbium-doped $LiYF_4$ (Yb:YLF) is commonly used for laser applications, photon upconversion and optical refrigeration. When synthesized as nanocrystals (NCs), this material is also of interest for biological applications and fundamental physical studies. Until now, it was unclear how Yb:YLF NCs grow from their ionic precursors into tetragonal NCs with a well-defined, bipyramidal shape. In this work, we show that the formation of bipyramidal Yb:YLF NCs is a multistep process starting with the formation of amorphous Yb:YLF spheres. Over time, these spheres grow via Ostwald ripening and crystallize, resulting in bipyramidal Yb:YLF NCs. We further show that prolonged heating of the NCs results in the degradation of the NCs, observed by the presence of large LiF cubes and small, irregular Yb:YLF NCs.

This chapter is based on: Jence T. Mulder, Kellie Jenkinson, Stefano Toso, Mirko Prato, Wiel H. Evers, Sara Bals, Liberato Manna, Arjan J. Houtepen. Submitted.

2

2.1 Introduction

Ytterbium-doped $LiYF_4$ (Yb:YLF) is an interesting material for a broad range of optical applications. As bulk Yb:YLF, it is used in lasers,[1–3] for photon upconversion (when co-doped with other lanthanide ions such as Pr^{3+}, Ho^{3+}, Er^{3+} or Tm^{3+})[4–8] and optical refrigeration[9–11]. When synthesized as nanocrystals (NCs), its applicability in biological[12–16] and physical studies[17–21] increases significantly. This becomes especially relevant when NC samples with a monodisperse size distribution[22–24] and excellent optical properties (*e.g.* a high photoluminescence quantum yield[22,25]) are synthesized.

Much work has been done on optimizing the synthesis of doped YLF NCs through a variety of routes, often yielding NCs with a bipyramidal shape (*vide infra*).[22,23,25–32] Little is known, however, about the complex nucleation and growth mechanisms of this material, with only a few works focusing on the nucleation stage.[27,29,30,33] When ammonium fluoride is used as the fluoride precursor, instead, reports mention that LiF[29] or YF_3[19,34] nucleate first. Reports using the thermal decomposition of trifluoroacetate (TFA) as the fluoride precursor show the initial formation of semi-spherical YLF particles.[27,30] None of these reports however discusses how these initial particles grow into a monodisperse ensemble of bipyramidal NCs. A better understanding of these important stages of NC formation may result in increased control of Yb:YLF NC synthesis and improvement of the quality of the obtained NC samples. This for example increases the applicability of Yb:YLF NCs for size- and shape-specific studies significantly.[18,21]

In this work, we report the investigation of the nucleation and growth of Yb:YLF NCs using TFA precursors. We have followed the synthesis by taking aliquots of the synthesis mixture and analyzed the recovered materials using transmission electron microscopy (TEM), including high-angle annular dark-field scanning transmission electron microscopy (HAADF-STEM), electron diffraction (ED) and elemental analysis through energy dispersive x-ray spectroscopy (EDX). ED and x-ray diffraction (XRD) of the initially formed spherical particles did not show any clear signs of crystallinity. We identified that these initial particles are amorphous, formed as a product of rapid aggregation. In agreement with similar works on hydrothermal syntheses of YLF, we initially observe local short-ranged YF_3 networks. However, in contrast to what was previously reported, we show that the particles already contain Li^+ ions (approximately in a ratio expected for Yb:YLF). These particles thus do not consist of Yb:YF_3 but of amorphous Yb:YLF, where the constituent ions are not yet arranged in the regular pattern of the YLF crystal structure. Over time, the Yb:YLF spheres crystallize into bipyramidal NCs, the intended product.

When the synthesis was extended for a day, large cube-shaped LiF crystals were recovered along with small, irregular Yb:YLF NCs. As along the LiF cubes no YF_3 was found, or could be synthesized using only $Y(TFA)_3$, we explain that the Yb:YLF NCs disintegrated due to dissolution of the material. As we furthermore show that LiF is much less soluble than YF_3, we rationalize that LiF recrystallizes and that the yttrium ions are dissolved in the synthesis solvents. This suggest that the thermodynamic ground state of the system in these conditions is formed by LiF crystals and dissolved Y^{3+} and F^- ions. The YLF NCs are a metastable intermediate that forms due to the more rapid kinetics of the nucleation.

As the initially formed, amorphous Yb:YLF spheres can be isolated and purified before the crystallization into YLF is complete, we recommend further studies on amorphous spherical Yb:YLF particles as low-reactivity Yb:YLF precursors. These particles may, when undoped, especially be useful for *e.g.* novel shelling methods.

2.2 Snapshots of an Yb:YLF Nanocrystal Synthesis

The synthesis of Yb:YLF NCs is carried out using a protocol we recently reported,[22] which is based on the synthesis of Yi *et al.*[33] with an additional precursor drying step from Homann *et al.*[35] which we modified for the TFA-based synthesis method. The synthesis starts when anhydrous metal TFA salts ($M^{x+}(TFA)_x$, $M = Li^+, Y^{3+}, Yb^{3+}$) are heated up in a high boiling point solvent (1-octadecene) with the addition of growth-controlling ligands (oleic acid). The TFA anion thermally decomposes between 267 °C[36] and 310 °C[37] releasing fluoride anions, as described in Equation 2.1.

$$3\ CF_3COO^- \rightarrow 3\ F^- + (CF_3COO)_2O + CO + CO_2 \qquad (2.1)$$

The temperature is increased stepwise (5 °C/ 30 s) to 330 °C, at which point all TFA is decomposed,[36] and the solution is maintained for an additional 25 minutes at this temperature to allow the NCs to grow. After this, the synthesis mixture is cooled down to stop further growth, and subsequently the formed NCs are recovered.

The release of the fluoride anions results in the supersaturation of one or more fluoride compounds, hence inducing the nucleation of the fluoride based NCs. As Yb:$LiYF_4$ is a ternary compound, and Yb^{3+}, Y^{3+}, Li^+ and F^- ions are all present in the reaction mixture, it is not obvious which material, LiF, YF_3, YbF_3 or Yb:YLF will form. Following the classical nucleation theory,[38,39] the activation energy ΔG for the nucleation of a spherical particle, which is composed of a volume free energy term and a surface energy term, equals:

$$\Delta G(r) = \frac{-4\pi r^3 \cdot k_B \cdot T \cdot \sigma}{3V_m} + 4\pi r^2 \cdot \gamma \qquad (2.2)$$

Where: r = radius of the nucleus, k_B = Boltzmann constant, T = temperature, σ = supersaturation = $(\mu_{ss}-\mu_{eq})/(k_B \cdot T)$, where μ_{ss} and μ_{eq} are the supersaturation and equilibrium chemical potentials, V_m = monomer volume and γ = surface tension.

The activation energy for nucleation corresponds to the maximum in the curve given by Equation 2.2, and is given by:

$$\Delta G^{\#}_{nucleation} = \frac{-16\pi r^3 \cdot V_m^2}{3k_B^2 \cdot T^2 \cdot \sigma^2} \qquad (2.3)$$

From here, it is clear that at a fixed synthesis temperature the surface tension and the supersaturation (or, at fixed precursor concentration, the solubility) are the most important parameters in the nucleation rate of NCs, and will determine which material (LiF, YF_3, YbF_3 or Yb:YLF) nucleates first.

To investigate the nucleation and growth of Yb:YLF NCs, a synthesis was followed by taking aliquots at different time steps, as shown in Figures 2.1 and A2.1. We first discuss

the general observation from TEM imaging and then go into a more detailed analysis. Aliquots taken up to 290 °C did not yield any particles, thus it can be concluded that the concentration of the released fluoride ions through thermal decomposition is up to this point too low to initiate the nucleation of the NCs. When reaching 300 °C, many spherical NCs of roughly 7 nm in diameter are recovered, as shown in Figure 2.1a. This indicates that at this temperature, lower than reported in some studies for $Y(TFA)_3$,[37] sufficient TFA-precursors have decomposed to initiate the nucleation. At 310 °C (Figure 2.1b) all NCs have grown, suggesting predominant growth from free precursors in solution, although the distribution splits in slightly larger and slightly smaller NCs (11.0 and 10.3

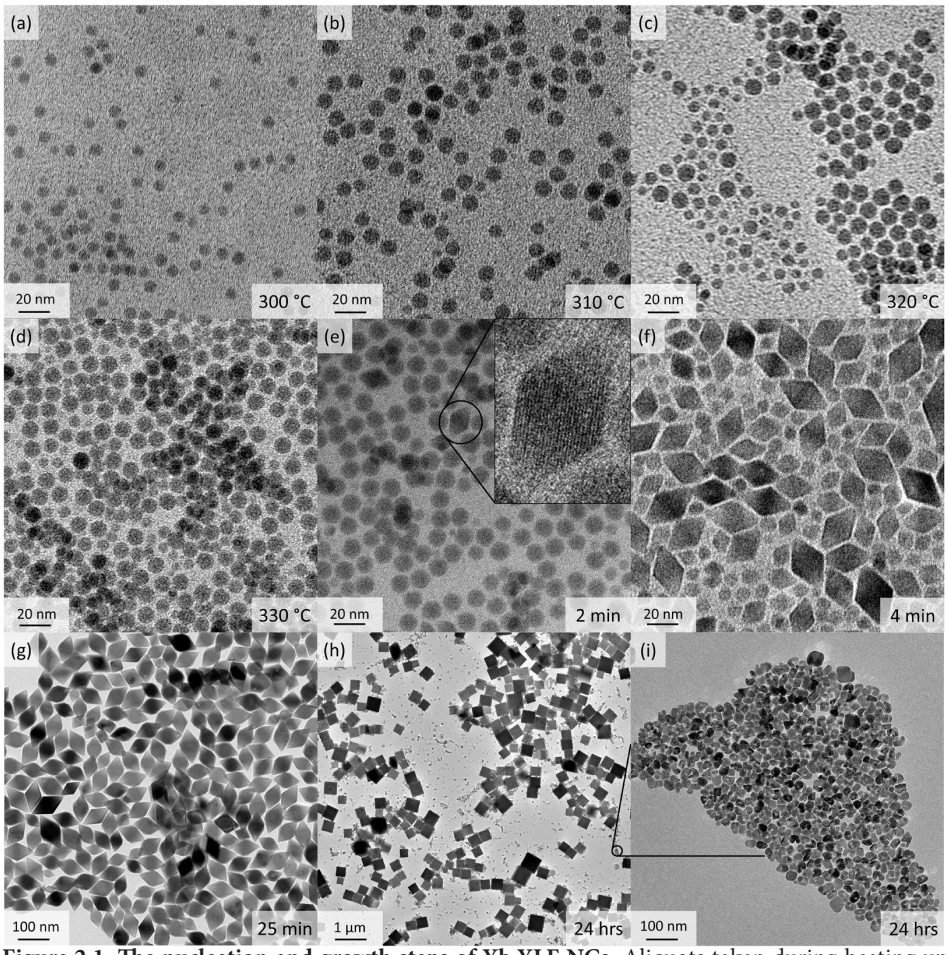


Figure 2.1. The nucleation and growth steps of Yb:YLF NCs. Aliquots taken during heating up at (a) 300 °C, (b) 310 °C, (c) 320 °C and (d) 330 °C, showcase the different stages of nucleation and growth of the Yb:YLF nanospheres. Aliquots taken during the NC growth at 330 °C, after (e) 2 minutes and (f) 4 minutes, highlight their transformation to crystalline NCs (see inset (e)). (g) After 25 minutes, the synthesis mixture is cooled down and after purification, the grown Yb:YLF NCs are recovered. (h) If the synthesis is continued at 330 °C for 24 hours, large cubic crystals are found, together with (i) small particles.

nm respectively). At 320 °C (Figure 2.1c) a bimodal size distribution of spheres is clearly visible, where the smaller particles (7.0 nm) are smaller than those observed at 310 °C. This implies that the system has entered the Ostwald ripening regime, where larger particles grow through accretion from monomers that are being released from the smaller ones. Oswald ripening causes a broadening of the size distribution, but in its simplest treatment it should not lead to a bimodal distribution. However, in real-world scenarios where local interactions among dissolving/coarsening particles cannot be neglected, bimodal particle distributions have been described.[40] Due to a large number of unknown parameters, we cannot pinpoint how or why this is the case for these nanospheres.

When reaching 330 °C, most of the small spheres have disappeared. After two minutes, the first crystalline, bipyramidal NCs appear (see inset Figure 2.1e). After four minutes, the majority of the NCs consist of crystalline bipyramids, although not yet with the narrowest size distribution. After 25 minutes (Figure 2.1g) a NC sample clear of any spherical particles and with a narrow size distribution is obtained. If the solution is kept at 330 °C for 24 hours, almost micron-sized, cube-shaped crystals are obtained together with a large amount of small, irregularly shaped but crystalline particles, as shown in Figures 2.1h and i.

These observations raise a number of questions. First of all, it is yet unclear what the small spheres that nucleate first are composed of. Understanding their composition is key, as these particles form the basis from which the Yb:YLF NCs grow. Secondly, is it not straightforward how spheres transform into strongly faceted Yb:YLF NCs. And thirdly, a clarification is required on how bipyramidal Yb:YLF NCs finally transform into cube-shaped crystals. Below, we investigate the various synthesis stages in more detail to answer these questions.

2.3 Analysis of the Initial Nanospheres

HAADF-STEM images of the first sample of spheres, recovered at 300 °C, are shown in Figures 2.2 and A2.2. From EDX measurements (Figure 2.2a–c) it is clear that the spheres contain fluoride, yttrium and ytterbium ions with a uniform Y:Yb distribution (Appendix 2.3). Lithium, however, is too light to be measured with EDX (atomic number Z = 3). The spheres can thus either consist of Yb:YF_3 or Yb:YLF. To better understand the composition of the spheres, ED and XRD were performed (on a separately synthesized scaled-up batch of spheres), as shown in Figure 2.2d. The diffractograms do not show any sharp diffraction peaks, even though the NCs are large enough to give defined diffraction signals. As both methods give the same diffraction pattern, which overlaps best with an XRD of YF_3, we conclude that the particles do have short-range YF_3-like order. In agreement with this conclusion, XRD patterns simulated through the application of the Debye scattering equation to isotropic crystalline domains of YF_3 about 1.5-2 unit cells in size show strong similarities with the experimental data, while similar simulations performed for YLF do not provide a reasonable match (Appendix 2.5). Together with the first frame of the HAADF-STEM image (Figure 2.2e), it can be concluded that the spheres do not show signs of high-order crystallinity and are thus mostly amorphous (see also Appendix 2.6). This is also in line with photoluminescence measurements (Appendix 2.7), that show a single sharp emission peak at 976 nm. If the material is crystalline YLF, three emission peaks, the

signatures of crystal field splitting on the Yb^{3+} transitions, are expected (Appendix 2.7). Instead, the emission spectrum is similar to that of free Yb^{3+} ions,[41] confirming that the Yb^{3+} ions are not yet incorporated in a crystalline YLF host configuration.

We can however conclude that the nanospheres are composed of amorphous Yb:YLF, as in a later frame of the HAADF-STEM measurement (Figure 2.2f and Appendix 2.8) clear crystal planes are visible. This indicates that the spheres partially crystallized under the electron beam (acceleration voltage of 300 kV). After crystallization, the lattice spacing corresponding to the (112) plane of YLF is observed (Appendices 2.8, 2.9 and 2.10). X-ray photoelectron spectroscopy (XPS) measurements furthermore confirm the presence of Li^{+} ions (Li:Y/Yb:F = 1 : 1.5 : 5.4) (Appendix 2.11). Additionally, thermal annealing of the spheres (which were washing thrice, in order to remove any non-incorporated ions) results in the formation of crystalline material, as shown in Figure A2.13c. In agreement with the XPS results, the XRD of the annealed spheres shows a strong diffraction signal corresponding to Yb:YLF, with the presence of a minor fraction of YF_3. From the obtained lattice spacing, XPS, and XRD after annealing we conclude that the original nanospheres consist of amorphous Yb:YLF.

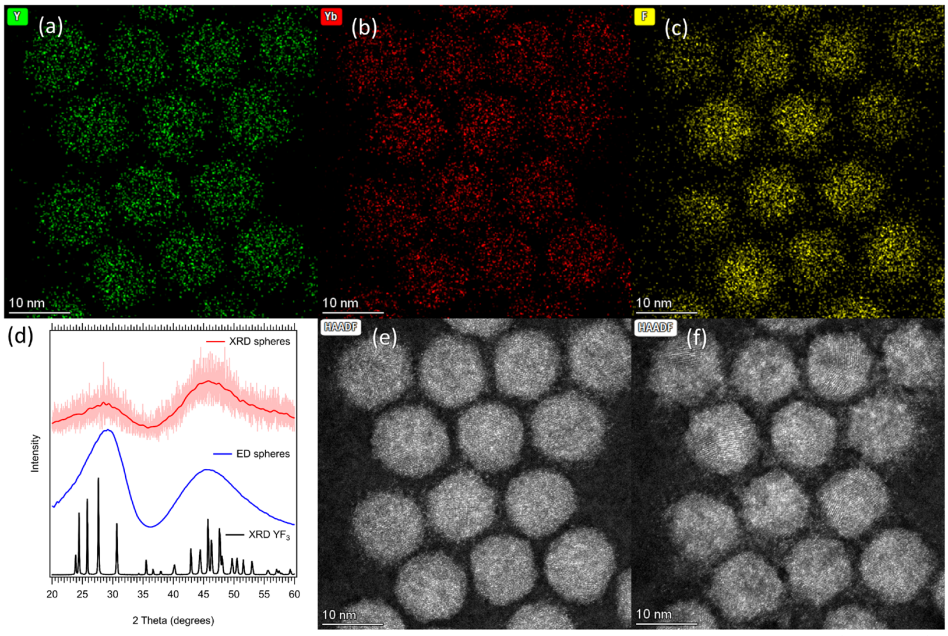


Figure 2.2. Analysis of the initially nucleated nanospheres. (a) EDX-measurements showing the presence and location of yttrium, (b) ytterbium and (c) fluoride ions in the Yb:YLF nanospheres. (d) ED and XRD both show no signs of sharp reflections indicating the material is mostly amorphous. There is a similar structure in both sphere-measurements, which overlaps well with an XRD of YF_3. This indicates that there is short-range Y-F order in the spheres, however the particle is still mostly amorphous. (e) The first and (f) twelfth frame of an HAADF-STEM measurement, showing the crystallization of the initially amorphous nanospheres (e) as a result of electron beam exposure. From the crystallized particles (f), the lattice spacing of Yb:YLF was obtained.

We explain the formation of amorphous Yb:YLF as a result of a rapid nucleation of Yb:YLF once fluoride ions are released, capturing the ions in the location where they arrive without annealing into a crystalline structure.

HAADF-STEM measurements on a sample isolated at 320 °C, similar to Figure 2.1c, show no difference between the smaller and larger spheres in the bimodal size distribution (see Figure A2.14). Therefore, we conclude that both sizes consist of amorphous Yb:YLF, hence no second material has nucleated. To answer why the different sizes of spheres are found, we performed a size analysis on the TEM images that are shown Figure 2.1a–e.

2.4 Growth *via* Ostwald Ripening and Metamorphosis into Bipyramidal Nanocrystals

Figure 2.3 shows the size distributions of the first growth stages by fitting a lognormal distribution to the distribution of measured diameters obtained from the TEM-images. From here, we observe that initially all nanospheres grow equally (Figure 2.3a). This indicates that volume is added to all NCs and that, therefore, growth takes place via the addition of monomers from a supersaturated solution. Subsequently, a bimodal distribution of diameters is observed, where roughly half of the spheres reduce in size and half of the spheres grow (Figure 2.3b). Over time, the smaller nanospheres, which are abundant at first (Figures 2.3c and A2.15), reduce in number until solely the larger spheres are left (Figures 2.3d and e). This clearly shows that growth becomes dominated by the dissolution of the smaller particles. Most likely the concentration of free monomers

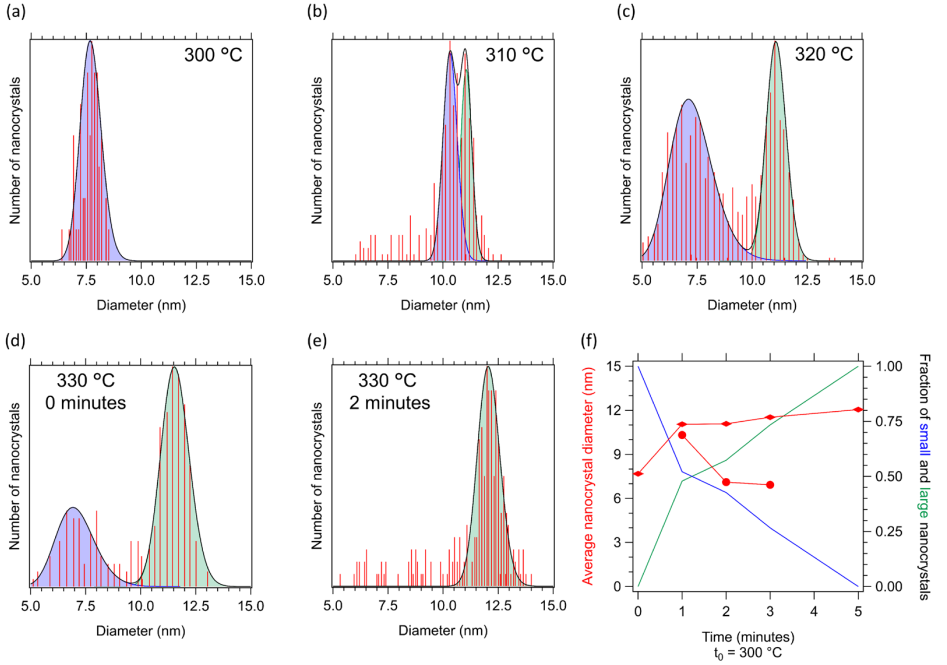


Figure 2.3. (a-e) Size distributions of NCs based on the TEM images shown in Figure 2.1a–e. All fits are lognormal plots, used to determine the in (f) shown average size and sphere ratios.

is depleted to the equilibrium concentration of the Yb:YLF spheres after a temperature of 310 °C is reached and further growth can only take place via Ostwald ripening. Around the same time that the small spheres are practically gone, the first crystalline YLF NCs appear. As the volume of the large spheres and the initial Yb:YLF NCs are similar (Appendix 2.14), we conclude that the YF_3 structures have thermodynamically rearranged to form crystalline Yb:YLF NCs. Over time, all spheres disappear and the tetragonal Yb:YLF NCs increase in concentration and size.

2.5 From Bipyramidal to Cubic Crystals

When keeping the synthesis mixture at 330 °C for 24 hours instead of the usual 25 minutes, cube-shaped, almost micron-sized crystals were found (shown in Figure 2.4a). EDX measurements (Figure 2.4b) showed no presence of yttrium or ytterbium ions, but a strong fluoride signal was recorded. The analysis of a single crystal ED (Figure 2.4c and d) indicated that the crystal has a cubic crystal structure, for which the reflections correspond with those for LiF. Therefore, either (1) LiF crystals nucleated at longer timescales, from residual free Li^+ and F^- ions, or (2) the Yb:YLF NCs dissolved and the freed monomers

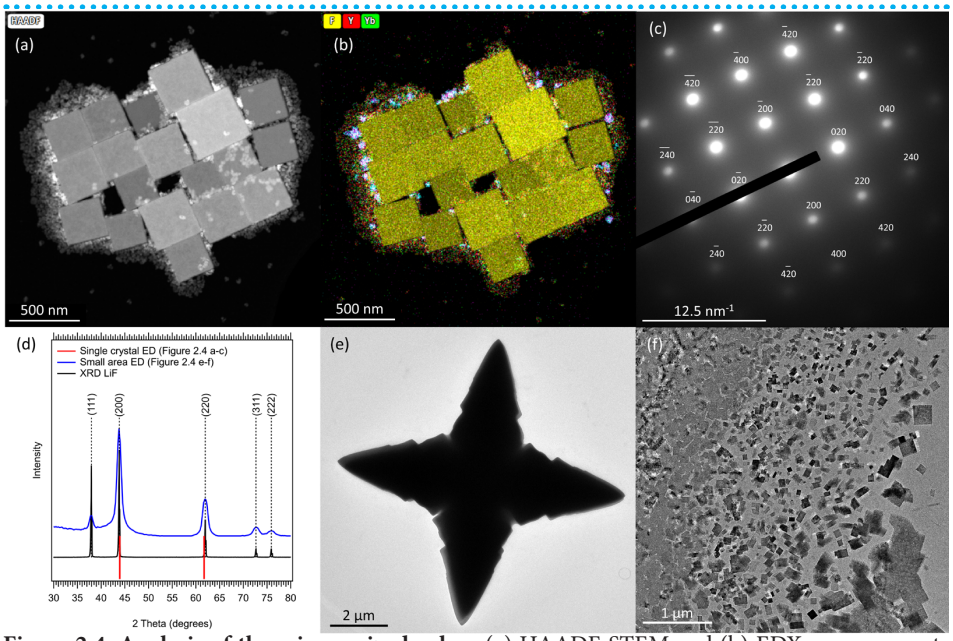


Figure 2.4. Analysis of the micron-sized cubes. (a) HAADF-STEM and (b) EDX measurements performed on the large cubic crystals, showcasing the absence of yttrium and ytterbium in the material. (c) Single crystal ED shows that the material has a face centered cubic crystal structure. The analysis of this ED, shown for the (200) and (220) reflections in (d) confirms that the cubes are composed of LiF. (e) Performing a synthesis identical to the Yb:YLF NC synthesis, but with solely LiTFA, yields large, shuriken-shaped LiF crystals. The crystal shown here was recovered during heating up when reaching 300 °C, the temperature where otherwise the small amorphous Yb:YLF nanospheres are recovered. (f) The shuriken-shaped crystals disintegrated swiftly under the electron beam, resulting in the formation of small cubic particles. The small area ED of these particles, shown in Figure 2.4d, confirms that this is, as expected, LiF.

recrystallized, forming LiF. As apart from small, irregularly shaped Yb:YLF NCs with a large surface area (Appendices 2.15 and 2.16) no bipyramidal Yb:YLF NCs (as shown in Figure 2.1g) were found, the LiF is most likely a product of the decomposition of the Yb:YLF NCs. The irregularly shaped Yb:YLF NCs are in that case remaining fragments of partially dissolved Yb:YLF NCs. This is furthermore in line with the observed shapes of the fragments, which have strong resemblance with (parts of) the original bipyramidal NCs.

Remarkably, no Yb:YF_3 was found, which would be the expected leftover material after removing LiF from Yb:YLF. This suggests that Yb:YF_3 is soluble in the synthesis mixture without the presence of free Li^+. To gain more insight, we attempted to synthesize LiF by performing an identical Yb:YLF NC synthesis (keeping [TFA] the same), but then by using only LiTFA. Starting at 285 °C, which is earlier than the first observed nuclei during the Yb:YLF NC synthesis, very large and out of equilibrium LiF crystals (*i.e.* with a large surface over volume ratio), resembling shurikens, were obtained (as shown in Figure 2.4e and Figure A2.19). This shows that the nucleation of LiF is slow, hence only few nuclei form which can then grow very large from the initial growth from solution. These crystals were swiftly affected by the electron beam, disintegrating into cubic LiF crystals (Figure 2.4f). These observations are all in line with a much higher activation barrier for LiF nucleation than that of Yb:YLF, determined by the surface tension γ, hence LiF nuclei are not observed in a regular Yb:YLF NC synthesis.

2.6 Proposed Nucleation and Degradation Model and Discussion

The observations and analyses we discussed so far are summarized in Figure 2.5. In short, all the cations that are free in solution (i.e. Li^+, Y^{3+} and Yb^{3+}) rapidly aggregate once sufficient F^- ions are released due to thermal decomposition of the TFA anion. The aggregation is random, and faster than the crystallization, so that all ions are incorporated into the amorphous spheres at the location where they arrive. Although ED and XRD show the presence of short-range YF_3 order, XPS reveals that the spheres contain a large fraction of lithium ions (Li:Y/Yb:F = 1:1.5:5.4). As, moreover, thermal annealing of the spheres shows that this material crystallizes as Yb:YLF, we conclude that the spheres consist of amorphous Yb:YLF. Over time, the spheres grow via Ostwald ripening, until the ions are incorporated into the YLF lattice positions (*i.e.* crystallization). At this moment, crystalline bipyramidal YLF NCs are formed. These NCs continue to grow due to the supply of ions from the amorphous spheres, until all spheres have either crystallized or dissolved. If, however, the temperature is not lowered, but the synthesis mixture is kept at 330 °C for one day, large LiF cubes and residual Yb:YLF fragments are observed. We conclude that this is caused by the slow dissolution of the bipyramidal Yb:YLF NCs and subsequent recrystallization of the product with the lowest solubility: LiF.

The proposed model leaves room to speculate what happens to the remaining Y^{3+}, Yb^{3+} and F^- ions. To understand this, we performed multiple attempts to synthesize YF_3 NCs in a similar manner as the LiF, by using solely $Y(TFA)_3$. This repeatedly did not yield any particles, hence we conclude that the solubility of YF_3 is too high under the synthesis conditions to initiate nucleation in the absence of Li^+ ions. This also explains why no YF_3 crystals were found after the decomposition of YLF into LiF: the freed Y^{3+} and F^- ions are

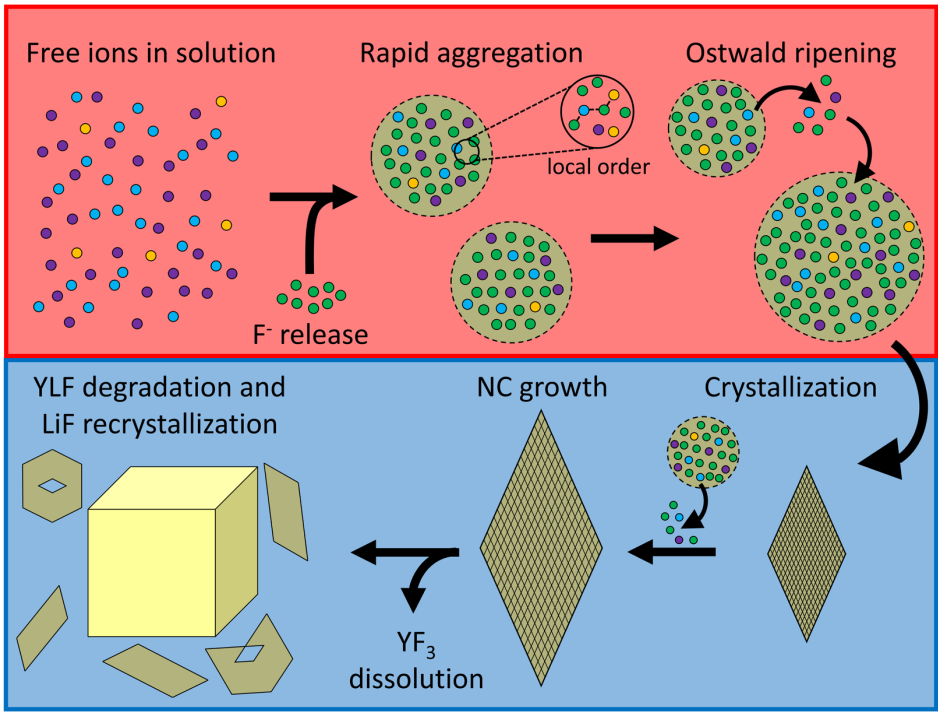


Figure 2.5. Schematic of the proposed nucleation and growth mechanism. The nanocrystal synthesis starts from the release of fluoride ions through thermal decomposition of the TFA precursor, followed by a rapid aggregation of all ions, resulting in amorphous YLF-spheres with local YF_3 order. Once the fluoride concentration in the solution lowers, Ostwald ripening is observed. Subsequently, the largest spheres crystallize in bipyramidal YLF NCs which can be recovered, or grown until the solution is depleted from spheres. If the synthesis mixture is kept at the synthesis conditions for 24 hours, YLF NCs degrade through slow dissolution. The freed lithium and fluoride ions recrystallize as large LiF cubes.

simply dissolved, following Equation 2.4.

$$LiYF_4 \rightarrow Li^+ + Y^{3+} + 4F^- \rightarrow LiF + Y^{3+} + 3F^- \qquad (2.4)$$

The rapid initial aggregation of all ions, resulting in the formation of amorphous Yb:YLF spheres, is thus driven by the presence of Li^+ ions, and key in the formation of Yb:YLF. We conclude that LiF has the lowest solubility, hence this material corresponds to the thermodynamic ground state under the synthesis conditions. However, due to the much faster nucleation of Yb:YLF this material forms first, and only prolonged heating induces the conversion to LiF.

The facile synthesis of the amorphous (Yb:)YLF nanospheres may be interesting for other uses. As these particles can easily be purified, they can be used as a much less reactive Yb:YLF precursor in comparison with the TFA-based precursors. Beneficially, they can be applied at any temperature independent of the F^- release from the TFA-precursors.

In a somewhat analogous manner, for hexagonal $NaYF_4$ NC shelling methods, small cubic $NaYF_4$ NCs are used as a sacrificial shell growth precursor for core-shell $NaYF_4$@Ln:$NaYF_4$,[35,42–45] where Ln is any trivalent lanthanide ion. We recommend further research in using these amorphous YLF nanospheres as YLF precursors, especially for lower-temperature syntheses and shelling methods.

2.8 Conclusions

In this work, we followed an Yb:YLF NC synthesis using aliquots and electron microscopy techniques. We concluded that the formation of bipyramidal Yb:YLF NCs by using the thermal decomposition of TFA-precursors is a multistep process, which starts from the formation of amorphous Yb:YLF spheres. These spheres grow via Ostwald ripening, until thermodynamic rearrangement results in the formation of crystalline Yb:YLF NCs. Additional experiments show that if the synthesis mixture is kept at the synthesis conditions for 24 hours, the Yb:YLF NCs degrade by dissolution. This results in the recrystallization of highly insoluble LiF crystals, whereas the remaining Y^{3+} and F^- ions remain in solution. From this, we inferred that Yb:YLF is a metastable intermediate that forms due to more rapid kinetics of the nucleation.

Experimental Methods

Materials

1-octadecene (ODE, technical grade, 90%) and lithium fluoride (LiF, 99.995%, precipitated) were purchased from Sigma Aldrich. Oleic acid (extra pure), trifluoroacetic acid (HTFA, ≥99.0%, for HPLC), trifluoroacetic anhydride (TFAA, ≥99.0%), lithium carbonate (Li_2CO_3, 99.999%, trace metal basis), yttrium oxide (Y_2O_3, 99.9999%, REO) and ytterbium oxide (Yb_2O_3, 99.998%, REO) were purchased from Fisher Scientific. Toluene (≥99.8%, anhydrous) and methanol (anhydrous, max 0.003% H_2O) and yttrium fluoride (YF_3, 99.9%, anhydrous) were purchased from VWR Chemicals.

All chemicals were used as received, unless specified differently. All manipulations were performed under N_2 atmosphere, using standard Schlenk line techniques or a nitrogen-filled glove box (<0.1 ppm H_2O; <0.1 ppm O_2), unless otherwise mentioned.

Milli-Q water was obtained from a Milli-Q Advantage A10 system (Merck Millipore, 18.2 MΩ·cm, 2 ppb TOC).

Synthesis and Drying of Metal Trifluoroacetate Precursors

Metal trifluoroacetate salts, $M^{x+}(TFA)_x$ ($M = Li^+, Y^{3+}, Yb^{3+}$), were synthesized by adding 5 mmol of Li_2CO_3 (369 mg), Y_2O_3 (1129 mg) or Yb_2O_3 (1970 mg), and 5 mL of Milli-Q water to a 25 mL 2-necked flask with a fused thermocouple insert containing a PTFE-coated stirring bar. The flask was connected to a Schlenk line equipped with a water-cooled condenser, and 5 mL of trifluoroacetic acid (HTFA; ~65 mmol) was added dropwise under stirring. *Note: as the reaction between HTFA and Li_2CO_3 is strongly exothermic and results in the release of a large volume of CO_2, the acid should be added carefully to avoid splashing.* After all of the acid had been added, the necks of the flask were closed with septa, and the reaction mixture was placed under a N_2 gas flow. The mixture was heated to 120 °C and left under reflux until a clear, colorless solution was obtained (generally <1

minute for Li_2CO_3, >1 hour for Y_2O_3 and Yb_2O_3). At this point, the reaction mixture was cooled to below 50 °C, and a vacuum was applied to evaporate all water and acid. The resulting solids were transferred to a glove box and crushed to form a white powder. These powders may appear dry, but are very likely to contain crystal water, especially in the case of lithium trifluoroacetate, which is extremely hygroscopic.

To remove the undesired crystal water, the precursor salts were dried further using trifluoroacetic anhydride (TFAA). Briefly, the powdered metal TFA salts were added to a 250 mL round-bottom flask, connected to a Schlenk line, and placed under nitrogen flow. TFAA (5 mL, ~36 mmol) was added, resulting in a rise in the temperature of the reaction mixture. This mixture was left to stir for 1 h, after which the TFAA and HTFA were removed under vacuum. The remaining solids were transferred back to a nitrogen-filled glovebox and crushed to a powder. *Note: TFAA reacts aggressively with water and can damage plastic and rubber tubing. To protect the Schlenk line tubing and the vacuum pump, the evaporated TFAA was collected in an additional cold trap which was placed directly after the reaction flask. The cold trap contents were carefully quenched with isopropanol before disposal.*

Following the Synthesis of Yb:YLF NCs

Yb:YLF NCs were synthesized according to the protocol that is worked out in Chapter 3. To a two-necked round-bottom flask (25 mL) with fused thermocouple insert, 2 mmol of LiTFA (240 mg) and 2 mmol of a mixture of $Y(TFA)_3$ (428 mg/mmol) and $Yb(TFA)_3$ (515 mg/mmol) in the ratios required were added inside a nitrogen filled glovebox. To this, a mixture of 6.5 mL of ODE and 6.5 mL of OA, both previously degassed, was added. The flask was then attached to a Schlenk line without exposure to the air, and the contents were degassed at 100 °C for 1 hour. Thereafter, the flask was put under a flow of N_2, and the temperature was increased stepwise to 330 °C with increments of 5°C/30 seconds. Aliquots of 200 µL were taken after every 10 °C and injected in 2 mL of toluene to monitor the NC nucleation and growth. Once the contents reached 330 °C, aliquots were taken after 2, 4 and 25 minutes. The reaction was left at 330 °C for 24 hours and subsequently cooled down to room temperature using compressed air. The resulting mixture was yellow and opaque. Using a syringe, 2 mL of toluene was added to facilitate transfer from the flask to a nitrogen-filled vial. Methanol (~ 5 mL) was added to the final synthesis mixture. The mixture was centrifuged at a relative centrifugal force of 1800 × g (3800 rpm) for 10 minutes, the supernatant was discarded and the solid NC pellet was redispersed in 2 mL of toluene. To this, 1 mL of methanol was added, and after centrifugation, the NC pellet was redispersed in 2 mL of toluene. This step was repeated once more and the final NC sample, dispersed in 2 mL of toluene, was stored in air. The aliquots were washed in a similar manner, however solely 0.5 mL of methanol was used per washing step, and the samples were redispersed in 1 mL of toluene each time.

Synthesis of Yb:YLF Nanospheres

For the XRD measurement, shown in Figure 2.2d, a similar synthesis was carried out as explained above, however, once the synthesis mixture reached 300 °C, it was directly cooled down using compressed air. The nanospheres were isolated in an identical manner as described above for the final synthesis mixture, however, 20 mL of methanol was used

for the first washing step in order to obtain as much product as possible. The final product, obtained after three washing steps, was again stored in 2 mL of toluene.

Synthesis of Shuriken-Shaped LiF Crystals

Large LiF crystals were synthesized following the same procedure as described for the regular Yb:YLF NC synthesis, but by solely using 8 mmol of LiTFA (960 mg). 8 mmol was chosen in order to keep the total amount of released fluoride ions the same. Aliquots of 1mL were taken at 270 °C, 285 °C, 300 °C, 315 °C and 330 °C and added to 2 mL of toluene. After 25 minutes at 330 °C, the remaining synthesis mixture was washed following the washing steps described above, using 5 mL of methanol for the first washing step of the synthesis mixture, and 1 mL of methanol for the aliquots. The final samples were all stored in 1 mL of toluene.

Attempted Synthesis of YF_3 Crystals

Identical to the synthesis of the shuriken-shaped LiF crystals mentioned above, we attempted to synthesize YF_3 using ⅔ mmol $Y(TFA)_3$ (1141 mg).

Optical Characterization

Emission spectra were obtained using an Edinburgh Instruments FLS980 spectrometer equipped with a liquid nitrogen-cooled NIR PMT-based detector from Hamamatsu. A Xenon arc lamp from XBO was used as an excitation source.
TRPL spectra were also obtained using an Edinburgh Instruments FLS980 spectrometer equipped with a liquid nitrogen cooled NIR PMT-based detector from Hamamatsu. The measurements were performed using time-correlated single photon counting, with 930 nm nanosecond laser pulses from a M8903-01 Hamamatsu laser unit as an excitation source.

Structural Characterization

TEM and ED images were acquired using a JEOL JEM1400 transmission electron microscope operating at 120 kV. ED analysis was performed using CrysTbox[40] software.
High-angle annular dark field scanning transmission electron microscopy images and energy-dispersive X-ray spectral maps were acquired using an aberration-corrected cubed Thermo Fisher Scientific-Titan electron microscope operated at an acceleration voltage of 300 kV equipped with a Super-X detector.
XRD measurements were performed with a Bruckner D8 ADVANCE diffractometer (Cu Kα, λ = 0.15406 nm). The NC samples were drop-casted on zero diffraction (911) silicon substrates unless stated differently. XRD simulations were performed using the Diffraction Analysis for Nanopowders (DIANNA) software,[47] which implements the Debye scattering equation for the simulation of finite-size atomistic models of nanoparticles.
The XPS analyses were performed with a Kratos Axis Ultra spectrometer using a monochromatic Al Kα source (20 mA, 15 kV). Survey scan analyses were performed with an analysis area of 300 × 700 μm^2 and a pass energy of 160 eV, whereas high-resolution analyses were performed with a pass energy of 20 eV. Specimens for XPS measurements were prepared by dropping a concentrated NC solution onto a freshly cleaved highly oriented pyrolytic graphite substrate (HOPG, ZYB).

References

1. Demirbas, U.; Thesinga, J.; Kellert, M.; Reuter, S.; Pergament, M.; Kärtner, F. X. Semiconductor Saturable Absorber Mirror Mode-Locked Yb:YLF Laser with Pulses of 40 Fs. Opt. Lett. 2022, 47 (4), 933.
2. Lelii, F. D.; Jun, S.; Pirzio, F.; Piccinno, G.; Tonelli, M.; Agnesi, A. Laser Investigation of Yb:YLF Crystals Fabricated with the Micro-Pulling-down Technique. Appl. Opt. 2018, 57 (9), 2223.
3. Körner, J.; Krüger, M.; Reiter, J.; Münzer, A.; Hein, J.; Kaluza, M. C. Temperature Dependent Spectroscopic Study of Yb^{3+}-Doped $KG(WO_4)_2$, $KY(WO_4)_2$, $YAlO_3$ and $YLiF_4$ for Laser Applications . Opt. Mater. Express 2020, 10 (10), 2425.
4. Rapaport, A.; Milliez, J.; Bass, M.; Cassanho, A.; Jenssen, H. Review of the Properties of Up-Conversion Phosphors for New Emissive Displays. J. Disp. Technol. 2006, 2 (1), 68–78.
5. Kück, S.; Osiac, E.; Sokólska, I. Phase-Sensitive Detection of Excited-State Absorption Transitions in Yb^{3+}-Codoped, Ho^{3+}-Doped $YLiF_4$. J. Opt. Soc. Am. B 2005, 22 (2), 323.
6. Sandrock, T.; Heumann, E.; Huber, G.; Chai, B. H. T. Continuous-Wave Pr,Yb:$LiYF_4$ Upconversion Laser in the Red Spectral Range at Room Temperature. In Advanced Solid State Lasers; OSA: Washington, D.C., 1996; Vol. I, p PM1.
7. Heine, F.; Ostroumov, V.; Heumann, E.; Jensen, T.; Huber, G.; Chai, B. H. T. CW Yb,Tm:$LiYF_4$ Upconversion Laser at 650 Nm, 800 Nm, and 1500 Nm. Adv. Solid State Lasers 1995, 24, VL4.
8. Zhang, X. X.; Hong, P.; Bass, M.; Chai, B. H. T. Blue Upconversion with Excitation into Tm Ions at 780 Nm in Yb- and Tm-Codoped Fluoride Crystals. Phys. Rev. B 1995, 51 (14), 9298–9301.
9. Melgaard, S.; Seletskiy, D.; Polyak, V.; Asmerom, Y.; Sheik-Bahae, M. Identification of Parasitic Losses in Yb:YLF and Prospects for Optical Refrigeration down to 80K. Opt. Express 2014, 22 (7), 7756.
10. Püschel, S.; Kalusniak, S.; Kränkel, C.; Tanaka, H. Temperature-Dependent Radiative Lifetime of Yb:YLF: Refined Cross Sections and Potential for Laser Cooling. Opt. Express 2021, 29 (7), 11106.
11. Demirbas, U.; Thesinga, J.; Kellert, M.; Kärtner, F. X.; Pergament, M. Comparison of Different in Situ Optical Temperature Probing Techniques for Cryogenic Yb:YLF. Opt. Mater. Express 2020, 10 (12), 3403.
12. Roder, P. B.; Smith, B. E.; Zhou, X.; Crane, M. J.; Pauzauskie, P. J. Laser Refrigeration of Hydrothermal Nanocrystals in Physiological Media. Proc. Natl. Acad. Sci. U. S. A. 2015, 112 (49), 15024–15029.
13. Gharde, S. I.; Senthil, A.; Reymatias, M. V.; Sharma, A.; Murphy, C. R.; Withers, N. J.; Smolyakov, G. A.; Ivanov, S. A.; Watt, J. D.; Huber, D. L.; Osinski, M. Colloidal Synthesis and Characterization of Ytterbium-Doped YLF Nanocrystals. In Colloidal Nanoparticles for Biomedical Applications XVII; Osiński, M., Kanaras, A. G., Eds.; SPIE, 2022; p 25.
14. Song, C.; Zhang, S.; Zhou, Q.; Hai, H.; Zhao, D.; Hui, Y. Upconversion Nanoparticles for Bioimaging. Nanotechnol. Rev. 2017, 6 (2), 233–242.
15. Qiao, Y.; Qiao, S.; Yu, X.; Min, Q.; Pi, C.; Qiu, J.; Ma, H.; Yi, J.; Zhan, Q.; Xu, X. Plant Tissue Imaging with Bipyramidal Upconversion Nanocrystals by Introducing

Tm^{3+} Ions as Energy Trapping Centers. Nanoscale 2021, 13 (17), 8181–8187.

16. Tsang, M. Y.; Fałat, P.; Antoniak, M. A.; Ziniuk, R.; Zelewski, S. J.; Samoć, M.; Nyk, M.; Qu, J.; Ohulchanskyy, T. Y.; Wawrzyńczyk, D. Pr^{3+} Doped $NaYF_4$ and $LiYF_4$ Nanocrystals Combining Visible-to-UVC Upconversion and NIR-to-NIR-II Downconversion Luminescence Emissions for Biomedical Applications. Nanoscale 2022, 14 (39), 14770–14778.
17. Li, J.; Chen, Z.; Liu, Y.; Kollipara, P. S.; Feng, Y.; Zhang, Z.; Zheng, Y. Opto-Refrigerative Tweezers. Sci. Adv. 2021, 7 (26), 1–7.
18. Rahman, A. T. M. A.; Barker, P. F. Laser Refrigeration, Alignment and Rotation of Levitated Yb^{3+}:YLF Nanocrystals. Nat. Photonics 2017, 11 (10), 634–638.
19. Carl, F.; Birk, L.; Grauel, B.; Pons, M.; Würth, C.; Resch-Genger, U.; Haase, M. $LiYF_4$:Yb/$LiYF_4$ and $LiYF_4$:Yb,Er/$LiYF_4$ Core/Shell Nanocrystals with Luminescence Decay Times Similar to YLF Laser Crystals and the Upconversion Quantum Yield of the Yb,Er Doped Nanocrystals. Nano Res. 2021, 14 (3), 797–806.
20. Zhou, J.; Leaño, J. L.; Liu, Z.; Jin, D.; Wong, K. L.; Liu, R. S.; Bünzli, J. C. G. Impact of Lanthanide Nanomaterials on Photonic Devices and Smart Applications. Small 2018, 14 (40), 1–29.
21. Rademacher, M.; Gosling, J.; Pontin, A.; Toroš, M.; Mulder, J. T.; Houtepen, A. J.; Barker, P. F. Measurement of Single Nanoparticle Anisotropy by Laser Induced Optical Alignment and Rayleigh Scattering for Determining Particle Morphology. Appl. Phys. Lett. 2022, 121 (22), 221102.
22. Mulder, J. T.; Meijer, M. S.; van Blaaderen, J. J.; du Fossé, I.; Jenkinson, K.; Bals, S.; Manna, L.; Houtepen, A. J. Understanding and Preventing Photoluminescence Quenching to Achieve Unity Photoluminescence Quantum Yield in Yb:YLF Nanocrystals. ACS Appl. Mater. Interfaces 2023, 15 (2), 3274–3286.
23. Komban, R.; Spelthann, S.; Steinke, M.; Ristau, D.; Ruehl, A.; Gimmler, C.; Weller, H. Bulk-like Emission in the Visible Spectrum of Colloidal $LiYF_4$:Pr Nanocrystals Downsized to 10 Nm. Nanoscale Adv. 2022, 4 (14), 2973–2978.
24. Wang, J.; Wang, F.; Xu, J.; Wang, Y.; Liu, Y.; Chen, X.; Chen, H.; Liu, X. Lanthanide-Doped $LiYF_4$ Nanoparticles: Synthesis and Multicolor Upconversion Tuning. Comptes Rendus Chim. 2010, 13 (6–7), 731–736.
25. Purohit, B.; Jeanneau, E.; Guyot, Y.; Amans, D.; Mahler, B.; Joubert, M.; Dujardin, C.; Ledoux, G.; Mishra, S. Incorporation of Upconverting $LiYF_4$:Yb^{3+},Tm^{3+} Nanoparticles with High Quantum Yield in TiO_2 Metallogels for Near Infrared-Driven Photocatalytic Dye Degradation. ACS Appl. Nano Mater. 2023.
26. Jiang, X.; Cao, C.; Feng, W.; Li, F. Nd^{3+}-Doped $LiYF_4$ Nanocrystals for Bio-Imaging in the Second near-Infrared Window. J. Mater. Chem. B 2016, 4 (1), 87–95.
27. Cheng, T.; Marin, R.; Skripka, A.; Vetrone, F. Small and Bright Lithium-Based Upconverting Nanoparticles. J. Am. Chem. Soc. 2018, 140 (40), 12890–12899.
28. Panov, N.; Marin, R.; Hemmer, E. Microwave-Assisted Solvothermal Synthesis of Upconverting and Downshifting Rare-Earth-Doped $LiYF_4$ Microparticles. Inorg. Chem. 2018, 57 (23), 14920–14929.
29. Sui, J.; Yan, J.; Wang, K.; Luo, G. Efficient Synthesis of Lithium Rare-Earth Tetrafluoride Nanocrystals via a Continuous Flow Method. Nano Res. 2020, 13 (10), 2837–2846.

30. Du, Y.-P.; Zhang, Y.-W.; Sun, L.-D.; Yan, C.-H. Optically Active Uniform Potassium and Lithium Rare Earth Fluoride Nanocrystals Derived from Metal Trifluroacetate Precursors. Dalt. Trans. 2009, No. 40, 8574.
31. Zhang, L.; Wang, Z.; Lu, Z.; Xia, K.; Deng, Y.; Li, S.; Zhang, C.; Huang, Y.; He, N. Synthesis of $LiYF_4$:Yb,Er Upconversion Nanoparticles and Its Fluorescence Properties. J. Nanosci. Nanotechnol. 2014, 14 (6), 4710–4713.
32. Zhang, Q.; Yan, B. Hydrothermal Synthesis and Characterization of $LiREF_4$ (RE = Y, Tb–Lu) Nanocrystals and Their Core–Shell Nanostructures. Inorg. Chem. 2010, 49 (15), 6834–6839.
33. Yi, G. S.; Lee, W. B.; Chow, G. M. Synthesis of $LiYF_4$, $BaYF_5$, and $NaLaF_4$ Optical Nanocrystals. J. Nanosci. Nanotechnol. 2007, 7 (8), 2790–2794.
34. Zhang, X.; Wang, M.; Ding, J.; Song, X.; Liu, J.; Shao, J.; Li, Y. $LiYF_4$:Yb^{3+},Er^{3+} upconverting Submicro-Particles: Synthesis and Formation Mechanism Exploration. RSC Adv. 2014, 4 (76), 40223–40231.
35. Homann, C.; Krukewitt, L.; Frenzel, F.; Grauel, B.; Würth, C.; Resch-Genger, U.; Haase, M. $NaYF_4$:Yb,Er/$NaYF_4$ Core/Shell Nanocrystals with High Upconversion Luminescence Quantum Yield. Angew. Chemie Int. Ed. 2018, 57 (28), 8765–8769.
36. Mosiadz, M.; Juda, K. L.; Hopkins, S. C.; Soloducho, J.; Glowacki, B. A. An In-Depth in Situ IR Study of the Thermal Decomposition of Yttrium Trifluoroacetate Hydrate. J. Therm. Anal. Calorim. 2012, 107 (2), 681–691.
37. Eloussifi, H.; Farjas, J.; Roura, P.; Camps, J.; Dammak, M.; Ricart, S.; Puig, T.; Obradors, X. Evolution of Yttrium Trifluoroacetate during Thermal Decomposition. J. Therm. Anal. Calorim. 2012, 108 (2), 589–596.
38. Kalikmanov, V. I. Nucleation Theory; Lecture Notes in Physics; Springer Netherlands: Dordrecht, 2013; Vol. 860.
39. Wang, Y.; He, J.; Liu, C.; Chong, W. H.; Chen, H. Thermodynamics versus Kinetics in Nanosynthesis. Angew. Chemie Int. Ed. 2015, 54 (7), 2022–2051.
40. Bucci, G.; Gadelrab, K.; Carter, W. C. Mesoscale Model for Ostwald Ripening of Catalyst Nanoparticles. J. Electrochem. Soc. 2021, 168 (5), 054515.
41. Dragic, P.; Cavillon, M.; Kucera, C.; Hawkins, T.; Ballato, J. Low Nonlinearity Yb-Doped Fluorosilicate Optical Fiber With Ultra-Flat Absorption Spectrum. In Conference on Lasers and Electro-Optics; OSA: Washington, D.C., 2017; Vol. 2017–Janua, p JW2A.61.
42. Meijer, M. S.; Natile, M. M.; Bonnet, S. 796 Nm Activation of a Photocleavable Ruthenium(II) Complex Conjugated to an Upconverting Nanoparticle through Two Phosphonate Groups. Inorg. Chem. 2020, 59 (20), 14807–14818.
43. Jia, Y.; Sun, T.-Y.; Wang, J.-H.; Huang, H.; Li, P.; Yu, X.-F.; Chu, P. K. Synthesis of Hollow Rare-Earth Compound Nanoparticles by a Universal Sacrificial Template Method. CrystEngComm 2014, 16 (27), 6141–6148.
44. Yang, D.; Kang, X.; Ma, P.; Dai, Y.; Hou, Z.; Cheng, Z.; Li, C.; Lin, J. Hollow Structured Upconversion Luminescent $NaYF_4$:Yb^{3+},Er^{3+} Nanospheres for Cell Imaging and Targeted Anti-Cancer Drug Delivery. Biomaterials 2013, 34 (5), 1601–1612.
45. Hossan, M. Y.; Hor, A.; Luu, Q.; Smith, S. J.; May, P. S.; Berry, M. T. Explaining the Nanoscale Effect in the Upconversion Dynamics of β-$NaYF_4$:Yb^{3+},Er^{3+} Core and Core–Shell Nanocrystals. J. Phys. Chem. C 2017, 121 (30), 16592–16606.

46. Klinger, M. More Features, More Tools, More CrysTBox. J. Appl. Crystallogr. 2017, 50 (4), 1226–1234.
47. Yatsenko, D.; Tsybulya, S. DIANNA (Diffraction Analysis of Nanopowders) – a Software for Structural Analysis of Nanosized Powders. Zeitschrift für Krist. - Cryst. Mater. 2018, 233 (1), 61–66.

Appendix 2.1

Nucleation, Growth and Degradation of Yb:YLF Nanocrystals

Figure A2.1 summarizes the most important steps of the nucleation, growth and degradation of Yb:YLF nanocrystals (NCs). At 300 °C, Yb:YLF spheres nucleate as a result of the sudden release of fluoride ions from the thermal decomposition of the TFA-based precursors (Figure A2.1a). At 330 °C, shown in Figure A2.1b, a bimodal distribution of nanospheres is observed. After 5 minutes (Figure A2.1c), a mixture of amorphous Yb:YLF nanospheres and crystalline Yb:YLF bipyramidal NCs are found. Generally, after 25 minutes, the synthesis is stopped and the product is recovered (Figure A2.1d). If the synthesis is not stopped at 25 minutes, but kept at 330 °C for 24 hours, the Yb:YLF NCs disintegrated, resulting in the presence of recrystallized microcrystalline LiF cubes (Figure A2.1e), and remaining Yb:YLF crystals (Figure A2.1f).

Figures A2.1a–c were obtained from a different synthesis batch, showing the reproducibility of the formation and transformation of the Yb:YLF spheres.

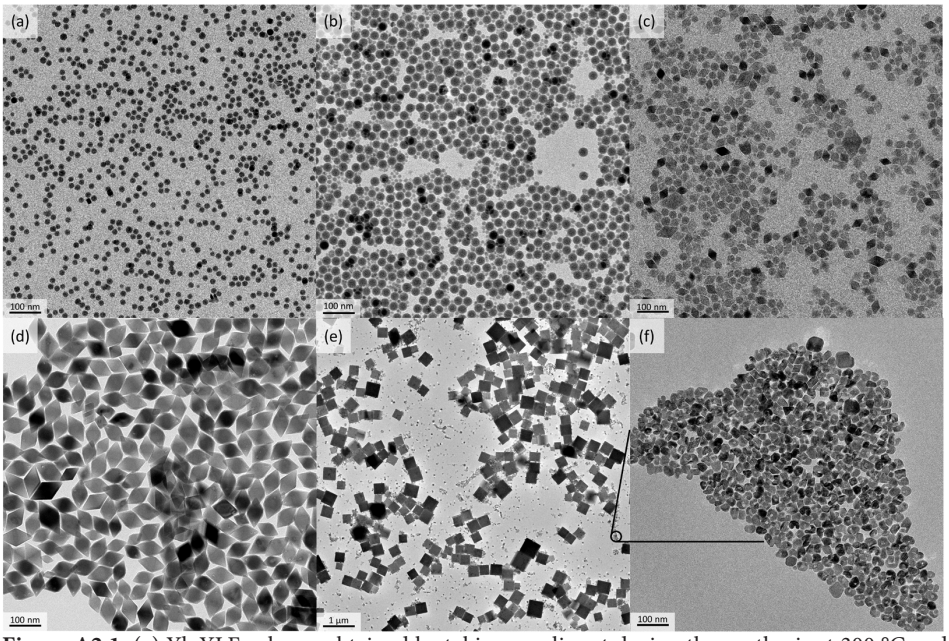


Figure A2.1. (a) Yb:YLF spheres obtained by taking an aliquot during the synthesis at 300 °C and (b) 330°C during heating up. (c) After 5 minutes at 330 °C, bipyramidal, crystalline Yb:YLF NCs were found among the Yb:YLF nanospheres. (d) NCs obtained after 25 minutes at 330 °C show the intended end product. (e) If the NCs are kept at the synthesis conditions for 24 hours, large cubes and (f) small irregular crystals are recovered. The image shows that no bipyramidal Yb:YLF NCs were present, indicating the observed particles are a degradation product of the Yb:YLF NCs.

Appendix 2.2

HAADF-STEM and EDX Images of Yb:YLF Spheres

In addition to Figure 2.2 in the main text, Figure A2.2 shows larger-area HAADF-STEM and EDX images of the Yb:YLF nanospheres obtained at 300 °C.

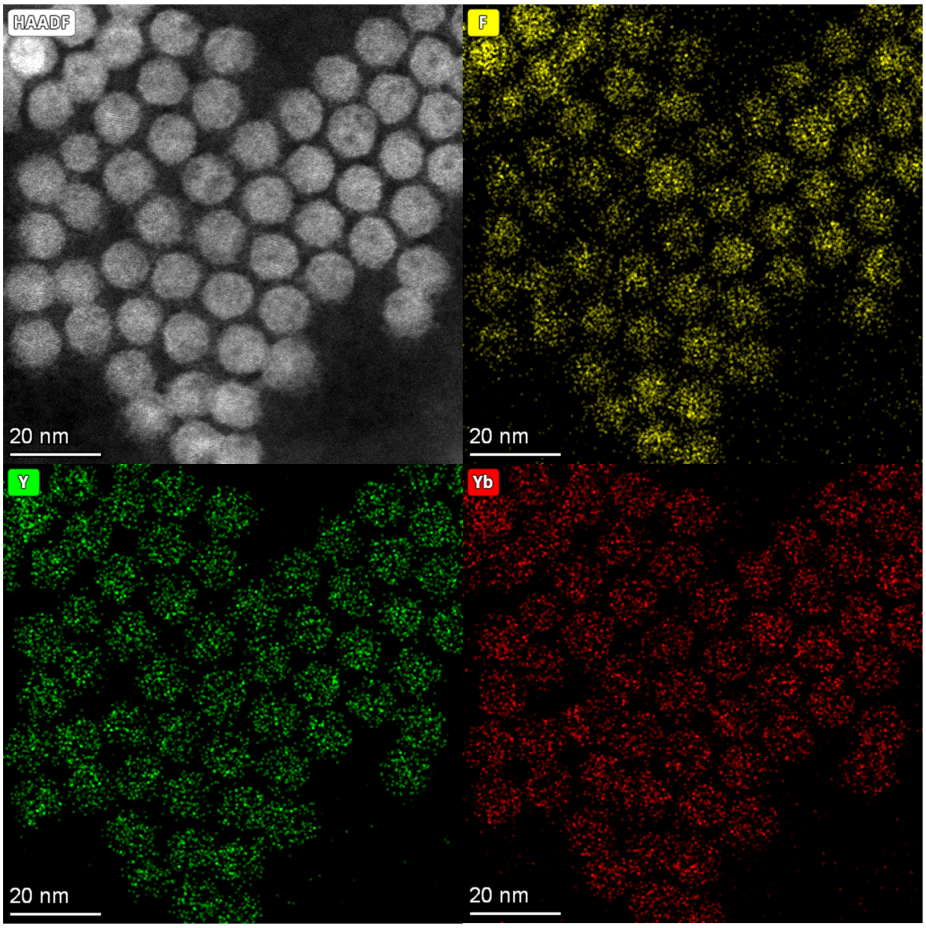


Figure A2.2. HAADF-STEM images and EDX elemental maps of the nanospheres obtained at 300 °C, during the heating up stage. This image shows the presence of yttrium, ytterbium and fluoride in the spheres.

Appendix 2.3

Yttrium and Ytterbium Distribution in Yb:YLF Spheres

For the nanosphere sample shown in Figure 2.2 of the main text, the yttrium and ytterbium distribution was determined using EDX. As can be seen in Figure A2.3, little to no signal of Y and Yb is outside of the spheres and a very similar signal ratio is found for Y:Yb in the nanospheres.

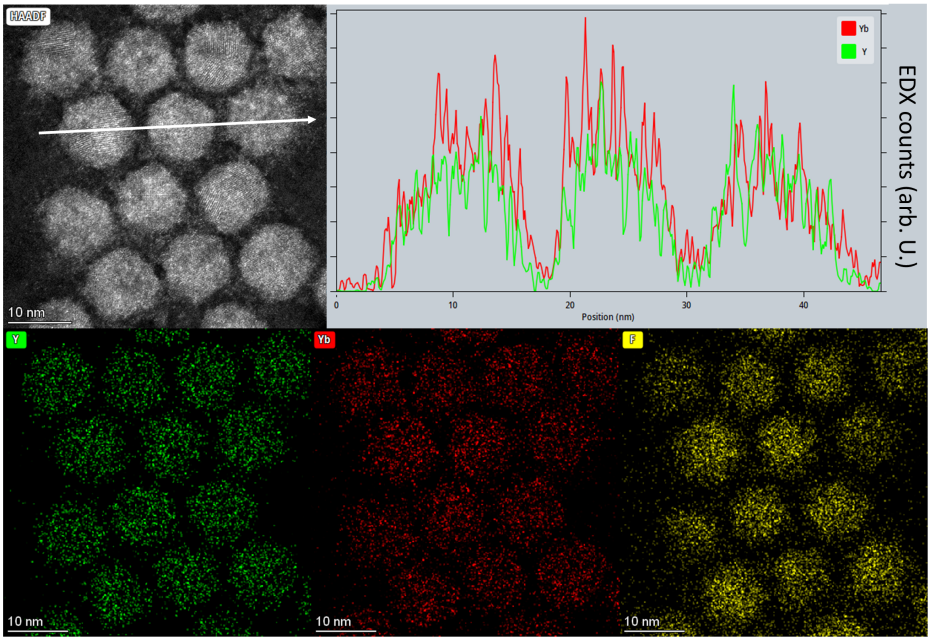


Figure A2.3. An EDX map of the nanospheres shown in Figure 2.2, performed in the direction of the arrow shown in the HAADF-STEM image, shows that the Y:Yb ratio is consistent in the nanospheres.

Appendix 2.4

XRD References of LiF, YF_3 and $LiYF_4$

Figure A2.4 shows the crystallographic information obtained using XRD from research grade LiF (99.995%) from Sigma Aldrich and YF_3 (99.9% from VWR). The XRD of $LiYF_4$ is obtained from synthesized NCs (without Yb-dopant). Important to notice is the large difference in the number and positions of the reflections between each material, significantly facilitating the differentiation between the materials. The values of a, b and c were calculated using the XRD diffractograms and the shown Miller indices were determined using the values for a, b and c. These values are used to determine the composition of the nanospheres, as shown in Appendix 2.10.

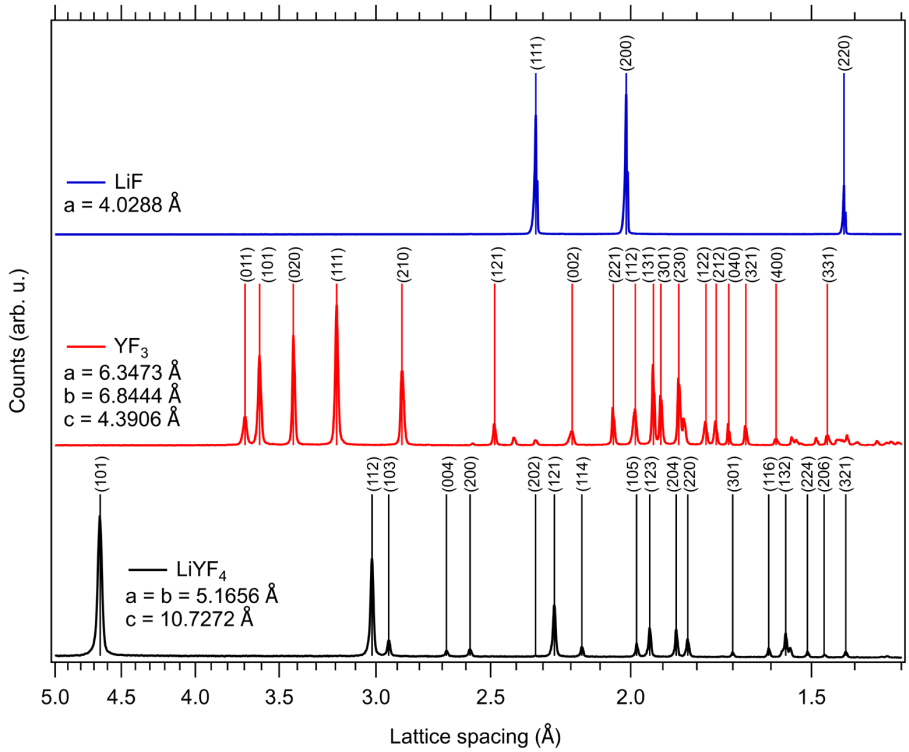


Figure A2.4. XRD diffractograms of LiF, YF_3 and undoped $LiYF_4$ (YLF) with their calculated unit cell parameters and assigned reflections. All values are converted from 2 theta to lattice spacing in the unit cell, in order to obtain the values for a, b and c as indicated in the figure.

Appendix 2.5

Structural Analysis of Yb:YLF Spheres and Simulations of Unit Cell Reflections

Figure A2.5a shows the ED and XRD of the nanospheres, and the XRDs of the materials the nanospheres are most likely composed of. This figure shows that the nanospheres ED and XRD are most comparable with the XRD of YF_3. Although it is clear that the spheres are not composed of LiF (as additionally confirmed through EDX), unit cell reflections of $LiYF_4$ could possibly still result in the ED as shown in Figure A2.5b. To confirm that the reflections observed are not coming from $LiYF_4$, we simulated the expected reflections for $(1)^3$, $(1.5)^3$ and $(2)^3$ unit cells of $LiYF_4$ and YF_3, as shown in Figure A2.5c. This figure again shows that the experimental data is in best agreement with the simulated ED of $(1.5)^3$ to $(2)^3$ unit cells of YF_3. We therefore conclude that any signs of crystallinity in these spheres comes from local, short-range YF_3 order.

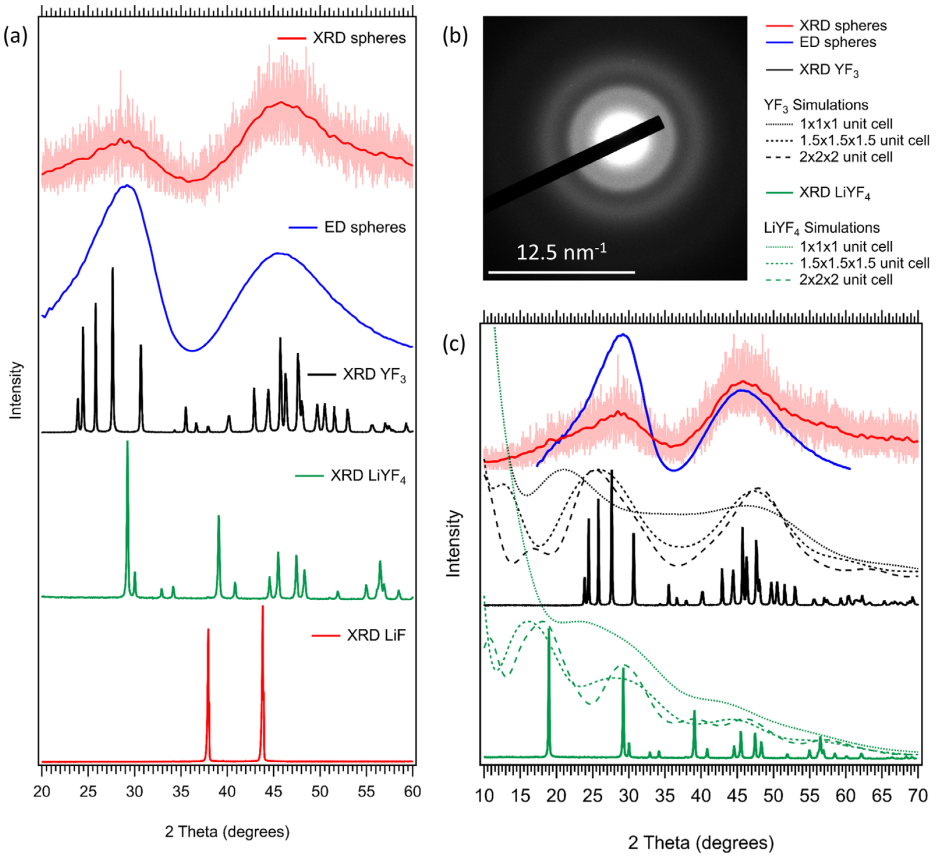


Figure A2.5. (a) XRD and ED diffractograms from the nanosphere sample, and XRD diffractograms of YF_3, $LiYF_4$ and LiF for reference. (b) ED from the nanospheres, of which the extracted pattern is shown in (a) and (c). (c) Simulations of the expected reflections of YF_3 and $LiYF_4$ for a 1x1x1, 1.5x1.5x1.5 and 2x2x2 unit cells.

Appendix 2.6

Nanocrystal Analysis Using Electron Diffraction

Figure A2.6 shows EDs of amorphous Yb:YLF nanospheres (top), undoped YLF NCs (middle) and LiF cubes (bottom). Comparing the XRD patterns from Figure A2.4 to the extracted diffraction patterns shows the accuracy of ED in this case. This figure shows that indeed the first sample of nanospheres is mostly amorphous due to the absence of sharp reflections.

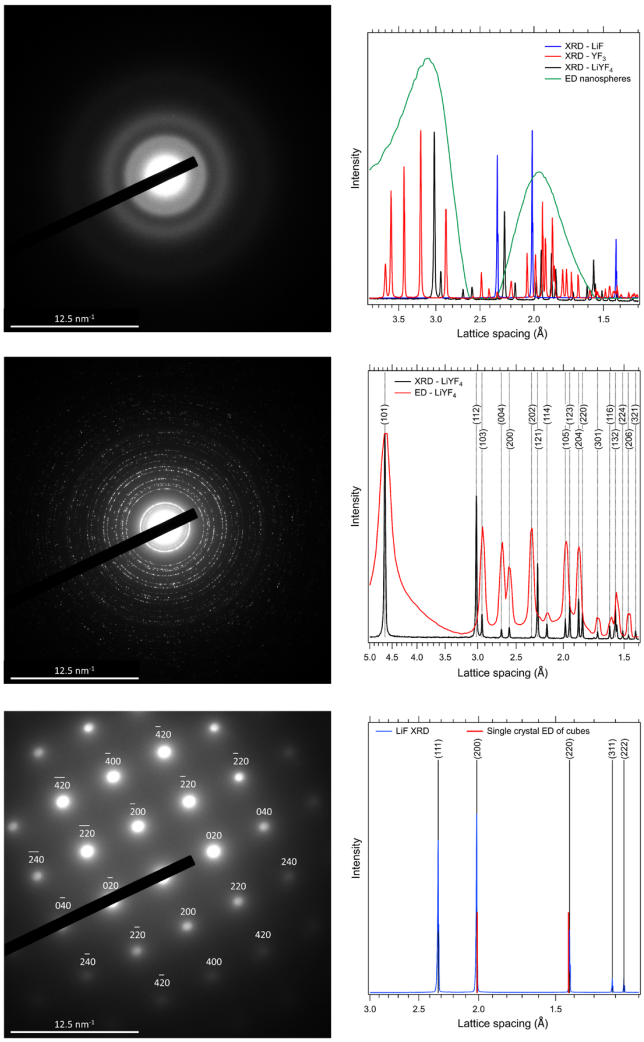


Figure A2.6 EDs and their extracted diffraction patterns from (top) the Yb:YLF nanospheres, (middle) Yb:YLF NCs and (bottom) LiF cubes. The first two EDs are small area EDs and hence show up as rings. The LiF ED is obtained from a single cube and hence shows a single crystal diffraction pattern.

Appendix 2.7

Optical Properties of Yb:YLF Nanospheres

Emission spectra were taken of both the Yb:YLF nanospheres and the bipyramidal NCs. Figure A2.7 shows the emission spectra for 25% ytterbium-doped particles. The emission spectrum of the spheres is similar to the emission of free Yb^{3+} ions, indicating the spheres are not consisting of crystalline Yb:YLF. The emission of the bipyramidal NCs shows more emission features due to crystal field splitting, which is not observed in the spectrum of the spheres. The photoluminescence lifetime of the Yb-emission of the spheres (Figure A2.8) is much lower than usually seen for the parity forbidden transition (~2 ms), indicating that most of the excitations are lost to non-radiative processes.

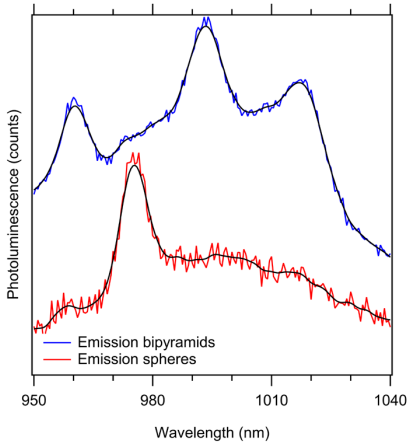


Figure A2.7. Emission spectra of 25% doped Yb:YLF nanospheres isolated at 300 °C, and 25% doped Yb:YLF bipyramidal NCs isolated after 25 minutes at 330 °C. λ_{ex} = 930 nm for both samples.

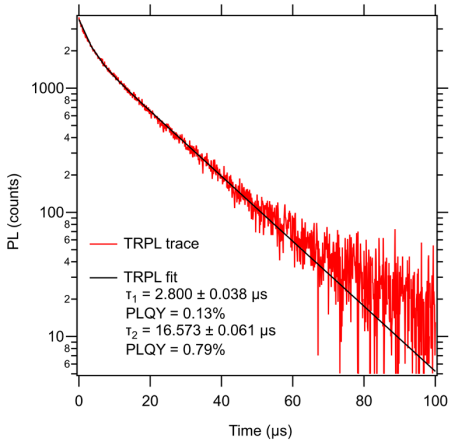


Figure A2.8. Photoluminescence decay of 25% doped Yb:YLF nanospheres of Figure A2.7. λ_{ex} = 930 nm and λ_{em} = 995 nm.

Appendix 2.8

Analysis of Nanosphere Material Composition Through e-Beam Crystallization

Because lithium is too light to be imaged with EDX, and because the spheres are initially amorphous, analyzing the composition of the spheres is not straightforward. The material can either be Yb:YF_3, or Yb:YLF. However, the amorphous spheres showed an increase of crystallinity when exposed to the electron beam during the HAADF-STEM measurements. From the arrangement of the yttrium ions in the crystallized spheres, we can already get more information to differentiate between Yb:YF_3 and Yb:YLF, as explained in Appendix 2.9.

From Figure A2.9, it is clear that the yttrium ions arrange into a hexagonal lattice. This structure is identical to that observed in Figure A2.10d-f. Therefore, it indicates that the spheres consist of $LiYF_4$, and not of YF_3. However, more proof is needed.

The increase of crystallinity furthermore allows to extract a lattice parameter from the nanospheres, allowing to distinguish the material from its crystal structure, as is shown in Appendix 2.10.

Performing small area ED on these crystallized spheres remains practically impossible, due to the limited crystallized area, as well as the overall stability of the nanospheres. In Figure A2.9, the transformation from amorphous spheres at the 1st frame to the spheres showing crystallized areas in the 12th frame is clear. However, at the 100th frame, apart from crystallized areas, clear beam damage has affected the nanospheres.

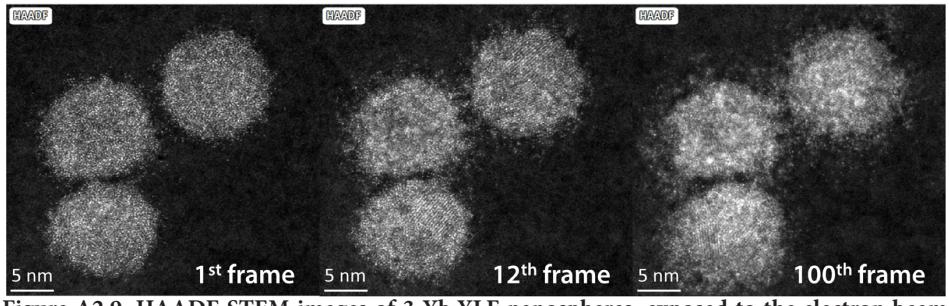


Figure A2.9. HAADF-STEM images of 3 Yb:YLF nanospheres, exposed to the electron beam for different amounts of time (*i.e.* measurement frames). The images show the 1st, 12th and 100th frame taken. The 1st frame shows fully amorphous spheres with no signs of crystallinity. The 12th frame however shows clear presence of crystal lattices. The particles are however not stable under these conditions, as the 100th frame shows much more degradation of the spheres.

Appendix 2.9

Using the Location of Yttrium Ions to Distinguish Between YF_3 and $LiYF_4$

For samples where too little crystalline material is present, analyzing the material's composition through XRD and ED becomes impossible. However, as long as a small amount of material is crystalline (or crystallizes), a proper idea of the bulk composition can be obtained. In the case shown in Figure A2.10, only the yttrium ions are imaged (as the fluoride and lithium ions are in comparison too light).

In the top part of Figure A2.10, we show the arrangement of yttrium ions in YF_3 nanowires, found as a minor side product in one of the syntheses performed. The bottom part of Figure A2.10 shows yttrium ions in $LiYF_4$, obtained from the irregular Yb:YLF crystals (Figure A2.17), which were imaged through both HAAFD-STEM (right) and integrated differential phase contrast measurements (iDPC, middle). This figure clearly shows that the yttrium ions in YF_3 are found in pairs. The yttrium ions in $LiYF_4$ form a continuous and evenly spaced network throughout the lattice.

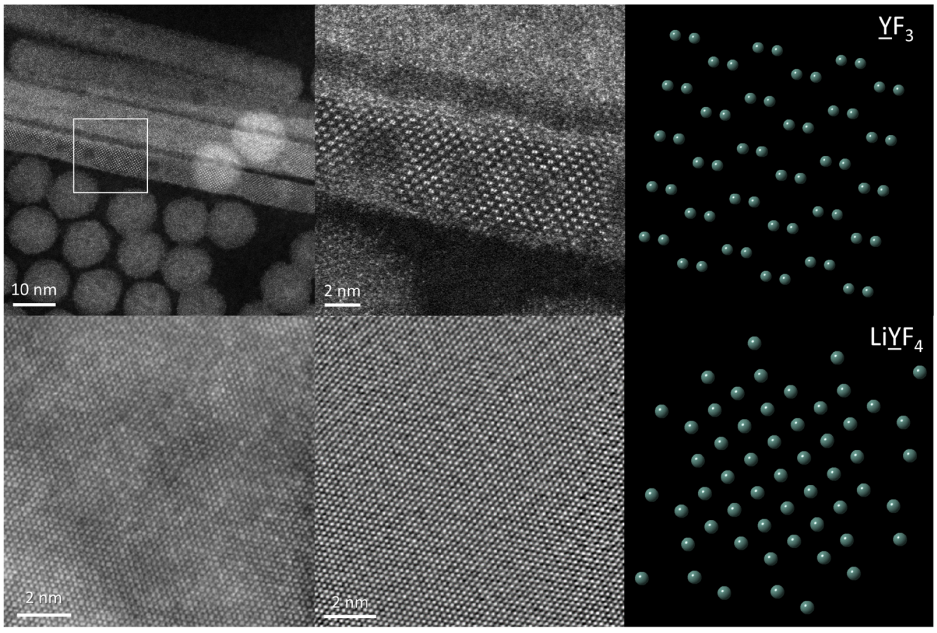


Figure A2.10. (top) HAADF-STEM images of YF_3 nanowires, found as a minor side product in one of the syntheses performed. When zooming in to an atomic level, it can be seen that the yttrium ions are paired, as shown in the top left. (bottom) For $LiYF_4$, the location of the yttrium ions is very different. Both by HAADF-STEM and iDPC imaging, it can be seen that the yttrium ions are unpaired and reside in a continuous hexagonal network.

Appendix 2.10

Analysis of Nanosphere Composition Using its Lattice Parameter

From the under the e-beam crystallized nanospheres, the d_{hkl} value was determined from the observed atomic lattices. In this case, the HAADF-STEM image shown in the main text was used. Due to the lack of contrast, and the possibility of slight misalignments, this analysis is not error-free.

To reduce the error, the value for d_{hkl} was averaged over 11 lattices, as shown in Figure A2.11. The d_{hkl} value determined equals 3.03(6) Å. By using the XRDs of YF_3 and YLF (Appendix 2.4), it was concluded that this value corresponds to the (112) plane of YLF, which has a d_{khl} value of 3.02 Å as shown in Figure A2.11.

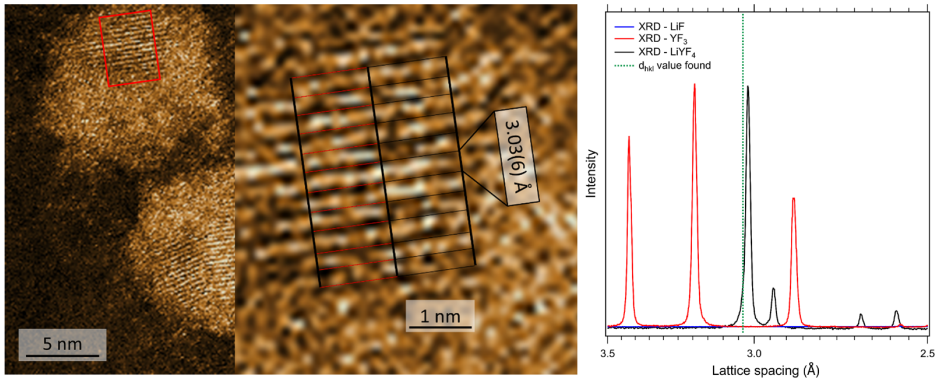


Figure A2.11. An analysis of the lattice parameter of the partially crystallized nanospheres. The image used is the same as shown in Figure 2.2 of the main text, but with enhanced contrast. The obtained d_{hkl} value is 3.03(6) Å, which corresponds to the (112)-reflection of $LiYF_4$.

Appendix 2.11

XPS Measurements on Yb:YLF Nanospheres

XPS measurements were performed to measure if lithium ions are present in the nanospheres and, if so, in what ratio it is found compared to the lanthanide and fluoride ions. As shown in Figure A2.12a, lithium is clearly measured, and in roughly a 0.75:1 ratio Li:Ln, which of the expected compounds resembles Yb:YLF best. This is a strong indication that the analyses shown in Appendix 2.9 and Appendix 2.10 correctly identify the nanospheres as Yb:YLF.

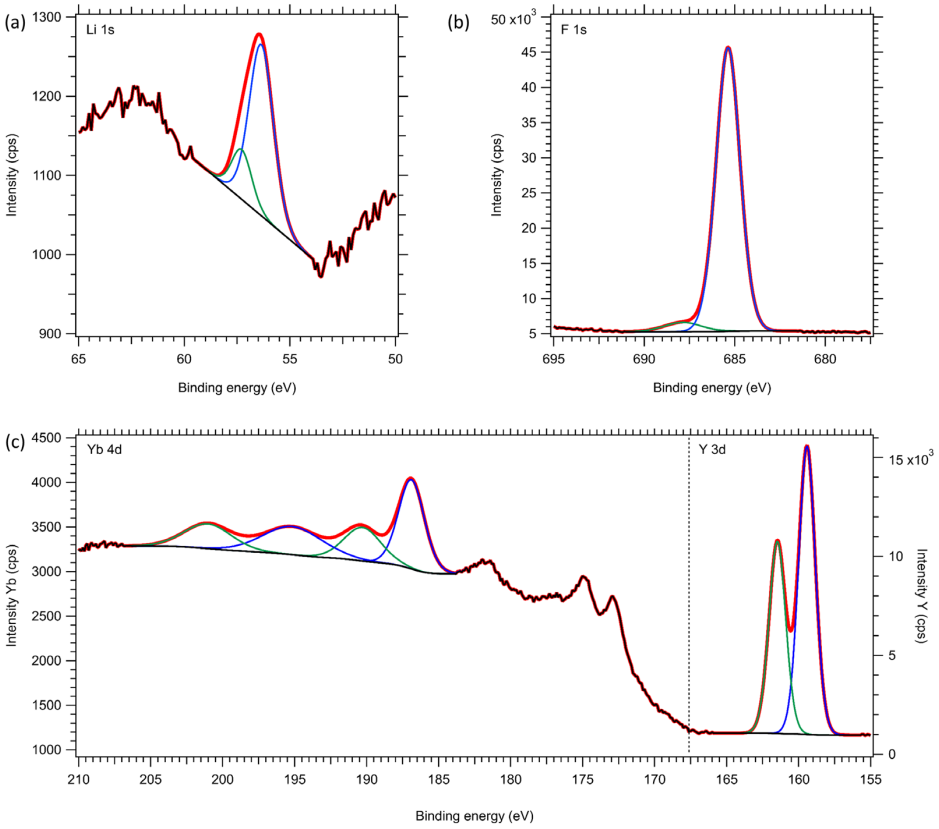


Figure A2.12. XPS spectra at element-specific binding energies, showcasing the presence of (a) Li, (b) F and (c) Y and Yb. Especially the presence of Li, which can hardly be measured using other techniques, aids in proving that the spheres consist of Yb:YLF, and not of Yb:YF_3.

Appendix 2.12

XRD on Thermally Annealed Nanospheres

In order to fully analyze the composition of the nanospheres, the sample (that was washed thrice to remove any residual non-incorporated ions) was thermally annealed at 330 °C for 25 minutes (mimicking the NC synthesis) under inert atmosphere. The material was then analyzed using XRD. As shown in Figure A2.13, the XRD pattern after annealing shows strong similarities with that of $LiYF_4$, with only a minor YF_3 impurity present. This proves that lithium is present in the nanospheres, and that the material thus consists of amorphous Yb:YLF. A slight shift of the corresponding angles is observed for the thermally annealed nanospheres compared to pure $LiYF_4$, which is likely a result of a slight lattice contraction due to the presence of 25% Yb^{3+}.

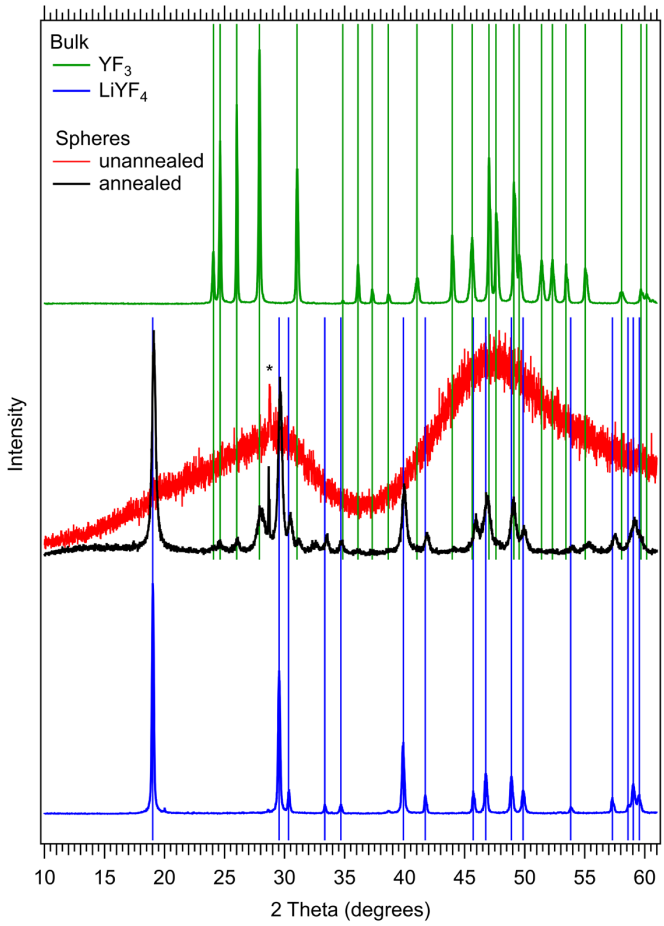


Figure A2.13. XRD diffractograms of YF_3 (green), $LiYF_4$ (blue) and the nanospheres before (red) and after (black) thermal annealing. The nanosphere-diffractogram after annealing shows strong similarities with $LiYF_4$. The sharp reflection at 28.7 degrees (*) corresponds to the (111) reflection of the silicon substrate that was used.

Appendix 2.13

HAADF-STEM and EDX Imaging of the Bimodal Sphere Sample

Figure A2.14 shows two HAADF-STEM images and corresponding EDX mapping of the bimodal sphere sample. From these images, no difference is observed between the large and small spheres. As in the main text we conclude that YF_3 alone is too soluble, it was concluded that these spheres are both Yb:YLF, undergoing Ostwald ripening as shown in Figure A2.15.

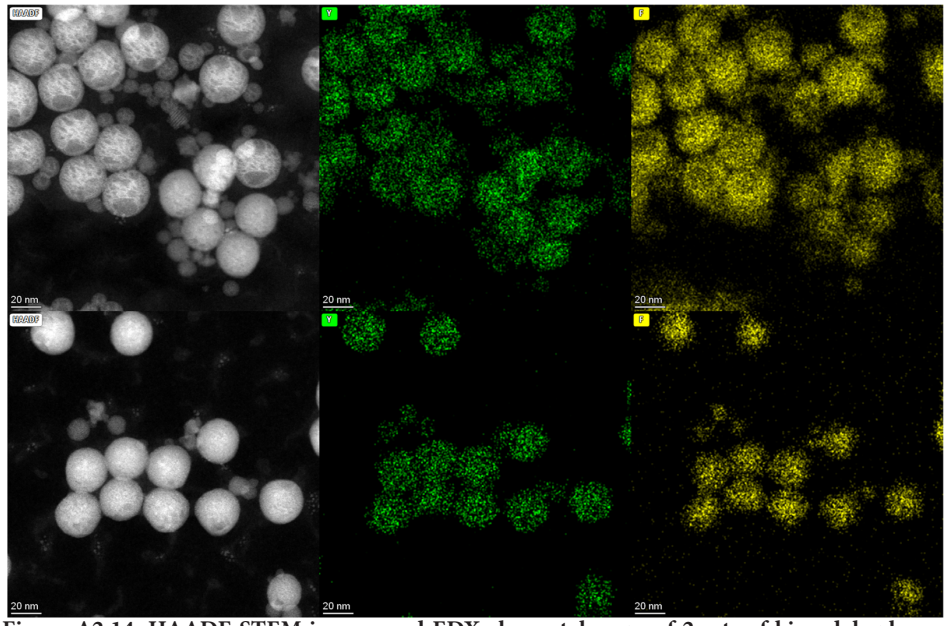


Figure A2.14. HAADF-STEM images and EDX elemental maps of 2 sets of bimodal spheres. Composition-wise, these spheres are concluded to be no different than the spheres observed and isolated at 300 °C.

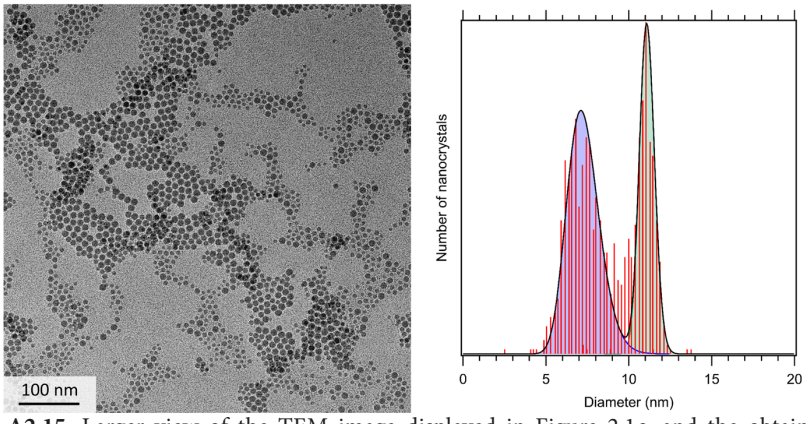
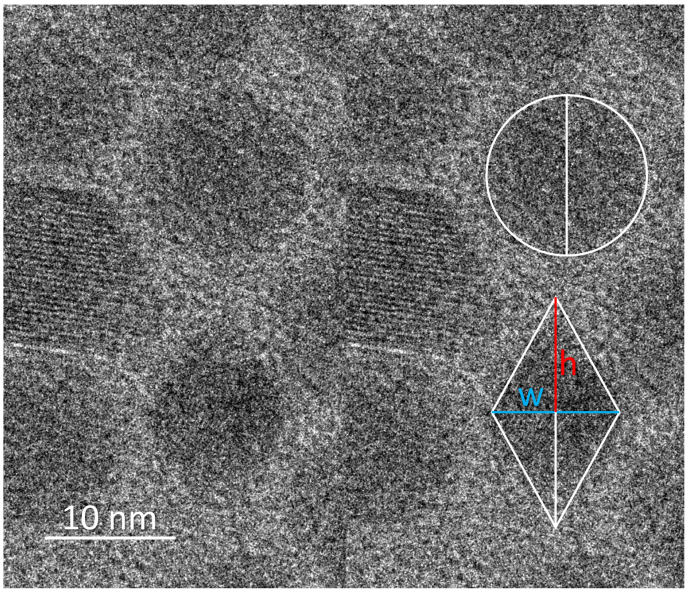


Figure A2.15. Larger view of the TEM image displayed in Figure 2.1c, and the obtained size distribution shown in Figure 2.3c showcasing the Ostwald ripening stage of the Yb:YLF spheres.

Appendix 2.14

Approximate Calculation of NC Volumes During NC Growth

In order to understand whether or not the Yb:YLF spheres crystallized into bipyramidal NCs, or that they nucleate on longer times scales only, the approximate volumes of both NC types were calculated. From Figure A2.16, where we selected a large sphere and a small bipyramidal NC, it can be seen that the volumes are relatively similar, although slightly larger for the chosen spherical NCs.



$V = \frac{\pi}{6} D^3$

$V = 638\ nm^3$

$V = \frac{2}{3} w^2 h$

$V = 562\ nm^3$

Figure A2.16. TEM image used for calculating the NC volumes. As can be seen, the volumes of the spherical NCs and the bipyramidal NCs do not differ much.

Appendix 2.15

HAADF-STEM Images of the Irregular Yb:YLF Crystals

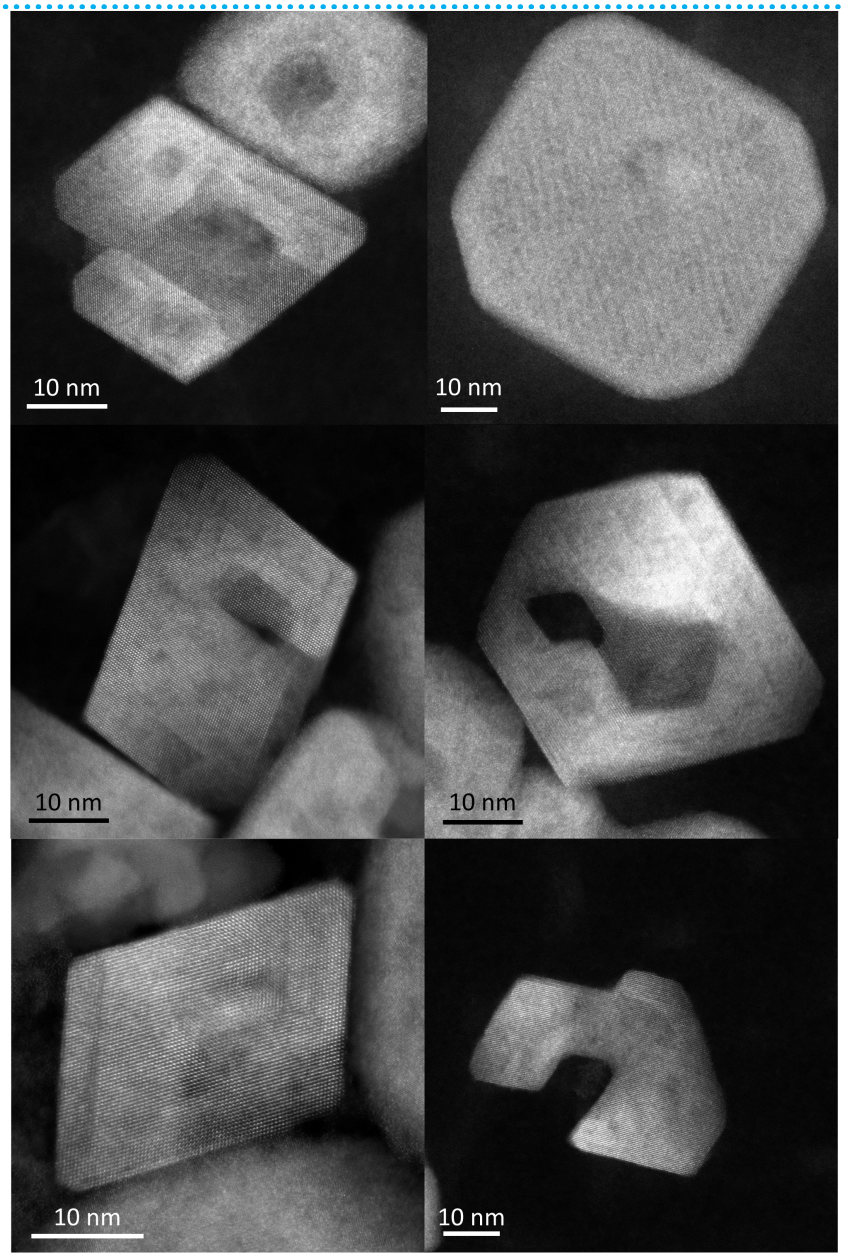


Figure A2.17. HAADF-STEM images of the irregular crystals. These images show the large variety in shapes, the large surface area and the high crystallinity for each particle. From the location of the yttrium ions (Appendix 2.9), it was concluded that these NCs consist of Yb:YLF.

Appendix 2.16

EDX of the Irregular Yb:YLF Crystals

EDX elemental mapping was performed on certain crystals, as shown below. All particles showed the presence of yttrium, ytterbium and fluoride.

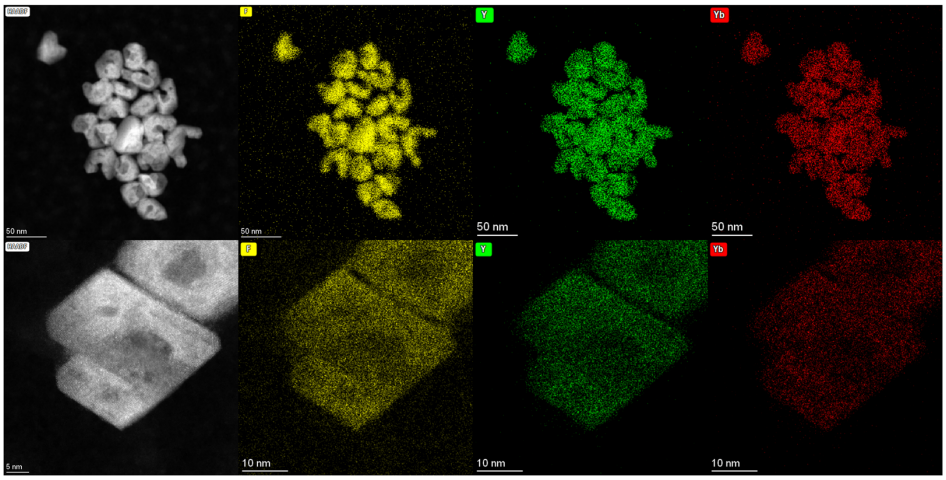


Figure A2.18. HAADF-STEM images and EDX maps of fluoride, yttrium and ytterbium showing that all the irregularly shaped crystals recovered after 24 hours consist of YLF.

Appendix 2.17

Growth of Shuriken-Shaped LiF Microcrystals

In order to understand how LiF cubes were recovered after 24 hours, a synthesis similar to the Yb:YLF NC synthesis was performed, but using solely LiTFA in order to form LiF. No particles were found at 270 °C, however at 285 °C, 300 °C, 315 °C, and 330 °C large shuriken-shaped LiF crystals were found. These crystals and their growth are shown in Figure A2.19. It is clear that these crystals are in a thermodynamically unfavorable state, due to the large surface area. When irradiating the crystals with an intense electron beam they burst, releasing a large number of smaller, cubic and highly crystalline LiF fragments (as shown in Figure 2.4f). It is important to note that the formation of Yb:YLF NCs is thus a symbiotic phenomenon between the cracking of LiTFA and $Y(TFA)_3$, preventing these LiF crystals from nucleating.

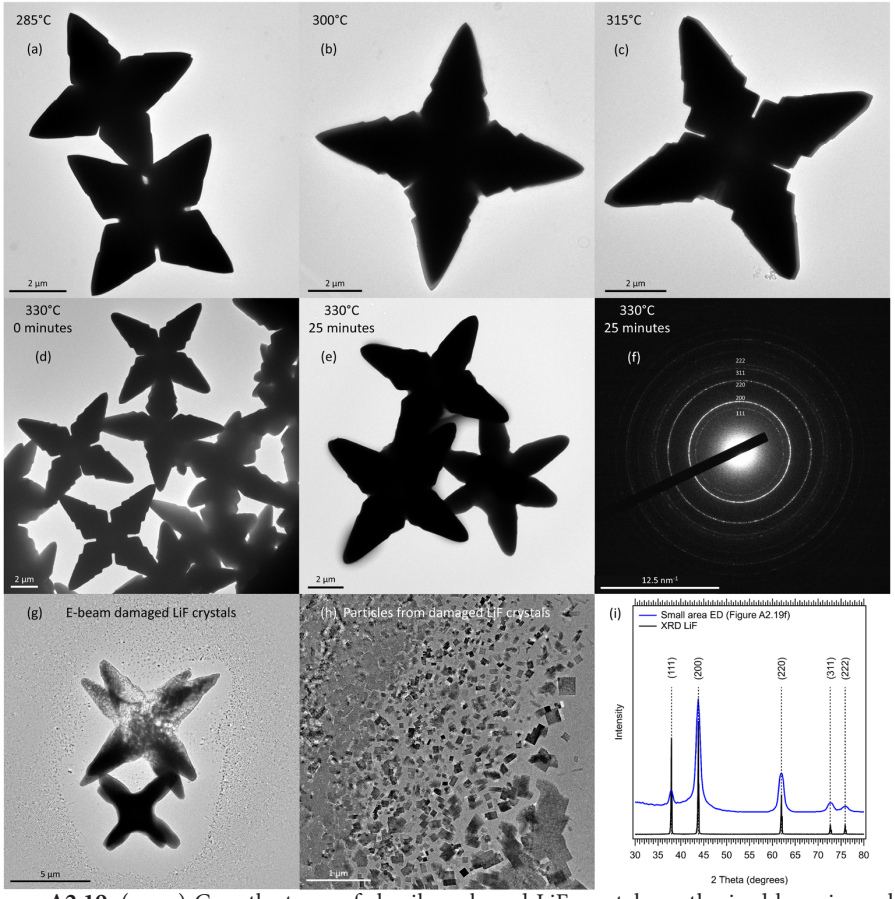


Figure A2.19. (a – e) Growth stages of shuriken-shaped LiF crystals synthesized by using solely LiTFA in the YLF synthesis. From 285 °C large crystals are found, which are unstable under the electron beam of the TEM and, as shown in (g – h) "explode" into small fragments. (i) ED on the fragments (f) of the damaged crystals confirms the material synthesized is LiF.

Appendix 2.18

Confirmation of the Shape of the LiF Cubes

Due to the limited electron density in LiF, TEM images alone could not confirm the dimensions of the LiF cubes that were found. To confirm that the material is indeed cube-shaped, tomographic measurements were performed in the TEM (JEOL JEM1400). As shown in Figure A2.20, the LiF material is indeed a near-perfect cube, and not (for example) a platelet.

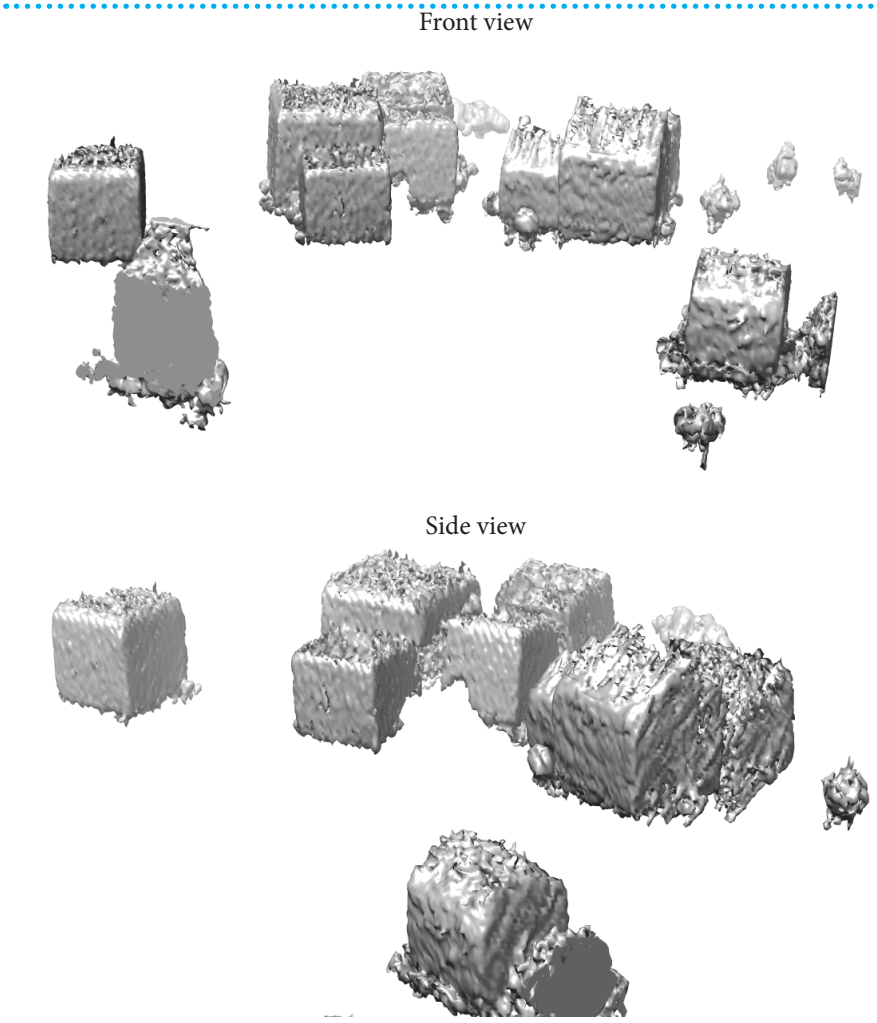
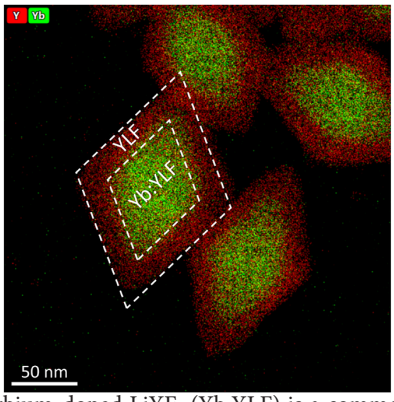


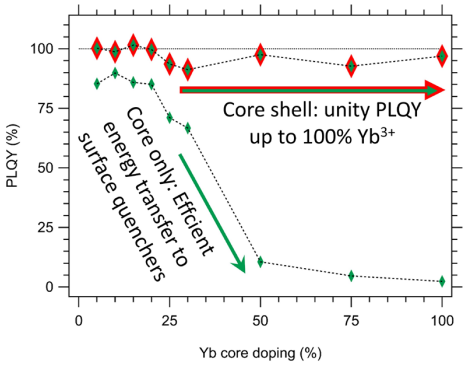
Figure A2.20. Side and front views of the LiF obtained after 24 hours, showcasing that the material is indeed present as cubes.

3

Chapter 3

Understanding and Preventing Photoluminescence Quenching to Achieve Unity Photoluminescence Quantum Yield in Yb:YLF Nanocrystals





Ytterbium-doped $LiYF_4$ (Yb:YLF) is a commonly used material for laser applications, as a photon upconversion medium, and for optical refrigeration. As nanocrystals (NCs), the material is also of interest for biological and physical applications. Unfortunately, as with most phosphors, with the reduction in size comes a large reduction of the photoluminescence quantum yield (PLQY), which is typically associated with an increase in surface-related PL quenching. Here, we report the synthesis of bipyramidal Yb:YLF NCs with a short axis of ~60 nm. We systematically study and remove all sources of PL quenching in these NCs. By chemically removing all traces of water from the reaction mixture, we obtain NCs that exhibit a near-unity PLQY for an Yb^{3+} concentration below 20%. At higher Yb^{3+} concentrations, efficient concentration quenching occurs. The surface PL quenching is mitigated by growing an undoped YLF shell around the NC core, resulting in near-unity PLQY values even for fully Yb^{3+}-based $LiYbF_4$ cores. This unambiguously shows that the only remaining quenching sites in core-only Yb:YLF NCs reside on the surface and that concentration quenching is due to energy transfer to the surface. Monte Carlo simulations can reproduce the concentration dependence of the PLQY. Surprisingly, Förster resonance energy transfer does not give satisfactory agreement with the experimental data, whereas nearest-neighbor energy transfer does. This work demonstrates that Yb^{3+}-based nanophosphors can be synthesized with a quality close to that of bulk single crystals. The high Yb^{3+} concentration in the $LiYbF_4/LiYF_4$ core/shell nanocrystals increases the weak Yb^{3+} absorption, making these materials highly promising for fundamental studies and increasing their effectiveness in bioapplications and optical refrigeration.

This chapter is based on: Jence T. Mulder, Michael S. Meijer, J. Jasper van Blaaderen, Indy du Fossé, Kellie Jenkinson, Sara Bals, Liberato Manna, Arjan J. Houtepen. ACS Appl. Mater. Interfaces 2023, 15, 2, 3274–3286.

3.1 Introduction

Ytterbium-doped $LiYF_4$ (Yb:YLF) is a well-known luminescent material, much used in, *e.g.*, laser applications, for its unity photoluminescence quantum yield (PLQY) that is commonly achieved in bulk single crystals.[1,2] Co-doped with other rare earth ions, it is broadly investigated for PL upconversion,[3–6] whereas Yb:YLF itself has also been shown to exhibit optical refrigeration, allowing the remote cooling of samples.[7–10] For many applications, a small size of the crystals, in the nanometer range, is desired.[11] This is, for example, the case when miniaturizing the application, as in microleds.[12] Another important application is in biological experiments,[13] where nanocrystals (NCs) of <50 nm are required.[14] Moreover, optical refrigeration using NCs allows the reduction of the internal temperature remotely. This is especially relevant for physical studies of the properties of single nanocrystals at low temperatures.[15]

There are various challenges in using and researching Yb:YLF NCs. First, the unity PLQY that is achieved for bulk Yb:YLF crystals is strongly reduced in NCs, limiting their applicability. There are many potential causes for this poor PLQY (as will be discussed in detail below). The literature suggests that internal quenching *via* hydroxide (OH^-) impurities and surface quenching by hydroxyl groups of solvent molecules (–OH) or OH^- surface groups are dominant.[16–21] Second, concentration quenching of the PLQY is almost always observed, leading to the use of low dopant concentrations (≤20%) with concomitant low absorption.[22,23]

Systematic studies that determine which quenching routes are dominant are scarce and focus on $NaYF_4$ and upconverting NCs.[24,25] A major challenge in the study of PL quenching in these materials is that it is notoriously hard to determine the PLQY of Yb:YLF NCs by conventional means, such as making use of reference dyes or calibrated integrating spheres. This is caused by (1) the low absorption of the parity-forbidden $^2F_{7/2} \rightarrow {}^2F_{5/2}$ transition, complicating the quantification of the number of absorbed photons, and (2) the emission wavelength around 1000 nm, where good reference dyes are absent.

This leads to the following research questions that we address in the current work: (1) Can we identify the primary quenching routes in Yb:YLF NC samples and improve the PLQY by systematically removing the possible quenching routes? (2) Does concentration quenching in Yb:YLF disappear when we remove the quenching routes?

Here, we systematically study the processes that reduce the PLQY in Yb:YLF NCs with a well-defined bipyramidal crystal shape and with a core size of ~100 × 60 nm (Figure 3.1a) in an effort to understand and mitigate these processes. To reliably determine the PLQY of these NCs, we use and verify the optical model reported by Rabouw *et al.*[24,26] This model allows one to extract the PLQY from the PL lifetime, correcting for the difference in refractive index between the particle and solvent. To remove the uncertainty from the latter correction, we used refractive index-matched chloroform as solvent. In addition, we verified the PLQY values obtained with two independent measurements based on the absolute emission of photons.

We first show that water plays a significant role in quenching the PL, likely through OH^- inclusion in the lattice during synthesis, but that this can be avoided by actively removing water through the addition of trifluoroacetic anhydride (TFAA) to the precursors before the synthesis, which has not yet been reported for the synthesis method we use. Next, we show that at low doping concentrations, the PLQY of these Yb:YLF NCs can be >90%

but that at higher Yb^{3+} concentrations, significant concentration quenching occurs. This concentration quenching is completely eliminated by growing a 15 nm Yb^{3+} free YLF shell, allowing one to reach PLQY values of near unity even for cores consisting of pure $YbLiF_4$. The PLQY in core-only samples is not dependent on the surface ligands and only weakly dependent on the solvent. Only when water or methanol is used, a slightly lower PLQY is observed for high Yb^{3+} concentrations. These results clearly show that all the processes that limit the PLQY in Yb:YLF NCs no longer happen inside the crystal but only take place at the surface; hence, all internal quenching is removed. Quenching is not related to the native oleate ligands or the BF_4^- surfactants (after ligand removal). Also, a wide range of tested solvent molecules were not found to be responsible for PL quenching. Rather, we suggest that impurities are present on the surface that cause the PL quenching in core-only Yb:YLF NCs. We propose that OH^- ions are present as surface complexes, in line with the observation that the PLQY increases if the NCs are exposed to D_2O in an effort to replace surface OH^- by OD^-. Alternatively, it is possible that phonons at the YLF surface are involved in PL quenching. To understand the mechanism of Yb-Yb energy transfer, we modeled the PLQY of our NCs using Monte Carlo simulations. Using Förster resonance energy transfer (FRET), the PLQY trend can only be modeled if FRET is restricted to nearest-neighbor Yb ions. This short-range energy transfer suggests that Dexter-type energy transfer may be the dominant mechanism. Simulations employing a Dexter-type mechanism give a better agreement with the experimental data, although more complex quenching mechanisms cannot be excluded. We do conclude that energy transfer to the surface does not occur *via* FRET to localized Yb^{3+} ions. Our results shed light on the relevant quenching processes in Yb:YLF nanophosphors and offer a method to produce Yb:YLF NCs with very high Yb^{3+} content and a near-unity PLQY. These materials are promising for optical refrigeration and lasing applications.

3.2 Synthesis of Core and Core/Shell NCs Using Chemically Dried Precursors

Yb:YLF core and core/shell NCs were prepared *via* a modification of the synthesis reported by Yi *et al.*[27] Figure 3.1a shows that this synthesis results in well-defined tetragonal bipyramidal NC cores with a narrow size distribution (Figure 3.1b). Energy dispersive X-ray spectroscopy (EDX) measurements, shown in Figure 3.1c and Figures A3.1 and A3.2, indicate that the incorporation of Y and Yb follows the feed fraction of their respective precursors. XRD on core NCs (Figure A3.3) indicates that all NCs have the same crystal phase (scheelite structure) with a small lattice contraction for samples with higher fractions of Yb ions.

When shelling the NCs with a pure YLF shell, the expanded lattice of the shell does not result in any observable core/shell mismatch, as integrated differential phase contrast (iDPC) and scanning transmission electron microscopy (STEM) micrographs (Figure A3.4) display a continuous atomic lattice throughout the entire NC. TEM images of core/shell NCs indicate that the size distribution is furthermore not significantly affected by the shelling (Figure 3.1d,e).

A ligand exchange, following the general approach reported by Dong *et al.*,[28] is performed to remove the oleate ligands and replace them with charge-balancing BF_4^- anions. This allows the NCs to be dispersed and analyzed in polar solvents (Figure 3.1f and Figure A3.6). The samples absorb and emit in the near-infrared region (Figure 3.1g) *via* the

parity-forbidden $^2F_{7/2} \rightarrow {}^2F_{5/2}$ transition of the Yb^{3+} ions. The different peaks result from crystal field splitting and are usually labeled E_1–E_4 ($^2F_{7/2}$ ground-state levels) and E_5–E_7 ($^2F_{5/2}$ excited-state levels) in the literature, as indicated in Figure 3.1g.[29] As several of the 12 possible transitions overlap, we only indicate the most prominent transitions here.

Figure 3.1h shows a PLQY measurement using a calibrated integrating sphere (see Experimental Methods section for details) for core and core/shell NCs with 30% Yb^{3+} doping dispersed in methanol. The PLQY in this case is extracted from dividing the number of emitted photons (integrated PL spectrum minus background reference) by the number of absorbed photons (integrated reference excitation spectrum minus sample excitation spectrum around 930 nm). The extracted PLQY values are 31 and 87% for the core and core/shell NCs, respectively. By far the biggest uncertainty in this measurement lies in the small absorption fraction. This means that PLQY can only be determined for relatively high Yb^{3+} doping concentrations, where concentration quenching may significantly reduce the PLQY. Additionally, in the case shown in Figure 3.1h, the emission below 940 nm is not considered, resulting in an underestimation of the actual PLQY. Even for these relatively well absorbing samples containing 30% Yb^{3+}, we assume that the error in PLQY is significantly larger than a general 3–5% error for these measurements.[30–33]

3.3 Determination of the PLQY Using Time-Resolved Photoluminescence Spectroscopy

A faster and more reliable method to determine the PLQY was reported by Rabouw *et al.*[24,26] This method is based on fitting the time-resolved photoluminescence (TRPL) decay of the Yb^{3+} emission to extract the average PL lifetime (τ_{PL}). The PLQY φ is obtained as $\varphi = \Gamma_{PL}/\Gamma_{rad}$ by comparing the measured PL rate constant ($\Gamma_{PL} = 1/\tau_{PL}$) to the radiative rate constant Γ_{rad}, which itself is obtained from the bulk radiative rate constant Γ_{rad}^{bulk} corrected for the different refractive indices of bulk YLF (n_{YLF}) and NC dispersant (n):

$$\Gamma(n) = \frac{\Gamma_{rad}^{bulk} \cdot n}{n_{YLF}} \left(\frac{3n^2}{2n^2 + n_{YLF}^2} \right)^2 \qquad (3.1)$$

The approach is shown in Figure 3.1i, which reports TRPL measurements on the same Yb(30%):YLF core and Yb(30%):YLF/YLF core/shell NCs in methanol that were used for the integrating sphere measurement discussed above (Figure 3.1h). A single exponential fit is shown as the solid black lines and corresponds to a PL lifetime of 1.088 and 2.421 ms for the core and core/shell NCs, respectively. Following Equation 3.1, this corresponds to PLQY values of 40 and 88%.

For the TRPL-based measurements, it is important that no significant reabsorption, or photon recycling, of light emitted by the NCs occurs, as this will increase the measured PL lifetime, which will overestimate the PLQY for the TRPL model.[23,34] On the contrary, reabsorption leads to an underestimation of the PLQY for methods using an integrating sphere for any NC samples that do not have unity PLQY. To avoid errors in the estimation of the PLQY due to reabsorption, we have used dispersions with low concentrations of NCs, with <2% reabsorption at the emission wavelengths (Figure A3.7). Any applied corrections for reabsorption in the TRPL measurements show that the PLQY reduces by <1% for all samples (Figure A3.8). Furthermore, we have not observed any dependence

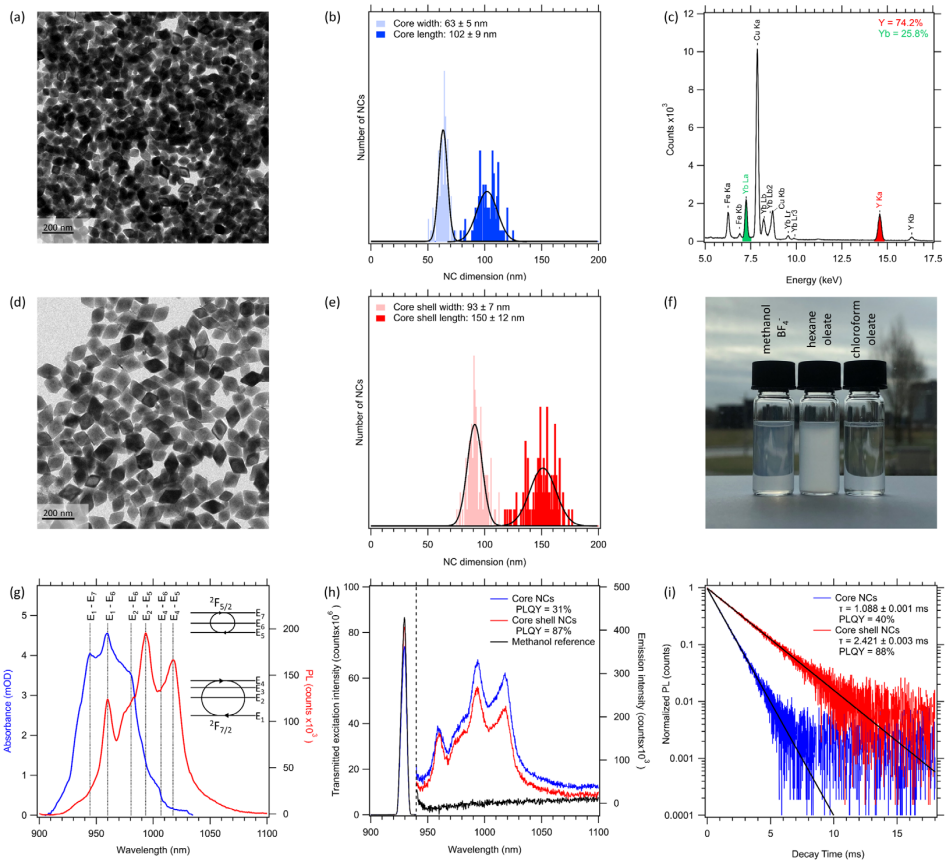


Figure 3.1. (a, d) TEM images and (b, e) size distributions of Yb(25%):YLF core and Yb(25%):YLF/YLF core/shell NCs, respectively. (c) EDX elemental analysis of the core NCs, showing the EDX peaks used for the determination of the Y:Yb ratio in red (Y) and green (Yb). (f) Yb(25%):YLF core/shell samples dispersed in different solvents showcasing the better dispersibility of NCs with BF_4^- ligands, as well as the reduced scattering with index-matched chloroform. (g) Absorbance and emission spectra (λ_{ex} = 930 nm) of a Yb(50%):YLF core/shell NC sample dispersed in chloroform. The most prominent transitions are indicated in the spectra and correspond to the energy levels indicated in the top right. (h) PLQY analyses of Yb(30%):YLF core and Yb(30%):YLF/YLF core/shell NCs dispersed in methanol using an integrating sphere method and (i) a TRPL-based method, both excited at 930 nm.

of the PLQY on the used excitation or emission wavelengths (Figure A3.9) or on the NC concentration or used excitation fluence (Figure A3.10).

The largest uncertainty in estimating the PLQY from TRPL measurements comes from the correction for the refractive index difference between NC and solvent, *i.e.*, the last term in Equation 3.1. This term is derived for spherical particles that are much smaller than the wavelength of the emitted light. Although in principle a further correction for the size of the particles can be applied (Appendix 3.9),[26] the correct analytical shape factor for bipyramidal NCs is unknown. To circumvent possible errors that result from this, we have chosen to use refractive-index matched chloroform

(n_{CHCl_3} = 1.4359,[35] n_{YLF} = 1.4485 [36]) for the TRPL-based PLQY measurements. Figure 3.1f shows a photograph of Yb(25%):YLF core/shell NCs dispersed hexane, chloroform, and methanol (after a ligand exchange to BF_4^- counterions). The sample in chloroform is fully transparent, demonstrating successful index matching. For chloroform then, the last term in Equation 3.1 approximates 1 even for other sizes and shapes.

The last remaining uncertainty in the application of Equation 3.1 then lies in the correct value of the bulk radiative rate constant Γ_{rad}^{bulk}. In the literature, for the bulk lifetime, a variety of values between 2.0 and 2.2 ms can be found.[1,15,37,38] Furthermore, previous reports have shown that the lifetime is temperature and Yb-concentration dependent. [1,4,37,38] For the purpose of this work, we have chosen to use the bulk lifetime of 5% Yb:YLF, 2.20 ms, accurately reported by Püschel *et al.*[1] as fixed radiative lifetime, and used this throughout the rest of this work.

To further confirm the validity of the TRPL approach for determining PLQY values, we have compared the extracted PLQY values for a range of samples with the PLQYs obtained from two independent measurements using integrating spheres. The first of these, already mentioned above, employed a calibrated photoluminescence spectrometer designed to measure PLQY values. The second was performed using an absorption photospectrometer and requires solely the assumption that the transmission of the sphere and sensitivity of the detector are the same for the photons absorbed and emitted, which is reasonable as the difference in wavelength is small (see Figure 3.1g). The details of this measurement are explained in Appendix 3.10. All obtained PLQY values are summarized in Table 3.1, which shows that within 10%, all methods agree and yield the same PLQY value.

Table 3.1. PLQY values obtained from integrating sphere measurements compared to PLQY values obtained from TRPL measurements on the same sample.

sample	method	obtained PLQY(%)	method	obtained PLQY (%)	figure
Yb(30%)YLF methanol	integrating sphere: emission	31	TRPL	40	3.1h/i
Yb(30%)YLF/YLF methanol	integrating sphere: emission	87	TRPL	88	3.1h/i
Yb(50%)YLF chloroform	integrating sphere: absorbance	16	TRPL	13	A3.12a
Yb(50%)YLF/YLF chloroform	integrating sphere: absorbance	91	TRPL	96	A3.12b

The above discussion and comparison with other PLQY measurement methods show that the TRPL model is a useful, faster, and more easily applicable method than methods that rely on an accurately measured absorbance. For this reason, the TRPL method is used throughout the remainder of this work to study various PL quenching pathways in these Yb:YLF NCs.

3.4 Overview of Potential Quenching Pathways in Yb:YLF

An overview of possible quenching pathways is shown in Figure 3.2. From the literature, it is known that crystal defects and impurity ions (*e.g.*, d-block metals and lanthanides other than Yb^{3+}) can reduce the PLQY *via* nonradiative recombination (process 3 in Figure

3.2) or parasitic absorption (process 6).[18] We have attempted to reduce the PL-quenching influence of these factors as much as possible by using the highest possible temperature for the synthesis (reported to reduce the formation of crystal defects[39,40]) and the highest possible precursor purities.

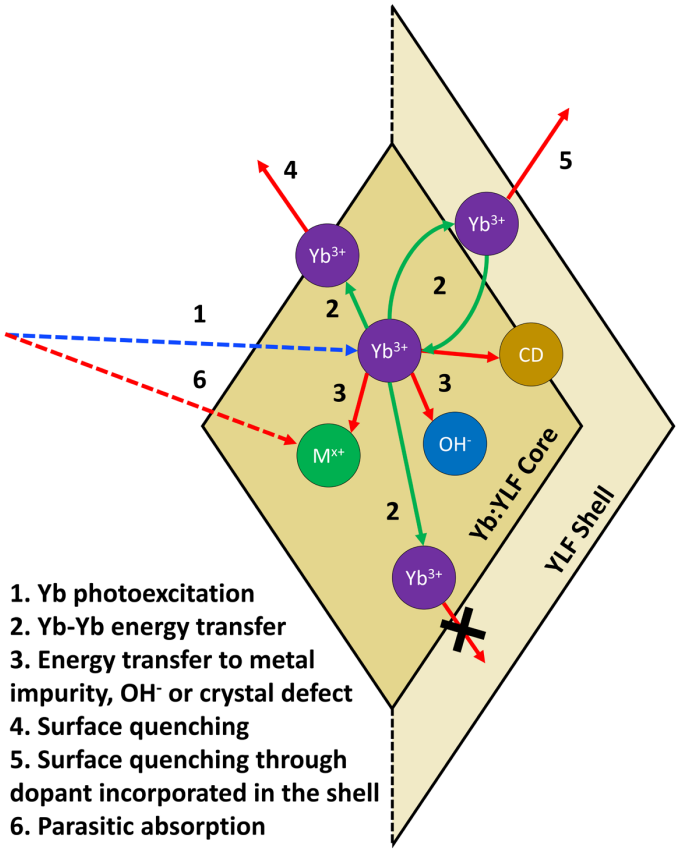


Figure 3.2. Photophysical pathways involved in photoluminescence and photoluminescence quenching. All red arrows indicate processes that result in a reduction of the PLQY, whereas the green arrows indicate energy transfer between Yb^{3+} sites.

3.5 Effect of Water During the Synthesis on the PLQY of Core NCs

It is reported that a main PL quenching pathway for Yb^{3+} emission is energy transfer to incorporated OH^- originating from water that is present during the synthesis.[24,25] As OH^- ions substitute F^- ions in the YLF host, removing incorporated OH^- postsynthesis is difficult. Therefore, the synthesis should be performed completely water-free. As the trifluoroacetate (TFA) precursors for the NC synthesis are made using water, it is important to remove any water that is still present. To minimize the presence of internal OH^- impurities in the crystal lattice, we adopted a recent method by Homann *et al.*[41] for the drying of metal acetate precursor salts and introduced it to our metal trifluoroacetate precursors (Figure 3.3a), which has not been reported before. To do this,

we first synthesize the TFA salts from the respective metal oxide or metal carbonate and aqueous trifluoroacetic acid (HTFA), remove all free water and acid under vacuum, and subsequently add trifluoroacetic anhydride (TFAA) that chemically reacts away all traces of (crystal) water (see Figure 3.3a), irreversibly forming HTFA. Therefore, a significant improvement is made for this synthesis method, as the newly introduced drying method removes any traces of water that are left without introducing any chemical species that are not already present for the TFA salt synthesis. Subsequent removal of unreacted TFAA and any free HTFA is swiftly done by applying a vacuum, resulting in very dry and pure TFA salts. This is an overall improvement for Yb:YLF NC syntheses using TFA salts, for which until now no drying method existed. This drying method can furthermore be expanded to any syntheses relying on very dry TFA-based precursors.

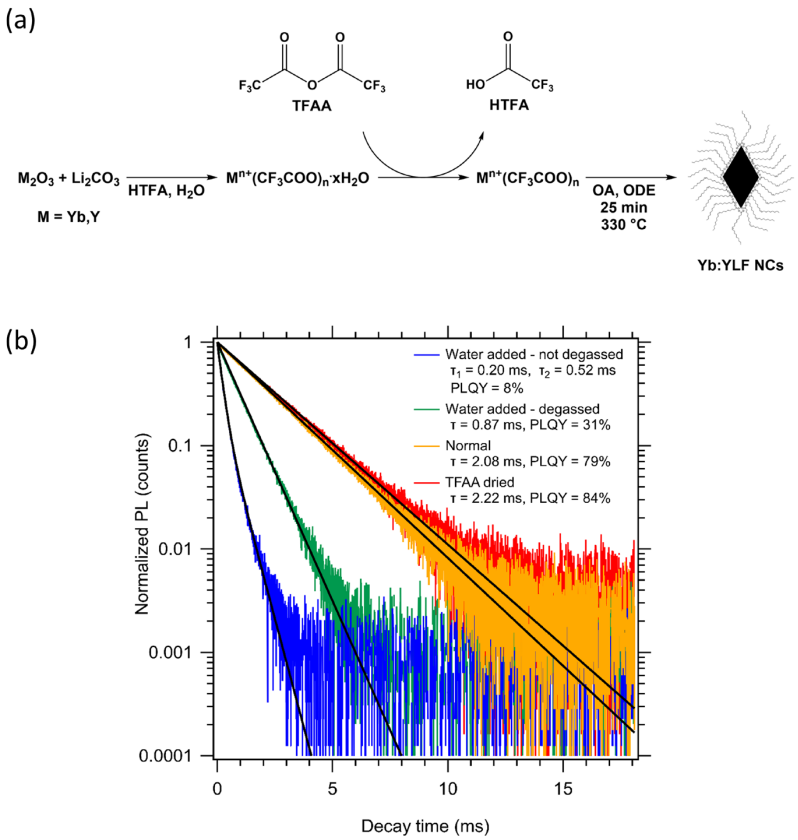


Figure 3.3. (a) A schematic representation of the synthesis of the TFA-based precursors from their oxides or carbonates with HTFA, the subsequent drying step utilizing TFAA, and the NC synthesis itself from the dried precursors. (b) TRPL spectra of Yb(10%):YLF core NCs dispersed in hexane (λ_{ex} = 930 nm). The blue and green curves correspond to samples where 250 µL of water was added before (green) or after (blue) the degassing step prior to the synthesis (see Experimental Methods and Appendix 3.11). The yellow and red curves correspond to samples synthesized with precursors that were (red) or were not (yellow) dried using TFAA.

The importance water has on the PLQY is shown in Figure 3.3b, where we show TRPL traces of NCs synthesized with water added and/or removed at different stages. The green and blue traces are obtained for samples where 250 μL of water (~14 mmol) was added before (green) and after (blue) the degassing step that precedes the synthesis. In both cases, the PL lifetime is much shorter, and the extracted PLQY is much lower (31 and 8%, respectively), than without the addition of water. As shown in Figure A3.13, many small particles are present next to the YLF NCs, explaining the biexponential PL decay shown in Figure 3.3b. The yellow curve corresponds to a normal synthesis without the use of TFAA. The PL lifetime in this case is 2.08 ms, and the extracted PLQY is 79%. A further increase of the lifetime and PLQY (to 84%, $\tau = 2.22$ ms) is observed for the samples synthesized with precursors that were additionally dried with TFAA. These results show the importance of removing water from the synthesis. To obtain the highest PLQYs, the TFA precursors need to be dried with TFAA.

3.6 Disappearance of Concentration Quenching by the Growth of a Shell

The factors discussed so far (metal impurities, crystal defects, and OH^- incorporation) cannot be improved by postsynthesis procedures and therefore set an upper limit for the PLQY of Yb:YLF NCs. As we show later, these parameters have no significant influence on our NC samples because near-unity PLQY values can be obtained. Additionally, an important factor that reduces the PLQY of nanometer-sized phosphors is quenching at surface sites (Figure 3.2, process 4).[42,43] This surface quenching can be mitigated by growing lattice matched shells of Yb-free YLF. This will prevent energy transfer to the surface and hence reduce surface-related PL quenching. It may inhibit surface quenching altogether if the shell is thick enough and Yb free. The latter is not trivial as Yb migration can potentially take place at the elevated temperatures usually employed to grow defect-free YLF shells, thereby introducing pathways for energy transfer to the NC surface (Figure 3.2, process 5).[44]

We synthesized Yb:YLF/YLF core/shell NCs by adding $Y(TFA)_3$ and LiTFA to previously synthesized and purified Yb:YLF core NCs at the core synthesis temperature in a clean and hence Yb-free solvent mixture (see Experimental Methods section). Figure 3.4a shows a high-angle annular dark field-STEM (HAADF-STEM) image of the resulting Yb(25%):YLF/YLF core/shell NCs. The shell thickness of 15 nm can be estimated because of the difference in the atomic number of Y^{3+} ($Z = 39$) and Yb^{3+} ($Z = 70$). EDX was used to visualize the location of Y and Yb ions (Figure 3.4b,c and, including F^-, Appendix 3.12). Only a very slight amount of Yb signal is recorded in the shell location, as well as in the exterior, potentially as a result of beam damage inflicted during the EDX measurements. An EDX line scan was performed (direction indicated in Figure 3.4c), confirming that the Yb signal quickly drops from the core to the shell (Figure 3.4d). This shows that no significant Yb^{3+} ion migration occurred during shell growth. This is likely due to our shelling method being much faster (45 min total) compared to the literature reporting ion migration (15 min per precursor addition plus a 2–12 h annealing step).[44]

The thickness of the YLF shell can in principle be increased at will by repeating the shelling procedure. Figure 3.4e,f demonstrates this for pure $LiYbF_4$ core NCs with a single shell of 15 nm (Figure 3.4e) and an increased shell thickness of 30 nm. In the remainder of this work, we employed only core–shell NCs with a 15 nm shell, as we will later discuss that

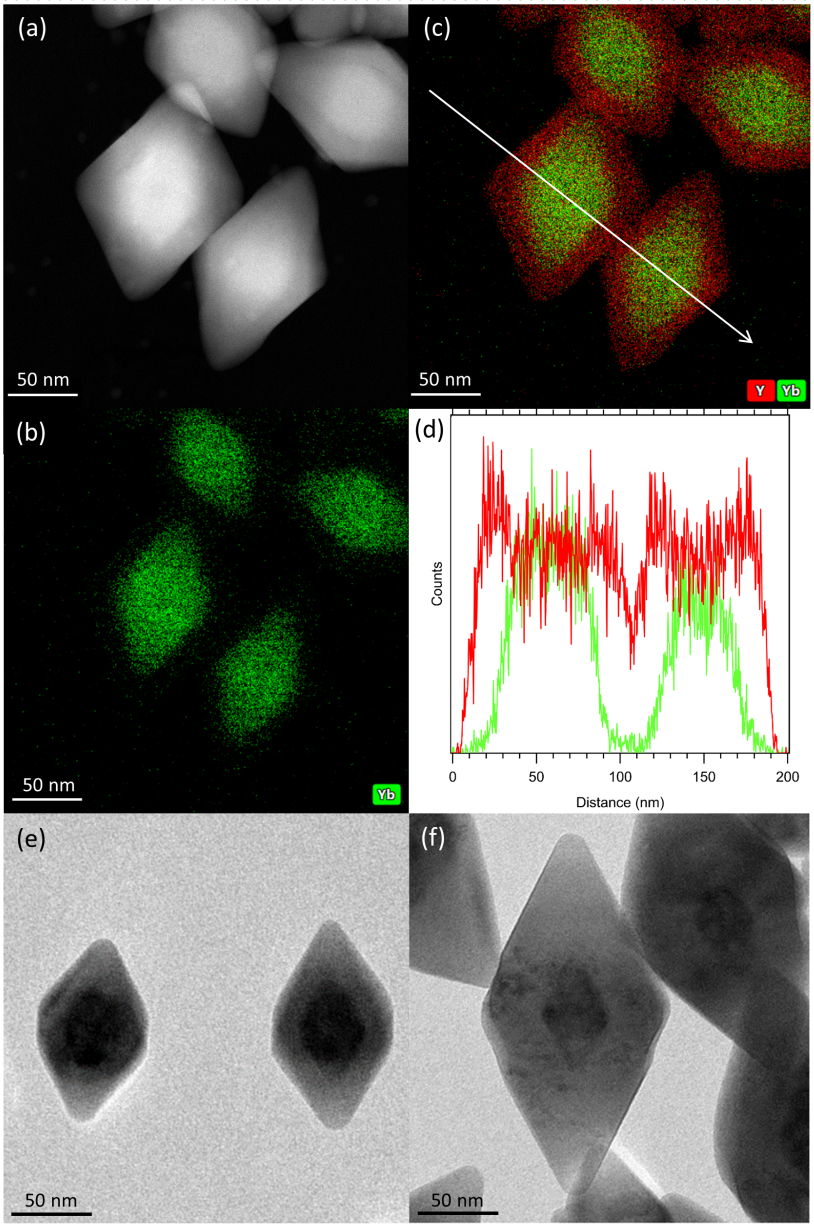


Figure 3.4. (a) HAADF-STEM image of Yb(25%):YLF/YLF core/shell NCs and (b) EDX analysis of Yb and (c) Y (red) and Yb (green) used to identify the Yb fraction in the YLF shell. The white arrow shows the direction of the line scan measurement shown in panel d. (d) EDX line scan of the NCs shown in panels a–c showing the intensity of Y (red) and Yb (green) through the NC shell and core. (e) TEM image of $LiYbF_4$/YLF core/shell NCs and (f) $LiYbF_4$/YLF/YLF core/shell/shell NCs showcasing a large contrast between the electron dense core and the less electron dense shell, as well as the possibility to grow additional layers of YLF in case Yb migration to the surface does affect the PLQY of the NC sample.

this is sufficient to remove the effect of surface quenching (Figure 3.5a,d,e, *vide infra*), in accordance to Rabouw *et al.*[24]

To investigate the effect of surface-related quenching, we studied the Yb^{3+} concentration-dependent PLQY. A set of core-only NC samples with different degrees of Yb doping was synthesized (using the extra dried precursor method) and dispersed in index-matched chloroform. The PLQY was determined from the PL lifetime using Equation 3.1. The results are shown as the open symbols in Figure 3.5a. At low doping densities, the PLQY is high (80–90%). However, from Yb(25%):YLF onward, the PLQY rapidly reduces with increasing doping density and drops to nearly 0 for >75% Yb^{3+}. The observed concentration quenching can be attributed to efficient energy transfer (ET) between Yb^{3+} ions, allowing the excitation to reach quenching sites located on the surface within the radiative lifetime of the Yb ion, as often reported in the literature.[45–47]
The solid symbols in Figure 3.5a represent samples where a 15 nm Yb-free YLF shell was grown around the same Yb:YLF core-only NCs. In this case, the PLQY is even higher (>90% at low Yb concentration, with 99.5 ± 2.4% at 20% Yb as the highest obtained value). Strikingly, for these core/shell NCs, there is no sign of concentration quenching even up to "100% Yb-doped" $LiYbF_4/LiYF_4$ NCs. In that specific case, the PLQY of the core-only sample is only 2% (τ = 50 µs), whereas the extracted PLQY of the core/shell sample is 91% (τ = 2.04 ms). The addition of a second shell increased this PLQY even further to 94% (τ = 2.10 ms). To show the uncertainty of the reported values, the average PLQY of the samples is plotted (as markers) together with the measurement error from performing multiple measurements (error bars), indicating the generally high reproducibility of the measurements. The influence of a deviation from the used bulk radiative lifetime (2.20 ms) is shown by the red shaded area. Here, a PLQY range is shown to indicate the accuracy of the measured PLQY when using a 10% increase or decrease of the bulk lifetime.
The clear concentration quenching of the core-only samples and the absence thereof in the core/shell NCs clearly demonstrate that the main PL quenching occurs on the surface. At low Yb concentrations, this results only in a marginal decrease of the PLQY in core-only NCs because photoexcitation predominantly takes place in the interior of the NCs. At higher Yb concentrations (>20%), efficient ET causes the photoexcitation to migrate through the NCs to the surface, where PL quenching takes place. An Yb-free YLF shell prevents migration of the excitation to the surface.

3.7 Modeling the PLQY *via* Yb-Yb Energy Transfer to the Surface

To confirm the above hypothesis and investigate the ET process, we simulated PL quenching by a full Monte Carlo simulation. Here, bipyramidal Yb:YLF NCs of varying sizes are modeled atomistically, with a stochastic distribution of Yb^{3+} ions in the lattice. The details of this approach are reported in Appendix 3.14. Initially, we considered that migration of the excitation occurs *via* FRET using $k_{FRET} = k_{rad} \times (R_0/R_{Yb})^6$, where $k_{rad} = 1/\tau_{PL} = 4.55 \times 10^{-4}$ µs^{-1} [48] and R_{Yb} is the distance to the other Yb atoms. The Förster radius R_0 was estimated to be 1.5 nm on the basis of a similar value reported for FRET in Er^{3+}/Yb^{3+}:$NaYF_4$.[49] We assume that efficient quenching at the surface takes place. This means that any excitation that migrates to the first two monolayers of the NC surface (see Appendix 3.14 for details) is removed from the simulation, reducing the PLQY. No other sources of PL quenching are included.

The black lines in Figure 3.5a show the PLQY as predicted by the MC simulations for a 22 nm large NC. The dotted black line, which assumes that FRET can occur to all other Yb^{3+} ions, predicts that concentration quenching already sets in at low concentrations. Regardless of the parameters used in the calculations, we do not find a plateau with constant PLQY values in combination with near-zero PLQY values at the highest Yb^{3+} concentrations, as is observed in the experiment. However, if we only allow FRET to nearest-neighbor Yb ions, the obtained trend for PLQY *vs*. Yb concentration, as given by the dashed black line, agrees well with the experimental data points. The simulated PLQY value in the low concentration plateau increases with increasing NC size (see Figure A3.16a), from ~50% at a long NC axis length of 10 nm to ~90% for 68 nm, simply reflecting the surface to volume ratio of the NCs. The reason that the simulated PLQY values in Figure 3.5a are lower than the experimental values is due to the smaller size of the simulated NCs ($22 \times 15 \times 15$ nm) *vs*. the experimental NCs ($100 \times 60 \times 60$ nm).

The observation that FRET to nearest-neighbor Yb^{3+} ions reproduces the experimental data shows that the range of the ET process is shorter than expected for FRET, suggesting that ET may be mediated *via* the exchange interaction rather than *via* electric dipole coupling, and hence may correspond to Dexter-type energy transfer (DET). There are however only few literature references that discuss DET in similar lanthanide-doped systems.[50–52]

We simulated DET in a manner identical to the FRET simulations discussed above but using a transfer rate constant $k_{Dexter} = A \times \exp(-\beta \times r)$ (see Appendix 3.14 for details). The distance dependence is mostly governed by the tunnel decay parameter β, whereas the prefactor A sets the overall rate constant. The solid black line in Figure 3.5a is the result of such a simulation. As can be seen, it gives similar results to FRET using nearest neighbors only and captures the trends seen in the experimental data. As above, the PLQY value in the plateau is artificially low because of the small simulated crystal size. We remark that the solid black line was obtained with $A = 2.38 \times 10^8$ μs^{-1} and $\beta = 0.5$ nm^{-1}. This tunnel decay parameter is higher than the value of 0.1 nm^{-1} that is more commonly used.[52] Lower values of β fail to reproduce the PLQY plateau at low Yb^{3+} concentrations. This shows that the ET mechanism must have a very steep distance dependence, but raises questions about the details of the DET simulations. The model used here is clearly an oversimplification. Finite surface quenching rates or a distribution of quenching sites on the surface could improve the model and perhaps allow the data to be described with more reasonable DET or FRET parameters.

Overall, the simulations validate that the Yb^{3+} concentration dependence of the PLQY is explained by energy transfer to the surface and suggest that Dexter-type energy transfer may be the dominant ET mechanism responsible. To understand the complete ET mechanism and concomitant quenching, modeling is required to distinguish between all the possible scenarios based on global fits to all the PL-decay curves rather than the PLQY trend that we have modeled. The main important observation here is that FRET alone does not describe the PLQY trends observed.

3.8 Effect of Surface Ligands, Solvents, and Unwanted Surface States on the PLQY

In an attempt to identify the nature of surface PL quenching, we measured the PLQY with different surfactants and in different solvents. As mentioned before, from all samples

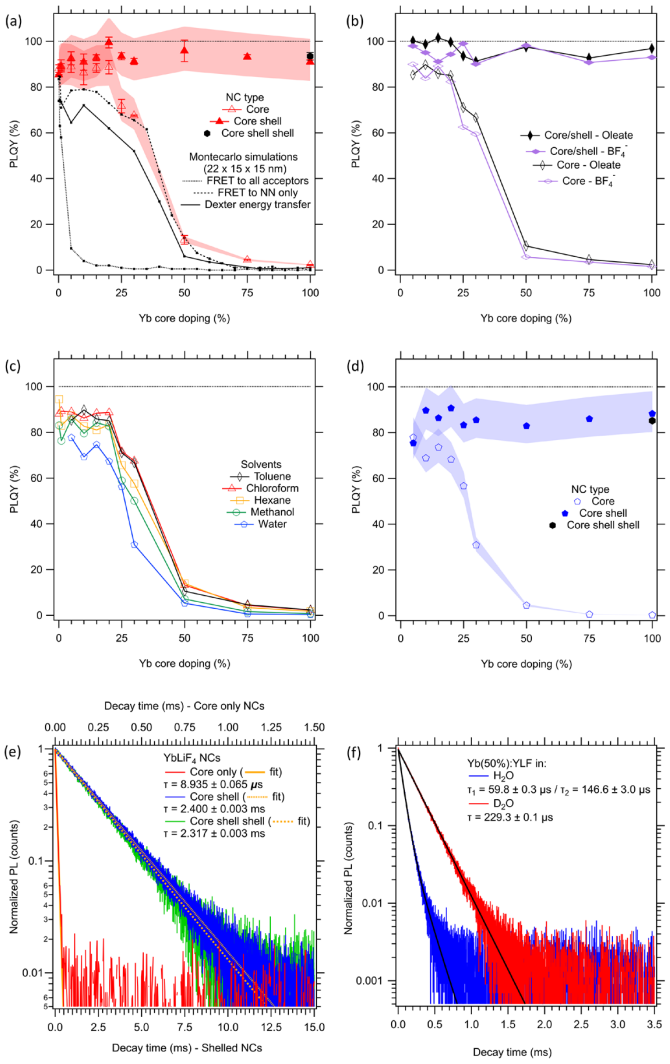


Figure 3.5. (a) PLQY values derived from PL lifetimes of core and core/shell NCs with different core Yb doping dispersed in index-matched chloroform. The error bars indicate the error of the PLQY value obtained by repeating the measurements. The red shaded area indicates the spread of PLQY when a 10% higher (2.42 ms) or lower (1.98 ms) bulk radiative lifetime is chosen than the 2.20 ms used in the rest of the analyses. The dotted, dashed, and solid black lines correspond to simulated PLQYs using Förster resonance ET or Dexter-type ET. (b) PLQY values calculated from PL lifetimes of core and core/shell NCs dispersed in toluene with either oleate or BF_4^- ligands and (c) core NCs dispersed in different solvents. (d) PLQY values derived from PL lifetimes of core and core/shell NCs with different core Yb doping dispersed in water. Similar to panel a, the influence of a 10% change of bulk PL lifetime is indicated by the blue shaded area. (e) TRPL spectra of 100% $LiYbF_4$ core (red), core–shell (blue), and core–shell–shell NCs (green) dispersed in water. (f) TRPL spectra of Yb(50%):YLF NC cores dispersed in H_2O (blue) and D_2O (red) showcasing a longer PL lifetime and single exponential PL decay when D_2O is used.

shown in Figure 3.5a, the native oleate ligands were reacted away and replaced by BF_4^- ligands following the procedure reported by Dong *et al.*[28] This allowed stable dispersion of the NCs in polar solvents (Figure 3.1f). Both the oleate- and BF_4^--containing NCs were dispersed in toluene (as the BF_4^--containing NCs do not disperse well in chloroform); the PLQYs were determined and are shown in Figure 3.5b. It is clear that the absolute PLQY values as well as the dependence on the Yb^{3+}-doping fraction are nearly identical for both surface molecules. Therefore, we conclude that the oleate surface ligands and BF_4^- counterions do not have a large influence on the overall PLQY of the NCs.

To identify the influence of ET to the surrounding solvent molecules on the PLQY, the PLQYs of NC samples dispersed in toluene, chloroform, and hexane (with oleate ligands) and in toluene, methanol, and water (with BF_4^- ligands) were compared. As shown in Figure 3.5c and Figure A3.17, the same concentration quenching trend is again clearly visible, and similar PLQY values of >80% are observed at low Yb^{3+} concentrations. This observation suggests that energy transfer to solvent vibrations is not the limiting factor for the PLQY. Indeed, energy transfer to overtones of C–H vibrations in, *e.g.*, hexane, toluene, and chloroform is reported to be roughly 15 times slower, and energy transfer to overtones of C–C and C–Cl vibrations is orders of magnitude slower than energy transfer to –OH vibrations in water or methanol.[53,54] This suggests that there is an additional source of PL quenching at the surface of the NCs. The samples in nonpolar solvents contain oleate surface ligands, which could potentially induce quenching by energy transfer to vibrations of the biding carboxylate group. In addition, we consider that there possibly could be OH^- groups binding to the surface that could act as quenchers. In the case of methanol and water, these oleate ligands have been removed, but here, the solvent –OH groups could act as quenchers for the core-only Yb:YLF NCs.[55–57]

To highlight the PLQY in water, which is the most important solvent for applications in, *e.g.*, biological systems, we show in Figure 3.5d how the PLQY of core-only and core–shell Yb:YLF NCs depends on Yb^{3+} doping concentration when dispersed in water (after ligand removal with $[Et_3O][BF_4]$). For the core-only samples, we observe concentration quenching for concentrations of >20%. The core–shell samples do not show concentration quenching even up to 100% Yb^{3+}, similar to the observation made for samples in chloroform (Figure 3.5a). Indeed, this is expected for the relatively thick shell of 15 nm that was used in this work, which should slow down energy transfer to solvent or surface states by several orders of magnitude.[24] To further exclude the effect of energy transfer to the solvent or surface, we also increased the shell thickness to 30 nm (black solid marker in Figure 3.5d) and found that the observed PL lifetime is the same, within the measurement uncertainty, as for the 15 nm shells (green and blue lines in Figure 3.5e).

Although these experiments exclude quenching *via* energy transfer to solvent vibrations in the core–shell samples, the PLQY in water does appear to be lower than that in chloroform. The average PLQY of the core–shell NCs for all Yb concentrations in water is 86 ± 4%, whereas in chloroform, we find 93 ± 3%. We consider however that accurate PLQYs in water are more difficult to determine exactly as water has a much larger mismatch of refractive index with YLF than chloroform, making the correction to the radiative lifetime *via* Equation 3.1 much larger and more prone to errors than in index-matched chloroform. We show in Figure A3.18 and the related discussion in the Appendix that the PLQY derived *via* Equation 3.1 decreases systematically with decreasing refractive index of the solvent. We therefore trust the derived PLQY values in chloroform better and

consider the values reported here for water to be a lower limit of the real PLQY.
As indicated before, quenching on the surface can also be due to unintentional surface molecules, which in that case are potentially equally present in all solvents, depending on their origin. The usual candidate in the literature is surface OH^- originating from water.[21,24,25,58] In principle, this should be removed by the ligand exchange procedure as OH^- is expected to react with triethyloxonium cations, which otherwise reacts with surface oleate ligands (see Experimental Methods), to form diethyl ether and ethanol. To test the role of OH^- in the observed PLQY quenching at the surface, an Yb(50%):YLF core NC sample dispersed in water was washed thrice and resuspended each time in pure D_2O. As protons readily exchange with deuterons, surface OH^- is expected to convert to OD^-. The vibrational energy of the OD^- stretch is about $\sqrt{2}$ times smaller than the OH^- vibrational stretch energy, lowering the probability of PL quenching *via* energy transfer to OD^-. As shown in Figure 3.5f, the PL lifetime of the sample in D_2O is significantly longer and hence the PLQY is larger than in H_2O. This is in accordance with previous observations on Yb:$NaYF_4$ [25,59] and with the notion that surface quenching may involve adsorbed OH^-. However, because the role of the solvent in the quenching process cannot be excluded here, we cannot definitively conclude that surface OH^- species are the dominant PL quencher. Alternatively, it is possible that phonons at the YLF surface are involved in PL quenching. It is well known that the phonon modes at the NC surface differ from bulk phonon modes, have a much broader spectrum, and extend to higher frequencies.[60] The maximum bulk optical phonon energy in YLF is 560 cm^{-1} (69 meV),[61,62] which implies that multiphonon relaxation to the ground state involves on average 18 phonons ($\overline{\lambda_{em}}$ = 992 nm, $\overline{E_{em}}$ = 10,082 cm^{-1} = 1.250 eV, Appendix 3.17) and is inefficient. Higher energy surface phonon modes could potentially speed up nonradiative multiphonon emission to the ground state.

3.9 Discussion

Yb:YLF NCs synthesized with chemically dried precursors have shown high PLQYs (>80%) for all samples with less than 25% Yb doping. Above this concentration, a rapid PLQY decrease is observed, which we attribute to efficient ET to the NC surface, where the photoexcitation is rapidly lost, reducing the PLQY for higher Yb-doped cores. Shelling these cores with an Yb-free YLF shell has shown to yield high PLQYs for all Yb doping fractions. The PLQY of Yb(20%):YLF/YLF NCs is practically unity (99.5 ± 2.4%), and as it is measured in index-matched chloroform, the only remaining insecurity is the correct assessment of the bulk lifetime. Even for "100% doped" $LiYbF_4$/$LiYF_4$ NCs, the obtained PLQY is above 90%, providing improved opportunities for applications where a higher absorption cross section is preferred, for example, in biomedical imaging or in optically pumped lasing media. NCs with PLQYs >96.3% (Appendix 3.17) can furthermore exhibit optical refrigeration when excited at the right wavelength. On the basis of their PLQY values, some of the samples reported here should show optical refrigeration (as a NC ensemble); however, this is within the uncertainty of the PLQY measurements. We have tried to measure optical refrigeration in solutions and on films by analyzing the change of emission peak ratios as mentioned by Luntz-Martin *et al.*[63] (influenced by the number of phonons present, Appendix 3.18 and 3.19), but the results do not yet convincingly show evidence of cooling, possibly as a result of too efficient heat transfer from the surroundings to the NCs. Efforts to measure optical refrigeration on single NCs using optical levitation, as reported before,[15,64–66] are currently under way.

3.10 Conclusions

We have reported an optimized protocol for the synthesis of large Yb:YLF NCs to reach near-unity quantum yields even for $LiYbF_4/LiYF_4$ core/shell NCs. We showed that any water present during the synthesis has a strongly negative effect of the PLQY but that we can remove all water from our precursors by extensive drying procedures using trifluoroacetic anhydride. Next, we showed that growing an undoped YLF-shell around the Yb:YLF core is essential to obtain high PLQYs even for full $YbLiF_4$-based core shell samples. We conclude that all internal quenching is removed and hence the main cause of PL quenching lies on the surface of the NCs. We show that this is not related to the intentional surface molecules (oleate or BF_4^-) or the solvent but is most likely due to unintentional surface moieties (*e.g.*, OH^-) or surface phonon modes. Numerical simulations confirm that the Yb^{3+} concentration dependence of the PLQY is explained by energy transfer to the surface and suggest that Dexter-type energy transfer may be the dominant ET mechanism or that more complex quenching mechanisms are predominant, and confirm that FRET is not the main route for energy transfer.

Experimental Methods

Materials

1-Octadecene (ODE, technical grade, 90%), triethyloxonium tetrafluoroborate ($[Et_3O][BF_4]$, ≥97.0%), acetonitrile (ACN, 99.8%, anhydrous), chloroform (≥99%, anhydrous), and methanol (≥99.9%, anhydrous) were purchased from Sigma-Aldrich. Oleic acid (extra pure), trifluoroacetic acid (HTFA, ≥99.0%, for HPLC), trifluoroacetic anhydride (TFAA, ≥99.0%), lithium carbonate (Li_2CO_3, 99.999%, trace metal basis), yttrium oxide (Y_2O_3, 99.9999%, REO), and ytterbium oxide (Yb_2O_3, 99.998%, REO) were purchased from Fisher Scientific. Toluene (≥99.8%, anhydrous) and ethanol (≥99.8%, anhydrous) were purchased from VWR Chemicals. Hexane (>96.0%, anhydrous) was purchased from TCI. Deuterium oxide (D_2O, >99.90% D) was purchased from Fluorochem Ltd.

All chemicals were used as received unless specified differently. All manipulations were performed under a N_2 atmosphere using standard Schlenk line techniques or a nitrogen-filled glove box (<0.1 ppm H_2O; <0.1 ppm O_2) unless otherwise mentioned.

Milli-Q water was obtained from a Milli-Q Advantage A10 system (Merck Millipore, 18.2 MΩ·cm, 2 ppb TOC).

Synthesis and Drying of Metal Trifluoroacetate Precursors

Metal trifluoroacetate salts, $M^{x+}(TFA)_x$ ($M = Li^+, Y^{3+}, Yb^{3+}$), were synthesized by adding 5 mmol Li_2CO_3 (369 mg), Y_2O_3 (1129 mg), or Yb_2O_3 (1970 mg) and 5 mL of Milli-Q water to a 25 mL two-necked flask with a fused thermocouple insert containing a PTFE-coated stirring bar. The flask was connected to a Schlenk line equipped with a water-cooled condenser, and 5 mL of trifluoroacetic acid (HTFA; ~65 mmol) was added dropwise under stirring. *Note: As the reaction between HTFA and Li_2CO_3 is strongly exothermic and results in the release of a large volume of CO_2, the acid should be added carefully to avoid splashing.* After all of the acid had been added, the necks of the flask were closed with septa, and the reaction mixture was placed under N_2 gas flow. The mixture was heated to 120 °C and left under reflux until a clear, colorless solution was obtained (generally <1 min

for Li_2CO_3 and >1 h for Y_2O_3 and Yb_2O_3). At this point, the reaction mixture was cooled to below 50 °C, and a vacuum was applied to evaporate all water and acid. The resulting solids were transferred to a glove box and crushed to form a white powder. These powders may appear dry but are very likely to contain crystal water, especially in the case of lithium trifluoroacetate, which is extremely hygroscopic.

To remove the undesired crystal water, the precursor salts were dried further using trifluoroacetic anhydride (TFAA). Briefly, the powdered metal TFA salts were added to a 250 mL round-bottom flask, connected to a Schlenk line, and placed under nitrogen flow. TFAA (5 mL, ~36 mmol) was added, resulting in a rise in the temperature of the reaction mixture. This mixture was left to stir for 1 h, after which the TFAA and HTFA were removed under a vacuum. The remaining solids were transferred back to a nitrogen-filled glovebox and crushed to a powder. *Note: TFAA reacts aggressively with water and can damage plastic and rubber tubing. To protect the Schlenk line tubing and the vacuum pump, the evaporated TFAA was collected in an additional cold trap. The cold trap contents were carefully quenched with isopropanol before disposal.*

Synthesis of Yb:YLF Core Nanocrystals

Yb:YLF core nanocrystals were synthesized according to a protocol modified from the protocol reported by Yi *et al.*[27]

To a two-necked round-bottom flask (25 mL) with a fused thermocouple insert, 2 mmol of LiTFA (240 mg) and 2 mmol of a mixture of $YTFA_3$ (428 mg/mmol) and $YbTFA_3$ (515 mg/mmol) in the ratios required were added inside a nitrogen-filled glovebox. To this, a mixture of 6.5 mL of ODE and 6.5 mL of OA, both previously degassed, was added. The flask was then attached to a Schlenk line without exposure to the air, and the contents were degassed at 100 °C for 1 h. Thereafter, the flask was put under a flow of N_2, and the temperature was increased stepwise to 330 °C with increments of 5 °C/30 s. Once the contents reached 330 °C, the reaction was left at this temperature for 25 min and subsequently cooled down to room temperature using compressed air. The resulting mixture was yellow and opaque at high temperatures but became transparent again at <100 °C. Using a syringe, 2 mL of anhydrous toluene was added to facilitate transfer from the flask to a nitrogen-filled vial. Anhydrous ethanol (~10 mL) was added to the crude NC mixture until it turned slightly opaque. Addition of too much ethanol generally results in the presence of smaller NCs in the sample as a byproduct. The mixture was centrifuged at a relative centrifugal force of 1800g (3800 rpm) for 10 min, the supernatant was discarded, and the solid NC pellet was redispersed in 2 mL of anhydrous hexane. To this, 1 mL of anhydrous ethanol was added, and after centrifugation, the NC pellet was redispersed in 2 mL of anhydrous hexane. This step was repeated once more, and the final NC sample, dispersed in 2 mL of anhydrous hexane, was stored in a nitrogen-filled glovebox.

For the syntheses shown in Figure 3.3b, 250 µL (~14 mmol) of Milli-Q water was added before (green trace) or after (blue trace) the degassing step at 100 °C for 1 h. For the yellow trace, TFA precursors were used as described but without the additional drying step with TFAA.

Synthesis of Yb:YLF/YLF Core/Shell Nanocrystals

A shell precursor mixture was prepared by adding 2 mmol LiTFA (240 mg) and 2 mmol $YTFA_3$ (856 mg) to 5 mL of ODE and 5 mL of OA, both previously degassed. While

stirring, the mixture was heated up, and once the salts were completely dissolved, the shelling mixture was loaded into a 20 mL syringe.
On a Schlenk line, a two-necked flask with a glass thermocouple insert was degassed and filled with dry nitrogen. To this flask, 1 mL of the Yb:YLF core NCs (half a batch) and 13 mL of a previously degassed mixture of ODE and OA (1:1 ratio) were added, and hexane was removed by applying a vacuum at room temperature for 5 min. The mixture was placed under nitrogen flow and heated quickly (<2 min) to 330 °C. When the temperature reached 100 °C, the injection of the shelling precursors was started at a rate of 0.5 mL/min using a syringe pump. When the injection was completed (20 min), the solution was kept at 330 °C for another 25 min before it was cooled down quickly using a compressed air flow on the outside of the flask. The NCs were purified in an identical manner as the NC cores by washing the sample three times with ethanol and redispersing in hexane. Ultimately, the NCs were redispersed in 4 mL of hexane and stored inside a glovebox.

Ligand Exchange

To disperse the NCs in polar solvents, the nonpolar oleate ligands were exchanged for tetrafluoroborate anions (BF_4^-) following the procedure adapted from Dong *et al.*[28] In short, inside of a nitrogen-filled glovebox, 2 mL of a ~100 mM solution of triethyloxonium tetrafluoroborate ($[Et_3O][BF_4]$) in acetonitrile (ACN) (20 mg/mL) was added to 1 mL of the stock solution of NCs in hexane. This solution was shaken and left standing for 5 min to react. Subsequently, the particles were directly centrifuged without the addition of an antisolvent. Then, the supernatant was discarded, and 3 mL of the 10 mM solution of $[Et_3O][BF_4]$ in ACN was added to the solid pellet. Using a vortex, the NCs were dispersed in the solution, and 5 min later, the NCs were centrifuged and the supernatant was discarded. This was performed once more, for a total of three exchange steps, and subsequently, the NCs were dispersed in 4 mL of methanol.

Optical Characterization

Absorption spectra were recorded on a PerkinElmer Lambda 1050 with an integrating sphere. All samples for the shown absorbance measurements were dispersed in chloroform. Emission spectra were obtained using an Edinburgh Instruments FLS980 spectrometer equipped with a liquid-nitrogen-cooled NIR PMT-based detector from Hamamatsu. A Xenon arc lamp from XBO was used as the excitation source.
TRPL spectra were also obtained using an Edinburgh Instruments FLS980 spectrometer equipped with a liquid-nitrogen-cooled NIR PMT-based detector from Hamamatsu. The measurements were performed using time-correlated single photon counting, with 930 nm nanosecond laser pulses from a M8903-01 Hamamatsu laser unit as the excitation source.
PLQYs were determined using an Edinburgh Instruments FLS980 spectrometer with a calibrated integrating sphere. Measurements were performed using identical 1 × 1 cm quartz cuvettes. The emission was recorded in a 900–1100 nm window, where the samples were excited at 930 nm. The emission was recorded for 1 s per 0.25 nm, and the full measurement was repeated three times. The used excitation and emission slits were set at 5 and 2 nm, respectively.
Furthermore, PLQYs were determined through absorbance measurements using a

PerkinElmer Lambda 1050 with an integrating sphere. The method is fully explained in Appendix 3.10. The spectra were recorded in a 900–1035 nm window. The absorbance was recorded for 0.5 s with a step size of 0.1 nm.

Structural Characterization

TEM and ED images were acquired using a JEOL JEM1400 transmission electron microscope operating at 120 kV, equipped with an SSD-EDX detector for spot (>75 nm) analysis.

High-angle annular dark field scanning transmission electron microscopy images and energy dispersive X-ray spectral maps were acquired using an aberration-corrected cubed Thermo Fisher Scientific-Titan electron microscope operated at an acceleration voltage of 300 kV equipped with a Super-X detector.

XRD measurements were performed with a Bruckner D8 ADVANCE diffractometer (Cu Kα, $\lambda = 0.15406$ nm). The NC samples were dropcasted on zero diffraction (911) silicon substrates.

References

1. Püschel, S.; Kalusniak, S.; Kränkel, C.; Tanaka, H. Temperature-Dependent Radiative Lifetime of Yb:YLF: Refined Cross Sections and Potential for Laser Cooling. Opt. Express 2021, 29 (7), 11106.
2. Mobini, E.; Rostami, S.; Peysokhan, M.; Albrecht, A.; Kuhn, S.; Hein, S.; Hupel, C.; Nold, J.; Haarlammert, N.; Schreiber, T.; Eberhardt, R.; Tünnermann, A.; Sheik-Bahae, M.; Mafi, A. Laser Cooling of Ytterbium-Doped Silica Glass. Commun. Phys. 2020, 3 (1), 134.
3. Courrol, L. C.; Ranieri, I. M.; Tarelho, L. V. G.; Baldochi, S. L.; Gomes, L.; Júnior, N. D. V. Enhancement of Blue Upconversion Mechanism in $YLiF_4$:Yb:Tm:Nd Crystals. J. Appl. Phys. 2005, 98 (11), 113504.
4. Carl, F.; Birk, L.; Grauel, B.; Pons, M.; Würth, C.; Resch-Genger, U.; Haase, M. $LiYF_4$:Yb/$LiYF_4$ and $LiYF_4$:Yb,Er/$LiYF_4$ Core/Shell Nanocrystals with Luminescence Decay Times Similar to YLF Laser Crystals and the Upconversion Quantum Yield of the Yb,Er Doped Nanocrystals. Nano Res. 2021, 14 (3), 797–806.
5. Anbharasi, L.; Bhanu Rekha, E. A.; Rahul, V. R.; Roy, B.; Gunaseelan, M.; Yamini, S.; Adusumalli, V. N. K. B.; Sarkar, D.; Mahalingam, V.; Senthilselvan, J. Tunable Emission and Optical Trapping of Upconverting $LiYF_4$:Yb,Er Nanocrystal. Opt. Laser Technol. 2020, 126, 106109.
6. Secu, C. E.; Bartha, C.; Matei, E.; Negrila, C.; Crisan, A.; Secu, M. Gd^{3+} Co-Doping Influence on the Morphological, up-Conversion Luminescence and Magnetic Properties of $LiYF_4$:Yb^{3+}/Er^{3+} Nanocrystals. J. Phys. Chem. Solids 2019, 130 (December 2018), 236–241.
7. Melgaard, S. D.; Albrecht, A. R.; Hehlen, M. P.; Sheik-Bahae, M. Solid-State Optical Refrigeration to Sub-100 Kelvin Regime. Sci. Rep. 2016, 6, 2–7.
8. Volpi, A.; Kock, J.; Albrecht, A. R.; Hehlen, M. P.; Epstein, R. I.; Sheik-Bahae, M. Open-Aperture Z-Scan Study for Absorption Saturation: Accurate Measurement of Saturation Intensity in YLF:Yb for Optical Refrigeration. Opt. Lett. 2021, 46

(6), 1421.
9. Di Lieto, A.; Sottile, A.; Volpi, A.; Zhang, Z.; Seletskiy, D. V.; Tonelli, M. Influence of Other Rare Earth Ions on the Optical Refrigeration Efficiency in Yb:YLF Crystals. Opt. Express 2014, 22 (23), 28572.
10. Cittadino, G.; Damiano, E.; Di Lieto, A.; Tonelli, M. First Demonstration of Optical Refrigeration Efficiency Greater than 4% at Room Temperature. Opt. Express 2020, 28 (10), 14476.
11. Rademacher, M.; Gosling, J.; Pontin, A.; Toroš, M.; Mulder, J. T.; Houtepen, A. J.; Barker, P. F. Measurement of Single Nanoparticle Anisotropy by Laser Induced Optical Alignment and Rayleigh Scattering for Determining Particle Morphology. Appl. Phys. Lett. 2022, 121 (22), 221102.
12. Zhou, J.; Leaño, J. L.; Liu, Z.; Jin, D.; Wong, K. L.; Liu, R. S.; Bünzli, J. C. G. Impact of Lanthanide Nanomaterials on Photonic Devices and Smart Applications. Small 2018, 14 (40), 1–29.
13. Tsang, M. Y.; Fałat, P.; Antoniak, M.; Ziniuk, R.; Zelewski, S. J.; Samoc, M.; Nyk, M.; Qu, J.; Ohulchanskyy, T. Y.; Wawrzynczyk, D. Pr^{3+} Doped $NaYF_4$ and $LiYF_4$ Nanocrystals Combining Visible-to-UVC Upconversion and NIR-to-NIR-II Downconversion Luminescence Emissions for Biomedical Applications. Nanoscale 2022.
14. Nemova, G.; Caloz, C. Mie Resonance Enhancement of Laser Cooling of Rare-Earth Doped Nanospheres. In OSA Advanced Photonics Congress 2021; OSA: Washington, D.C., 2021; p IW4A.3.
15. Rahman, A. T. M. A.; Barker, P. F. Laser Refrigeration, Alignment and Rotation of Levitated Yb^{3+}:YLF Nanocrystals. Nat. Photonics 2017, 11 (10), 634–638.
16. Boulon, G.; Guyot, Y.; Ito, M.; Bensalah, A.; Goutaudier, C.; Panczer, G.; Gâcon, J. C. From Optical Spectroscopy to a Concentration Quenching Model and a Theoretical Approach to Laser Optimization for Yb^{3+}-Doped $YLiF_4$ Crystals. Mol. Phys. 2004, 102 (11–12 SPEC. ISS.), 1119–1132.
17. Zhang, J.; Lu, Y.; Cai, M.; Tian, Y.; Huang, F.; Guo, Y.; Xu, S. 2.8 Mm Emission and OH Quenching Analysis in Ho^{3+} Doped Fluorotellurite-Germanate Glasses Sensitized by Yb^{3+} and Er^{3+}. Sci. Rep. 2017, 7 (1), 16794.
18. Seletskiy, D. V.; Hehlen, M. P.; Epstein, R. I.; Sheik-Bahae, M. Cryogenic Optical Refrigeration. Adv. Opt. Photonics 2012, 4 (1), 78.
19. Hehlen, M. P.; Epstein, R. I.; Inoue, H. Model of Laser Cooling in the Yb^{3+}-Doped Fluorozirconate Glass ZBLAN. Phys. Rev. B - Condens. Matter Mater. Phys. 2007, 75 (14), 1–13.
20. Würth, C.; Grauel, B.; Pons, M.; Frenzel, F.; Rissiek, P.; Rücker, K.; Haase, M.; Resch-Genger, U. Yb- and Er Concentration Dependence of the Upconversion Luminescence of Highly Doped $NaYF_4$:Yb,Er/$NaYF_4$:Lu Core/Shell Nanocrystals Prepared by a Water-Free Synthesis. Nano Res. 2022, 15 (10), 9639–9646.
21. Qin, X.; Liu, X. First-Principles Calculations of Strain Engineering in $NaYF_4$-Based Nanocrystals with Hydroxyl Impurities. Nanoscale 2021, 13 (46), 19561–19567.
22. Mobini, E.; Peysokhan, M.; Abaie, B.; Hehlen, M. P.; Mafi, A. Spectroscopic Investigation of Yb-Doped Silica Glass for Solid-State Optical Refrigeration. Phys. Rev. Appl. 2019, 11 (1), 1.
23. Auzel, F.; Baldacchini, G.; Laversenne, L.; Boulon, G. Radiation Trapping and

Self-Quenching Analysis in Yb^{3+}, Er^{3+}, and Ho^{3+} Doped Y_2O_3. Opt. Mater. (Amst). 2003, 24 (1–2), 103–109.

24. Rabouw, F. T.; Prins, P. T.; Villanueva-Delgado, P.; Castelijns, M.; Geitenbeek, R. G.; Meijerink, A. Quenching Pathways in $NaYF_4$:Er^{3+},Yb^{3+} Upconversion Nanocrystals. ACS Nano 2018, 12 (5), 4812–4823.
25. Arppe, R.; Hyppänen, I.; Perälä, N.; Peltomaa, R.; Kaiser, M.; Würth, C.; Christ, S.; Resch-Genger, U.; Schäferling, M.; Soukka, T. Quenching of the Upconversion Luminescence of $NaYF_4$:Yb^{3+},Er^{3+} and $NaYF_4$:Yb^{3+},Tm^{3+} Nanophosphors by Water: The Role of the Sensitizer Yb^{3+} in Non-Radiative Relaxation. Nanoscale 2015, 7 (27), 11746–11757.
26. Senden, T.; Rabouw, F. T.; Meijerink, A. Photonic Effects on the Radiative Decay Rate and Luminescence Quantum Yield of Doped Nanocrystals. ACS Nano 2015, 9 (2), 1801–1808.
27. Yi, G. S.; Lee, W. B.; Chow, G. M. Synthesis of $LiYF_4$, $BaYF_5$, and $NaLaF_4$ Optical Nanocrystals. J. Nanosci. Nanotechnol. 2007, 7 (8), 2790–2794.
28. Dong, A.; Ye, X.; Chen, J.; Kang, Y.; Gordon, T.; Kikkawa, J. M.; Murray, C. B. A Generalized Ligand-Exchange Strategy Enabling Sequential Surface Functionalization of Colloidal Nanocrystals. J. Am. Chem. Soc. 2011, 133 (4), 998–1006.
29. Demirbas, U.; Thesinga, J.; Kellert, M.; Kärtner, F. X.; Pergament, M. Detailed Investigation of Absorption, Emission and Gain in Yb:YLF in the 78–300 K Range. Opt. Mater. Express 2021, 11 (2), 250.
30. Ahn, T.-S.; Al-Kaysi, R. O.; Müller, A. M.; Wentz, K. M.; Bardeen, C. J. Self-Absorption Correction for Solid-State Photoluminescence Quantum Yields Obtained from Integrating Sphere Measurements. Rev. Sci. Instrum. 2007, 78 (8), 086105.
31. Fries, F.; Reineke, S. Statistical Treatment of Photoluminescence Quantum Yield Measurements. Sci. Rep. 2019, 9 (1), 15638.
32. Yanai, N.; Suzuki, K.; Ogawa, T.; Sasaki, Y.; Harada, N.; Kimizuka, N. Absolute Method to Certify Quantum Yields of Photon Upconversion via Triplet–Triplet Annihilation. J. Phys. Chem. A 2019, 123 (46), 10197–10203.
33. Suzuki, K.; Kobayashi, A.; Kaneko, S.; Takehira, K.; Yoshihara, T.; Ishida, H.; Shiina, Y.; Oishi, S.; Tobita, S. Reevaluation of Absolute Luminescence Quantum Yields of Standard Solutions Using a Spectrometer with an Integrating Sphere and a Back-Thinned CCD Detector. Phys. Chem. Chem. Phys. 2009, 11 (42), 9850.
34. Sheik-Bahae, M.; Epstein, R. I. Laser Cooling of Solids. Laser Photonics Rev. 2009, 3 (1–2), 67–84.
35. Kedenburg, S.; Vieweg, M.; Gissibl, T.; Giessen, H. Linear Refractive Index and Absorption Measurements of Nonlinear Optical Liquids in the Visible and Near-Infrared Spectral Region. Opt. Mater. Express 2012, 2 (11), 1588.
36. Radhakrishnan, T. Temperature Variation of the Refractive Index of Lithium Fluoride. Proc. Indian Acad. Sci. - Sect. A 1950, 31 (4), 224–228.
37. Demirbas, U.; Thesinga, J.; Kellert, M.; Pergament, M.; Kärtner, F. X. Temperature and Doping Dependence of Fluorescence Lifetime in Yb:YLF (Role of Impurities). Opt. Mater. (Amst). 2021, 112 (November 2020).
38. Körner, J.; Krüger, M.; Reiter, J.; Münzer, A.; Hein, J.; Kaluza, M. C. Temperature

Dependent Spectroscopic Study of Yb^{3+}-Doped $KG(WO_4)_2$, $KY(WO_4)_2$, $YAlO_3$ and $YLiF_4$ for Laser Applications . Opt. Mater. Express 2020, 10 (10), 2425.

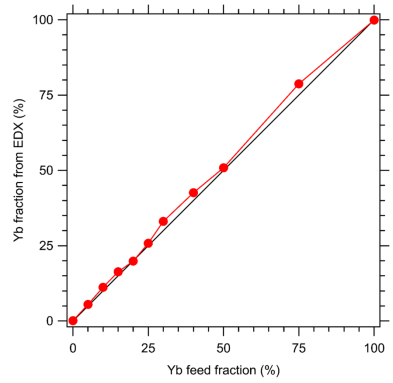
39. Adachi, N.; Hisatomi, T.; Sano, M.; Tsuya, H. Reduction of Grown-In Defects by High Temperature Annealing. J. Electrochem. Soc. 2000, 147 (1), 350.
40. Zhao, J.; Lu, Z.; Yin, Y.; McRae, C.; Piper, J. A.; Dawes, J. M.; Jin, D.; Goldys, E. M. Upconversion Luminescence with Tunable Lifetime in $NaYF_4$:Yb,Er Nanocrystals: Role of Nanocrystal Size. Nanoscale 2013, 5 (3), 944–952.
41. Homann, C.; Krukewitt, L.; Frenzel, F.; Grauel, B.; Würth, C.; Resch-Genger, U.; Haase, M. $NaYF_4$:Yb,Er/$NaYF_4$ Core/Shell Nanocrystals with High Upconversion Luminescence Quantum Yield. Angew. Chemie Int. Ed. 2018, 57 (28), 8765–8769.
42. Wang, F.; Wang, J.; Liu, X. Direct Evidence of a Surface Quenching Effect on Size-Dependent Luminescence of Upconversion Nanoparticles. Angew. Chemie Int. Ed. 2010, 49 (41), 7456–7460.
43. Fischer, S.; Bronstein, N. D.; Swabeck, J. K.; Chan, E. M.; Alivisatos, A. P. Precise Tuning of Surface Quenching for Luminescence Enhancement in Core-Shell Lanthanide-Doped Nanocrystals. Nano Lett. 2016, 16 (11), 7241–7247.
44. Liu, L.; Li, X.; Fan, Y.; Wang, C.; El-Toni, A. M.; Alhoshan, M. S.; Zhao, D.; Zhang, F. Elemental Migration in Core/Shell Structured Lanthanide Doped Nanoparticles. Chem. Mater. 2019, 31 (15), 5608–5615.
45. Deng, R.; Wang, J.; Chen, R.; Huang, W.; Liu, X. Enabling Förster Resonance Energy Transfer from Large Nanocrystals through Energy Migration. J. Am. Chem. Soc. 2016, 138 (49), 15972–15979.
46. Marin, R.; Labrador-Paéz, L.; Skripka, A.; Haro-González, P.; Benayas, A.; Canton, P.; Jaque, D.; Vetrone, F. Upconverting Nanoparticle to Quantum Dot Förster Resonance Energy Transfer: Increasing the Efficiency through Donor Design. ACS Photonics 2018, 5 (6), 2261–2270.
47. Melle, S.; Calderón, O. G.; Laurenti, M.; Mendez-Gonzalez, D.; Egatz-Gómez, A.; López-Cabarcos, E.; Cabrera-Granado, E.; Díaz, E.; Rubio-Retama, J. Förster Resonance Energy Transfer Distance Dependence from Upconverting Nanoparticles to Quantum Dots. J. Phys. Chem. C 2018, 122 (32), 18751–18758.
48. Garcia, E.; Ryan, R. R. Structure of the Laser Host Material $LiYF_4$. Acta Crystallogr. Sect. C Cryst. Struct. Commun. 1993, 49 (12), 2053–2054.
49. Bednarkiewicz, A.; Nyk, M.; Samoc, M.; Strek, W. Up-Conversion FRET from Er^{3+}/Yb^{3+}:$NaYF_4$ Nanophosphor to CdSe Quantum Dots. J. Phys. Chem. C 2010, 114 (41), 17535–17541.
50. Lu, H.; Peng, Y.; Ye, H.; Cui, X.; Hu, J.; Gu, H.; Khlobystov, A. N.; Green, M. A.; Blower, P. J.; Wyatt, P. B.; Gillin, W. P.; Hernández, I. Sensitization, Energy Transfer and Infra-Red Emission Decay Modulation in Yb^{3+}-Doped $NaYF_4$ Nanoparticles with Visible Light through a Perfluoroanthraquinone Chromophore. Sci. Rep. 2017, 7 (1), 5066.
51. Lu, S.; Ke, J.; Li, X.; Tu, D.; Chen, X. Luminescent Nano-bioprobes Based on NIR Dye/Lanthanide Nanoparticle Composites. Aggregate 2021, 2 (5).
52. Yu, D. C.; Rabouw, F. T.; Boon, W. Q.; Kieboom, T.; Ye, S.; Zhang, Q. Y.; Meijerink, A. Insights into the Energy Transfer Mechanism in Ce^{3+}-Yb^{3+} Codoped YAG Phosphors. Phys. Rev. B 2014, 90 (16), 165126.
53. Shi, R.; Mudring, A.-V. Phonon-Mediated Nonradiative Relaxation in Ln^{3+}-Doped

Luminescent Nanocrystals . ACS Mater. Lett. 2022, 1882–1903.
54. Monguzzi, A.; Milani, A.; Lodi, L.; Trioni, M. I.; Tubino, R.; Castiglioni, C. Vibrational Overtones Quenching of near Infrared Emission in Er^{3+} Complexes. New J. Chem. 2009, 33 (7), 1542.
55. Skripka, A.; Benayas, A.; Marin, R.; Canton, P.; Hemmer, E.; Vetrone, F. Double Rare-Earth Nanothermometer in Aqueous Media: Opening the Third Optical Transparency Window to Temperature Sensing. Nanoscale 2017, 9 (9), 3079–3085.
56. Li, H.; Wang, X.; Li, X.; Zeng, S.; Chen, G. Clearable Shortwave-Infrared-Emitting $NaErF_4$ Nanoparticles for Noninvasive Dynamic Vascular Imaging. Chem. Mater. 2020, 32 (8), 3365–3375.
57. Abel, K. A.; Boyer, J.-C.; Andrei, C. M.; van Veggel, F. C. J. M. Analysis of the Shell Thickness Distribution on $NaYF_4$/$NaGdF_4$ Core/Shell Nanocrystals by EELS and EDS. J. Phys. Chem. Lett. 2011, 2 (3), 185–189.
58. Mei, S.; Zhou, J.; Sun, H. T.; Cai, Y.; Sun, L. D.; Jin, D.; Yan, C. H. Networking State of Ytterbium Ions Probing the Origin of Luminescence Quenching and Activation in Nanocrystals. Adv. Sci. 2021, 8 (6), 1–9.
59. Pedroni, M.; Piccinelli, F.; Passuello, T.; Polizzi, S.; Ueda, J.; Haro-González, P.; Martinez Maestro, L.; Jaque, D.; García-Solé, J.; Bettinelli, M.; Speghini, A. Water (H_2O and D_2O) Dispersible NIR-to-NIR Upconverting Yb^{3+}/Tm^{3+} Doped MF_2 (M = Ca, Sr) Colloids: Influence of the Host Crystal. Cryst. Growth Des. 2013, 13 (11), 4906–4913.
60. Bozyigit, D.; Yazdani, N.; Yarema, M.; Yarema, O.; Lin, W. M. M.; Volk, S.; Vuttivorakulchai, K.; Luisier, M.; Juranyi, F.; Wood, V. Soft Surfaces of Nanomaterials Enable Strong Phonon Interactions. Nature 2016, 531 (7596), 618–622.
61. Elder, I. F.; Payne, M. J. P. Lasing in Diode-Pumped Tm:YAP, Tm,Ho:YAP and Tm,Ho:YLF. Opt. Commun. 1998, 145 (1–6), 329–339.
62. Basiev, T. T.; Orlovskii, Y. V.; Pukhov, K. K.; Sigachev, V. B.; Doroshenko, M. E.; Vorob'ev, I. N. Multiphonon Relaxation in the Rare-Earth Ions Doped Laser Crystals. In Advanced Solid State Lasers; OSA: Washington, D.C., 1996; Vol. 1, p PM6.
63. Luntz-Martin, D. R.; Felsted, R. G.; Dadras, S.; Pauzauskie, P. J.; Vamivakas, A. N. Laser Refrigeration of Optically Levitated Sodium Yttrium Fluoride Nanocrystals. Opt. Lett. 2021, 46 (15), 3797.
64. Roder, P. B.; Smith, B. E.; Zhou, X.; Crane, M. J.; Pauzauskie, P. J. Laser Refrigeration of Hydrothermal Nanocrystals in Physiological Media. Proc. Natl. Acad. Sci. U. S. A. 2015, 112 (49), 15024–15029.
65. Nemova, G. Laser Cooling and Trapping of Rare-Earth-Doped Particles. Appl. Sci. 2022, 12 (8), 3777.
66. Ortiz-Rivero, E.; Prorok, K.; Martín, I. R.; Lisiecki, R.; Haro-González, P.; Bednarkiewicz, A.; Jaque, D. Laser Refrigeration by an Ytterbium-Doped $NaYF_4$ Microspinner. Small 2021, 17 (46), 2103122.
67. Moutzouris, K.; Papamichael, M.; Betsis, S. C.; Stavrakas, I.; Hloupis, G.; Triantis, D. Refractive, Dispersive and Thermo-Optic Properties of Twelve Organic Solvents in the Visible and near-Infrared. Appl. Phys. B Lasers Opt. 2014, 116 (3), 617–622.

68. Hale, G. M.; Querry, M. R. Optical Constants of Water in the 200-Nm to 200-Mm Wavelength Region. Appl. Opt. 1973, 12 (3), 555.
69. Kozma, I. Z.; Krok, P.; Riedle, E. Direct Measurement of the Group-Velocity Mismatch and Derivation of the Refractive-Index Dispersion for a Variety of Solvents in the Ultraviolet. J. Opt. Soc. Am. B 2005, 22 (7), 1479.
70. Chatzigoulas, A.; Karathanou, K.; Dellis, D.; Cournia, Z. NanoCrystal: A Web-BasedCrystallographic Tool for the Construction of Nanoparticles Based on Their Crystal Habit. J. Chem. Inf. Model. 2018, 58 (12), 2380–2386.
71. Demirbas, U.; Thesinga, J.; Kellert, M.; Kärtner, F. X.; Pergament, M. Comparison of Different in Situ Optical Temperature Probing Techniques for Cryogenic Yb:YLF. Opt. Mater. Express 2020, 10 (12), 3403.

Appendix 3.1

EDX on Yb:YLF Core NCs



Yb feed fraction (%)	Yb fraction from EDX (%)	Yb feed fraction (%)	Yb fraction from EDX (%)
0	0.0925	25	25.8
5	5.48	30	33.1
10	11.2	50	50.8
15	16.3	75	78.7
20	19.9	100	100

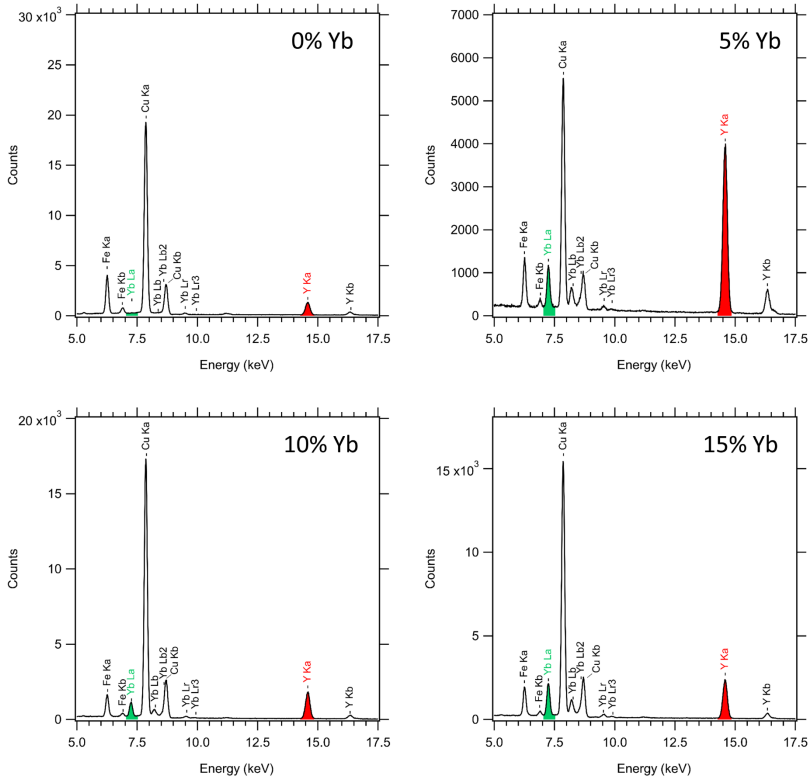


Figure A3.1. EDX measurements performed on the core NCs (doping concentration 0-15 %) indicate that the incorporation of Y (red) and Yb ions (green) is the same as the intended weighed out ratio. Therefore, the Yb core doping percentage (*e.g.* Figure 3.5) closely represents the actual doping percentage of the NC cores.

Appendix 3.1

EDX on Yb:YLF Core NCs

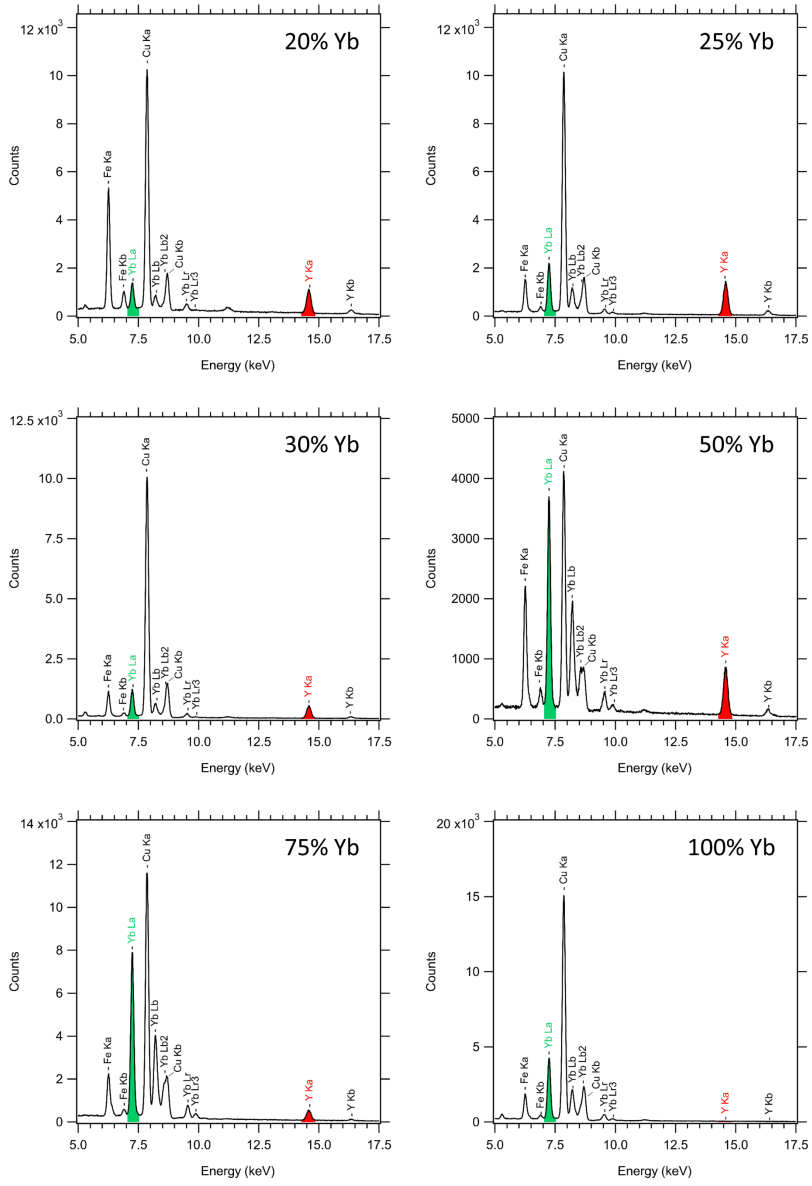


Figure A3.2. EDX measurements performed on the core NCs (doping concentration 20-100 %) indicate that the incorporation of Y (red) and Yb ions (green) is the same as the intended weighed out ratio. Therefore, the Yb core doping percentage (*e.g.* Figure 3.5) closely represents the actual doping percentage of the NC cores.

Appendix 3.2

XRD of $LiYF_4$, Yb(50%):$LiYF_4$ and $LiYbF_4$ Core NCs

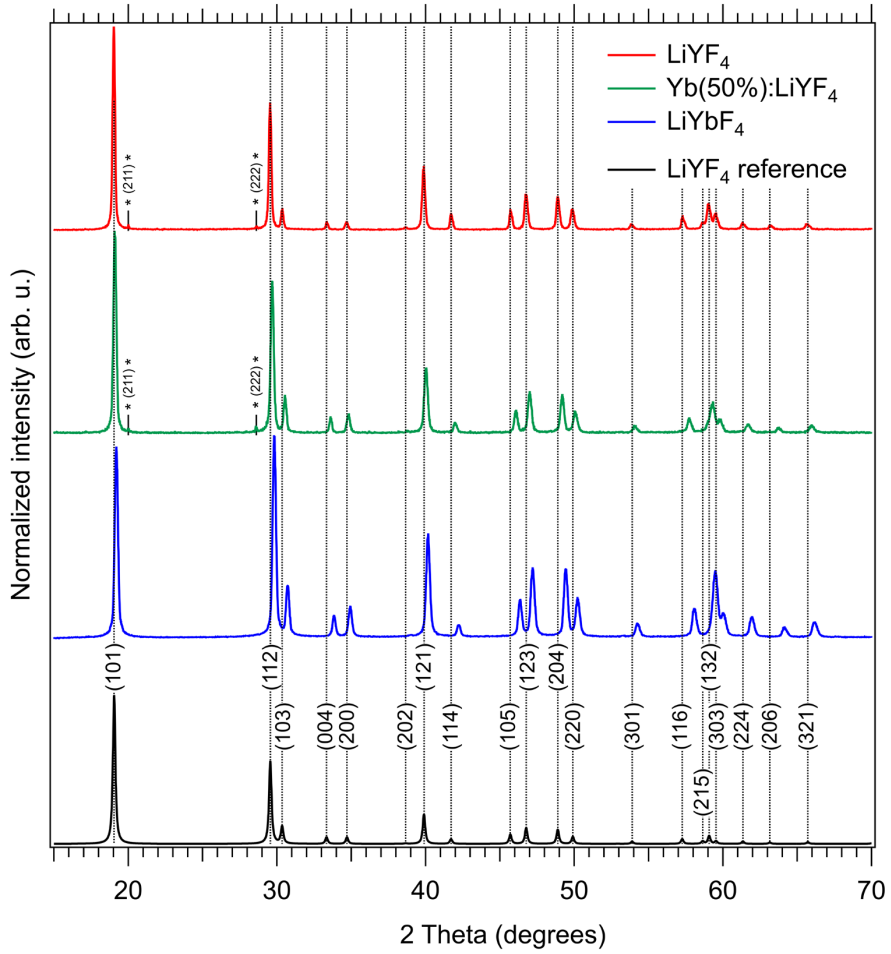


Figure A3.3. XRD diffractograms of $LiYF_4$, Yb(50%):$YLiF_4$ and $LiYbF_4$ NC cores. The shift to higher angles for higher Yb-fractions indicates a slight lattice contraction. The diffractograms of all samples correspond to the expected scheelite crystal structure without the presence of large, unattributable peaks. The NCs are therefore phase-pure. Small and sharp signals of the (211) and (222) reflections of $Y(b)_2O_3$ are present in the $LiYF_4$ and Yb(50%):$LiYF_4$ samples, indicating the presence of a minute amount of crystalline oxide.

Added as reference is a diffraction pattern of $LiYF_4$ (COD-2001129) reported by Garcia *et al.*[48]

Appendix 3.3

Crystallinity of Yb(25%):YLF/YLF Core/Shell NCs

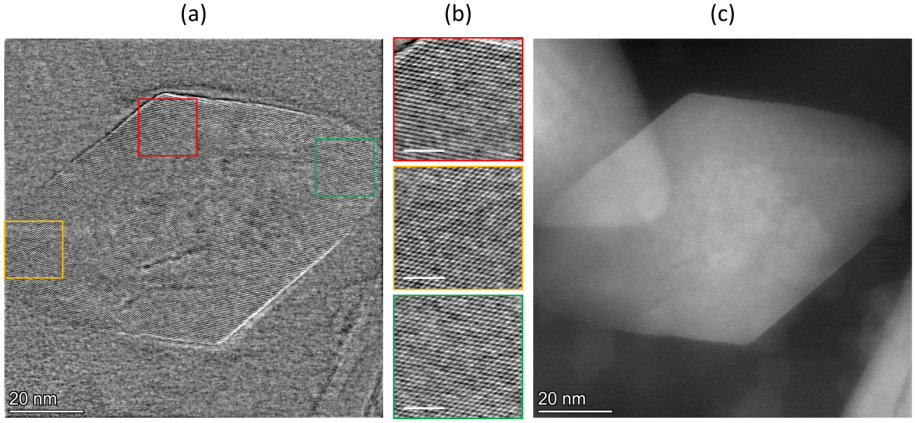


Figure A3.4. (a) To confirm that the NCs are highly crystalline and do not show a noticeable core/shell lattice mismatch, a core/shell NC was imaged using iDPC and (c) STEM. The image, as well as the constructed diffractogram (Figure A3.5) from the three indicated areas (a, b) reveal that the NC has a continuous atomic lattice throughout the entire NC, both core and shell (scale bar in (b) corresponds to 5 nm).

Integrated differential phase contrast (iDPC) imaging was used in combination with conventional HAADF STEM imaging to acquire atomic resolution information. It is possible to achieve atomic resolution images with HAADF STEM acquisition alone (Figure A3.4c), however the electron beam sensitivity of these NCs made it challenging to acquire atomic resolution detail at a sufficiently low magnification as to see the entire NC within a single image. Using a significantly reduced screen current (20 nA), the NC could survive a single atomic resolution image using both HAADF STEM and iDPC imaging. Although the atomic resolution HAADF STEM image is noisy and difficult to interpret, the corresponding iDPC image (Figure A3.4a,b) clearly shows a single crystalline NC shell.

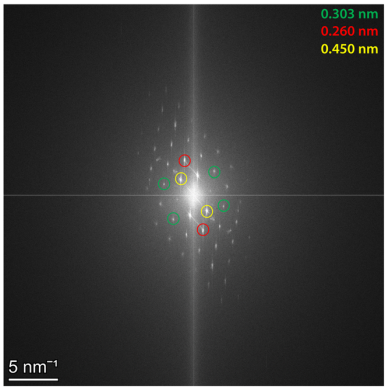


Figure A3.5. A constructed diffractogram from the three indicated areas of the iDPC image (Figure A3.4a,b), showing a single crystalline core/shell NC.

Appendix 3.4

Index Matching of NCs with Solvent

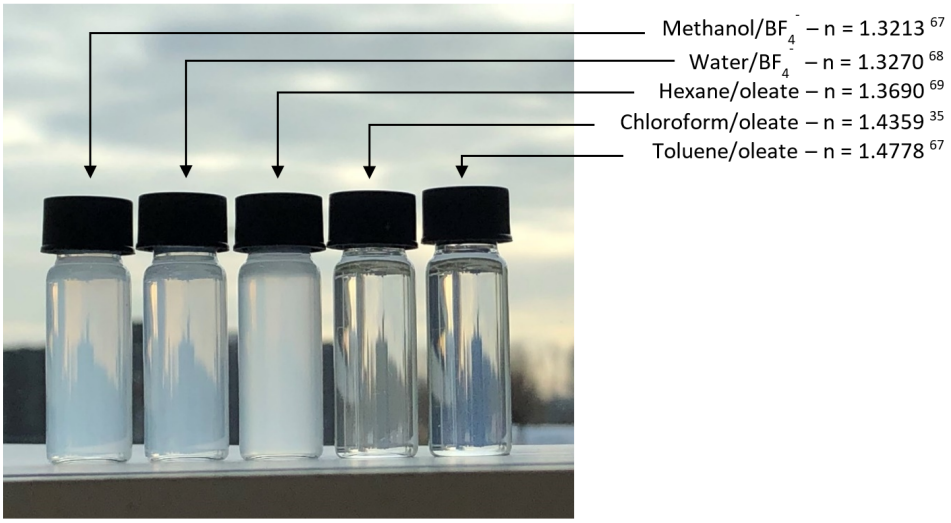


Figure A3.6. NCs dispersed in different solvents with different refractive indices and surface ligands, showcasing both the improved dispersability with BF_4^- counter ions (as reported by Dong *et al.*[28]) and the significant reduction of scattering due to index matching of the solvent with the NCs. As explained in the main text, using an index-matched solvent removes the correction factor(s) for different refractive indices (and the NC size and shape), resulting in a more accurate PLQY-analysis based on TRPL-spectra. The indicated values for n are used in the determination of the PLQY from the TRPL-model (Equation 3.1).[35,67–69]

Appendix 3.5

Influence of Reabsorption

For all PLQY measurements conducted it has to be ensured that there is no (significant) reabsorption. Reabsorption of the by NCs emitted light will result in a prolonged average lifetime[23] and hence an incorrect increase of the estimated PLQY when using TRPL. For integrating sphere measurements, the PLQY is lowered with increasing reabsorption, assuming the PLQY is not unity.

The maximum absorbance is <6 mOD. The transmittance is calculated by:

$T = 10^{-A} = 10^{-0.006} = 0.986$ at the absorbance peak wavelength.

The fraction of reabsorption at the main absorbance peak (*i.e.* not the average absorbance) is thus roughly 1.4%. Reabsorption thus does not play a large role and hence does not lead to a significant increase in PL decay time compared to the intrinsic bulk PL decay time. Therefore, there is no need to correct for reabsorption, as had to be done in *e.g.* the bulk lifetime-analysis reported by Püschel *et al.*[1] Note that for all samples, it was ensured that the overall absorbance was lower than 2% (A ≤ 8.8 mOD).

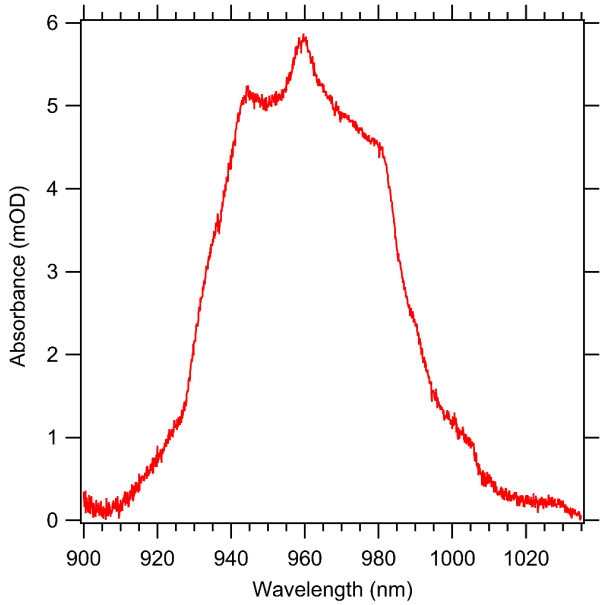


Figure A3.7. The absorbance spectrum of a Yb(50%):YLF/YLF NC sample in chloroform.

Appendix 3.6

PLQY Correction for Reabsorption

To confirm that reabsorption has no influence, we have corrected the reported PLQY (Figure 3.5a) for reabsorption. We used the following formula from Auzel *et al.*[23] to determine the corrected lifetime (τ_t) from the measured lifetime (τ_i) and a factor for reabsorption (σNl) (Equation A3.1). We rewrite σNl as a function of the transmittance (T), and obtain the transmittance from, in this case, the PLQY (φ) measurement shown in Appendix 3.10, and the integrated counts of the TRPL spectrum of this measurement (I_{tot}). From this, we determined the value for constant k, and subsequently used this constant, together with the Itot and the φ from the TRPL measurements to determine T (Equation A3.6).
With the transmittance obtained for each sample, we calculated the difference between the measured lifetime (τ_i) and the corrected lifetime (τ_t) (Equation A3.4). The results of this calculation are shown in Figure A3.8.

$$\tau_t = \tau_i\,(1+\sigma Nl) \quad (A3.1)$$
$$\tau_t = \tau_i\,(1+A\cdot\ln(10)) \quad (A3.2)$$
$$\tau_t = \tau_i\,(1+(-\log(T))\cdot\ln(10)) \quad (A3.3)$$
$$\tau_t = \tau_i\,(1+\log(1/T)\cdot\ln(10)) \quad (A3.4)$$

$$I_{tot} = \varphi(1-T)\cdot k \quad (A3.5)$$
$$1-I_{tot}/(\varphi\cdot k) = T \quad (A3.6)$$

$$k = 7.5\cdot10^{8}$$

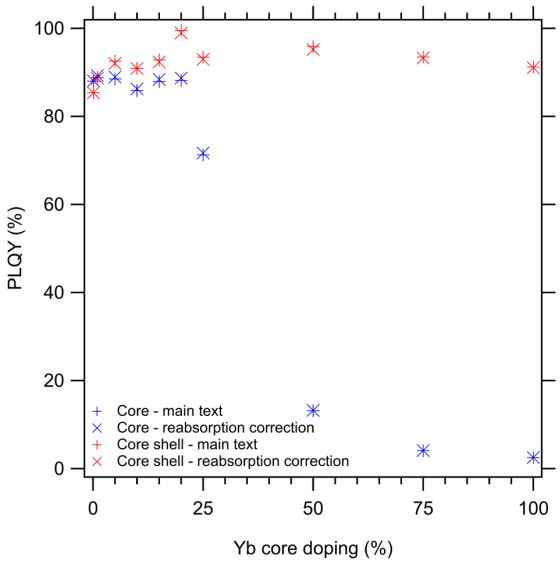


Figure A3.8. PLQY of the samples shown in Figure 3.5 of the main text, corrected for any reabsorption of the samples.

Appendix 3.7

Excitation and Emission Wavelength Dependencies

To validate the TRPL model for a broad range of analyses, it has to be ensured that the PLQY obtained from TRPL-data is not excitation or emission wavelength dependent. Therefore, lifetime measurements were performed for the three emission peaks (shown in Figure A3.9a), as well as at the lifetime of the generally used emission wavelength (995 nm) when excited at different wavelengths (Figure A3.9b). From both figures, we can conclude that there is no influence of excitation or emission wavelengths on the obtained PLQY-values.

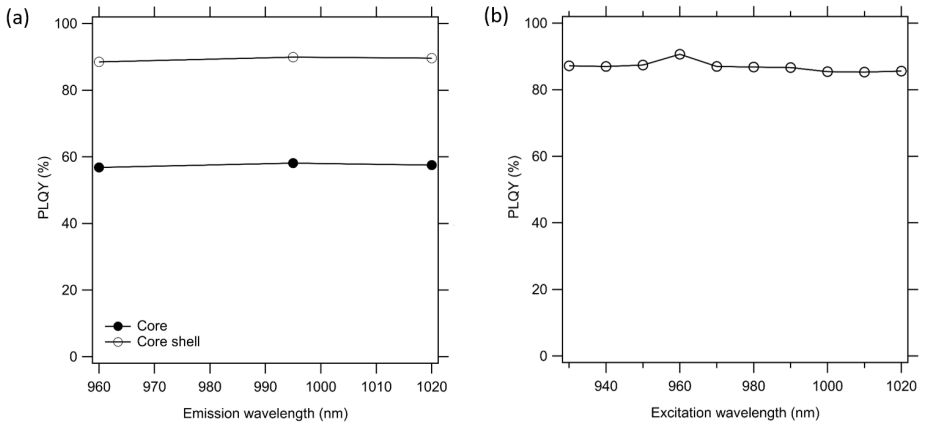


Figure A3.9. (a) The PLQY extracted for core and core/shell NCs at different emission wavelengths (λ_{ex} = 930 nm), as well as (b) for core/shell NCs at different excitation wavelengths (λ_{em} = 995 nm) show that there is no large dependency of the extracted PLQY to different excitation or emission conditions.

Appendix 3.8

Concentration and Fluence Dependency

In addition to Appendix 3.7, we also checked if lowering the excitation fluences and NC concentrations changed any of the obtained PLQY values. As is clear from Figures A3.10a and A3.10b, there seems to be no influence on these parameters, again confirming that any reabsorption is not influencing the obtained PLQY values (Appendix 3.6).

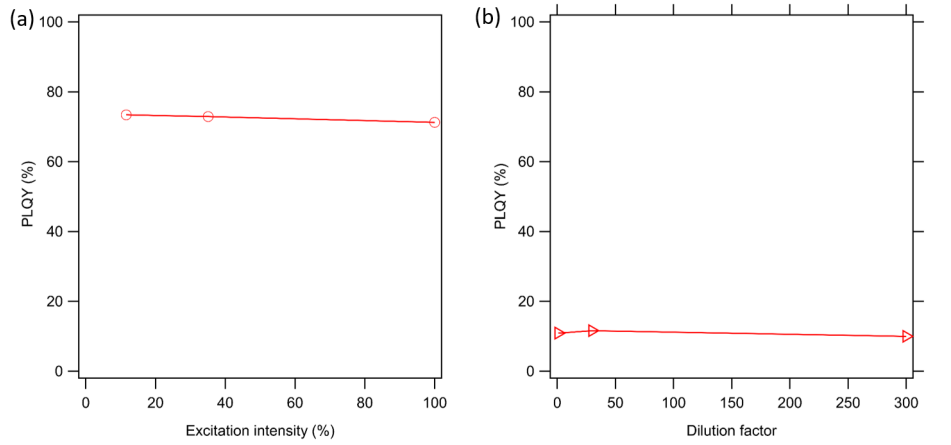


Figure A3.10. (a) The PLQY extracted for core/shell NCs at different excitation intensities (using gray-filters), as well as (b) for core NCs at different concentrations (by diluting the sample) show that there is no large dependency of the beam intensity or NC concentration. For both figures, λ_{ex} = 930 nm and λ_{em} = 995 nm.

Appendix 3.9

Extended TRPL-Model

The PLQYs of our NC samples have all been calculated using Equation A3.7 published by Rabouw *et al.*[26]

$$\Gamma_{rad}(n) = \frac{\Gamma_{rad}^{bulk} \cdot n}{n_{YLF}} \left(\frac{3n^2}{2n^2 + n_{YLF}^2} \right)^2 \tag{A3.7}$$

In this publication Equation A3.8 is also given, which additionally corrects for the NC size and emission wavelength. However, it is mentioned that the product of the free space wave vector ($k = 2\pi/\lambda$) and radius of the spherical(!) particle (a) should be <<1. For the data shown in Figure A3.11, the ka-value of the non-spherical YLF NCs is roughly 0.45 (a = 90 nm).

$$\Gamma_{rad}(n) = \frac{\Gamma_{rad}^{bulk} \cdot n}{n_{YLF}} \left(\frac{3n^2}{2n^2 + n_{YLF}^2} \right)^2 \left(1 + \frac{(n_{YLF}^2 - n^2)(n_{YLF}^2 + 10n^2)}{5(2n^2 + n_{YLF}^2)} (ka)^2 \right) \tag{A3.8}$$

The changes in the eventual outcome are relatively small for these samples, and due to our NCs being non-spherical and essentially too large for this correction factor, in the main text we have solely used Equation A3.7. The effect of Equation A3.8 is shown in Figure A3.11a and b for NCs dispersed in chloroform and methanol respectively. These figures show that the correctionfactor will go to 1 for index-matched solvents, effectively removing the need of the correction.

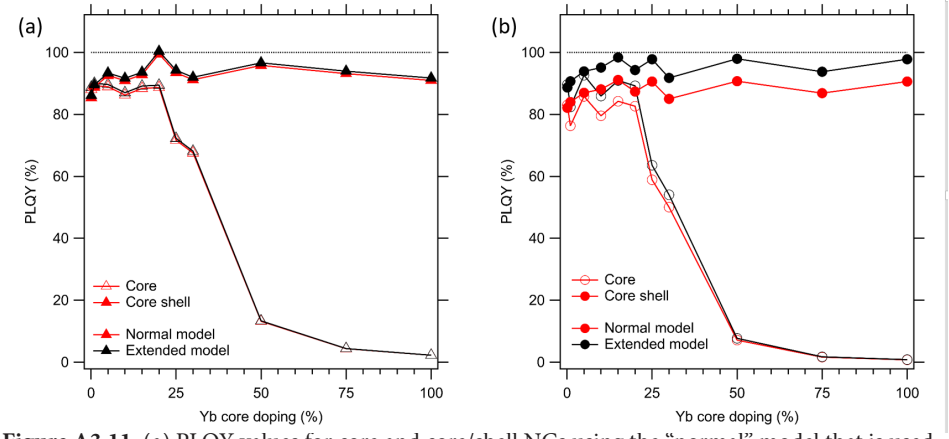


Figure A3.11. (a) PLQY values for core and core/shell NCs using the "normal" model that is used in the main text, and the extended model described above in chloroform and (b) methanol. For index-matched solvents (*i.e.* chloroform), the correction factor goes to 1 (similar to Equation S7), reducing the error of the analysis.

Appendix 3.10

PLQY from Integrating Sphere (Absorbance)

Another method to estimate the PLQY is using an absorption photospectrometer equipped with an integrating sphere. Here we use a Perkin-Elmer lambda 1050 UV-VIS-NIR photospectrometer, where we compare the measured absorption spectra of samples placed either inside, or well before the integrating sphere. For the sample inside the sphere, emitted photons will be collected on the detector and will decrease the apparent absorption. For a small Stokes shift between absorbance and emission, the wavelength of an absorbed an emitted photon is nearly the same and so will be the sensitivity of the detector and the transmission of the integrating sphere. This implies that if the PLQY is 100% no absorption appears to take place. When the same sample is measured outside of the integrating sphere (far enough from the entrance so that the fraction of emitted light collected by the sphere is negligible) the detected transmitted light does not contain emitted photons. It is furthermore important to either have a non-scattering sample (indexmatched solvent or small enough NCs), or to correct for scattering. In the measurements below, the sample was dispersed in chloroform, and hence practically index matched. From these two absorbance spectra, an estimate of the PLQY can be given, according to:

Sample placed outside of the sphere:

$$A_{out} = -\log\left(\frac{I_0 - I_0 \cdot F_A}{I_0}\right) = -\log(1 - F_A)$$
$$10^{-A_{out}} = 1 - F_A \qquad \text{(A3.9)}$$

(where A = absorbance, I_0 = incident intensity, F_A = fraction of absorbed light)

Sample inside the sphere (when writing A here, it is understood that this is the apparent absorbance, not the true absorbance):

$$A_{in} = -\log\left(\frac{I_0 - I_0 \cdot F_A + I_0 \cdot F_A \cdot PLQY}{I_0}\right) = -\log(1 - F_A + F_A \cdot PLQY) \qquad \text{(A3.10)}$$

$$10^{-A_{in}} = 1 - F_A + F_A \cdot PLQY$$

$$\frac{10^{-A_{in}} - 10^{-A_{out}}}{1 - 10^{-A_{out}}} = \frac{F_A \cdot PLQY}{F_A} = PLQY \qquad \text{(A3.11)}$$

Again, the difference of this measurement is relatively small compared to the obtained PLQY from TRPL, confirming that the TRPL-model is adequate at determining the PLQY of Yb:YLF NC samples.

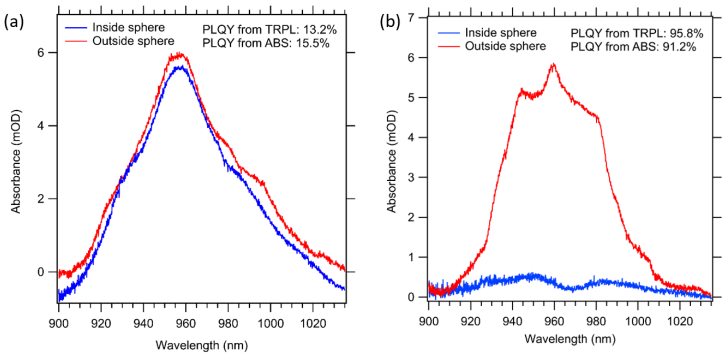


Figure A3.12. (a) The absorbance spectra of a Yb(50%):YLF core and (b) Yb(50%):YLF/YLF core/shell NC sample in chloroform inside (blue) and outside (red) of an integrating sphere.

Appendix 3.11

Syntheses With Water – TEM and ED Analysis of Samples

Electron diffraction (ED) analysis (Figure A3.13a) of the samples synthesized with water added before or after the degassing step reveal that the samples do not significantly change in crystal structure (within the error margin of the measurement). However, TEM images clearly show that the growth of both samples is significantly affected by the presence of (residual) water. Both the sample where water is added after the degassing step (Figure A3.13b) and before (Figure A3.13c) show the presence of small particles, next to the expected bipyramidal NCs, indicating that the OH^- likely acts as a growth controlling ligand. For the sample shown in Figure A3.13b, two PL-lifetimes were found, likely related to the smaller and larger particles. The absence of a biexponential PL-decay for the sample shown in Figure A3.13c is because the concentration of the smaller particles is far less. Therefore the PL-intensity of these small particles is negligible compared to the large ones. Figure A3.13d-f shows the EDs of (d) a general YLF sample, (e) the sample that is not degassed after adding water and (f) the sample that has been degassed prior to starting the synthesis.

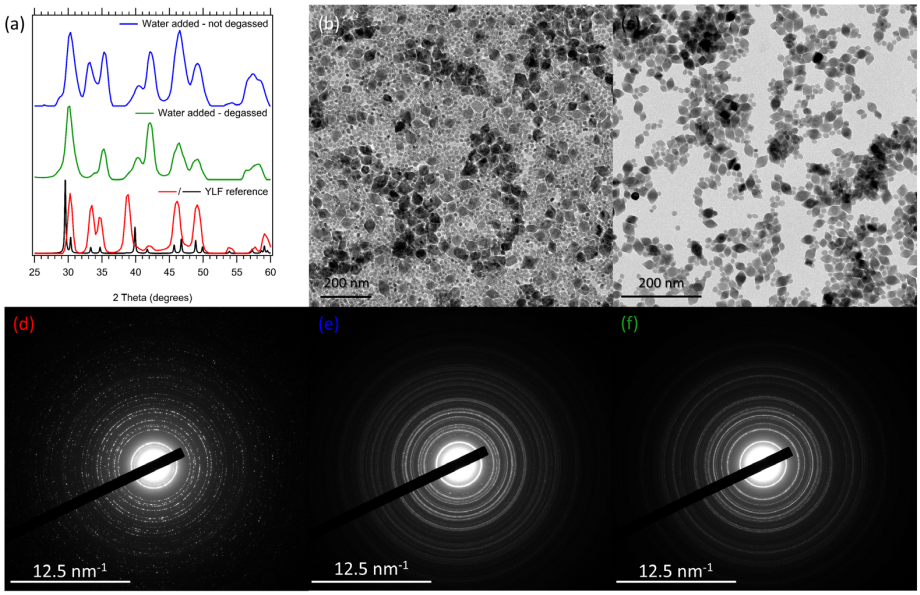


Figure A3.13. (a) Extracted ED profiles from the raw EDs, shown in Figure A3.13d-f. (b) TEM image of the sample where, after adding water to the precursor mixture, no degassing step was performed before the synthesis was started. (c) TEM image of a sample where after adding water, the water was removed again by degassing under vacuum. (d) The ED of a general YLF sample, and (e) the ED of the sample shown in Figure A3.13b, and (f) Figure A3.13c.

Appendix 3.12

EDX of Yb(25%):YLF/YLF Core/Shell NCs – Lower Magnification

A lower magnification EDX mapping of the sample shown in Figure 3.4a-c indicates the uniformity of the samples. Furthermore added is the fluoride signal (yellow), showcasing the location of fluoride ions is throughout the entire NC, as expected.

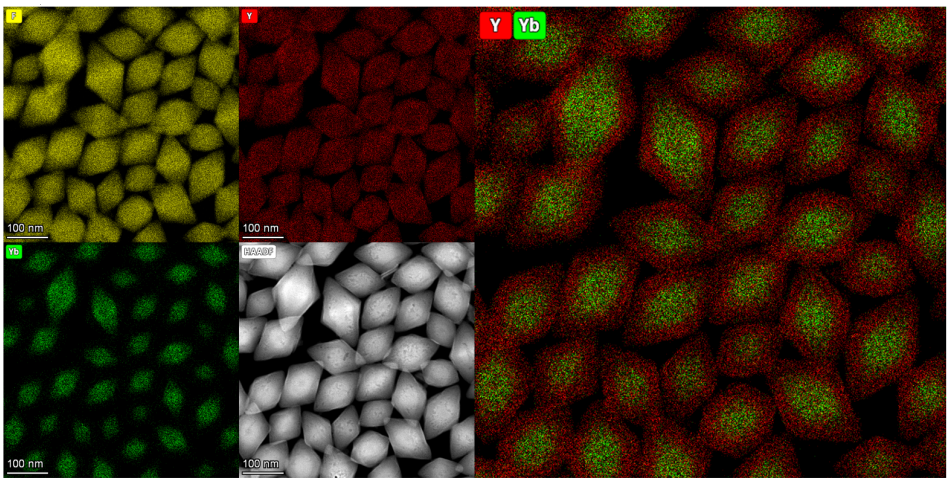


Figure A3.14. Lower magnification EDX mapping (compared to Figure 3.4) of Yb(25%):YLF/YLF core/shell NCs confirms the uniformity of the sample. The elemental distribution shown in Figure 3.4 is thus representative for the sample in general.

Appendix 3.13

EELS Analysis of Yb(25%):YLF/YLF Core/Shell NCs

Apart from using EDX to image the elemental composition, EELS (electron energy loss spectroscopy) was also applied on the same sample as shown in Figure 3.4a-c and Figure A3.14. Figure A3.15a shows again that the location of Yb is mostly isolated to the NC core. Most of the Y signal is found in the shell. Figure A3.15b indicates that some Yb signal is found in the shell, similar to Figure 3.4b. An EELS elemental linescan was performed over the NC, as indicated in Figure A3.15c, and the results shown in Figure A3.14d indicate again that practically all Yb-signal is found in the core only. Figure A3.15e shows the full EELS spectrum, with the location of the Y and Yb-signals indicated.

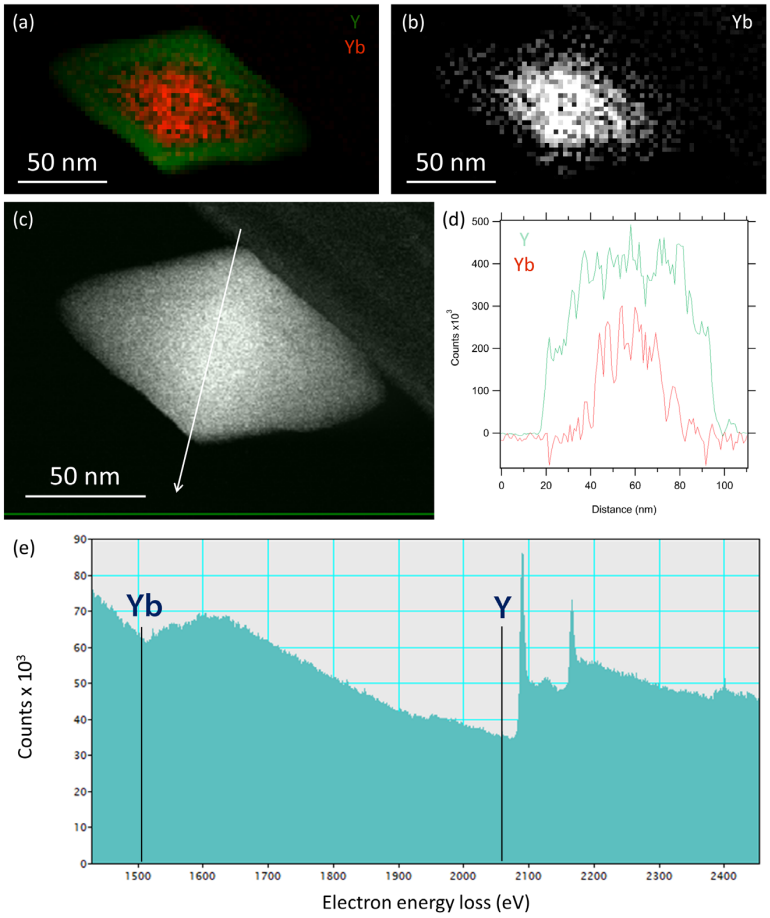


Figure A3.15. (a) The by EELS measured locations of Y and Yb, as well as (b) solely Yb indicate that most of the Yb-ions remained in the core NC. (c, d) An EELS-linescan over the NC shows that indeed the Yb-signal in the shell is at the level of the background noise. (e) The full EELSspectrum, used for the determination of the locations of Y and Yb in the NC shown.

Appendix 3.14

Förster Resonance- and Dexter-Type Energy Transfer Simulations

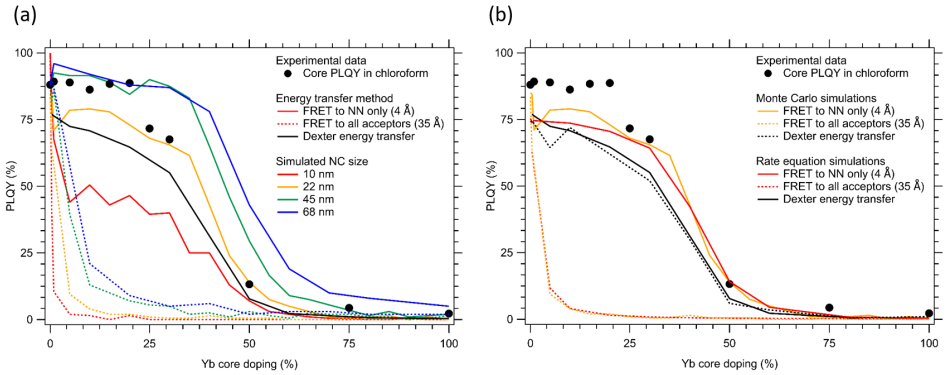


Figure A3.16. (a) PLQYs derived from Monte Carlo simulations modelling FRET or Dexter-type energy transfer. The models used different NC sizes, as well as a differing FRET-search radius, including either all acceptors or only nearest neighbors (NN). (b) A comparison between Monte Carlo simulations and rate-equation based simulations for the 22 × 15 × 15 nm NC.

Modelling FRET in Yb:YLF

FRET from excited Yb atoms to the NC surface was modelled in two ways: Monte Carlo imulations, and rate equation calculations. Both methods make use of a NC model that is cut from the YLF bulk,1 with the NanoCrystal tool,[70] exposing only (101) facets. The data shown in the main text is based on a 22 × 15 × 15 nm NC. The Monte Carlo simulations shown here were also carried out for NC models of different sizes (as summarized in Table A3.1). For computational efficiency, the Li and F atoms are not taken into account, leaving only the Y atoms. At the start of each simulation, part of the Y atoms (the total amount depending on the doping concentration) is randomly changed to Yb. As only the Yb are relevant for modelling FRET, the remaining Y atoms are then discarded.

Monte Carlo simulations

To determine the quantum yield *via* Monte Carlo simulations, 200 independent excitations paths (100 for the 68 × 46 × 46 nm NC to limit computational costs) are simulated for each doping concentration. At t=0, 200 random Yb sites are selected as "excited". If the number of Yb atoms is lower than 200 (which may happen for small NCs at low doping

Table A3.1. General parameters of the different modeled NCs for the Monte Carlo simulations.

NC name	atoms	surface atoms	dimensions (nm)	used in main text
NC - 10nm	1,430	686	10 × 7 × 7	no
NC - 22nm	13,706	3,446	22 × 15 × 15	yes
NC - 45nm	105,952	9,440	45 × 30 × 30	no
NC - 68nm	353,600	32,006	68 × 46 × 46	no

Appendix 3.14

Förster Resonance- and Dexter-Type Energy Transfer Simulations

concentrations), the same Yb atom can be selected multiple times. Next, for each "excited" Yb atom, the distance to all other Yb atoms (excited or not) in a radius of R_{search} is computed. For "normal" FRET, where the excitation can be transferred to any nearby Yb atom, R_{search} = 3.5 nm. For the simulations where FRET transfer is restricted to nearest neighbors only, R_{search} = 0.4 nm. Based on the distance to the surrounding Yb atoms, the FRET rate is computed to each of these Yb sites, using $k_{FRET} = k_{rad} \times (R_0/R_{Yb})^6$, where $k_{rad} = 4.55 \times 10^{-4}$ μs^{-1}, R_0 = 1.5 nm, and R_{Yb} the distance to the other Yb atoms. The probability of FRET to each atom is then determined with $P_{FRET} = k_{FRET} \times dt$, with dt = 0.04 μs. The probability of radiative decay is given by $P_{rad} = k_{rad} \times dt$.

To determine the location of the "excitations" at the next time step, a randomly generated number then determines which event takes place (the probability that nothing happens given by $P_{nothing} = 1 - P_{rad} - \Sigma P_{FRET}$). The "excitations" are propagated in this way for a maximum of 20,000 μs. If an excitation reaches a surface atom within the time limit of the simulation, it is removed and no longer propagated. We define surface atoms as any atom that has ≤ 50 neighbors within a 1 nm radius. Practically, this amounts to the first 1-2 monolayers of the NC surface. At the end of the simulation, the quantum yield is determined through PLQY = $n_{rad}/(200 - n_{act})$, where n_{rad} is the number of excitations that have decayed radiatively, and n_{act} the number of excitations that have neither decayed nor reached the surface.

Rate equation calculations

The rate equation calculations use the same parameters (*i.e.*, k_{rad}, R_0, dt) as used in the Monte Carlo simulations. However, instead of 200 explicit excitation pathways, all Yb sites now start with 1 "excitation". The radiative decay rate and the FRET rates between all Yb sites are stored in an $(n_{Yb} + 1) \times (n_{Yb} + 1)$ matrix, where n_{Yb} is the number of Yb atoms in the system. In this matrix, element $k_{i,j}$, gives the FRET rate from Yb_i to Yb_j. The last element of each row (*i.e.*, $k_{i,(nYb+1)}$) gives the radiative decay rate. All the rates from Yb sites at the surface are set to 0, to prevent excitations from leaving the surface. For "normal" FRET (*i.e.*, not restricted to nearest neighbors), rates smaller than $k_{rad}/50$ are also set to 0 for computational efficiency. For simulations where only transfer to nearest neighbors is allowed, all rates smaller than 1.9 μs^{-1} ≈ $k_{FRET,nearest\text{-}neighbor}$ are set to 0.

The "excitation populations" are then propagated *via* $n_{t+1} = n_t + (n_t \cdot K_{rate}) \times dt$, where nt is the "excitation population" of each Yb atom at time=t, and K_{rate} is the matrix with all rates. For doping concentration <10%, only few Yb are present. To reduce the numerical noise, the average quantum yield from 5 independent runs was taken.

Comparison with experimental results

Figure A3.16a compares the experimentally measured PLQY decay as function of Yb doping concentration, with the results from the Monte Carlo simulations. As also discussed in the main text, simulation of "normal" FRET leads to an immediate decrease

Appendix 3.14

Förster Resonance- and Dexter-Type Energy Transfer Simulations

in PLQY and hence fails to reproduce the experimentally observed plateau at lower doping concentrations. In contrast, the plateau is obtained when only allowing transfer to nearest neighbors. Figure A3.16b shows that these results are not dependent on the computation method. Both Monte Carlo simulations and the rate equations methods give the same results for both "normal" and nearest neighbor FRET.

Modelling Dexter-type electron transfer in Yb:YLF

Like FRET, Dexter-type electron transfer (DET) was modelled for the 22 × 15 × 15 nm NC, using both Monte Carlo simulations, and rate equations calculations. In both cases, the methods were completely analogous to those described in the previous section for FRET, with the exception

that now $k_{Dexter} = A \times \exp(-\beta \times r)$. Here, $\beta = 0.5\ nm^{-1}$. This value is higher than the value of $0.1\ nm^{-1}$ that is more often used. Lower values of β fail to reproduce the PLQY plateau at low Yb^{3+} concentration. This shows that the ET mechanism must have a very steep distance dependence. Since we showed already that FRET to nearest neighbors gives an accurate description of the experimentally observed PLQY curves, the DET rate at the nearest neighbor distance must be the same as the FRET rate in that case. This defines the prefactor $A = 2.38 \times 10^8\ \mu s^{-1}$.

Comparison with experimental results

Figure A3.16a compares the experimentally measured PLQY decay as function of Yb doping concentration, with the results from the Monte Carlo simulations of FRET. As also discussed in the main text, simulation of "normal" FRET leads to an immediate decrease in PLQY and hence fails to reproduce the experimentally observed plateau at lower doping concentrations. In contrast, the plateau is obtained when only allowing transfer to nearest neighbors.

Such very short-range transfer may be more consistent with Dexter-type electron transfer, where the transfer rate depends exponentially on the distance between the Yb atoms. Indeed, as shown in Figure 3.5a, as well as Figure A3.16a, Dexter-type transfer can accurately describe the plateau at lower doping concentrations. It must be noted that the values of β and A were not fitted to the data, but estimated based on previous research[52] and the ability of the simulation to describe the experimental data. Thus, although the values of β and A may not be exactly correct, it is possible to describe the experimental data with a Dexter-type model, whereas we were unable to describe the data with FRET, regardless of the values of the parameters.

Figure A3.16b shows that these results are not dependent on the computation method. Both Monte Carlo simulations and the rate equations methods give the same results for both "normal" and nearest neighbor FRET, and Dexter-type electron transfer.

Appendix 3.15

PLQY of NCs in Different Solvents

To test the influence of solvents and solvent-related PL quenching on the obtained PLQY values, the PLQY of both core and core/shell NCs were measured for a large range of doping fractions. As can be seen from Figure A3.17a (identical to Figure 3.5c of the main text) and Figure A3.17b, all NC samples follow the exact same trend, albeit that the PLQY of the more polar solvents (containing –OH groups) is systematically slightly lower. As explained in the main text, especially for the core NCs in water we observe a systematically lower PLQY compared to all other solvents, indicating that this is not solely related to the difference in refractive index. However, as the PLQY values obtained are not significantly different, and the trends are the same for all particles, we conclude that the influence of the solvent on the PLQY is not negligible, but still small compared to other PL quenching factors that likely reside on the surface of the core NCs.

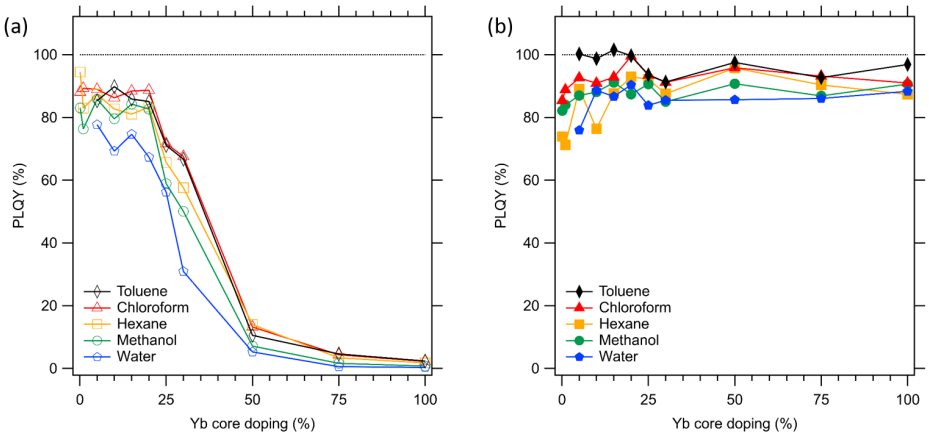


Figure A3.17. (a) PLQY of Yb:YLF core and (b) core/shell NCs in different solvents. The trends discussed in the main text are true for all different solvents measured. This means that the errors introduced by the differences in refractive indices are relatively small.

Appendix 3.16

Effect of the Refractive Index on the Average PLQY

TRPL-measurements on Yb:YLF NCs showed a systematically lower PLQY for samples in water than for the same samples in chloroform (Figure 3.5d). As this can either be (1) a solvent quenching effect, indicating that the 15 nm shells are insufficient to mitigate all PL-quenching from core through the shell to the surface or (2) a direct effect of a larger mismatch in refractive index with YLF (n=1.4485) to water (n=1.327) than to chloroform (n=1.4359), apart from measuring $LiYbF_4$ NCs with a 15 nm or 30 nm thick shell (showcasing no difference in PLQY and hence making (1) unlikely), we also measured the PLQY of the 30 nm thick core shell shell NCs in all other solvents, and averaged the PLQY for samples with a low doping density (0.1-15 %) and samples with a high doping density (75 and 100%), and observed the PLQY trends for core and core shell NCs, as shown in Figure A3.18. Figure A3.18a shows the average PLQY for core and core shell NCs with low doping densities (0.1-15% Yb), and showcases a roughly linear trend of increasing PLQY with increasing refractive index. The same is trend can be observed for high Yb-doped (b) cores, and (c) core shell and core shell shell (only 100% $LiYbF_4$ core-based) NCs. Furthermore, from Figure A3.18c it is clear that the 30 nm thick shells are not better than the 15 nm thick shells, showcasing that the 15 nm thick shell is sufficient to mitigate any energy transfer from core to the NC surface. It has to be noted that the core samples in water systematically have lower PLQY.

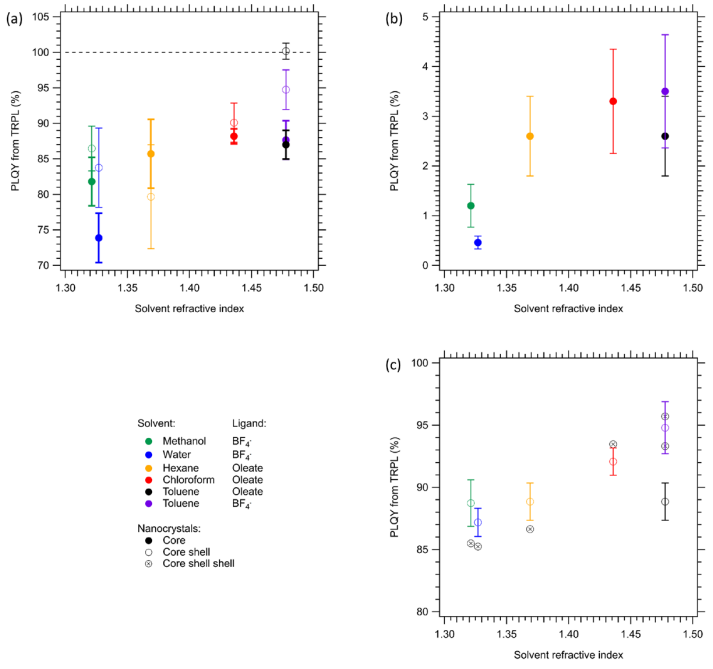


Figure A3.18. (a) Average PLQY for low and (b) high doped core and (c) core shell NCs. All three figures show a roughly linear increase of PLQY with increasing refractive index.

Appendix 3.17

PLQY for Optical Refrigeration

A quick calculation shows what the PLQY of the NC sample should be, in order to optically refrigerate (effective phonon absorption), instead of heat (effective phonon emission). Note that the average emission energy ($\overline{E_{em}}$) depends on the temperature (*i.e.* available phonons) and hence will move to lower energies when cooling down. This results in a different required PLQY to optically refrigerate for any given temperature.

Heating = Cooling

$$(1 - \varphi)\, E_{ex} = \varphi(\overline{E_{em}} - E_{ex}) \quad \text{(A3.12)}$$

$$E_{ex} - \varphi \cdot E_{ex} = \varphi(\overline{E_{em}} - E_{ex}) \quad \text{(A3.13)}$$

$$\varphi \geq E_{ex}/\overline{E_{em}} \quad \text{(A3.14)}$$

For λ_{ex} = 1030 nm (E_{ex} = 1.204 eV) and $\overline{\lambda_{em}}$ = 992 nm ($\overline{E_{em}}$ = 1.250 eV), $\varphi \geq 96.3\%$

Appendix 3.18

Temperature Dependent Emission Spectra

It is reported that the temperature of Yb:YLF can be derived from the bulk emission spectrum.[29,71] To set a proper reference, the emission of Yb:YLF NCs was obtained at different temperatures ranging between 80K and 200K. It is clear from the spectra in Figure A3.19a, that the lower wavelength emission peaks get reduced in intensity at lower temperatures, indicating the lower number of phonons in the NCs. Note that these temperatures are applied in a cryostat, and hence not optically induced. (b) The ratio of peak B/A (indicated in Figure A3.19a) has an almost linear trend, shown in Figure A3.19b, as well as (c) the average emission wavelength at different temperatures. These trends were used to identify any optical cooling from the emission spectra, as shown in Appendix 3.19.

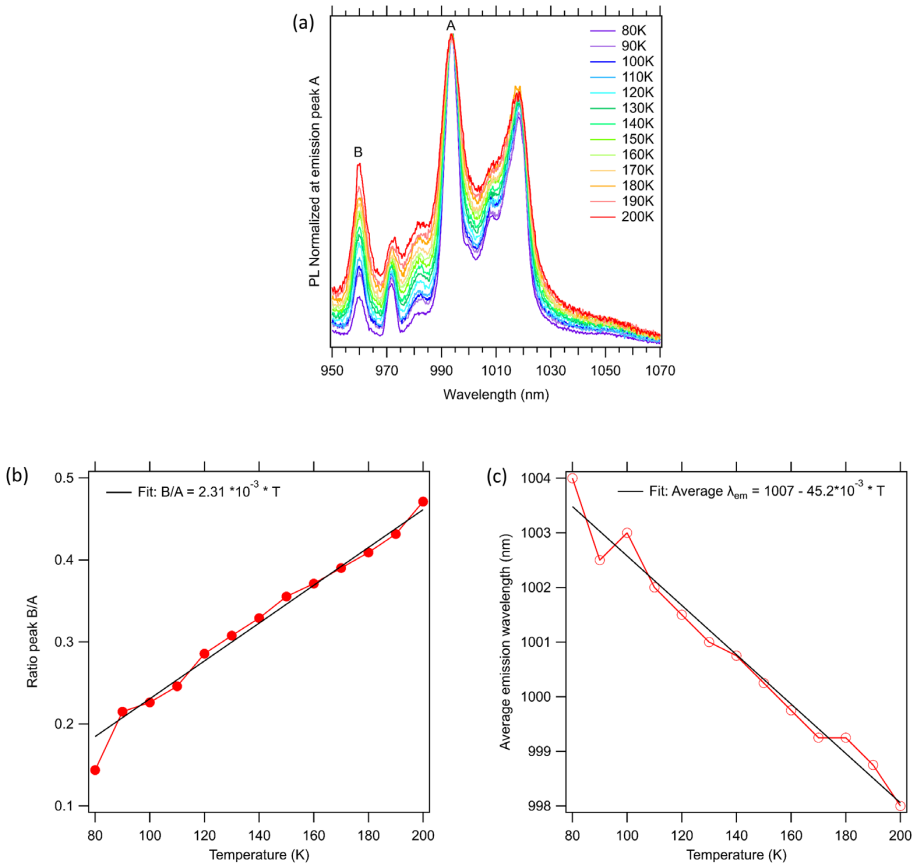


Figure A3.19. (a) Emission spectra of Yb:YLF NCs at different temperatures (applied by a cryostat) and the trends of (b) emission peaks and (c) average emission wavelength *versus* temperature. Both (b) and (c) show linear trends that can be used to determine the temperature of the NCs from their emission spectra.

Appendix 3.19

Temperature of NCs from Emission Spectra

As shown in Figure A3.20, the PL-spectrum of Yb:YLF changes when the temperature changes, due to a lower number of available phonons at lower temperature, resulting in a reduced intensity of higher energy PL-peaks. In reports, this phenomenon is used to conclude that Yb:YLF and Yb:$NaYF_4$ are showing optical refrigeration.[63] However, as shown in Figure A3.20, a sample with low PLQY (13.2%, Figure A3.20a) shows practically identical PL-spectra as a sample with a high PLQY (95.8%, Figure A3.20b) when excited at 930 nm (to increase heating) and 1030 nm (to reduce heating). Similarly, the average emission wavelength (indicated by the straight lines in Figure A3.19) is similar for both samples.

The peak ratio B/A for both NC samples is shown in Table A3.2. From this data we see that the analysis of PL-spectra and the extraction of the NC temperature is per definition not straightforward, and in our case not applicable as indication for the temperature. This, because a low PLQY-sample (that should heat significantly) gives the same temperature and temperature change as a high PLQY sample (that should at least show far less heating than the low PLQY sample). Note that the above shown PL-spectra (Figure A3.20) are obtained from a NC film on PTFE, to reduce heating of the NCs through the substrate as much as possible. Identical results are obtained when measuring a dispersion in chloroform. Therefore, it is likely that the temperature of the NCs in these measurements is determined by the temperature of the environment, and that the PL-spectra change at different excitation WLs. Only PL-spectra of NCs that are isolated from external heating can therefore be applied for a proper temperature analysis. The analysis of PLQY through TRPL is therefore in all practical cases a much better analysis.

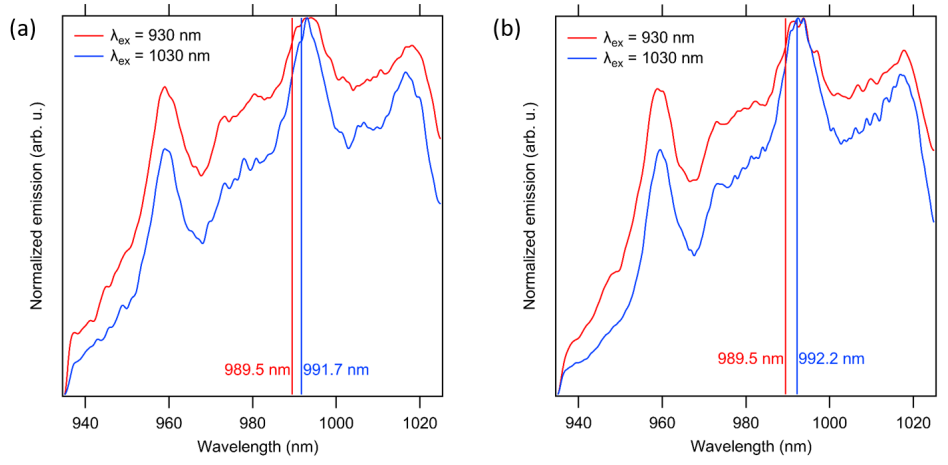


Figure A3.20. (a) Emission spectra of NCs excited at 930 nm (resulting in phonon-emission for all samples) and 1030 nm (to significantly reduce phonon-emission in high PLQY samples) for a low and (b) a high PLQY sample. As is clear from this image, the large difference in PLQY does not show a significant difference in the average emission, nor in the ratio of peak B/A (see Figure A3.19a).

Appendix 3.19

Temperature of NCs from Emission Spectra

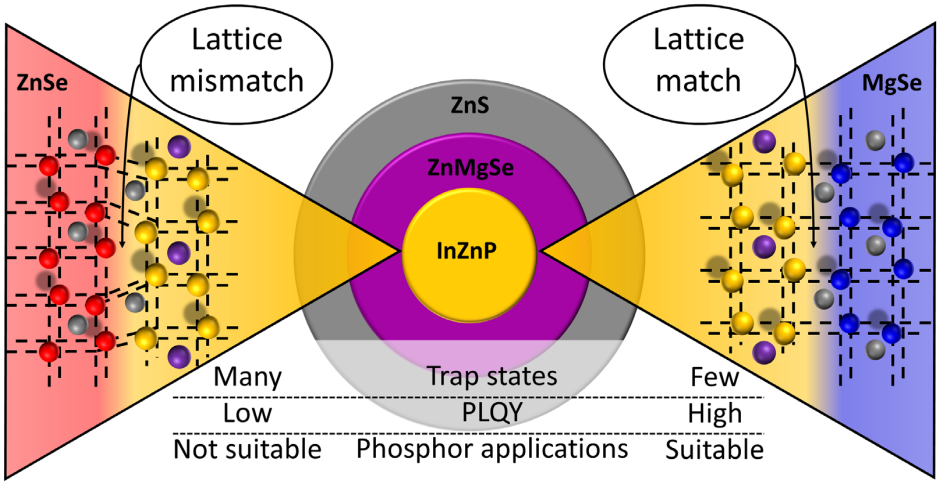
Table A3.2. The extracted temperatures for two NC samples (high and low PLQY), excited at 930 nm and 1030 nm, calculated using the fitted functions shown in Figures A3.19b and c.

excitation wavelength - PLQY	temperature according to peak ratio (K)	temperature according to average emission wavelength (K)
930 nm - Low	354.1	389.4
930 nm - High	354.1	389.4
1030 nm - Low	282.7	340.8
1030 nm - High	282.0	329.7

4

Chapter 4

Developing Lattice Matched ZnMgSe Shells on InZnP Quantum Dots for Phosphor Applications



Indium phosphide quantum dots (QDs) have drawn attention as alternatives to cadmium- and lead-based QDs that are currently used as phosphors in lamps and displays. The main drawbacks of InP QDs are, in general, a lower photoluminescence quantum yield (PLQY), a decreased color purity, and poor chemical stability. In this research, we attempted to increase the PLQY and stability of indium phosphide QDs by developing lattice matched InP/MgSe core–shell nanoheterostructures. The choice of MgSe comes from the fact that, in theory, it has a near-perfect lattice match with InP, provided MgSe is grown in the zinc blende crystal structure, which can be achieved by alloying with zinc. To retain lattice matching, we used Zn in both the core and shell and we fabricated InZnP/$Zn_xMg_{1-x}Se$ core/shell QDs. To identify the most suitable conditions for the shell growth, we first developed a synthesis route to $Zn_xMg_{1-x}Se$ nanocrystals (NCs) wherein Mg is effectively incorporated. Our optimized procedure was employed for the successful growth of $Zn_xMg_{1-x}Se$ shells around In(Zn)P QDs. The corresponding core/shell systems exhibit PLQYs higher than those of the starting In(Zn)P QDs and, more importantly, a higher color purity upon increasing the Mg content. The results are discussed in the context of a reduced density of interface states upon using better lattice matched $Zn_xMg_{1-x}Se$ shells.

Jence T. Mulder, Nicholas Kirkwood, Luca De Trizio, Chen Li, Sara Bals, Liberato Manna and Arjan J. Houtepen. ACS Appl. Nano Mater. 2020, 3, 4, 3859–3867.

4.1 Introduction

Quantum dots (QDs) are semiconductor nanocrystals that exhibit unique, size-dependent optical and electrical properties.[1] This makes QDs very interesting for various optoelectronic applications. Currently, QDs are applied as phosphors in displays and lamps,[2–6] and they are further investigated for, among others, solar cells[7,8] and several types of sensors[9,10]. Also, QDs can be used as biological labels for *in vivo* tracking.[11,12]

The main drawback of currently used QDs is their toxicity. The QDs with the highest photoluminescence quantum yield (PLQY) and color purity are all based on cadmium or lead.[13–16] Because of the high toxicity of these metals, their use is restricted or banned from the use in consumer products.[17] Hence, there is an active search to find alternatives for cadmium- and lead-based QD materials.[18–21] One of the best candidates is indium phosphide (InP). Much has been tried to optimize InP QDs by both computational[16] and experimental work.[5,6,22–27] However, in terms of color purity and chemical stability, these QDs (maximum reported full width at half-maximum (FWHM) of 35 nm)[27] are not yet on par with Cd-based QDs (maximum reported FWHM of 20 nm).[28–30]

QDs with a high PLQY and good stability are generally formed by growing a protective shell around the core of the emitting material. The shell passivates possible in-gap states on the surface of the emitting core. Furthermore, the shell protects the QD core from hydrolysis and oxidation. Requirements for a well-passivating shell are a type I band alignment for the shell material (*i.e.*, the valence band should be lower and the conduction band higher in energy for the shell material than the core material), a matching crystal structure, and a good match in lattice parameters between the core and the shell material.[31] If there is no type I band alignment, delocalization of charge carriers from the core to the shell occurs. This leads to trapping of charge carriers in in-gap states on the shell surface and hence a reduction of the PLQY.[31] If the lattice parameters of both materials do not match, epitaxial shell growth is not possible, resulting in interfacial defects that can form trap states.

Growing epitaxial shells has been the main challenge in developing high quality InP QDs. Zinc sulfide (ZnS), which is most commonly used as a shell material, has a −7.8% lattice mismatch with the InP core (Table 4.1), which leads to a low PLQY.[32] ZnSe matches better, with a −3.4% mismatch, and very recent work has shown >90% PLQY for InP/ZnSe/ZnS QDs.[25,26] However, on paper, the best lattice match can be achieved with zinc blende MgSe,

Table 4.1. Material Properties of InP and Different Shell Materials .[a]

material	crystal structure	lattice parameter (Å)	mismatch *vs.* InP (%)	bulk bandgap (eV)	band alignment
InP	zinc blende	5.87		1.34	
ZnS	zinc blende	5.41	−7.8	3.78	type I
ZnSe	zinc blende	5.67	−3.4	2.82	type I
MgSe	zinc blende	5.90	0.51	4.05	type I [34]
MgSe	rock salt	5.46	-7.0	2.53 [35]	quasi-type II to type I

[a] All values were taken from Madelung[33] if not indicated differently.

which has a lattice mismatch of 0.5%. Furthermore, MgSe is a wide bandgap material (~4 eV) assuring a type I band alignment with InP (see Table 4.1).[33] This has motivated us to investigate the possibility of growing lattice matched MgSe shells onto InP QDs.

A challenge is that the native crystal structure of MgSe is not zinc blende but rock salt,[33,36] resulting in a significant lattice mismatch with InP. Potentially MgSe could adopt the zinc blende crystal structure when grown epitaxially on zinc blende InP QDs. However, our attempts to do so where unsuccessful. On the other hand, by alloying MgSe with zinc, $Zn_xMg_{1-x}Se$ can be formed with a zinc blende crystal structure.[36] Therefore, we attempted to grow $Zn_xMg_{1-x}Se$, protected by a ZnS shell, as a novel shell material around InP QDs, as illustrated in Figure 4.1. For simplicity, from now on we will refer to this $Zn_xMg_{1-x}Se$ alloy as ZnMgSe. To compensate for the smaller lattice parameter of ZnMgSe compared to that of MgSe, we included a small fraction of Zn in the InP cores, termed InZnP, so that the core lattice parameter could be also reduced.[32,37] This way it would be possible to, in theory, achieve a perfect core–shell lattice match.

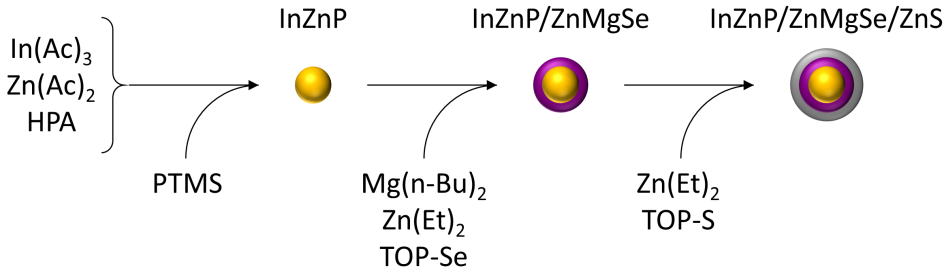


Figure 4.1. Schematic of the synthesis steps taken in the synthesis of InZnP/ZnMgSe/ZnS QDs.

4.2 Shell Growth Using Stearate Precursors

InZnP quantum dots were synthesized by a heat-up method reported by Ramasamy *et al.*[38] (see Experimental Methods) as it allows for a large production of QDs (scale up) with a good size distribution (Figure A4.1). After their synthesis, the QDs were purified to remove any unreacted precursors that could potentially react during the shell growth and therefore resulting in larger and less well-defined QDs (Figure A4.2). Initially, we studied the growth of ZnMgSe shells by employing a method similar to the one reported by Ramasamy *et al.* for growing ZnSe onto InP QDs,[38] in which part of the zinc stearate was substituted for magnesium stearate. Unfortunately, by using of this procedure no Mg was incorporated, and the optical properties were much worse for these shells than for pure ZnSe shells, including strongly increased defect emission (Figure A4.3). Hence, we sought another method to grow ZnMgSe. Therefore, we first focused on developing a synthesis route to produce ZnMgSe NCs and, subsequently, to employ the optimized reaction conditions for the growth of ZnMgSe shells on InZnP QDs.

4.3 ZnMgSe NCs

We first tried to synthesize MgSe NCs using Mg-stearate and TOP-Se, but no reaction occurred. Also, the addition of Mg-stearate to a ZnSe synthesis procedure[39] did not result in any change in lattice parameter as observed by electron diffraction measurements

(Figure A4.4). These results suggested that Mg-stearate is not reactive enough to yield either MgSe or ZnMgSe NCs. Hence, we switched to more reactive organometallic Mg precursors. We synthesized ZnMgSe NCs by adapting a procedure reported by Boldt *et al.*,[40] and employing diethylzinc ($Zn(Et)_2$), di-n-butylmagnesium ($Mg(n\text{-}Bu)_2$), and TOP-Se together with oleylamine, used as both solvent and stabilizing ligand. Various ZnMgSe samples having different compositions were prepared by systematically varying the Zn/Mg precursors ratio. However, we found that these NCs were relatively unstable toward purification, as the samples irreversibly precipitated (Figure A4.5). To enhance their stability, we grew a thin ZnS shell around these NC cores, forming Zn(Mg)Se/ZnS core/shell NCs, whose absorption spectra are reported in Figure 4.2a.

Without any Mg, blue emitting and relatively monodisperse ZnSe NCs were formed (red lines in Figure 4.2a). Upon the addition of $Mg(n\text{-}Bu)_2$ to the reaction, the first absorption peak initially red-shifted for low feed fractions of Mg (25%), followed by a blue-shift upon further increasing the Mg feed fraction (Figure 4.2a). On the other hand, emission spectroscopy showed a blue-shift for all samples when increasing the Mg feed fraction. This blue-shift was expected, as ZnMgSe should have a higher band gap energy than ZnSe. We note, however, that part of the PL blue-shift is in fact due to a reduced Stokes shift. The initial red-shift of the absorption is most likely related to an increase in particle size. This assumption is strengthened by TEM imaging (Figure A4.6), which shows that the red-shifted sample has a slightly larger crystallite size. The morphology of the different NCs is furthermore unchanged.

More importantly, the XRD analysis revealed that our reaction conditions led to the

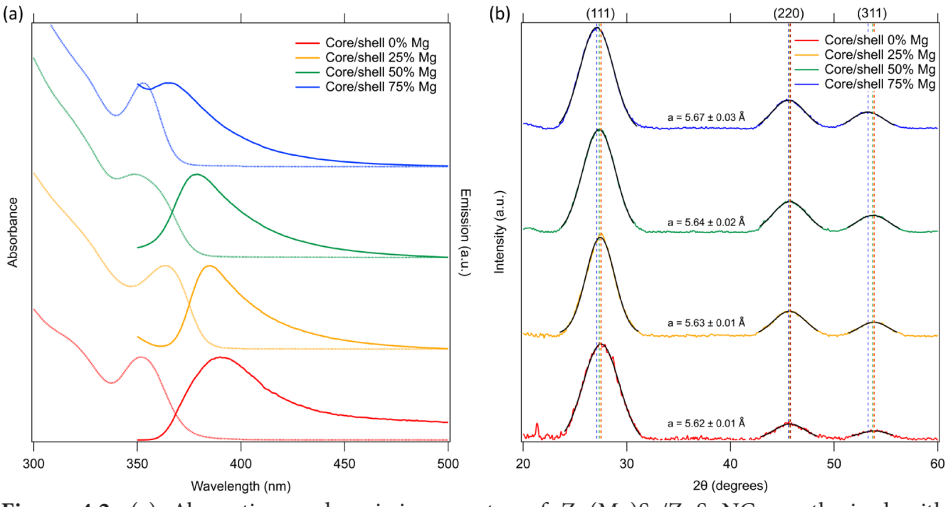


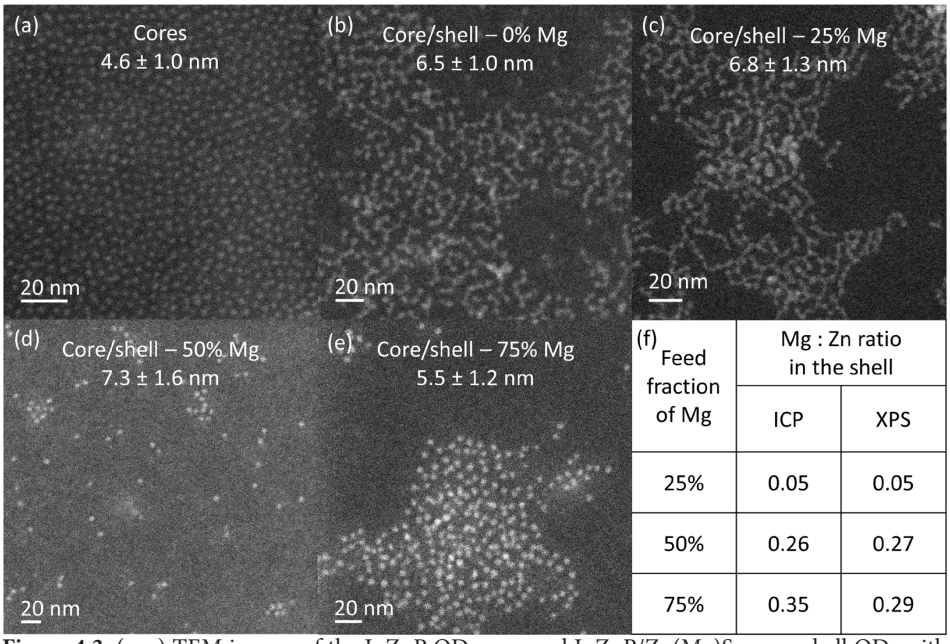
Figure 4.2. (a) Absorption and emission spectra of Zn(Mg)Se/ZnS NCs synthesized with organometallic precursors with varying feed fractions of $Mg(n\text{-}Bu)_2$. The spectra are normalized to 1 for the first excitonic peak. (b) XRD diffractograms of Zn(Mg)Se/ZnS NCs synthesized with organometallic precursors with varying feed fractions of $Mg(n\text{-}Bu)_2$. The lattice parameter values a were calculated with Bragg's law, using the peak values of the fits (black lines) for the (111), (220), and (311) crystal planes. The data are normalized to 1 for the (111) reflection peak.

formation of ZnMgSe NCs having a zinc blende crystal structure (see Figure 4.2b). Indeed, the diffractograms showed a slight lattice expansion for the NCs synthesized with a higher Mg feed fraction, indicating the effective inclusion of Mg with the formation of ZnMgSe alloys (see Table 4.1). This was also observed by EDX analysis, where Mg was found in all ZnMgSe samples (Figure A4.7).

4.4 InZnP/ZnMgSe Core–Shell QDs

InZnP QD cores (with an In:Zn feed ratio of 2:1 and an experimental 6:1 In:Zn ratio determined by ICP-OES and XPS) were added to a 1:1 mixture of degassed ODE and OLA. The organometallic precursors ($Mg(n\text{-}Bu)_2$ and $Zn(Et)_2$, dissolved in heptane) and TOP-Se were slowly added to the QD mixture at 200 °C using separate syringe pumps for the $Mg(n\text{-}Bu)_2$ and the $Zn(Et)_2$/TOP-Se mixture to ensure a controlled shell growth without initiating secondary nucleation of ZnMgSe NCs.

TEM images of the resulting core–shell QDs are presented in Figure 4.3. All core–shell particles have a larger size compared to the cores and are equal in size within the measurement error for all feed fractions of magnesium. We used XPS and ICP to measure the Mg and Zn contents in all samples. The results are shown in Figure 4.3f and Figure A4.8. The measured Mg:Zn ratio matched for both techniques and increased up to a value of ~30% for a 75% Mg:Zn feed ratio. The combination of similar measured shell thicknesses and the presence of measured Mg through XPS and ICP suggests that in all cases Mg is incorporated into the shell.



(f)

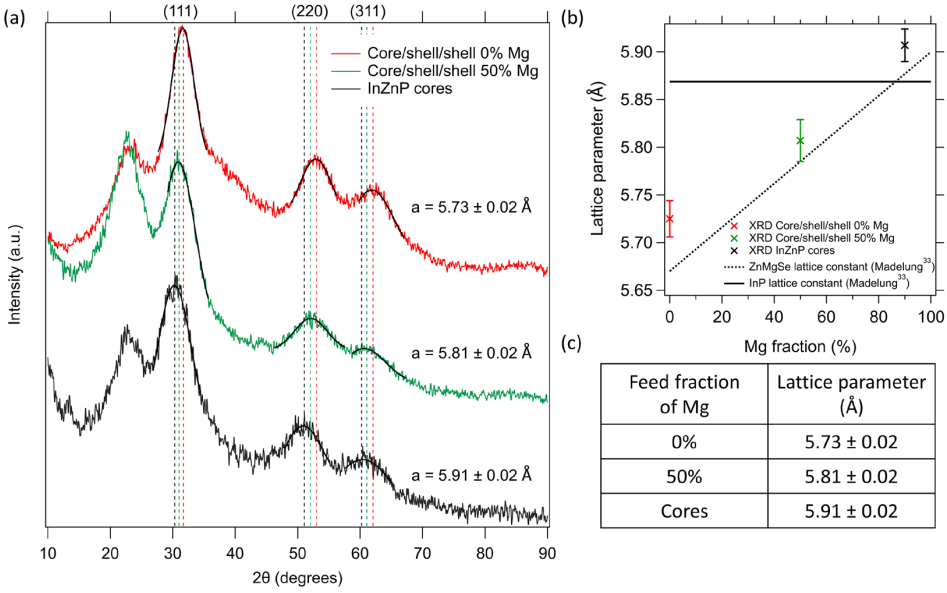
Feed fraction of Mg	Mg : Zn ratio in the shell	
	ICP	XPS
25%	0.05	0.05
50%	0.26	0.27
75%	0.35	0.29

Figure 4.3. (a–e) TEM images of the InZnP QD cores and InZnP/Zn(Mg)Se core–shell QDs with a varying $Mg(n\text{-}Bu)_2$ precursor feed fraction as indicated in the figures. (f) Table of Mg:Zn ratio in the shell measured by ICP and XPS measurements. For all samples, the same cores were used. The amount of Zn in the core (In:Zn 6:1) was subtracted from the core–shell samples to obtain the estimated Mg:Zn ratio in the shell.

4.5 InZnP/ZnMgSe/ZnS Core–Shell–Shell QDs

As already stated above for the ZnMgSe NCs, this material is very unstable. To improve the stability, a second, protective ZnS shell was grown around the ZnMgSe shell. This was done by the subsequent injection of $Zn(Et)_2$ and TOP-S to the unpurified reaction mixture containing the core–shell QDs by the use of syringe pumps. We find that the additional ZnS shell strongly increased the colloidal stability of the QDs. In particular, washing of the InZnP/ZnMgSe QDs easily caused irreversible precipitation, while the same samples covered with a ZnS shell could be washed several times (see the Experimental Methods section for details on the washing procedure). The structural and optical analyses below were performed on purified core–shell–shell QDs.

To confirm that the incorporation of Mg still resulted in a zinc blende ZnMgSe shell with the expected lattice expansion, XRD measurements were performed. For the samples with thin Zn(Mg)Se shells shown in Figure 4.3 (shell radial thickness between approximately 0.5 and 1 nm), no clear changes in the XRD diffractograms are observed compared to the core only QDs (see Figure A4.9). However, samples with thicker shells (tripled amount of ZnMgSe shell precursors) and an additional thin ZnS shell do show a systematic



Feed fraction of Mg	Lattice parameter (Å)
0%	5.73 ± 0.02
50%	5.81 ± 0.02
Cores	5.91 ± 0.02

Figure 4.4. (a) XRD diffractogram of InZnP core and InZnP/Zn(Mg)Se/ZnS core–shell–shell QDs. The shells were synthesized with organometallic precursors with a 0% and 50% fraction of $Mg(n\text{-}Bu)_2$ in the feed. A clear shift to lower values of 2θ for the Mg containing shells can be observed, indicating a lattice expansion compared to ZnSe, and therefore a better match to the InZnP core. The data are normalized to 1 for the (111) reflection peak. (b) Calculated lattice parameters show a slightly expanded value for the lattice parameter compared to a linearization of the lattice parameters from pure ZnSe and MgSe in the zinc blende structure. The lattice constant for ZnMgSe was obtained from the data from Madelung[33] and linearly extrapolated following Vegard's law. (c) Calculated values of the lattice parameters of the samples measured in Figure 4.3a. The lattice parameter values were calculated with Bragg's law by using the peak values of the fits (black lines) for the (111), (220), and (311) crystal planes.

lattice expansion upon increasing the amount of Mg, as indicated by the shift of the XRD reflections to lower 2θ values in Figure 4.4. Hence, the incorporation of Mg in the shell indeed decreases the lattice mismatch. The peak in the XRD diffractograms around 25°, unexpected for zinc blende crystals, has been found more often in the literature for a variety of zinc blende materials[25,41–43] and can be assigned to metal–ligand complexes on the surface of the QDs.[42,43] We remark that the InZnP QD cores showed a lattice parameter similar to bulk InP, suggesting only little Zn was incorporated. ICP-OES and XPS revealed that the In:Zn ratio (6:1) was indeed much lower than the feed fraction (2:1). This leaves room for further improvement of the lattice matching. Yet, the expected lattice mismatch for the 50% Mg feed fraction in the shell is only 1.7%.

Figure 4.5 summarizes the optical properties of the InZnP/Zn(Mg)Se/ZnS QDs, synthesized according to the synthesis procedure reported. Figures 4.5a and 4.5b show photographs of samples prepared with 0–75% of magnesium feed fraction in the shell under ambient light and UV illumination, respectively. A clear color change is visible

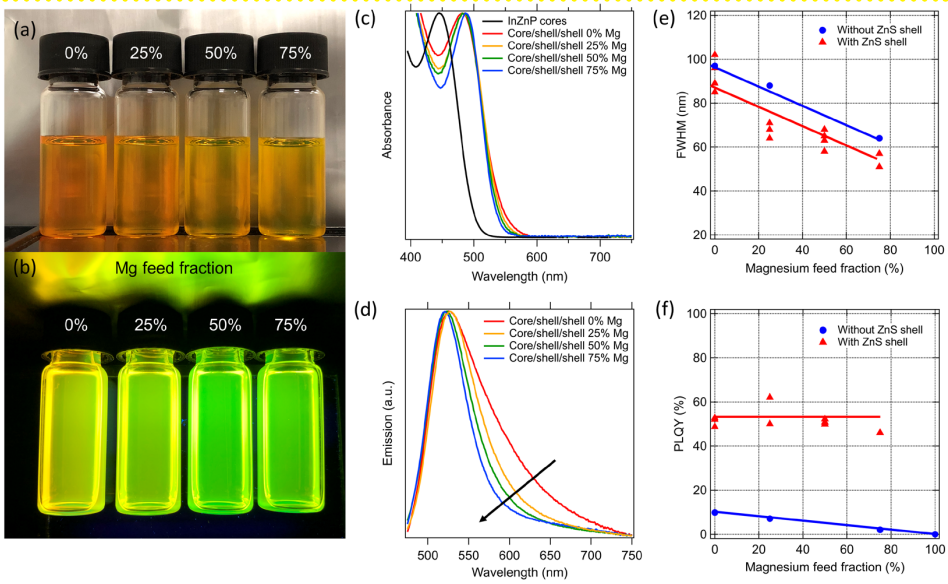


Figure 4.5. Photographs of dispersions of InZnP/Zn(Mg)Se/ZnS core–shell–shell QDs under ambient (a) and UV light (b). The change in color of the emission is clearly visible by eye, going from yellow for a pure ZnSe shell to green for samples with a high Mg feed fraction for the shell synthesis. (c) Absorption spectra of InZnP cores and InZnP/Zn(Mg)Se/ZnS core–shell–shell QDs (normalized to 1 for the first excitonic peak), showing a similar red-shift for all core–shell–shell QDs compared to the cores. The higher the Mg feed fraction, the sharper the absorbance peak. (d) Emission spectra of the InZnP/Zn(Mg)Se/ZnS core–shell–shell QDs (normalized to 1 for the emission peak) and (e) FWHM of the emission peak for different Mg feed fractions. The FWHM decreases strongly for increasing the feed fraction of Mg. This effect is enhanced when passivating the susceptible material with a protective ZnS shell. (f) Photoluminescence quantum yield *vs.* Mg feed fraction with (red triangles) and without (blue circles) final ZnS shell. Only when growing the ZnS shell, QDs are stable enough to retain a high PLQY. Solid lines in (e) and (f) are a guide to the eye.

in Figure 4.5b, from yellow emission at 0% Mg to bright green emission at 75% Mg. Absorption spectra are plotted in Figure 4.5c. The absorption spectra for core–shell samples all showed a red-shift compared to the InZnP core only sample, possibly due to wave function delocalization over the shell.[44] The differences in the absorption spectra for different Mg feed ratios are small, but clearly noticeable. For an increased feed fraction of Mg the absorption spectra become sharper and shift slightly more to the red.

The emission spectra, displayed in Figure 4.5d, exhibit much larger differences for the different magnesium fractions. In contrast to the small red-shift of the absorption maximum, the PL maximum shifts to the blue for increasing Mg fractions, implying a reduced Stokes shift (see Figure A4.12 for a plot of the Stokes shift *vs.* Mg fraction). At the same time, the photoluminescence spectra become much narrower, especially due to a decrease of the red tail of the emission peak. The FWHM *vs.* Mg feed fraction is plotted in Figure 4.5e, and it was found to decrease from 90 nm without Mg to 50 nm for a 75% Mg feed fraction. As presented in Figure 4.5f, the PLQY of all samples was around 50% within error (red triangles). If the material was not protected by the final ZnS shell, the PLQY was much lower and decreased with increasing Mg fraction (blue circles in Figure 4.5f), probably as a result of rapid degradation of the ZnMgSe shell.

The relatively broad emission that characterizes InP-based QDs was recently addressed in several studies.[16,25,44,45] Especially the very thorough study by the Talapin group convincingly showed that the broad emission spectra are due to radiative recombination of delocalized conduction band electrons with localized holes.[16] Combined with strong electron–phonon coupling this explains the relatively large Stokes shift and the large FWHM. Temperature-dependent PL measurements on InP QDs[45] and on InP/ZnS and InP/ZnSe[25] indeed show structure in the emission spectra associated with trap emission at reduced temperatures. Janke *et al.*[16] associated the hole traps with structural disorder, *e.g.*, as a result of a core–shell lattice mismatch, or in particular *via* the incorporation of substitutional Zn^{2+} in the InP core. The latter should form a shallow acceptor state that could trap holes and be responsible for the broadened and red-shifted emission.

The InZnP/ZnMgSe/ZnS QDs shown here exhibit very similar features as InP/ZnSe QDs. As plotted in Figure A4.12, the Stokes shift decreases with increasing amounts of Mg, and this Stokes shift correlates positively with the FWHM of the emission. This is in line with hole localization on shallow states just above the valence band and strong electron–phonon coupling associated with this hole localization. This would imply that the inclusion of Mg in the shell material reduces the number of hole traps and/or reduces the electron–phonon coupling. While all investigated samples contained Zn^{2+} in the core, and this likely did not change upon ZnMgSe shell growth, the decreasing lattice mismatch for higher Mg amounts in the shell could lead to reduced structural disorder at the core–shell interface. This was in fact the ansatz of this work.

The fact that the PLQY does not increase while the FWHM becomes narrower suggests a reduction of interfacial trap states, which can be explained by the fact that the shallow hole traps responsible for the broad emission are in fact radiative. In general, high PLQY often correlates with broad emission in InP/ZnSe QDs,[44] demonstrating the high efficiency of free electron–localized hole recombination for this system. Reducing the number of localized hole states thus results in a blue-shift and narrower emission lines but not in an increased PLQY.

The reported values for the PLQY and FWHM of the InZnP/ZnMgSe/ZnS QDs in this work are inferior to those of InP/ZnSe/ZnS QDs reported in recent literature. We consider that this may be because the InP/ZnSe/ZnS system has been extensively studied and optimized by a large number of research groups.[6,24–27,38,44] This optimization has not yet happened for the InZnP/ZnMgSe/ZnS QDs. The current work does show that it is possible to use ZnMgSe as a shell material with a smaller lattice mismatch than that of the commonly used ZnSe and ZnS shells. This offers increased flexibility in designing shell materials for InP QDs.

4.6 Conclusions

Magnesium selenide shells, alloyed with zinc to grow in the zinc blende crystal structure, were grown around indium zinc phosphide quantum dots in an attempt to improve lattice matching between the core and the shell material. To grow magnesium containing shells, we employed highly reactive organometallic precursors. The shell material was thereafter protected by a second zinc sulfide shell to increase the stability of the quantum dots. With this method we can reliably synthesize InZnP/ZnMgSe/ZnS QDs with variable Mg content in the shell and with reduced lattice mismatch. The inclusion of Mg in the shell results in much narrower emission features, which can be attributed to a reduced formation of shallow hole traps at the core–shell interface. These narrower emission features may be of large interest for the production of high quality phosphors for optoelectronic applications.

Experimental Methods

Materials

Methyl acetate (anhydrous, 99.5%), toluene (anhydrous, 99.8%), 1-octadecene (ODE, technical grade, 90%), tris(trimethylsilyl)phosphine (PTMS, 95%), trioctylphosphine (TOP, 97%), selenium (99.99%), palmitic acid (HPA, >99%), indium acetate ($In(Ac)_3$, 99.99% trace metal basis), zinc acetate ($Zn(Ac)_2$, 99.99% trace metal basis), diethylzinc (≥52 wt % Zn basis), and di-n-butylmagnesium (1 M in heptane) were purchased from Sigma-Aldrich. Ethanol (absolute, SupraSolv for GC-EDC/FID) was purchased from Merck. Oleylamine (OLA, 80–90% C18, ≥96.0% (primary amine)) was purchased from Acros Organics. n-Hexane (anhydrous) and sulfur (Puratronic , 99.9995%) were purchased from Alfa Aesar.

The used tris(trimethylsilyl)phosphine, diethylzinc, and di-n-butylmagnesium are spontaneously reactive with air and moisture and should therefore be handled with care and solely under inert atmosphere.

Overview of All Samples Discussed in This Work

Many different types of samples are discussed and compared in this chapter. For clarity, we list all different types in Table 4.2 together with the figure they are discussed in. In this work the mentioned Mg fractions always relate to the Mg feed fraction, unless stated differently.

Table 4.2. List of all samples used in the figures displayed in this article.

Sample type	Core	1st shell	2nd shell	Displayed in	Analysis performed
1	Zn(Mg)Se	ZnS	–	Figure 4.2	optical (a), XRD (b)
2	InZnP	Zn(Mg)Se	–	Figure 4.3	TEM (a – e), ICP (f), XPS (f)
2	InZnP	Zn(Mg)Se	–	Figure 4.5	optical (e, f)
3	InZnP	Zn(Mg)Se (thicker)	ZnS (thinner)	Figure 4.4	XRD (a – c)
4	InZnP	Zn(Mg)Se	ZnS	Figure 4.5	optical (a – f)

Synthesis of InZnP Core Quantum Dots by the Heating-Up Method

The core synthesis method is adapted from the heating-up procedure of Ramasamy *et al.*[38] In short, 44 mg of $In(Ac)_3$ (0.15 mmol), 14 mg of $Zn(Ac)_2$ (0.075 mmol), 147 mg of HPA (0.575 mmol), and 5 mL of ODE were added to a suitable three necked flask. Subsequently, the flask was attached to a Schlenk line and heated to 120 °C while stirring at 800 rpm. When the contents reached 120 °C, the flask was put under a vacuum of 1 mbar to remove water and oxygen from the reaction mixture. After 1 min, the flask was put under dry nitrogen and then back under vacuum to purge the mixture further. This purging process was repeated for a total of three times. Afterward, the flask was put under vacuum at 120 °C overnight, to completely remove any residual water and oxygen as well as any acetic acid that formed. Then, the flask was put back under nitrogen to atmospheric pressure and cooled to 50 °C, and under a continuous flow of nitrogen 29 µL (0.1 mmol) of PTMS dissolved in 1 mL of TOP was injected while stirring at 800 rpm. After injection, the temperature was increased with increments of 5 °C every 20 s until it reached 305 °C. The flask was kept stirring for 2 min at this temperature, before it was rapidly cooled to 80 °C by the use of compressed air. Thereafter, 2 mL of anhydrous toluene was injected to facilitate the transfer of the solution from the flask to a vial, which was filled with nitrogen prior to use. The solution was brought into a glovebox, and ethanol was added as antisolvent until the reaction mixture became turbid, which indicated the precipitation of the formed quantum dots. The quantum dot precipitate was centrifuged for 15 min at a relative centrifugal force of 1800g, and subsequently the supernatant was removed under an inert atmosphere. The quantum dot cores, often found as an oily orange droplet, were redispersed in 1 mL of anhydrous hexane.

Synthesis of ZnMgSe Nanocrystals

The synthesis method for ZnMgSe NCs is adapted from the synthesis of ZnSe NCs by Boldt *et al.*[40] In a 25 mL three-necked flask, 8.61 mL (7 g) of degassed OLA was stirred and heated to 300 °C. When the contents reached 300 °C, 785 µL of 1 M TOP-Se (in TOP) with an additional 1.6 mL of TOP was injected. Immediately after, a total of 785 µL of 1 M organometallic compounds (diethylzinc and/or di-n-butylmagnesium) was swiftly added. The particles were grown further by the addition of 0.245 mmol of both precursors every 30 min (TOP-Se dissolved in a total of 750 µL of TOP) in the same order as previously described, until the desired size was reached. After the last injection of precursors, the mixture was stirred for another 30 min to anneal any defects. Subsequently, the mixture was cooled rapidly by the use of compressed air, and 2 mL of anhydrous toluene was

added. The solution was then transferred to a glovebox, and by the addition of ethanol the particles were precipitated. After centrifuging the solution, the supernatant was decanted, and the particles were resuspended in 1 mL of anhydrous toluene.
To protect the nanoparticles from oxidation and hydrolysis, a ZnS shell was grown around the ZnMgSe NCs. This was done by adding a total of 1 mmol of TOP-S (in TOP) and 1 mmol of diethylzinc ($Zn(Et)_2$) with syringe pumps over the course of 2 h at 200 °C, starting 30 min after the last injection of ZnMgSe precursors.

ZnMgSe and ZnS Shell Growth on InZnP Quantum Dots

To grow ZnMgSe shells around InZnP quantum dot cores, 1 mL of freshly prepared InZnP QD cores in hexane was filtered through a 0.2 µm syringe filter and added to 10 mL of a 1:1 mixture of anhydrous ODE and OLA. The contents were placed in a nitrogen filled flask, attached to a Schlenk line, after which the hexane in the mixture was removed by applying a vacuum for a few minutes. Subsequently, the flask was put back under nitrogen, and the contents were heated to 200 °C. At the moment the solution reached 50 °C, 350 µL of 1 M TOP-Se (in TOP) with an additional 300 µL of TOP and 200 µL of 1 M organometallic precursors (diethylzinc and/or di-n-butylmagnesium) in the preferred ratio were added dropwise over the course of 1 h by the use of syringe pumps. The $Zn(Et)_2$ and the TOP-Se were mixed prior to the injection; the di-n-butylmagnesium ($Mg(n\text{-}Bu)_2$) was added by a separate syringe. After the injection was completed, the mixture was heated further to 240 °C. Once the temperature was stable, 1 mL of 1 M TOP-S in TOP and 1 mL of 1 M $Zn(Et)_2$ in hexane were added by a syringe pump over the course of 1 h. When all precursors were added completely, the temperature was kept at 240 °C for another 30 min to ensure all precursors reacted and any surface defects were annealed. Subsequently, the reaction mixture was cooled by compressed air, and 2 mL of anhydrous toluene was added to facilitate the transfer of the reaction mixture from the flask to the glovebox by the use of nitrogen-filled vials. Anhydrous methyl acetate was added to the reaction mixture until it became turbid. After centrifuging the mixture for 10 min at a relative centrifugal force of 1800g, the supernatant was removed, and the solids were resuspended in 1 mL of toluene. This washing step was repeated for two more times, and the final product was stored in 1 mL of toluene under nitrogen gas in a glovebox.

Structural Characterization

TEM micrographs were acquired with a FEI Technai G2 F20 microscope at 200 kV. Samples for TEM imaging were prepared by drop-casting a toluene solution of QDs onto a carbon-coated copper (400-mesh) TEM grid. HR-STEM micrographs were acquired with a FEI Titan microscope operating at 300 kV. The convergence angle for the electron probe is ~21 mrad. XRD measurements were performed with a Bruker D8 ADVANCE diffractometer (Co Kα, $\lambda = 0.1789$ nm).

Optical Characterization

Optical characterization was performed by using gastight 1 cm quartz cuvettes loaded in a N_2-filled glovebox. Absorbance measurements were acquired by using a PerkinElmer Lambda 365 absorbance spectrometer. Fluorescence spectra were acquired by using an Edinburgh Instruments FLS980 spectrometer. Photoluminescence quantum yields were collected by using a reference dye method with fluorescein in 0.1 M sodium hydroxide in

water (λ_{ex} = 465 nm).[46]

Elemental Analysis

ICP-OES was performed on a Prodigy 7 spectrometer (LEEMAN LABORATORIES Ltd.) so that the elemental composition of the synthesized QD solutions could be quantified. The samples were digested overnight in aqua regia prior to the ICP measurements. All chemical analyses performed by ICP-OES were affected by a systematic error of about 5%. The ratio of HCl to HNO_3 was 3:1 (v/v).

The XPS analyses were performed with a Kratos Axis Ultra spectrometer using a monochromatic Al Kα source (20 mA, 15 kV). Survey scan analyses were performed with an analysis area of 300 × 700 μm^2 and a pass energy of 160 eV, whereas high-resolution analyses were performed with a pass energy of 10 eV. Specimens for XPS measurements were prepared by dropping a concentrated NC solution onto a freshly cleaved highly oriented pyrolytic graphite substrate (HOPG, ZYB). Spectra were analyzed by using CasaXPS software (version 2.3.17).

References

1. Alivisatos, A. P. Semiconductor Clusters, Nanocrystals, and Quantum Dots. Science 1996, 271 (5251), 933–937.
2. Bourzac, K. Quantum Dots Go on Display. Nature 2013, 493 (7432), 283–283.
3. Anikeeva, P. O.; Halpert, J. E.; Bawendi, M. G.; Bulović, V. Quantum Dot Light-Emitting Devices with Electroluminescence Tunable over the Entire Visible Spectrum. Nano Lett. 2009, 9 (7), 2532–2536.
4. Caruge, J. M.; Halpert, J. E.; Wood, V.; Bulović, V.; Bawendi, M. G. Colloidal Quantum-Dot Light-Emitting Diodes with Metal-Oxide Charge Transport Layers. Nat. Photonics 2008, 2 (4), 247–250.
5. Zhang, H.; Hu, N.; Zeng, Z.; Lin, Q.; Zhang, F.; Tang, A.; Jia, Y.; Li, L. S.; Shen, H.; Teng, F.; Du, Z. High-Efficiency Green InP Quantum Dot-Based Electroluminescent Device Comprising Thick-Shell Quantum Dots. Adv. Opt. Mater. 2019, 7 (7), 1801602.
6. Cao, F.; Wang, S.; Wang, F.; Wu, Q.; Zhao, D.; Yang, X. A Layer-by-Layer Growth Strategy for Large-Size InP/ZnSe/ZnS Core–Shell Quantum Dots Enabling High-Efficiency Light-Emitting Diodes. Chem. Mater. 2018, 30 (21), 8002–8007.
7. Sargent, E. H. Colloidal Quantum Dot Solar Cells. Nat. Photonics 2012, 6 (3), 133–135.
8. Crisp, R. W.; Pach, G. F.; Kurley, J. M.; France, R. M.; Reese, M. O.; Nanayakkara, S. U.; Macleod, B. A.; Talapin, D. V.; Beard, M. C.; Luther, J. M. Tandem Solar Cells from Solution-Processed CdTe and PbS Quantum Dots Using a ZnTe-ZnO Tunnel Junction. Nano Lett. 2017, 17 (2), 1020–1027.
9. Frasco, M.; Chaniotakis, N. Semiconductor Quantum Dots in Chemical Sensors and Biosensors. Sensors 2009, 9 (9), 7266–7286.
10. Silvi, S.; Credi, A. Luminescent Sensors Based on Quantum Dot–molecule Conjugates. Chem. Soc. Rev. 2015, 44 (13), 4275–4289.
11. Michalet, X. Quantum Dots for Live Cells, in Vivo Imaging, and Diagnostics.

Science 2005, 307 (5709), 538–544.
12. Gao, X.; Cui, Y.; Levenson, R. M.; Chung, L. W. K.; Nie, S. In Vivo Cancer Targeting and Imaging with Semiconductor Quantum Dots. Nat. Biotechnol. 2004, 22 (8), 969–976.
13. McBride, J.; Treadway, J.; Feldman, L. C.; Pennycook, S. J.; Rosenthal, S. J. Structural Basis for Near Unity Quantum Yield Core/Shell Nanostructures. Nano Lett. 2006, 6 (7), 1496–1501.
14. Pan, J.; Shang, Y.; Yin, J.; De Bastiani, M.; Peng, W.; Dursun, I.; Sinatra, L.; El-Zohry, A. M.; Hedhili, M. N.; Emwas, A. H.; Mohammed, O. F.; Ning, Z.; Bakr, O. M. Bidentate Ligand-Passivated $CsPbI_3$ Perovskite Nanocrystals for Stable Near-Unity Photoluminescence Quantum Yield and Efficient Red Light-Emitting Diodes. J. Am. Chem. Soc. 2018, 140 (2), 562–565.
15. Greytak, A. B.; Allen, P. M.; Liu, W.; Zhao, J.; Young, E. R.; Popović, Z.; Walker, B. J.; Nocera, D. G.; Bawendi, M. G. Alternating Layer Addition Approach to CdSe/CdS Core/Shell Quantum Dots with near-Unity Quantum Yield and High on-Time Fractions. Chem. Sci. 2012, 3 (6), 2028.
16. Janke, E. M.; Williams, N. E.; She, C.; Zherebetskyy, D.; Hudson, M. H.; Wang, L.; Gosztola, D. J.; Schaller, R. D.; Lee, B.; Sun, C.; Engel, G. S.; Talapin, D. V. Origin of Broad Emission Spectra in InP Quantum Dots: Contributions from Structural and Electronic Disorder. J. Am. Chem. Soc. 2018, 140 (46), 15791–15803.
17. Akkerman, Q. A.; Rainò, G.; Kovalenko, M. V.; Manna, L. Genesis, Challenges and Opportunities for Colloidal Lead Halide Perovskite Nanocrystals. Nat. Mater. 2018, 17 (5), 394–405.
18. Kim, J.-Y.; Yang, J.; Yu, J. H.; Baek, W.; Lee, C.-H.; Son, H. J.; Hyeon, T.; Ko, M. J. Highly Efficient Copper–Indium–Selenide Quantum Dot Solar Cells: Suppression of Carrier Recombination by Controlled ZnS Overlayers. ACS Nano 2015, 9 (11), 11286–11295.
19. Song, W.-S.; Yang, H. Efficient White-Light-Emitting Diodes Fabricated from Highly Fluorescent Copper Indium Sulfide Core/Shell Quantum Dots. Chem. Mater. 2012, 24 (10), 1961–1967.
20. Brichkin, S. B. Synthesis and Properties of Colloidal Indium Phosphide Quantum Dots. Colloid J. 2015, 77 (4), 393–403.
21. Chibli, H.; Carlini, L.; Park, S.; Dimitrijevic, N. M.; Nadeau, J. L. Cytotoxicity of InP/ZnS Quantum Dots Related to Reactive Oxygen Species Generation. Nanoscale 2011, 3 (6), 2552.
22. Gary, D. C.; Glassy, B. A.; Cossairt, B. M. Investigation of Indium Phosphide Quantum Dot Nucleation and Growth Utilizing Triarylsilylphosphine Precursors. Chem. Mater. 2014, 26 (4), 1734–1744.
23. Tessier, M. D.; De Nolf, K.; Dupont, D.; Sinnaeve, D.; De Roo, J.; Hens, Z. Aminophosphines: A Double Role in the Synthesis of Colloidal Indium Phosphide Quantum Dots. J. Am. Chem. Soc. 2016, 138 (18), 5923–5929.
24. Pietra, F.; Kirkwood, N.; De Trizio, L.; Hoekstra, A. W.; Kleibergen, L.; Renaud, N.; Koole, R.; Baesjou, P.; Manna, L.; Houtepen, A. J. Ga for Zn Cation Exchange Allows for Highly Luminescent and Photostable InZnP-Based Quantum Dots. Chem. Mater. 2017, 29 (12), 5192–5199.
25. Kim, Y.; Ham, S.; Jang, H.; Min, J. H.; Chung, H.; Lee, J.; Kim, D.; Jang, E. Bright

and Uniform Green Light Emitting InP/ZnSe/ZnS Quantum Dots for Wide Color Gamut Displays. ACS Appl. Nano Mater. 2019, 2 (3), 1496–1504.
26. Li, Y.; Hou, X.; Dai, X.; Yao, Z.; Lv, L.; Jin, Y.; Peng, X. Stoichiometry-Controlled InP-Based Quantum Dots: Synthesis, Photoluminescence, and Electroluminescence. J. Am. Chem. Soc. 2019, 141 (16), 6448–6452.
27. Won, Y.-H.; Cho, O.; Kim, T.; Chung, D.-Y.; Kim, T.; Chung, H.; Jang, H.; Lee, J.; Kim, D.; Jang, E. Highly Efficient and Stable InP/ZnSe/ZnS Quantum Dot Light-Emitting Diodes. Nature 2019, 575 (7784), 634–638.
28. Hanifi, D. A.; Bronstein, N. D.; Koscher, B. A.; Nett, Z.; Swabeck, J. K.; Takano, K.; Schwartzberg, A. M.; Maserati, L.; Vandewal, K.; van de Burgt, Y.; Salleo, A.; Alivisatos, A. P. Redefining Near-Unity Luminescence in Quantum Dots with Photothermal Threshold Quantum Yield. Science 2019, 363 (6432), 1199–1202.
29. Chen, O.; Zhao, J.; Chauhan, V. P.; Cui, J.; Wong, C.; Harris, D. K.; Wei, H.; Han, H.-S.; Fukumura, D.; Jain, R. K.; Bawendi, M. G. Compact High-Quality CdSe–CdS Core–shell Nanocrystals with Narrow Emission Linewidths and Suppressed Blinking. Nat. Mater. 2013, 12 (5), 445–451.
30. Shendre, S.; Delikanli, S.; Li, M.; Dede, D.; Pan, Z.; Ha, S. T.; Fu, Y. H.; Hernández-Martínez, P. L.; Yu, J.; Erdem, O.; Kuznetsov, A. I.; Dang, C.; Sum, T. C.; Demir, H. V. Ultrahigh-Efficiency Aqueous Flat Nanocrystals of CdSe/CdS@$Cd_{1-x}Zn_xS$ Colloidal Core/Crown@alloyed-Shell Quantum Wells. Nanoscale 2019, 11 (1), 301–310.
31. Donegá, C. D. M. Synthesis and Properties of Colloidal Heteronanocrystals. Chem. Soc. Rev. 2011, 40 (3), 1512–1546.
32. Pietra, F.; Koole, R.; Grozema, F. C.; Prato, M.; De Trizio, L.; Baesjou, P. J.; Renaud, N.; Houtepen, A. J.; Manna, L.; Hoekstra, A. W. Tuning the Lattice Parameter of In_xZn_yP for Highly Luminescent Lattice-Matched Core/Shell Quantum Dots. ACS Nano 2016, 10 (4), 4754–4762.
33. Madelung, O. Semiconductors: Data Handbook, 3rd ed.; Springer Berlin Heidelberg: Berlin, Heidelberg, 2004.
34. Yoshikawa, A.; Matsunami, H.; Nanishi, Y. Development and Applications of Wide Bandgap Semiconductors. In Wide Bandgap Semiconductors; Springer Berlin Heidelberg: Berlin, Heidelberg, 2007; p 8.
35. Elsayed, H.; Olguín, D.; Cantarero, A.; Hernández-Calderón, I. Ab Initio Structural and Electronic Band-Structure Study of MgSe. Phys. status solidi B 2015, 252 (4), 663–669.
36. Sohel, M.; Muñoz, M.; Tamargo, M. C. Molecular Beam Epitaxial Growth and Characterization of Zinc-Blende ZnMgSe on InP (001). Appl. Phys. Lett. 2004, 85 (14), 2794–2796.
37. Kirkwood, N.; De Backer, A.; Altantzis, T.; Winckelmans, N.; Longo, A.; Antolinez, F. V.; Rabouw, F. T.; De Trizio, L.; Geuchies, J. J.; Mulder, J. T.; Renaud, N.; Bals, S.; Manna, L.; Houtepen, A. J. Locating and Controlling the Zn Content in In(Zn)P Quantum Dots. Chem. Mater. 2020, 32 (1), 557–565.
38. Ramasamy, P.; Kim, N.; Kang, Y.-S.; Ramirez, O.; Lee, J.-S. Tunable, Bright, and Narrow-Band Luminescence from Colloidal Indium Phosphide Quantum Dots. Chem. Mater. 2017, 29 (16), 6893–6899.
39. Li, L. S.; Pradhan, N.; Wang, Y.; Peng, X. High Quality ZnSe and ZnS Nanocrystals

Formed by Activating Zinc Carboxylate Precursors. Nano Lett. 2004, 4 (11), 2261–2264.

40. Boldt, K.; Schwarz, K. N.; Kirkwood, N.; Smith, T. A.; Mulvaney, P. Electronic Structure Engineering in ZnSe/CdS Type-II Nanoparticles by Interface Alloying. J. Phys. Chem. C 2014, 118 (24), 13276–13284.
41. Mirzai, H.; Nordin, M. N.; Curry, R. J.; Bouillard, J.-S.; Zayats, A. V.; Green, M. The Room Temperature Phosphine-Free Synthesis of near-Infrared Emitting HgSe Quantum Dots. J. Mater. Chem. C 2014, 2 (12), 2107–2111.
42. Wegner, K. D.; Pouget, S.; Ling, W. L.; Carrière, M.; Reiss, P. Gallium – a Versatile Element for Tuning the Photoluminescence Properties of InP Quantum Dots. Chem. Commun. 2019, 55 (11), 1663–1666.
43. Carević, M. V.; Čomor, M. I.; Mitrić, M. N.; Barudžija, T. S.; Ahrenkiel, S. P.; Abazović, N. D. The Influence of Reaction Media on $CdIn_2S_4$ and $ZnIn_2S_4$ Nanocrystallite Formation and Growth of Mesocrystal Structures. CrystEngComm 2015, 17 (44), 8492–8499.
44. Hahm, D.; Chang, J. H.; Jeong, B. G.; Park, P.; Kim, J.; Lee, S.; Choi, J.; Kim, W. D.; Rhee, S.; Lim, J.; Lee, D. C.; Lee, C.; Char, K.; Bae, W. K. Design Principle for Bright, Robust, and Color-Pure InP/$ZnSe_xS_{1-x}$/ZnS Heterostructures. Chem. Mater. 2019, 31 (9), 3476–3484.
45. Cho, E.; Kim, T.; Choi, S.; Jang, H.; Min, K.; Jang, E. Optical Characteristics of the Surface Defects in InP Colloidal Quantum Dots for Highly Efficient Light-Emitting Applications. ACS Appl. Nano Mater. 2018, 1 (12), 7106–7114.
46. Grabolle, M.; Spieles, M.; Lesnyak, V.; Gaponik, N.; Eychmüller, A.; Resch-Genger, U. Determination of the Fluorescence Quantum Yield of Quantum Dots: Suitable Procedures and Achievable Uncertainties. Anal. Chem. 2009, 81 (15), 6285–6294.

Appendix 4.1

Core Synthesis Scaled Up

A fair comparison of the influence of different shells on the optical properties of InZnP QD cores is most correct if for all shells, the same core sample is used. Therefore, we scaled up the QD core synthesis 6 or 8 times, and analyzed whether the optical properties of the cores changed due to scaling up. As can be seen in Figure A4.1, the optical properties can deviate slightly (*e.g.* absorbance peak position), but all spectra showcase that InZnP QD cores have been grown with similar optical features, facilitating comparing the influence of the different shell materials grown.

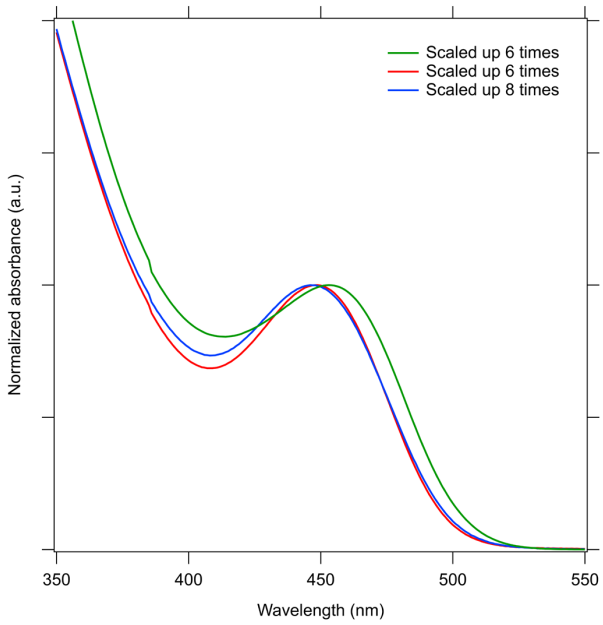


Figure A4.1. Absorbance spectra of different batches of synthesized InZnP core QDs. The batches are scaled up 6 or 8 times compared to the synthesis protocol.

Appendix 4.2

Necessity of Purifying Cores Before Shell Growth

Continuing the shell growth directly after the core synthesis is finished reduces potential exposure of the cores with, among others, oxygen and water from the air. To analyze if it is possible to grow core-shell QDs without washing the cores with anti-solvents, yet retaining the same optical properties as with washed cores, a shelling was performed directly after finishing the core synthesis. As shown in Figure A4.2, a large red-shift and significant defect emission is observed from the absorbance and emission spectra when the cores are not washed on beforehand. With these results, we conclude that the cores, understandably, first have to be purified in order to remove any unreacted precursors from the initial core synthesis.

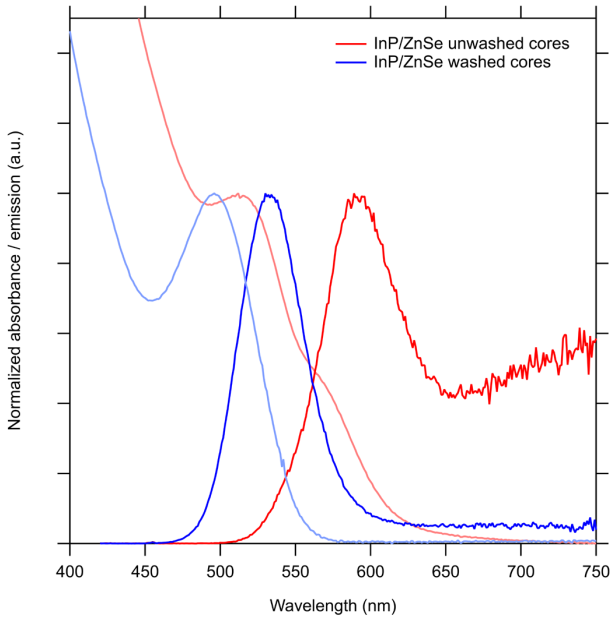


Figure A4.2. Absorbance and emission spectra of InP/ZnSe core/shell QDs for shell growth on washed and unwashed cores. The double peak in the absorbance spectrum and the increased defect emission of the unwashed sample indicate secondary nucleation of shell precursors with unreacted core precursors, which is detrimental to the quality of the core/shell QDs.

Appendix 4.3

Growth of ZnMgSe Shells Using Stearate Precursors

We attempted to synthesize ZnMgSe shells on InP QDs using stearate-precursors, directly following the protocol of Ramasamy *et al.*[38] As shown in Figure A4.3, although still strongly luminescent, the main difference is an increase of the defect emission when using Mg-stearate. We attribute the strong luminescence to the passivation of the core QD with ZnSe solely, and relate the increase of defect emission to the addition of Mg-stearate. Therefore, in agreement with the ED shown in Appendix 4.4, we concluded that other precursors are necessary to grow ZnMgSe.

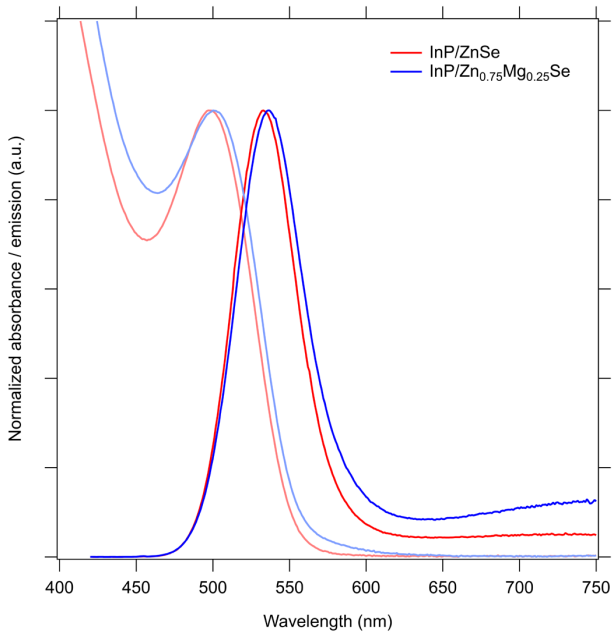


Figure A4.3. Absorbance and emission spectra of InP/ZnMgSe core/shell QDs synthesized following the procedure of Ramasamy *et al.*[38] The use of magnesium stearate as a shell precursor does not improve the quality of the QDs, but negatively affects the emission by an increased fraction of defect emission.

Appendix 4.4

Electron Diffraction on ZnMgSe From Stearate Precursors

To analyze whether ZnMgSe was grown on the InP/ZnMgSe QDs shown in Appendix 4.3, we synthesized ZnSe and ZnMgSe NCs (without InP QD core), in order to analyze if a difference in lattice parameter could be found. In agreement with the observations and conclusions displayed in Appendix 4.3, we find that the lattice parameters of the ZnSe and ZnMgSe NCs are identical (Figure A4.4). Therefore, indeed, it seems more likely that solely ZnSe has been grown, without the incorporation of Mg. As we attributed this to a too low reactivity of the Mg-precursor, we used organometallic precursors which have a significantly higher reactivity.

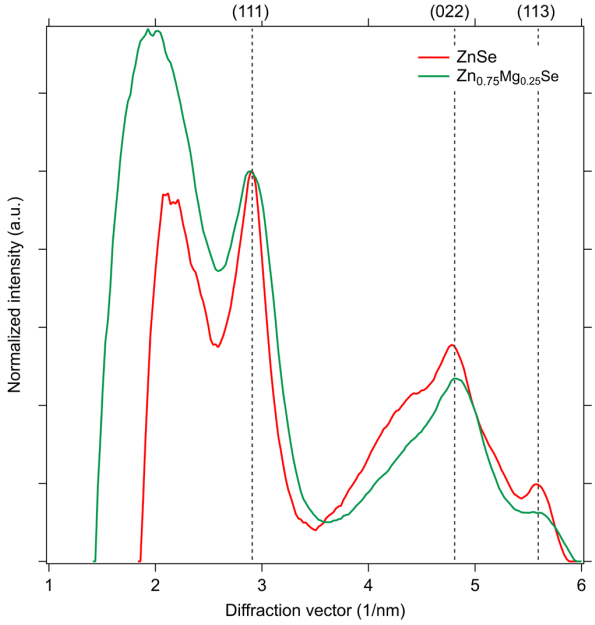


Figure A4.4. Electron diffractogram of ZnMgSe NCs synthesized with metal stearate precursors. The addition of magnesium stearate does not change the lattice parameter of the synthesized material, hence the addition of magnesium stearate does not lead to the expected lattice expansion (which would be indicated by a shift of the signals to lower diffraction vector values). The diffraction patterns of both materials suggest they possess the zinc blende crystal structure.

Appendix 4.5

TEM Images of Zn(Mg)Se Grown With Organometallic Precursors

We used TEM to analyze if Zn(Mg)Se NCs were growth when using organometallic precursors instead of stearate precursors. As shown in Figure A4.5a, ZnSe NCs are observed. When $Zn_{0.50}Mg_{0.50}Se$ NCs were imaged, no NCs but solely a large macrostructure of the material was found (Figure A4.5b and c). This indicated that, by addition of the Mg-component, the susceptibility towards degradation increased significantly.

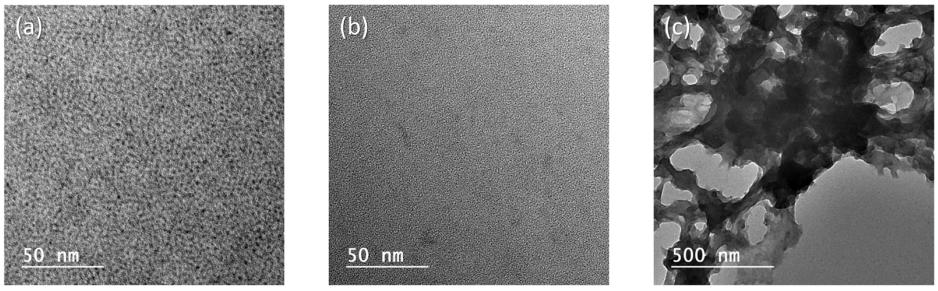


Figure A4.5. TEM images of (a) ZnSe and (b) $Zn_{0.50}Mg_{0.50}Se$ (b, c) NCs without protective ZnS shell. The ZnSe NCs are stable towards the purification method and therefore distinguishable in the image. The $Zn_{0.50}Mg_{0.50}Se$ NCs rapidly degraded, creating a macrostructure of decomposed NCs and residual precursors.

Appendix 4.6

Stabilizing Zn(Mg)Se Nanocrystals With a ZnS Shell

In order to analyze the Zn(Mg)Se NCs, a protective ZnS shell was grown around the NC cores. As shown in Figure A4.6, the NCs are much less susceptible to degradation. Due to the protective shell, these samples could be analyzed using XRD and EDX (Figure 4.2 and Appendix 4.7).

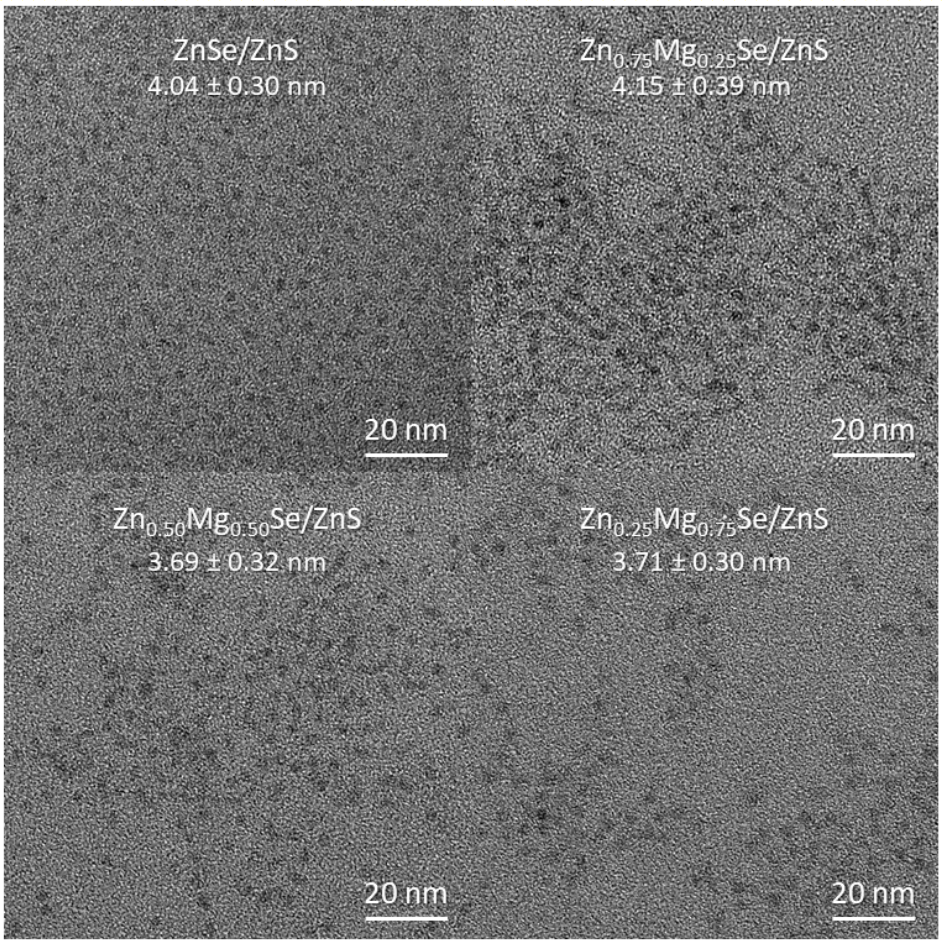


Figure A4.6. TEM images of Zn(Mg)Se NCs with protective ZnS shells. The addition of the ZnS shell made it possible to purify and image the NCs.

Appendix 4.7

EDX Elemental Analysis on Zn(Mg)Se/ZnS Nanocrystals

To confirm if Mg is indeed incorporated in the ZnMgSe NCs when organometallic precursors are used, and in what fraction it is incorporated, we used EDX analysis. As shown in Figure A4.7, both Zn and Mg are observed in a washed NC sample, indicating that Mg is indeed present in the materials. Note that the fraction of Mg is lower than the feed fraction in all cases, and that (possibly due to simplifications in the analysis), the fraction of Mg in the 75% sample is lower than that of the 50% sample. This is due to a correction of the Zn that is present in the ZnS shell.

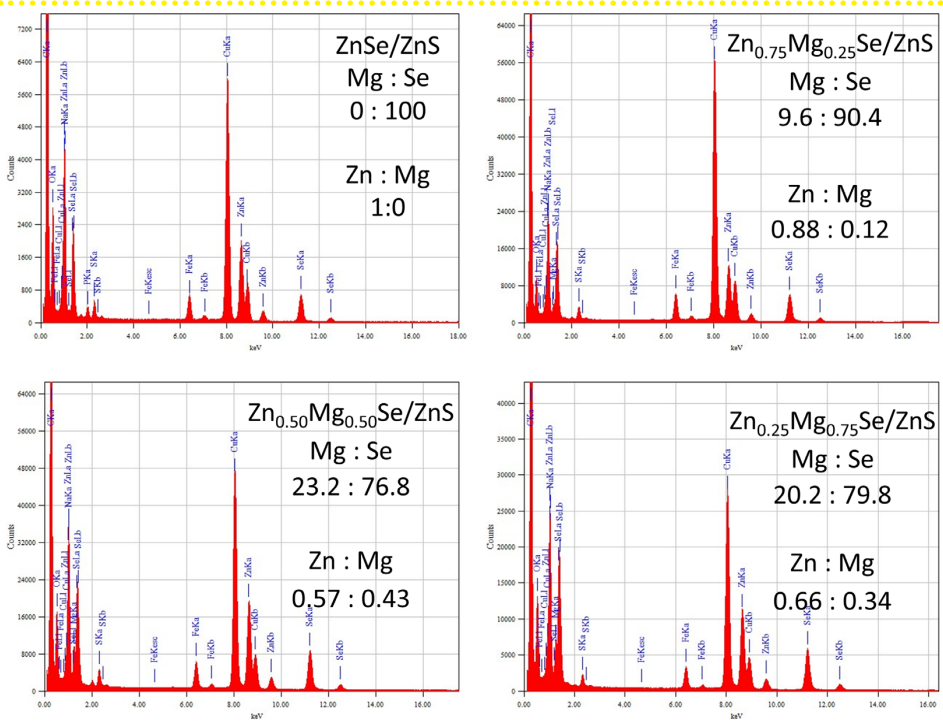


Figure A4.7. EDX analysis on the Zn(Mg)Se/ZnS NCs, indicating that in all ZnMgSe samples, Mg is indeed incorporated in the material. The Mg fraction in the material is in all cases lower than the Mg fraction in the feed. To determine the Zn:Mg ratio in the core, the approximation was made that the metal to selenium ratio is 1:1 for the ZnMgSe core.

Appendix 4.8

XPS on InZnP/ZnMgSe Core/Shell Quantum Dots

In addition to the values obtained from ICP, XPS measurements on InZnP/ZnMgSe were also performed to measure the Mg-content in the samples, and the corresponding Se:Mg ratio of the shell. The values are presented in Figure 4.3f, which originate from the spectra shown in Figure A4.8.

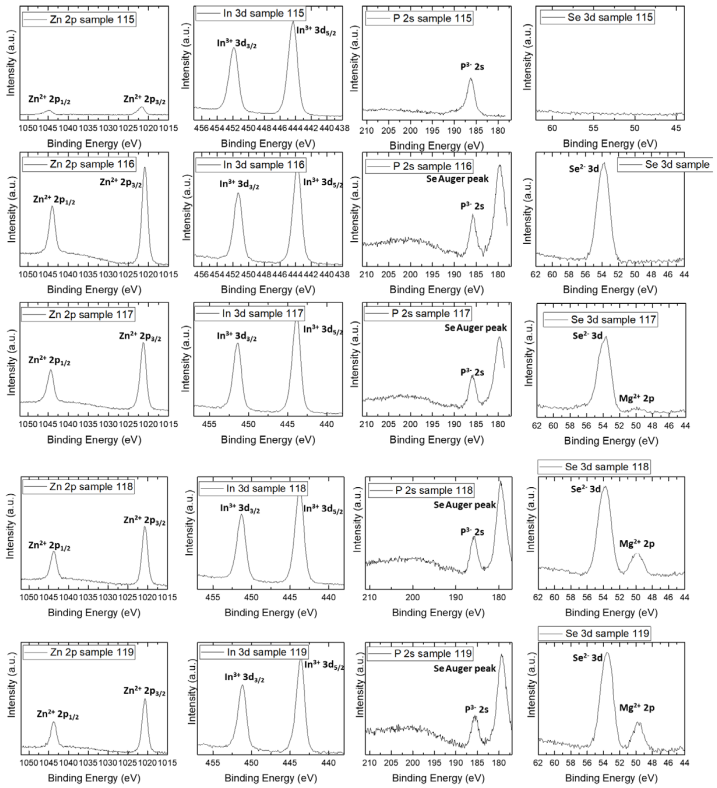


Figure A4.8. XPS data indicating an increasing Mg:Se ratio when increasing the Mg feed fraction.

Appendix 4.9

XRD on Thin-Shelled InZnP/ZnMgSe Quantum Dots

XRD measurements, in an attempt to measure the change of lattice parameter of the ZnMgSe shells, did not show a measurable difference, as shown in Figure A4.9. As the XRD is dominated by the signal of the core QDs, we decided to synthesize thicker shelled QDs (shown in Figure 4.4) for the same analysis.

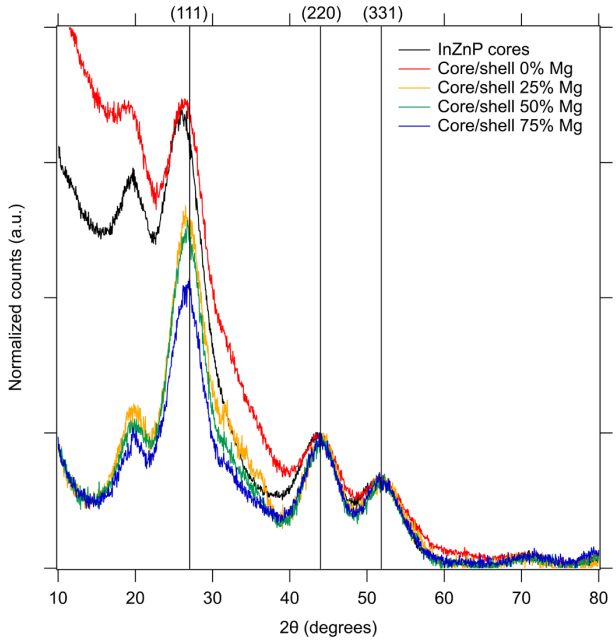


Figure A4.9. XRD diffractograms of InP/ZnMgSe QDs with a thin ZnMgSe shell and no ZnS shell (used for ICP and XPS) had a too thin shell to be measured by XRD. For the ZnSe shell, only the InP core lattice parameter is visible. For the ZnMgSe shells, the results were inconclusive. Therefore, thick shelled InP/ZnMgSe/ZnS QDs were used for the XRD analysis.

Appendix 4.10

HR-STEM Imaging of an InZnP/ZnMgSe Quantum Dot

In order to identify if the successful growth of ZnMgSe around the InZnP QDs could be measured from their lattice parameters directly, HR-STEM images were made of InZnP/ZnMgSe QDs. The image shown in Figure A4.10 represents the best image obtained. Due to the high instability of these QDs under the electron beam, we have not further used this technique for the analysis. We do observe the zinc blende crystal structure, showcasing that the ZnMgSe indeed grows in the correct crystal structure.

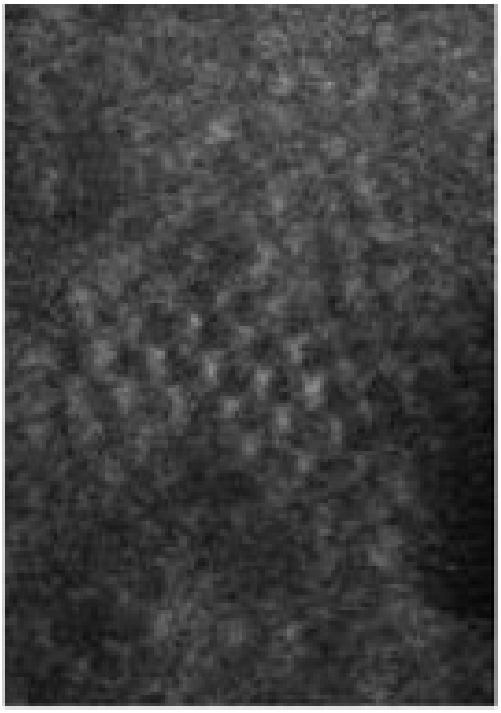


Figure A4.10. HR-STEM image of an InZnP/ZnMgSe QD, showing a zinc blende crystal structure. The field of view is 4.0 × 5.7 nm.

Appendix 4.11

Reproducibility of Shell Growth

Especially for the qualitative comparisons in this chapter, it is important to check the reproducibility of the shell growth itself. As shown in Figure A4.11, the emission spectra are practically identical per material made, and both samples shown the same reduction of FWHM when Mg is incorporated in the middle shell.

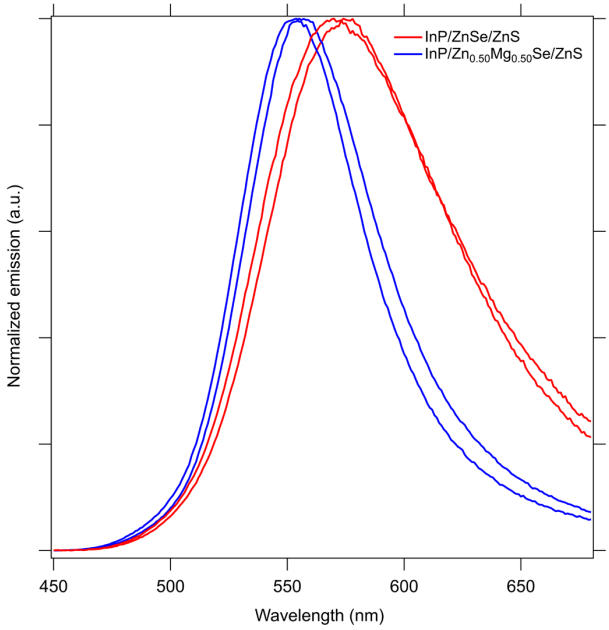


Figure A4.11. Emission spectra of different ZnSe and ZnMgSe shell syntheses on the same core batch, indicating the reproducibility of the improved optical properties for ZnMgSe shells compared to the ZnSe shells.

Appendix 4.12

Correlation Between FWHM and Stokes Shift

Figure A4.12 shows how the FWHM of the emission relates to the stokes shift of the emission peak. Although not fully conclusive, there seems to be a relationship between the reduction of the FWHM and the reduction of the Stokes shift.

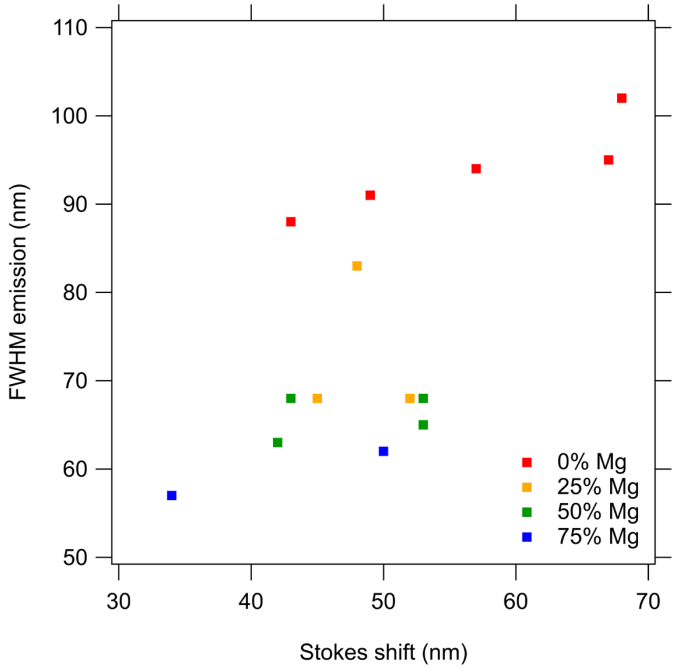
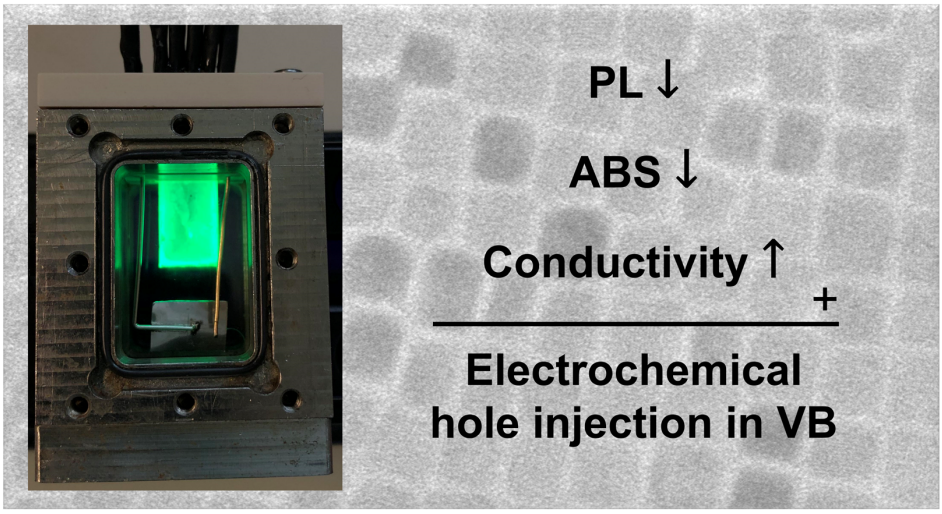


Figure A4.12. Correlation between the FWHM of the emission peak and the Stokes shift. Both decrease with increasing Mg fraction in the shell.

5

Chapter 5

Electrochemical p-Doping of $CsPbBr_3$ Perovskite Nanocrystals



Lead halide perovskite nanocrystals have drawn attention as active light-absorbing or -emitting materials for opto-electronic applications due to their facile synthesis, intrinsic defect tolerance, and color-pure emission ranging over the entire visible spectrum. To optimize their application in, *e.g.*, solar cells and light-emitting diodes, it is desirable to gain control over electronic doping of these materials. However, predominantly due to the intrinsic instability of perovskites, successful electronic doping has remained elusive. Using spectro-electrochemistry and electrochemical transistor measurements, we demonstrate here that $CsPbBr_3$ nanocrystals can be successfully and reversibly p-doped *via* electrochemical hole injection. From an applied potential of ~0.9 V *vs.* NHE, the emission quenches, the band edge absorbance bleaches, and the electronic conductivity quickly increases, demonstrating the successful injection of holes into the valence band of the $CsPbBr_3$ nanocrystals.

This chapter is based on: Jence T. Mulder, Indy du Fossé, Maryam Alimoradi Jazi, Liberato Manna, Arjan J. Houtepen. ACS Energy Lett. 2021, 6, 7, 2519–2525.

5.1 Introduction

Since the discovery of lead halide perovskite nanocrystals (NCs) in 2014,[1] these materials have been investigated as candidates for downconversion phosphors,[2–4] absorber layers in solar cells,[5–7] and emitting layers in light-emitting diodes (LEDs).[8–14] Important advantages of perovskite NCs are their facile synthesis[15–18] and their intrinsic defect tolerance.[19–24] As with all semiconductor materials, controlling the carrier density *via* electronic doping is key to tailoring the optoelectronic properties and implementation in devices.[25,26] This could allow, for instance, rational design of pn junction LEDs[27–29] or low threshold lasers.[30]

However, electronic doping is often challenging, and effects like doping compensation or self-purification can prevent control over the carrier concentration.[31,32] Especially for perovskites, which are complex compound semiconductors with a low stability, changing the Fermi level *via* doping could have many effects, including the decomposition of the material itself. As a result, electronic doping of perovskites, and perovskite NCs, has remained a challenge.[33] Some works have reported the use of, *e.g.*, Ag as a substitutional dopant,[34] but this resulted in only mild p-doping (Fermi level still 0.6 eV above the VB edge). In addition, incorporation of impurities generally has detrimental effects on the structural and electronic properties of the NCs.[26] Use of external dopants, such as charge-transfer complexes, has the advantage of not introducing impurities into the crystal.[35,36] However, this has also resulted in only mild p-doping, with an increase of p-type conductivity of roughly a factor of 2 compared to undoped films.[35]

A much higher extent of charging with external dopants is possible for semiconductor films that are permeable to electrolyte ions by means of electrochemical electron or hole injection. The electrolyte ions act as external dopants, without compromising the structure of the semiconductor material, and without introducing dopant energy levels in the bandgap, as has been demonstrated for, *e.g.*, quantum dots,[37–41] conducting polymers,[42,43] and transition metal dichalcogenides.[44,45] Further advantages of electrochemical doping are that the Fermi level can be controlled by the applied potential and that charge injection is reversible. Electrochemical doping of perovskite NCs, however, has been challenging because the NCs can readily undergo electrochemical decomposition reactions. For instance, the application of negative potentials easily results in cathodic decomposition *via* lead ion reduction, an effect that we confirm here.[46] As a result, previous reports on the electrochemistry of perovskite NCs[47] and perovskite thin films[46] have not yet proven successful n- or p-doping.

Here we report reversible electrochemical p-doping of $CsPbBr_3$ perovskite NCs. First, we use spectro-electrochemistry to investigate the optical and electronic properties of $CsPbBr_3$ perovskite NCs as a function of electrochemical potential. While potentials more negative than −0.6 V *vs.* NHE (N.B.: All potentials reported in this work are referenced *vs.* NHE.) result in irreversible changes in the optical properties due to Pb^{2+} reduction before electrons can be injected into the conduction band (CB), the changes at positive potentials are much more controllable and reversible. At potentials more positive than +0.9 V, we observe reversible bleaching of the band edge absorption and quenching of the photoluminescence (PL). Electrochemical transistor measurements indicate a concomitant reversible increase in electronic conductivity, indicating that we can reversibly p-dope the

NCs by hole injection into the valence band (VB). In accordance with these experimental results, density functional theory (DFT) calculations demonstrate that injected holes remain delocalized in the VB, whereas electron injection leads to charge localization on Pb^{2+}, confirming the much higher stability of $CsPbBr_3$ NCs at positive than at negative potentials.

5.2 Spectro-Electrochemical Measurements on $CsPbBr_3$ Nanocrystals

The $CsPbBr_3$ NCs used in this work were synthesized by the method of Imran *et al.*[48] (see Experimental Methods), which employs benzoyl bromide as the halide source. This synthesis method was chosen over the method of Protesescu *et al.*[49] (used by previous work[46,47]) which uses lead bromide as the halide source, as the NCs synthesized with benzoyl bromide are not halide poor. The halide-rich conditions result in a larger fraction of oleylammonium ions, bound to bromide ions on the NC surface, which leads to a high photoluminescence quantum yield and improved resistance to washing.[48] The NCs have an average size of 10 nm, a band edge absorption at ~505 nm, and a PL maximum at 511 nm (see Figures A5.1 and A5.2). NC films were drop-cast on ITO substrates or interdigitated gold electrodes, with 1,8-octanedithiol as cross-linking ligands (see Experimental Methods for details). As shown in Figure A5.1, this resulted in highly luminescent NC films, and the fabrication of the films did not affect the absorption and emission spectra or the size or shape of the NCs. Subsequently, the absorption and PL of the NC electrodes were measured while varying the potential *via* cyclic voltammetry (CV, see Experimental Methods for details). The CV started at the open-circuit potential (V_{OC}) of −0.1 V *vs*. NHE (from here on, the reference "*vs*. NHE" will be omitted) and was first scanned to more positive potentials (scan rate 20 mV/s). As shown in Figure 5.1a, the CV features a significant irreversible anodic current at potentials >0.6 V, probably due to background currents, either with residual impurities such as water or with ligands or the perovskite material itself (*vide infra*). We therefore turn to spectro-electrochemical measurements to get more insight into the effect of the positive potential on the optical properties of the NCs. As can be seen in Figure 5.1b, the PL starts to decrease at potentials above +0.7 V, and at +1.2 V the PL is reduced to 84% of its initial value. However, unlike the current in the CV measurement, the PL decrease is reversible, returning to ~98% of its initial intensity in the reverse scan (inset of Figure 5.1c). The reversible reduction of the PL intensity could indicate hole injection into the VB, as this would give rise to Auger recombination of the positive trions that form after light absorption. However, a change of the PL intensity could also be related to filling of in-gap trap states or the formation of new traps due to electrochemical surface reactions.[50,51] Therefore, reversible PL quenching alone does not prove hole injection, and we turn to changes in the optical absorption and conductivity to further investigate what happens.

Figure 5.1d shows the differential absorbance of the NC electrode as a function of the applied potential. An increase or decrease of the absorbance, compared to the absorbance at V_{OC}, is marked by red and blue colors, respectively. In Figure 5.1d, a small bleach of the band edge absorption can be observed for potentials above +0.9 V. As also displayed in Figure 5.1e, this bleach is reversible and disappears again upon lowering the potential below +0.9 V (see inset), indicating that the feature is not due to the irreversible degradation of the NC electrode. In contrast to the quenching of the PL, a band edge absorption bleach

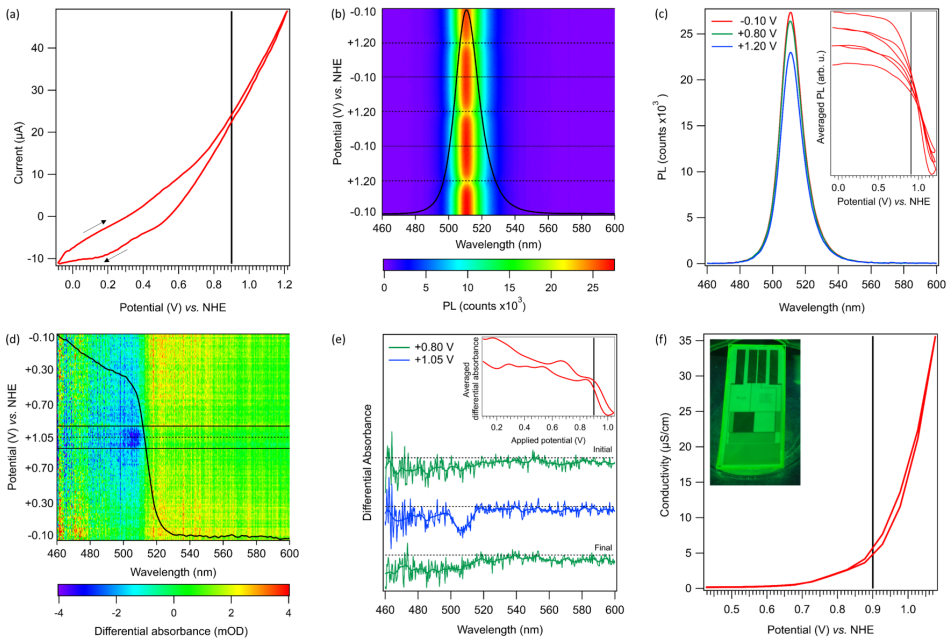


Figure 5.1. (a) CV of a $CsPbBr_3$ NC electrode (scan speed 20 mV/s). The estimated VB edge position is marked by the black line. (b) PL of a NC electrode as a function of the applied potential during three CV scans ranging from −0.10 to +1.20 V. Hole injection into the VB edge of the NCs, starting at +0.9 V, quenches the PL, which largely recovers when the applied potential is lowered to below +0.9 V. (c) PL spectra of the NC electrode shown in (b) at −0.10, +0.80, and +1.20 V during the first scan. Inset: the averaged PL between 500 and 520 nm as a function of applied potential, featuring a sharp decrease in intensity once the VB edge is reached, followed by nearly full recovery. (d) Differential absorbance of a NC electrode as a function of the applied potential, ranging from −0.10 to +1.05 V. The initial absorption spectrum is plotted in black. (e) Differential absorbance spectra at +0.80 and +1.05 V, characterized by a reversible bleach of the band edge absorption feature. Inset: differential absorbance at the band edge (averaged between 500 and 510 nm). (f) The conductivity of a NC film over the applied potential range obtained from a source–drain potential of 50 mV between the two electrodes. Inset: the NC electrode that was used for the conductivity measurements.

cannot be caused by the formation of trap states, but results from state filling of holes in the VB.

These $CsPbBr_3$ NCs are cubes with an edge length of ~10 nm. Since the exciton Bohr radius in $CsPbBr_3$ is ~7 nm,[52–54] this implies that they are only weakly confined.[55,56] For strongly confined quantum dots it is straightforward to derive the density of injected charges from the relative change in absorption. For weakly confined systems the relation is more complex. However, in order to obtain a rough estimate of the injected hole density, we assume that a state-counting method used for quantum-confined systems still holds, so that $\langle h \rangle = g_h \times \Delta A/A_0$, where $\langle h \rangle$ is the number of holes per NC, g_h the degeneracy of the lowest VB state, ΔA the absorption bleach, and A_0 the steady-state absorption.[51] Using a VB degeneracy of 2,[51,55] and a maximum bleach of $\Delta A/A_0 = 0.1$ (see Figure A5.8), we estimate a maximum doping density of ~0.2 h^+/NC, equivalent to a hole density of

$\sim 2 \times 10^{17}$ cm^{-3}.
The hallmark of successful electronic doping of semiconductors is an increase in the electronic conductivity. Therefore, we performed electrochemical transistor measurements using a film of perovskite NCs on an interdigitated gold source–drain electrode (see Figure 5.1f). Details of the measurements are given in Appendix 5.5. Figure 5.1f plots the conductivity of the film as a function of potential in a cyclic fashion and shows a rapid increase in conductivity at +0.9 V. As was the case for the PL and the absorption, the change in conductivity with potential is reversible. The maximum conductivity that we measured was 35 µS/cm at +1.05 V. Together with the hole density of 2×10^{17} cm^{-3} estimated above, this corresponds to a hole mobility of $\sim 1 \times 10^{-3}$ $cm^2/(V \cdot s)$. Both conductivity and mobility values are reasonable for nanocrystal films with relatively long ligands, and similar to those measured with electrochemical transistor measurements on n-doped CdSe NC films.[58,59]

The combination of the spectro-electrochemical absorption and PL experiments with the electrochemical transistor measurements clearly shows that the hole concentration is varied in a controllable and reversible way, demonstrating successful electrochemical p-doping of the $CsPbBr_3$ NC films. Quantification of the VB position is most easily done by the absorption bleach, as that scales linearly with the hole concentration. For strongly confined systems, when only the HOMO level would be populated, that is relatively straightforward. However, as already stated above, for weakly confined or bulk materials with excitonic absorption, the analysis is more complicated. Therefore, we refrain from a detailed quantification and only remark that the changes in absorption have an onset around +0.9 V *vs*. NHE (= –5.4 V *vs*. vacuum), which should roughly correspond to the VB edge.

In addition to investigating p-doping of $CsPbBr_3$ NCs, we also applied negative potentials to investigate n-doping. In accordance with previous reports by Samu *et al.*,[46] we observed that injected electrons were lost to Pb^{2+} reduction before the CB edge could be reached (see Figures A5.9 and A5.10). This caused rapid irreversible loss of the PL, irreversible changes of the absorption, and the formation of a clearly visible metallic Pb^0 layer, as confirmed by XRD and XPS measurements (Figures A5.11 and A5.12). Hence, for cathodic potentials, it seems impossible to inject electrons into the CB in a reversible way.

5.3 Simulating Electrochemical Doping Using DFT

To understand the difference between n- and p-doping, we performed DFT calculations on the charging of a $CsPbBr_3$ NC, as summarized in Figure 5.2. We built a cubic $CsPbBr_3$ NC model, following the approach of Ten Brinck *et al.*[60] As shown in Figure 5.2-ii, the intrinsic (*i.e.*, charge balanced) model NC has a clean bandgap and a HOMO that is delocalized over the entire system. Electrochemical injection of one hole into the system is achieved by adding a negative PF_6^- counterion so that the entire system retains charge neutrality.[61] As can be seen in Figure 5.2a-i, this does not significantly affect the electronic structure of the NC: the HOMO remains delocalized over the NC (Figure 5.2a-i) and is now singly occupied due to the presence of a hole; no localized states appear in the density of states (DOS) (Figure 5.2b-i). In contrast, injection of an electron (by adding a NH_4^+ counterion) introduces a singly populated localized state on a single lead ion (Figure 5.2a-iii) that

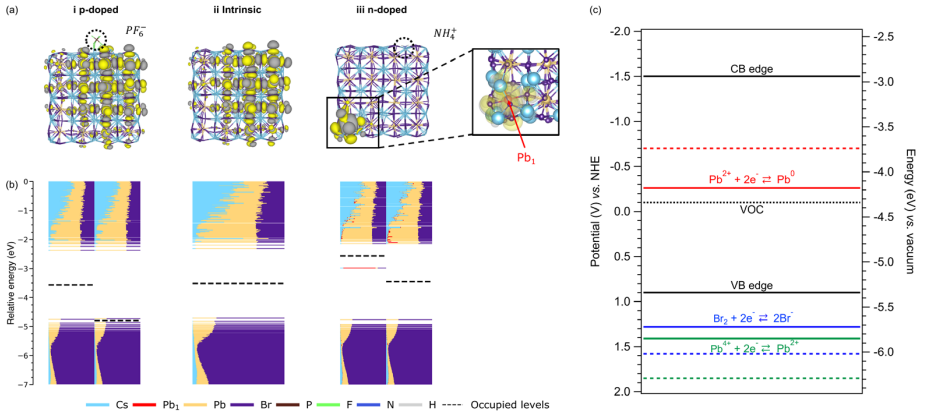


Figure 5.2. Effect of doping on the electronic structure of a $CsPbBr_3$ NC. (a) Contour plots of the (α−) HOMO at 0.005 $e^-/bohr^3$ for p-doped, n-doped, and intrinsic $CsPbBr_3$ NCs. The p-doped (n-doped) NC has been charged with one hole (electron), compensated by a PF_6^- (NH_4^+) counterion. (b) DOS of each NC, where every line corresponds to a molecular orbital (MO). The relative contributions of specific atoms or elements to each MO are given by the length of the colored line segments. MOs are occupied below the dotted line and empty above it. The doped systems have an odd number of electrons and are computed as spin-unrestricted. The spin-up and spin-down orbitals are plotted separately on the left and right side of the graph, respectively. (c) Energy diagram, indicating the energy level of the VB edge (+0.9 V, as found in the previous section), CB edge (−1.5 V, obtained by adding the optical bandgap to the VB edge position), and V_{OC} (−0.1 V) of the measured $CsPbBr_3$ NCs. Red, blue, and green lines are the formal potentials of various electrochemical half-reactions of Pb^{2+} and Br^- in propylene carbonate. The dashed lines indicate schematically the expected formal potentials of the cathodic and anodic decomposition reactions, shifted by $RT/nF \cdot \ln(K_{sp})$ compared to the normal lines, where in this example K_{sp} is taken to be 10^{-15} mol^5/L^5.

appears as a localized state in the bandgap (Figure 5.2b-iii). NH_4^+ was used instead of Bu_4N^+ due to its smaller size and consequently lower computational cost.[61] These results confirm that the addition of electrons immediately results in Pb^{2+} reduction. This is a form of doping compensation that prevents n-doping of the material and will result in cathodic decomposition before the Fermi level moves close enough to the CB to significantly change the electron concentration. On the other hand, the $CsPbBr_3$ NC is much less sensitive to anodic decomposition, allowing the addition of holes *via* electrochemical doping. This is in line with our experimental observation that p-doping can be performed reversibly, but that n-doping leads to Pb^{2+} reduction and cathodic decomposition.

5.4 Discussion on the Stability of Electrochemical Doping of $CsPbBr_3$

The fact that p-doping can be achieved does not imply the p-doped NCs are indefinitely stable. Samu *et al.* investigated halide perovskite thin films under anodic conditions and have not reported reversible p-doping, but rather a sequence of decomposition reactions.[46] When we performed identical experiments on $CsPbBr_3$ NCs synthesized *via* the method of Protesescu *et al.*,[49] we did not observe evidence of p-doping (Figure A5.13). This suggests that the electrochemical stability of perovskite NCs is subtle and likely dominated by the surface termination. The main difference between the NCs synthesized following Imran

et al. and Protesescu *et al.* is that the former synthesis results in a higher surface density of oleylammonium ligands (due to the bromide-rich synthesis conditions), as evidenced by a much higher colloidal stability upon washing. To illustrate our point, we show an overview of standard reduction potentials of possible decomposition reactions, as well as the CB and VB positions of the $CsPbBr_3$ NCs, in Figure 5.2c. The most likely candidate reaction for cathodic decomposition is the following:

$$CsPbBr_3 + 2e^- \rightleftarrows Pb^0 + Cs^+ + 3Br^- \quad (5.1)$$

Indeed, XPS spectra, acquired before and after application of an anodic potential (−1.46 V), show a shift of the Pb 4f XPS peaks to a lower binding energy, in agreement with the decrease of the oxidation state of Pb (Figure A5.12).

At the anodic side, we could consider bromide oxidation (reaction 5.2) or Pb^{2+} oxidation (reaction 5.3) to cause anodic decomposition:

$$CsPbBr_3 \rightleftarrows Pb^{2+} + Cs^+ + \tfrac{3}{2}Br_2 + 3e^- \quad (5.2)$$

$$CsPbBr_3 \rightleftarrows Pb^{4+} + Cs^+ + 3Br^- + 2e^- \quad (5.3)$$

XPS spectra acquired before and after application of a positive potential show no changes in the Pb 4f peaks and a shift of the Br 3d peaks to higher binding energies (Figure A5.12). This suggests that reaction 5.2 is the more relevant reaction. It also shows that, in spite of the reversible hole injection, some Br^- oxidation does take place. This probably explains the irreversible anodic current observed in the CV measurements (Figure 5.1a). Most likely Br^- oxidation occurs in parallel to, and in competition with, hole injection into the VB.

The standard reduction potentials of reactions 5.1–5.3 are related to the standard reduction potential of the free ions — $Pb^{2+} + 2e^- \rightarrow Pb^0$; $Br_2 + 2e^- \rightarrow 2Br^-$; and $Pb^{4+} + 2e^- \rightarrow Pb^{2+}$, respectively — although they are stabilized compared to those free ion reactions due to binding to the other ions in the perovskite crystal lattice. We estimated the standard reduction potentials of these latter reactions in propylene carbonate *via* CV (see Appendix 5.13). The obtained values are similar, albeit somewhat shifted, to those reported for the same reactions in water,[62] and are marked as red, blue, and green horizontal solid lines in Figure 5.2c, respectively.

As derived in Appendix 5.14, the formal reduction potential of reaction 1 is shifted by $RT/nF \cdot \ln(K_{sp})$ compared to the formal reduction potential of $Pb^{2+} + 2e^- \rightarrow Pb^0$. Here $K_{sp} = [Cs^+][Pb^{2+}][Br^-]^3$ is the solubility product of $CsPbBr_3$ in the same solvent and n is the number of electrons involved in the reaction. Similarly, the formal potentials of reactions 2 and 3 are shifted by $-RT/nF \cdot \ln(K_{sp})$ compared to the free ion reactions, with n = 3 for (5.2) and n = 2 for (5.3) (see Appendix 5.14).

This indicates that, in solvents wherein $CsPbBr_3$ is poorly soluble and K_{sp} is smaller than 1, the cathodic dissolution will occur at more negative potentials than the reduction of

free Pb^{2+} ions, and the anodic dissolution will occur at more positive potentials than the oxidation of free Br^- and free Pb^{2+}. For instance, the reported value of K_{sp} for $CsPbBr_3$ in a mixture of γ-butyrolactone (GBL) and dimethyl sulfoxide (DMSO) is ~10^{-3} mol^5/L^5, corresponding to a stabilization of ~177/n mV.[63] Propylene carbonate, the solvent used in the electrochemical experiments in the current paper, was chosen because the $CsPbBr_3$ NC films do not readily dissolve in it (unlike in, *e.g.*, DMSO), and hence the expected solubility product is much lower, and the expected stabilization greater, than in GBL/DMSO. Unfortunately, quantitative information on the solubility of $CsPbBr_3$ in propylene carbonate is, to the best of our knowledge, not available. The dashed lines in Figure 5.2c indicate schematically where the formal potential of the decomposition reactions 5.1–5.3 could lie, in this example for $K_{sp} = 10^{-15}$ mol^5/L^5.

Figure 5.2c shows that the cathodic decomposition potential of $CsPbBr_3$ lies well positive of the CB potential (unless $-RT/2F \cdot \ln(K_{sp}) < -1.25$ V, *i.e.*, $K_{sp} < 5 \times 10^{-43}$ mol^5/L^5, which seems unrealistic). This implies that the cathodic decomposition reaction will occur before electron injection into the CB, resulting in n-doping compensation through Pb^0 formation. At the anodic side, Br^- oxidation would be expected to occur well before Pb^{2+} oxidation. However, in both cases we estimate the formal potentials of the anodic decomposition to lie at more positive potentials than the VB of $CsPbBr_3$. It is interesting to note that the situation will be very different for Sn^{2+}-based perovskites. As the standard reduction potential of Sn^{4+}/Sn^{2+} in propylene carbonate lies at 0.11 V *vs.* NHE (see Appendix 5.13), oxidation of Sn^{2+} is expected to take place before Br^- oxidation and most likely before the VB is reached, making p-doping very difficult for these systems. In double perovskites, like, *e.g.*, $Cs_2AgBiBr_6$, the reduction of Ag^+ ($E^{0'}$ = 0.8 V *vs.* NHE in water)[62] and Bi^{3+} ($E^{0'}$ = 0.3 V *vs.* NHE in water)[62] will most likely prevent n-doping, while Br^- oxidation will be the limiting factor for p-doping.

The above discussion pertains to bulk $CsPbBr_3$. The initial electrochemical reactions on the surface of $CsPbBr_3$ NCs will occur at sites that are under-coordinated compared to the bulk, and hence the formal potentials of these will be less negative for surface reduction and less positive for surface oxidation, compared to the bulk formal potentials, and will likely lie between the solid and dashed lines in Figure 5.2c. Moreover, the formal potentials are also sensitive to bonds formed between ligands and surface ions.

From our measurements and the preceding discussion, it is likely that, upon moving the Fermi level to positive potentials, the VB of $CsPbBr_3$ NCs is reached before the formal potential of the anodic decomposition reactions. However, the difference in potential may be small. This suggests that the stability of p-doped $CsPbBr_3$ NCs will be sensitive to changes in surface Br– coordination (shifting the formal potential of reaction 5.2) and the solvent (affecting K_{sp}) as well as the exact position of the VB, which is known to be affected by the surface passivation.[64,65] In addition, if Br^- oxidation *via* reaction 5.2 is irreversible, the stability of p-doped $CsPbBr_3$ will be limited, since the oxidation rate will not be zero when the Fermi level is in, or near, the VB. This is in line with our observations that, over time scales of minutes, the PL of p-doped $CsPbBr_3$ decreases irreversibly and with the XPS results that show that some Br^- oxidation does take place at cathodic potentials. Increasing the stability of p-doped $CsPbBr_3$ NCs thus requires improved surface passivation strategies,

with strongly binding surfactants, to further reduce the rate of surface oxidation.

5.5 Conclusions

To summarize, we report reversible electrochemical p-doping of $CsPbBr_3$ NCs. We demonstrate that raising the applied potential above +0.9 V *vs.* NHE simultaneously quenches the PL, bleaches the band edge absorption, and significantly increases the conductivity, all consistent with charge injection in the VB edge. By combining experimental results with DFT calculations, we conclude that p-doping of $CsPbBr_3$ NC electrodes is possible, although their stability is limited due to Br^- oxidation. Increasing this stability further will require optimized surface passivation strategies. In contrast, n-doping is impossible due to facile Pb^{2+} reduction.

Experimental Methods

Materials

Lead acetate trihydrate ($Pb(CH_3COO)_2{\cdot}3H_2O$, 99.999% trace metal basis), lead nitrate ($Pb(NO_3)_2$, ≥99.95% trace metals basis), benzoyl bromide (97%), 1-octadecene (ODE, technical grade, 90%), oleic acid (OA, technical grade, 90%), toluene (anhydrous, 99.8%), methyl acetate (anhydrous, 99.5%), mercaptopropionic acid (≥99.0%), 1,8-octane dithiol (8DT, ≥97%), propylene carbonate (PC, anhydrous, 99.7%), tetrabutylammonium hexafluorophosphate ($TBAPF_6$, for electrochemical analysis, ≥99.0%), ferrocene (98%) were purchased from Sigma-Aldrich. Cesium carbonate (Cs_2CO_3, Puratronic, 99.994%) and tin(II) acetate ($Sn(CH_3COO)_2$, 95%) were purchased from Alfa Aesar. Oleylamine (OLA, 80–90% C18, ≥96.0% (primary amine)) was purchased from Acros Organics. Methanol (anhydrous, max 0.003% H_2O, Seccosolv) was purchased from VWR international. ITO conductive substrates (20 Ohms/sq) were purchased from PGO GmbH.

Precursor Preparation

A large-scaled batch of metal precursors was prepared by combining 760 mg of $Pb(CH_3COO)_2{\cdot}3H_2O$ and 160 mg Cs_2CO_3 together with 50 mL ODE, 10 mL OLA and 3 mL OA. This mixture was attached to a Schlenk line and flushed 3 times with dry nitrogen. Whilst stirring, the mixture was then heated to 120 °C for one hour under a vacuum pressure of <0.2 mbar, to remove any water, oxygen and other volatile chemical species from the reaction mixture. The precursor was subsequently cooled down to room temperature, collected in nitrogen filled vials and stored in a nitrogen filled glovebox.

$CsPbBr_3$ Synthesis

The following synthesis protocol has been adapted from Imran *et al.*[48]

6.3 mL of the metal/ligand precursor solution was added to a nitrogen filled 25 mL three necked flask with a thermocouple insert, attached to a Schlenk line. Subsequently, the mixture was quickly heated to 185 °C and under vigorous stirring, 71 µL of benzoyl bromide diluted in 500 µL degassed ODE was injected into the metal precursor mixture. The mixture directly turned yellow and after exactly 10 seconds, the heating mantle was removed and the flask was quickly cooled down using an air gun. Once the mixture was at room temperature, 2 mL of anhydrous toluene was added to the reaction mixture, and

subsequently, the contents were transferred to nitrogen filled vials. The crude mixture was centrifuged at 3800 rpm for 10 minutes to get the NCs out of solution. After centrifugation, the supernatant was discarded in a glove box, and the solid pellet was redispersed in 2 mL of anhydrous toluene.

To remove most of the residual excess precursors and solvents, the NC solution was purified by the addition of 2 mL of methyl acetate to destabilize the dispersion. The cloudy solution was centrifuged at 6000 rpm for 10 minutes and after discarding the supernatant, the NC pellet was finally redispersed in 4 mL of anhydrous toluene.

$CsPbBr_3$ NC Electrode Fabrication

ITO conductive substrates were cleaned by rinsing them thoroughly with isopropanol. Subsequently, the substrates were added to a methanolic solution of 1 $_{vol}$% MPA, to functionalize the oxide layer with surface thiol groups. After a day in the MPA solution, the substrates were submerged in clean methanol to remove excess MPA. On the functionalized, dry substrates 50 µL of NC solution was drop-cast and the toluene was evaporated over time without application of a vacuum or heating. To cross-link the NCs, the dry films were submerged in a 0.1 M 8DT solution in methyl acetate. Subsequently, the film was dipped in clean methyl acetate to remove residual ligands. To counter NC degradation, the films were directly put under vacuum, to remove any residual solvents. The films were thereafter stored in the glovebox until use.

For the preparation of NC films on interdigitated gold electrodes, the electrodes were cleaned with technical grade acetone and subsequently, in a glove box, the films were drop casted by adding 100 µL of NC solution on the substrate. After all the solvent evaporated, a second 100 µL of NC solution was drop casted. Once all solvent evaporated, the NC film was cross-linked in the same manner as the ITO-based electrode films.

Spectro-Electrochemical and Conductance Measurements

All electrochemical and spectro-electrochemical measurements were performed in a nitrogen-filled glovebox with H_2O and O_2 levels of respectively ≤0.5 ppm and ≤0.1 ppm. All measurements were performed with an Autolab PGSTAT128N potentiostat with a bipotentiostat BA module. The electrochemical cell consisted of a cuvette, containing an electrolyte (0.1 M $TBAPF_6$ in PC) in which the NC working electrode (WE), a Ag pseudo-reference electrode (RE) and a Pt sheet as a counter electrode (CE) were submerged. The potential was scanned at 10 or 20 mV/s in the positive/negative direction until charge was injected into the HOMO of the NCs. In general, the CVs were repeated three times. Directly after the measurements, the Ag pseudo-reference electrode was calibrated with a ferrocene/ferrocenium couple.

The absorbance and photoluminescence (PL) changes in the spectro-electrochemical measurements were measured as a function of the applied electrochemical potential with a fibre-based UV–vis spectrometer (Ocean Optics USB2000) using an Ocean Optics DH 2000 lamp as a light source.

Source-drain electronic conductance measurements were performed by the use of home-built gold interdigitated electrodes (see insert in Figure 5.1f, main text). During the measurements, two working electrodes were used in a source-drain configuration; the source-drain gap width was 25 μm while the gap length was 8.825 mm. The potential is stepped, and after the system reached equilibrium, the potential of WE1 was scanned in a CV manner around the fixed potential of WE2 with a difference of ±25 mV. The slope of the current *versus* the potential gives the conductance, G.

Characterization Methods

TEM images were acquired using a JEOL JEM1400 transmission electron microscope operating at 120 keV. XRD measurements were performed with a Bruckner D8 ADVANCE diffractometer (Co Kα, λ = 0.1789 nm). Profilometry measurements were performed with a Veeco DekTak 8 stylus profiler.

DFT Simulations

Geometry optimizations have been carried out at the DFT level with a PBE exchange-correlation functional[66] and double-ζ basis set, as implemented in the CP2K quantum chemistry software package.[67] Relativistic effects have been taken into account through the use of effective core-potentials. The calculations of the systems with an odd number of electrons were performed without spin restrictions. Geometry optimizations were carried out at 0 K in the gas phase.

Other Investigated Measurement Conditions

A number of other parameters were tested, but resulted in less optimal conditions, generally resulting in a faster degradation of the NC film

Crosslinking Ligands and Other Methods

Crosslinking has been tried with 1,7-diaminoheptane and fumaric acid. Furthermore, film stabilization has been tried by annealing at 80 °C. In the end, a ligand exchange with octane dithiol has shown to yield the most stable films while also retaining measurable PL.

Electrolyte Salt

$TBAClO_4$, $TBABF_4$ and $TBAPF_6$ were tested as electrolyte in all of the below mentioned solvents. $TBAPF_6$ was chosen, as the films showed to be stable and furthermore it has the largest electrochemical window.[68]

Electrolyte Solvent

Apart from propylene carbonate, we also tried to do the electrochemical measurements in DCM, methyl acetate and acetonitrile. Propylene carbonate as solvent, with $TBAPF_6$ as electrolyte, showed to be the most stable.

References

1. Schmidt, L. C.; Pertegás, A.; Gonzalez-carrero, S.; Malinkiewicz, O.; Agouram, S.; Espallargas, G. M.; Bolink, H. J.; Galian, R. E.; Pérez-Prieto, J.; González-carrero, S. Non-Template Synthesis of $CH_3NH_3PbBr_3$ Perovskite Nanoparticles. J. Am. Chem. Soc. 2014, 136, 850–853.
2. Adhikari, G. C.; Zhu, H.; Vargas, P. A.; Zhu, P. UV-Green Emission from Organolead Bromide Perovskite Nanocrystals. J. Phys. Chem. C 2018, 122 (26), 15041–15046.
3. Srivastava, A. K.; Zhang, W.; Schneider, J.; Halpert, J. E.; Rogach, A. L. Luminescent Down-Conversion Semiconductor Quantum Dots and Aligned Quantum Rods for Liquid Crystal Displays. Adv. Sci. 2019, 6 (22), 1–20.
4. Zou, T.; Liu, X.; Qiu, R.; Wang, Y.; Huang, S.; Liu, C.; Dai, Q.; Zhou, H. Enhanced UV-C Detection of Perovskite Photodetector Arrays via Inorganic $CsPbBr_3$ Quantum Dot Down-Conversion Layer. Adv. Opt. Mater. 2019, 7 (11), 1–8.
5. Yuan, J.; Hazarika, A.; Zhao, Q.; Ling, X.; Moot, T.; Ma, W.; Luther, J. M. Metal Halide Perovskites in Quantum Dot Solar Cells: Progress and Prospects. Joule 2020, 4 (6), 1160–1185.
6. Zhou, F.; Li, Z.; Chen, H.; Wang, Q.; Ding, L.; Jin, Z. Application of Perovskite Nanocrystals (NCs)/Quantum Dots (QDs) in Solar Cells. Nano Energy 2020, 73, 104757.
7. Kim, Y.-C.; Jeong, H.-J.; Kim, S.-T.; Song, Y. H.; Kim, B. Y.; Kim, J. P.; Kang, B. K.; Yun, J.-H.; Jang, J.-H. Luminescent Down-Shifting $CsPbBr_3$ Perovskite Nanocrystals for Flexible Cu(In,Ga)Se_2 Solar Cells. Nanoscale 2020, 12 (2), 558–562.
8. Palazon, F.; Di Stasio, F.; Akkerman, Q. A.; Krahne, R.; Prato, M.; Manna, L. Polymer-Free Films of Inorganic Halide Perovskite Nanocrystals as UV-to-White Color-Conversion Layers in LEDs. Chem. Mater. 2016, 28 (9), 2902–2906.
9. Yan, F.; Tan, S. T.; Li, X.; Demir, H. V. Light Generation in Lead Halide Perovskite Nanocrystals: LEDs, Color Converters, Lasers, and Other Applications. Small 2019, 15 (47), 1–15.
10. Hassan, Y.; Park, J. H.; Crawford, M. L.; Sadhanala, A.; Lee, J.; Sadighian, J. C.; Mosconi, E.; Shivanna, R.; Radicchi, E.; Jeong, M.; Yang, C.; Choi, H.; Park, S. H.; Song, M. H.; De Angelis, F.; Wong, C. Y.; Friend, R. H.; Lee, B. R.; Snaith, H. J. Ligand-Engineered Bandgap Stability in Mixed-Halide Perovskite LEDs. Nature 2021, 591 (7848), 72–77.
11. Kovalenko, M. V.; Protesescu, L.; Bodnarchuk, M. I. Properties and Potential Optoelectronic Applications of Lead Halide Perovskite Nanocrystals. Science 2017, 358 (6364), 745–750.
12. Zhang, C.; Wang, S.; Li, X.; Yuan, M.; Turyanska, L.; Yang, X. Core/Shell Perovskite Nanocrystals: Synthesis of Highly Efficient and Environmentally Stable $FAPbBr_3$/$CsPbBr_3$ for LED Applications. Adv. Funct. Mater. 2020, 30 (31), 1910582.
13. Stranks, S. D.; Snaith, H. J. Metal-Halide Perovskites for Photovoltaic and Light-Emitting Devices. Nat. Nanotechnol. 2015, 10 (5), 391–402.
14. Zhao, B.; Bai, S.; Kim, V.; Lamboll, R.; Shivanna, R.; Auras, F.; Richter, J. M.; Yang, L.; Dai, L.; Alsari, M.; She, X. J.; Liang, L.; Zhang, J.; Lilliu, S.; Gao, P.; Snaith, H. J.; Wang, J.; Greenham, N. C.; Friend, R. H.; Di, D. High-Efficiency Perovskite–

polymer Bulk Heterostructure Light-Emitting Diodes. Nat. Photonics 2018, 12 (12), 783–789.

15. Xu, B.; Wang, W.; Zhang, X.; Cao, W.; Wu, D.; Liu, S.; Dai, H.; Chen, S.; Wang, K.; Sun, X. Bright and Efficient Light-Emitting Diodes Based on MA/Cs Double Cation Perovskite Nanocrystals. J. Mater. Chem. C 2017, 5 (25), 6123–6128.
16. Lou, S.; Xuan, T.; Liang, Q.; Huang, J.; Cao, L.; Yu, C.; Cao, M.; Xia, C.; Wang, J.; Zhang, D.; Li, H. Controllable and Facile Synthesis of $CsPbBr_3$-Cs_4PbBr_6 Perovskite Composites in Pure Polar Solvent. J. Colloid Interface Sci. 2019, 537, 384–388.
17. Hassan, Y.; Ashton, O. J.; Park, J. H.; Li, G.; Sakai, N.; Wenger, B.; Haghighirad, A. A.; Noel, N. K.; Song, M. H.; Lee, B. R.; Friend, R. H.; Snaith, H. J. Facile Synthesis of Stable and Highly Luminescent Methylammonium Lead Halide Nanocrystals for Efficient Light Emitting Devices. J. Am. Chem. Soc. 2019, 141 (3), 1269–1279.
18. Wang, C.; Wang, Z.; Song, Y.; Zhang, X.; Wang, J.; Liu, P.; Cao, H.; Xu, B.; Zhao, M.; Miao, Y.; Guo, J. Facile Synthesis of Perovskite Phosphors and Nanocrystals Using Laundry Detergent by Ultra-Rapid Freezing for Light-Emitting Diodes Application. J. Lumin. 2021, 233, 117902.
19. Shamsi, J.; Urban, A. S.; Imran, M.; De Trizio, L.; Manna, L. Metal Halide Perovskite Nanocrystals: Synthesis, Post-Synthesis Modifications, and Their Optical Properties. Chem. Rev. 2019, 119 (5), 3296–3348.
20. Mandal, S.; Ghosh, S.; Mukherjee, S.; De, C. K.; Roy, D.; Samanta, T.; Mandal, P. K. Unravelling Halide-Dependent Charge Carrier Dynamics in $CsPb(Br/Cl)_3$ Perovskite Nanocrystals . Nanoscale 2021, 3654–3661.
21. Giovanni, D.; Righetto, M.; Zhang, Q.; Lim, J. W. M.; Ramesh, S.; Sum, T. C. Origins of the Long-Range Exciton Diffusion in Perovskite Nanocrystal Films: Photon Recycling vs Exciton Hopping. Light Sci. Appl. 2021, 10 (1), 2.
22. Kim, S. H.; Park, K.-D.; Lee, H. S. Growth Kinetics and Optical Properties of $CsPbBr_3$ Perovskite Nanocrystals. Energies 2021, 14 (2), 275.
23. Wang, S.; Yousefi Amin, A. A.; Wu, L.; Cao, M.; Zhang, Q.; Ameri, T. Perovskite Nanocrystals: Synthesis, Stability, and Optoelectronic Applications. Small Struct. 2021, 2 (3), 2000124.
24. Huang, H.; Bodnarchuk, M. I.; Kershaw, S. V.; Kovalenko, M. V.; Rogach, A. L. Lead Halide Perovskite Nanocrystals in the Research Spotlight: Stability and Defect Tolerance. ACS Energy Lett. 2017, 2 (9), 2071–2083.
25. Lu, C. H.; Biesold-Mcgee, G. V.; Liu, Y.; Kang, Z.; Lin, Z. Doping and Ion Substitution in Colloidal Metal Halide Perovskite Nanocrystals. Chem. Soc. Rev. 2020, 49 (14), 4953–5007.
26. Xu, L.; Yuan, S.; Zeng, H.; Song, J. A Comprehensive Review of Doping in Perovskite Nanocrystals/Quantum Dots: Evolution of Structure, Electronics, Optics, and Light-Emitting Diodes. Mater. Today Nano 2019, 6, 100036.
27. Cai, W.; Chen, Z.; Chen, D.; Su, S.; Xu, Q.; Yip, H. L.; Cao, Y. High-Performance and Stable $CsPbBr_3$ Light-Emitting Diodes Based on Polymer Additive Treatment. RSC Adv. 2019, 9 (47), 27684–27691.
28. Du, X.; Wu, G.; Cheng, J.; Dang, H.; Ma, K.; Zhang, Y. W.; Tan, P. F.; Chen, S. High-Quality $CsPbBr_3$ Perovskite Nanocrystals for Quantum Dot Light-Emitting Diodes. RSC Adv. 2017, 7 (17), 10391–10396.

29. Li, L.; Zheng, W.; Wan, Q.; Liu, M.; Zhang, Q.; Zhang, C.; Yan, R.; Feng, X.; Kong, L. $CsPbBr_3$ Nanocrystal Light-Emitting Diodes with Efficiency up to 13.4% Achieved by Careful Surface Engineering and Device Engineering. J. Phys. Chem. C 2021, 125 (5), 3110–3118.
30. Geuchies, J. J.; Brynjarsson, B.; Grimaldi, G.; Gudjonsdottir, S.; Van Der Stam, W.; Evers, W. H.; Houtepen, A. J. Quantitative Electrochemical Control over Optical Gain in Quantum-Dot Solids. ACS Nano 2021, 15 (1), 377–386.
31. Gerischer, H. On the Stability of Semiconductor Electrodes Against Photodecomposition. J. Electroanal. Chem. Interfacial Electrochem. 1977, 82 (1–2), 133–143.
32. Tsur, Y.; Riess, I. Self-Compensation in Semiconductors. Phys. Rev. B - Condens. Matter Mater. Phys. 1999, 60 (11), 8138–8146.
33. Phung, N.; Félix, R.; Meggiolaro, D.; Al-Ashouri, A.; Sousa E Silva, G.; Hartmann, C.; Hidalgo, J.; Köbler, H.; Mosconi, E.; Lai, B.; Gunder, R.; Li, M.; Wang, K. L.; Wang, Z. K.; Nie, K.; Handick, E.; Wilks, R. G.; Marquez, J. A.; Rech, B.; Unold, T.; Correa-Baena, J. P.; Albrecht, S.; De Angelis, F.; Bär, M.; Abate, A. The Doping Mechanism of Halide Perovskite Unveiled by Alkaline Earth Metals. J. Am. Chem. Soc. 2020, 142 (5), 2364–2374.
34. Zhou, S.; Ma, Y.; Zhou, G.; Xu, X.; Qin, M.; Li, Y.; Hsu, Y. J.; Hu, H.; Li, G.; Zhao, N.; Xu, J.; Lu, X. Ag-Doped Halide Perovskite Nanocrystals for Tunable Band Structure and Efficient Charge Transport. ACS Energy Lett. 2019, 4 (2), 534–541.
35. Gaulding, E. A.; Hao, J.; Kang, H. S.; Miller, E. M.; Habisreutinger, S. N.; Zhao, Q.; Hazarika, A.; Sercel, P. C.; Luther, J. M.; Blackburn, J. L. Conductivity Tuning via Doping with Electron Donating and Withdrawing Molecules in Perovskite $CsPbI_3$ Nanocrystal Films. Adv. Mater. 2019, 31 (27), 1–9.
36. Amerling, E.; Lu, H.; Larson, B. W.; Maughan, A. E.; Phillips, A.; Lafalce, E.; Whittaker-Brooks, L.; Berry, J. J.; Beard, M. C.; Vardeny, Z. V.; Blackburn, J. L. A Multi-Dimensional Perspective on Electronic Doping in Metal Halide Perovskites. ACS Energy Lett. 2021, 6 (3), 1104–1123.
37. Amelia, M.; Lincheneau, C.; Silvi, S.; Credi, A. Electrochemical Properties of CdSe and CdTe Quantum Dots. Chem. Soc. Rev. 2012, 41 (17), 5728–5743.
38. Haram, S. K.; Quinn, B. M.; Bard, A. J. Electrochemistry of CdS Nanoparticles: A Correlation between Optical and Electrochemical Band Gaps. J. Am. Chem. Soc. 2001, 123 (36), 8860–8861.
39. Boehme, S. C.; Walvis, T. A.; Infante, I.; Grozema, F. C.; Vanmaekelbergh, D.; Siebbeles, L. D. A.; Houtepen, A. J. Electrochemical Control over Photoinduced Electron Transfer and Trapping in CdSe-CdTe Quantum-Dot Solids. ACS Nano 2014, 8 (7), 7067–7077.
40. Van Der Stam, W.; Gudjonsdottir, S.; Evers, W. H.; Houtepen, A. J. Switching between Plasmonic and Fluorescent Copper Sulfide Nanocrystals. J. Am. Chem. Soc. 2017, 139 (37), 13208–13217.
41. Gudjonsdottir, S.; Van Der Stam, W.; Koopman, C.; Kwakkenbos, B.; Evers, W. H.; Houtepen, A. J. On the Stability of Permanent Electrochemical Doping of Quantum Dot, Fullerene, and Conductive Polymer Films in Frozen Electrolytes for Use in Semiconductor Devices. ACS Appl. Nano Mater. 2019, 2 (8), 4900–4909.
42. Tajik, S.; Beitollahi, H.; Nejad, F. G.; Shoaie, I. S.; Khalilzadeh, M. A.; Asl, M.

S.; Van Le, Q.; Zhang, K.; Jang, H. W.; Shokouhimehr, M. Recent Developments in Conducting Polymers: Applications for Electrochemistry. RSC Adv. 2020, 10 (62), 37834–37856.

43. Neusser, D.; Malacrida, C.; Kern, M.; Gross, Y. M.; van Slageren, J.; Ludwigs, S. High Conductivities of Disordered P3HT Films by an Electrochemical Doping Strategy. Chem. Mater. 2020, 32 (14), 6003–6013.
44. Pumera, M.; Sofer, Z.; Ambrosi, A. Layered Transition Metal Dichalcogenides for Electrochemical Energy Generation and Storage. J. Mater. Chem. A 2014, 2 (24), 8981–8987.
45. Chia, X.; Eng, A. Y. S.; Ambrosi, A.; Tan, S. M.; Pumera, M. Electrochemistry of Nanostructured Layered Transition-Metal Dichalcogenides. Chem. Rev. 2015, 115 (21), 11941–11966.
46. Samu, G. F.; Scheidt, R. A.; Kamat, P. V.; Janáky, C. Electrochemistry and Spectroelectrochemistry of Lead Halide Perovskite Films: Materials Science Aspects and Boundary Conditions. Chem. Mater. 2018, 30 (3), 561–569.
47. Lorenzon, M.; Sortino, L.; Akkerman, Q.; Accornero, S.; Pedrini, J.; Prato, M.; Pinchetti, V.; Meinardi, F.; Manna, L.; Brovelli, S. Role of Nonradiative Defects and Environmental Oxygen on Exciton Recombination Processes in $CsPbBr_3$ Perovskite Nanocrystals. Nano Lett. 2017, 17 (6), 3844–3853.
48. Imran, M.; Caligiuri, V.; Wang, M.; Goldoni, L.; Prato, M.; Krahne, R.; De Trizio, L.; Manna, L. Benzoyl Halides as Alternative Precursors for the Colloidal Synthesis of Lead-Based Halide Perovskite Nanocrystals. J. Am. Chem. Soc. 2018, 140 (7), 2656–2664.
49. Protesescu, L.; Yakunin, S.; Bodnarchuk, M. I.; Krieg, F.; Caputo, R.; Hendon, C. H.; Yang, R. X.; Walsh, A.; Kovalenko, M. V. Nanocrystals of Cesium Lead Halide Perovskites ($CsPbX_3$, X = Cl, Br, and I): Novel Optoelectronic Materials Showing Bright Emission with Wide Color Gamut. Nano Lett. 2015, 15 (6), 3692–3696.
50. Grimaldi, G.; Geuchies, J. J.; van der Stam, W.; du Fossé, I.; Brynjarsson, B.; Kirkwood, N.; Kinge, S.; Siebbeles, L. D. A.; Houtepen, A. J. Spectroscopic Evidence for the Contribution of Holes to the Bleach of Cd-Chalcogenide Quantum Dots. Nano Lett. 2019, 19 (5), 3002–3010.
51. Boehme, S. C.; Azpiroz, J. M.; Aulin, Y. V.; Grozema, F. C.; Vanmaekelbergh, D.; Siebbeles, L. D. A.; Infante, I.; Houtepen, A. J. Density of Trap States and Auger-Mediated Electron Trapping in CdTe Quantum-Dot Solids. Nano Lett. 2015, 15 (5), 3056–3066.
52. Yang, H.; Feng, Y.; Tu, Z.; Su, K.; Fan, X.; Liu, B.; Shi, Z.; Zhang, Y.; Zhao, C. Blue Emitting $CsPbBr_3$ Perovskite Quantum Dot Inks Obtained from Sustained Release Tablets. 2019, 12 (12), 3129–3134.
53. Ha, S. T.; Su, R.; Xing, J.; Zhang, Q.; Xiong, Q. Metal Halide Perovskite Nanomaterials: Synthesis and Applications. Chem. Sci. 2017, 8 (4), 2522–2536.
54. Worku, M.; Tian, Y.; Zhou, C.; Lin, H.; Chaaban, M.; Xu, L.; He, Q.; Beery, D.; Zhou, Y.; Lin, X.; Su, Y.; Xin, Y.; Ma, B. Hollow Metal Halide Perovskite Nanocrystals with Efficient Blue Emissions. Sci. Adv. 2020, 6 (17), eaaz5961.
55. Butkus, J.; Vashishtha, P.; Chen, K.; Gallaher, J. K.; Prasad, S. K. K.; Metin, D. Z.; Laufersky, G.; Gaston, N.; Halpert, J. E.; Hodgkiss, J. M. The Evolution of Quantum Confinement in $CsPbBr_3$ Perovskite Nanocrystals. Chem. Mater. 2017,

29 (8), 3644–3652.
56. Geiregat, P.; Maes, J.; Chen, K.; Drijvers, E.; De Roo, J.; Hodgkiss, J. M.; Hens, Z. Using Bulk-like Nanocrystals to Probe Intrinsic Optical Gain Characteristics of Inorganic Lead Halide Perovskites. ACS Nano 2018, 12, 10178–10188.
57. Makarov, N. S.; Guo, S.; Isaienko, O.; Liu, W.; Robel, I.; Klimov, V. I. Spectral and Dynamical Properties of Single Excitons, Biexcitons, and Trions in Cesium-Lead-Halide Perovskite Quantum Dots. Nano Lett. 2016, 16 (4), 2349–2362.
58. Yu, D.; Wehrenberg, B. L.; Jha, P.; Ma, J.; Guyot-Sionnest, P. Electronic Transport of N-Type CdSe Quantum Dot Films: Effect of Film Treatment. J. Appl. Phys. 2006, 99 (10), 104315.
59. Yu, D. N-Type Conducting CdSe Nanocrystal Solids. Science 2003, 300 (5623), 1277–1280.
60. Ten Brinck, S.; Zaccaria, F.; Infante, I. Defects in Lead Halide Perovskite Nanocrystals: Analogies and (Many) Differences with the Bulk. ACS Energy Lett. 2019, 4 (11), 2739–2747.
61. Du Fossé, I.; Ten Brinck, S.; Infante, I.; Houtepen, A. J. Role of Surface Reduction in the Formation of Traps in N-Doped II-VI Semiconductor Nanocrystals: How to Charge without Reducing the Surface. Chem. Mater. 2019, 31 (12), 4575–4583.
62. Haynes, W. M.; Lide, D. R.; Bruno, T. J. CRC Handbook of Chemistry and Physics, 97th ed.; CRC Press: Boca Raton, Florida, 2016.
63. Fan, Y.; Fang, J.; Chang, X.; Tang, M. C.; Barrit, D.; Xu, Z.; Jiang, Z.; Wen, J.; Zhao, H.; Niu, T.; Smilgies, D. M.; Jin, S.; Liu, Z.; Li, E. Q.; Amassian, A.; Liu, S.; Zhao, K. Scalable Ambient Fabrication of High-Performance $CsPbI_2Br$ Solar Cells. Joule 2019, 3 (10), 2485–2502.
64. Kroupa, D. M.; Vörös, M.; Brawand, N. P.; McNichols, B. W.; Miller, E. M.; Gu, J.; Nozik, A. J.; Sellinger, A.; Galli, G.; Beard, M. C. Tuning Colloidal Quantum Dot Band Edge Positions through Solution-Phase Surface Chemistry Modification. Nat. Commun. 2017, 8 (1), 15257.
65. Brown, P. R.; Kim, D.; Lunt, R. R.; Zhao, N.; Bawendi, M. G.; Grossman, J. C.; Bulovi, V. Energy Level Modification in Lead Sulfide Quantum Dot Thin Films through Ligand Exchange. ACS Nano 2014, 8, 1–17.
66. Perdew, J. P.; Burke, K.; Ernzerhof, M. Generalized Gradient Approximation Made Simple. Phys. Rev. Lett. 1996, 77 (18), 3865–3868.
67. Hutter, J.; Iannuzzi, M.; Schiffmann, F.; Vandevondele, J. Cp2k: Atomistic Simulations of Condensed Matter Systems. Wiley Interdiscip. Rev. Comput. Mol. Sci. 2014, 4 (1), 15–25.
68. Elgrishi, N.; Rountree, K. J.; McCarthy, B. D.; Rountree, E. S.; Eisenhart, T. T.; Dempsey, J. L. A Practical Beginner's Guide to Cyclic Voltammetry. J. Chem. Educ. 2018, 95 (2), 197–206.
69. Gudjonsdottir, S.; Houtepen, A. J. Permanent Electrochemical Doping of Quantum Dots and Semiconductor Polymers. Adv. Funct. Mater. 2020, 30 (49), 1–11.
70. Alimoradi Jazi, M.; Kulkarni, A.; Sinai, S. B.; Peters, J. L.; Geschiere, E.; Failla, M.; Delerue, C.; Houtepen, A. J.; Siebbeles, L. D. A.; Vanmaekelbergh, D. Room-Temperature Electron Transport in Self-Assembled Sheets of PbSe Nanocrystals with a Honeycomb Nanogeometry. J. Phys. Chem. C 2019, 123 (22),

14058–14066.
71. Boehme, S. C.; Wang, H.; Siebbeles, L. D. A.; Vanmaekelbergh, D.; Houtepen, A. J. Electrochemical Charging of CdSe Quantum Dot Films: Dependence on Void Size and Counterion Proximity. ACS Nano 2013, 7 (3), 2500–2508.
72. Crisp, R. W.; Kirkwood, N.; Grimaldi, G.; Kinge, S.; Siebbeles, L. D. A.; Houtepen, A. J. Highly Photoconductive InP Quantum Dots Films and Solar Cells. ACS Appl. Energy Mater. 2018, 1 (11), 6569–6576.

Appendix 5.1

Optical Spectra and TEM of NC Solution and Electrode

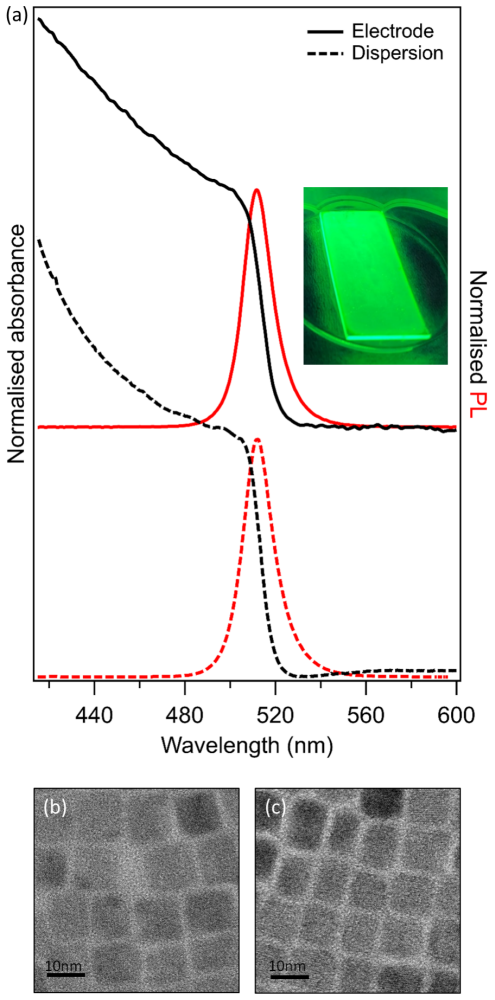


Figure A5.1. (a) Absorbance and PL of a $CsPbBr_3$ NC dispersion and electrode. The spectra are normalized at the band edge absorbance (505 nm) and PL maximum (511 nm), respectively. Inset: a $CsPbBr_3$ NC electrode showcasing the bright green PL of the NC film. (b) TEM image of $CsPbBr_3$ NCs (diameter 10 ± 1 nm) before and (c) after film formation (diameter: 10 ± 1 nm).

Appendix 5.2

Nanocrystal Electrodes

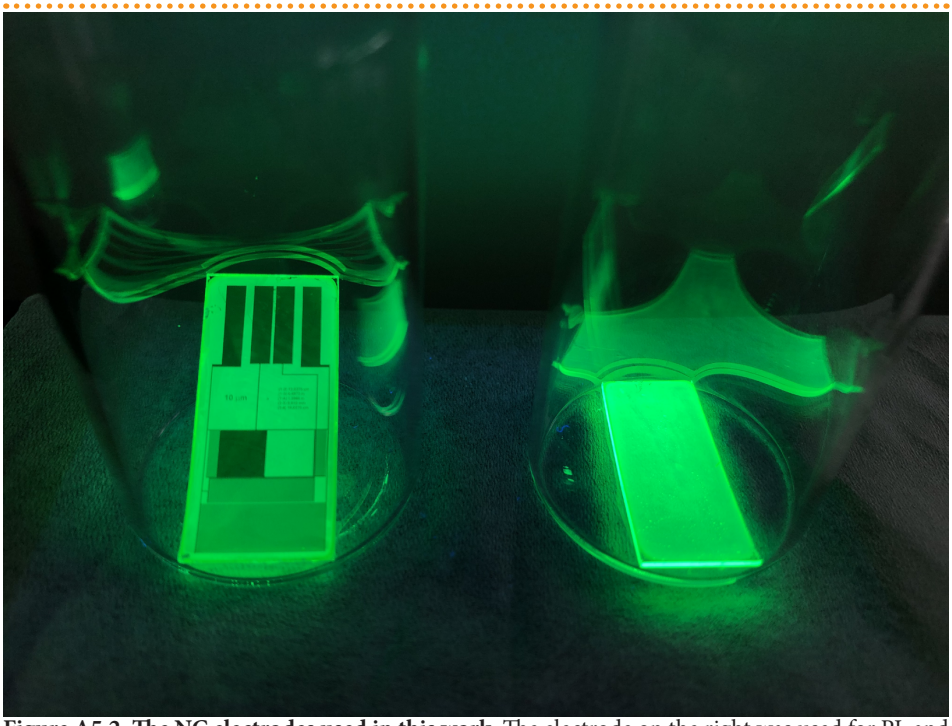


Figure A5.2. The NC electrodes used in this work. The electrode on the right was used for PL and absorbance measurements. The electrode on the left was used for conductivity measurements.

Appendix 5.3

p-Doping – NC Film Thickness

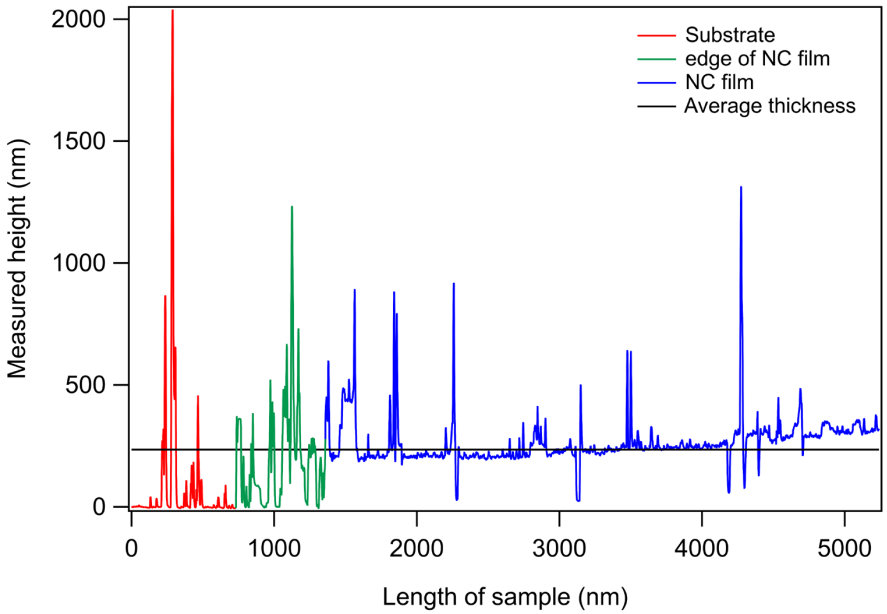


Figure A5.3. The thickness of the NC film on the electrode used for the conductance measurements was measured using a DEKTAK profilometer. The average thickness of the NC layer was measured to be roughly 235 nm.

Appendix 5.4

p-Doping – Reproducibility of PL Measurements

The observed PL quenching is not sample related, as different NC batches show the same behavior. In Figure A5.4, we compare a NC electrode with a high starting PL (~27500 counts) to a different NC electrode made from an entirely different NC batch which has a much lower starting PL (~1200 counts).

Apart from the reproducible PL quenching at positive applied potentials, also the shape of the PL decay and recovery (*i.e.* the rapid and more gradual recovery) is similar in both figures.

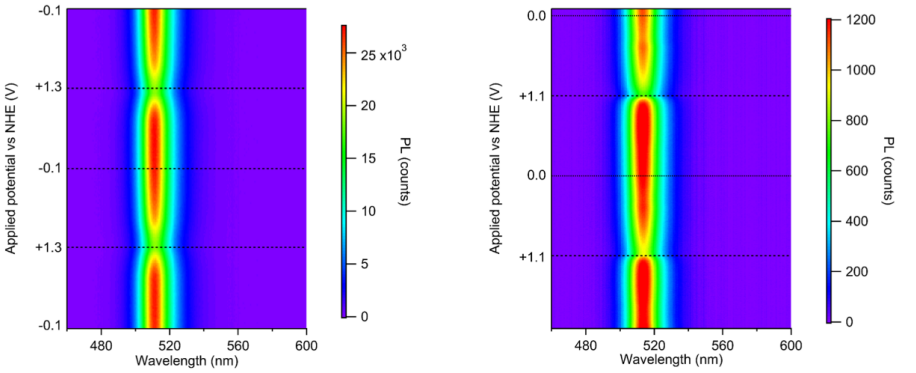


Figure A5.4. PL of two NC electrodes as function of the applied potential. The electrodes used were made on two separate days with a different batch of $CsPbBr_3$ NCs.

Furthermore, the same PL quenching was observed for the absorbance measurement shown in Figure 5.1d and e, as can be seen in Figure A5.5.

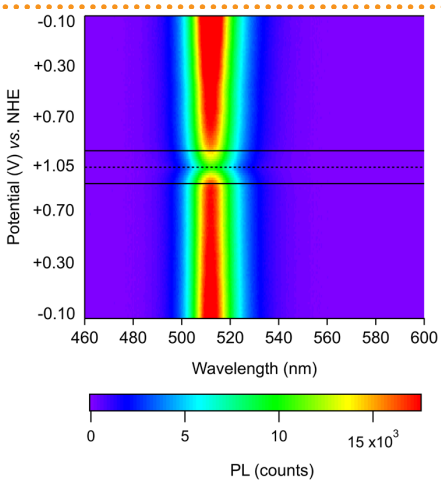


Figure A5.5. Corresponding PL of the NC electrode shown in Figure 5.1d and e.

Appendix 5.5

p-Doping – Conductance Measurements

To measure the conductance we use the approach outlined previously by Gudjonsdottir *et al.*[69] and Alimoradi Jazi *et al.*[70] The potential of both source and drain electrodes is changed simultaneously in potential steps of 50 mV. After a steady state is reached the potential of WE2 (the drain) is kept constant, while the potential of WE1 (the source) is changed slowly in a CV like fashion. This source-drain sweep is performed over a total bias of -25 mV to + 25 mV, with a scan rate of 1 mV/S. Resulting source-drain currents are shown in Figure A5.6a and b, for single drain potentials of 0.38 V and 1.03 V *vs*. NHE, respectively. The slope of the source-drain IV curve gives the conductance of the sample at that drain potential. Since we use a bipotentiostat we can record the current on either source or drain electrode. For a source-drain conductivity these curves should be mirrored around the x-axis, since a flow of electrons from source to drain is recorded as a negative current on the drain and a positive current on the source. In contrast, electrochemical background currents have the same sign and cause an offset of the signals.

Figure A5.6c shows all recorded source drain IV curves at different background (=drain) potentials. The conductivity is clearly recognizable as linear IV curves with opposite slopes for the source and drain electrodes, on top of an offset due to Faradaic background currents. The conductance is obtained as the slope of the source-drain curves at each background potential, and can be retrieved from either the current measured on the source or the drain (red and black dashed lines, respectively).

Appendix 5.5

p-Doping – Conductance Measurements

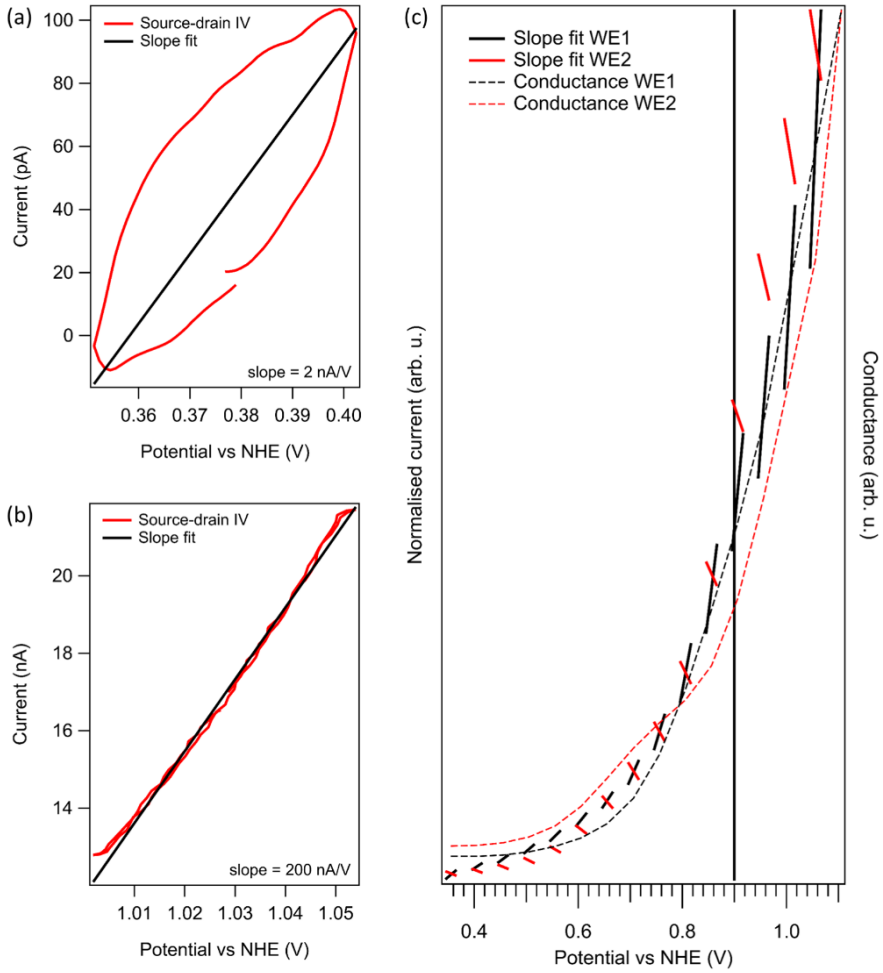


Figure A5.6. (a) The source-drain IV and fitted slope for WE1 for potentials inside the bandgap (+0.38 V) and (b) inside the VB (+1.03 V). (c) A set of IV slope fits for WEs 1 and 2, and the corresponding conductance obtained from these slopes. The potential of the VB edge has been added as a black line at +0.9 V as a guide to the eye.

Appendix 5.6

p-Doping – Conductivity and Mobility Calculations

With the measured conductance (G) shown in Figure A5.6c, the conductivity of the NC film (σ) can be calculated using Equation A5.1:

$$\sigma = \frac{G \cdot w}{l \cdot h} \qquad \text{(A5.1)}$$

w = width between the electrode fingers	25 µm for these measurement
l = total length of the electrode fingers	8.825 mm for these measurements
h = thickness of the NC film	235 nm (Figure A5.3)

Subsequently, with a number of approximations (see below), the mobility (µ) can be calculated following Equation A5.2:

$$\mu = \frac{\sigma \cdot V}{e \cdot N} \qquad \text{(A5.2)}$$

V = (average) volume of a NC	$1.06 \cdot 10^{-24}$ m^3 (from average size NC, TEM)
e = elementary charge	$1.602 \cdot 10^{-19}$ C
N = charge per NC	Estimated 0.2 from a ~10% ABS bleach

Assumptions and approximations

The total length of the fingers might be less than used in the calculations, as some fingers might have been broken. This means that the mobility and conductivity shown in Figure A5.7 may be slightly lower than the true value. Similarly, but only for the mobility calculation, the charge injected per NC (N) is approximated to be 0.2, from an absorbance bleach of ~10% (see Figure A5.8). The assumption here is a valence band degeneracy of 2.[55,57] With a higher degeneracy, the charge per NC might increase by maximally one order of magnitude. Lastly, since the NCs are p-doped (hole concentration ~$2 \cdot 10^{17}$ cm^{-3}), we have neglected the contribution of electrons to the conductivity.

Correctness of the calculated conductivity and mobility

The conductivity might be slightly underestimated, but a few broken fingers result in an error of <5% due to the large number of fingers present in the electrode. Therefore, the order of magnitude of the displayed results is not affected. As discussed above, the mobility might be overestimated to a maximum of roughly one order of magnitude due to the uncertainty in the VB degeneracy. The calculated mobility, on the order of 10^{-3} cm^2/Vs, is a reasonable value for NCs with relatively long, insulating ligands on the surface.[71,72] This strengthens our conclusion that the measured increase in conductivity from +0.9 V is related to hole injection into the VB edge, and not to side reactions.

Appendix 5.6

p-Doping – Conductivity and Mobility Calculations

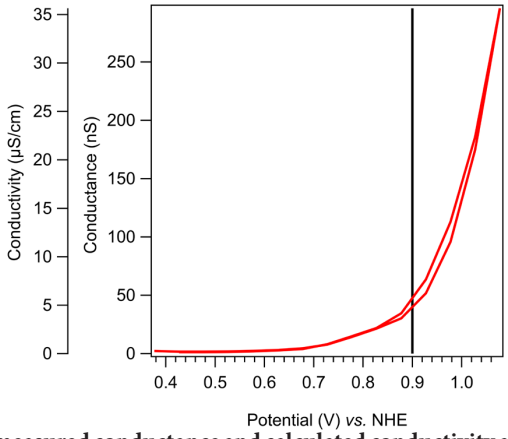


Figure A5.7. The measured conductance and calculated conductivity and mobility of the $CsPbBr_3$ NC film. A mobility on the order of 10^{-3} cm^2/Vs is expected for the NC system we measured.

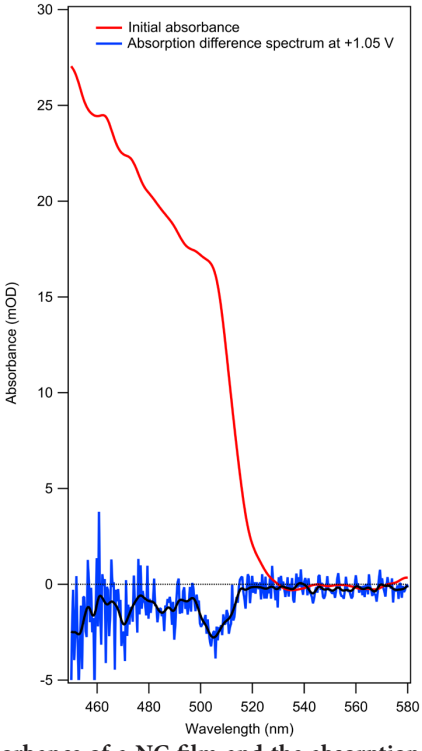


Figure A5.8. The initial absorbance of a NC film and the absorption bleach of the same film at +1.05 V. The integrated area of the absorption bleach is ~10% of the total area of the initial absorption between 495 and 515nm.

Appendix 5.7

n-Doping – Spectro-Electrochemical Data

As we have shown reversible p-doping at applied potentials above +0.9 V, a similar measurement was carried out in the negative scan direction, in order to attempt n-doping by crossing the CB edge. As can be seen from Figure A5.9a and A5.9b, the PL greatly reduces starting from -0.6 V, far more positive than the location of the CB edge (-1.5 V, based on the optical bandgap). In contrast to the reversible quenching of the PL shown in the main text for p-doping, the PL did not recover when scanning back from negative potentials to the open circuit potential (V_{OC}). The PL only recovered slightly when scanning over the VB edge and subsequently back to the V_{OC}. It was concluded that the quenching of PL at negative potentials was related to Pb^{2+} reduction, and not to n-doping, as furthermore can be observed from the absence of a band edge bleach in the differential absorbance shown in Figure A5.9c. We attribute the subsequent observed recovery of the PL to Pb oxidation and the partial re-formation of $CsPbBr_3$ perovskite.

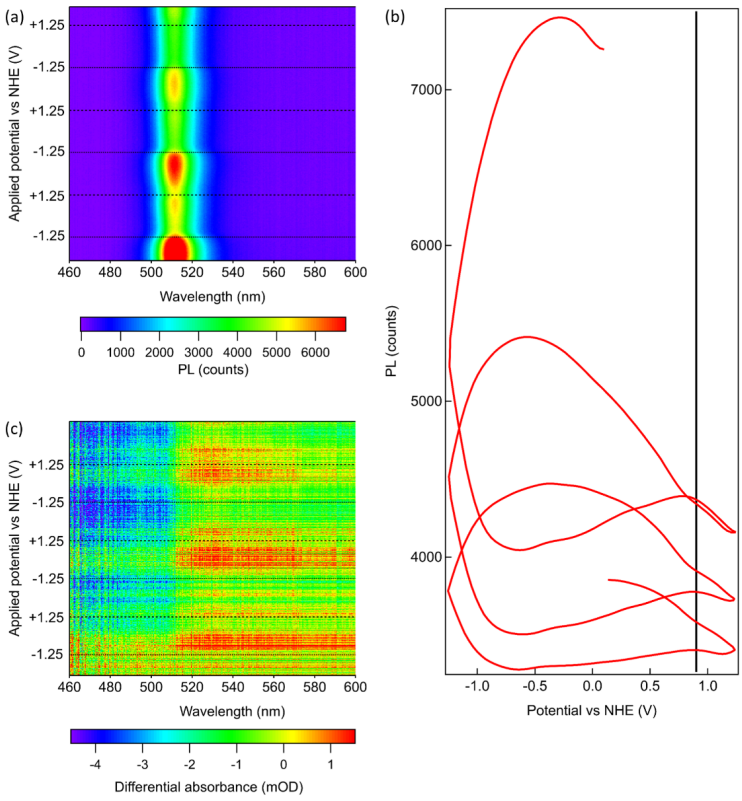


Figure A5.9. (a) PL of a NC electrode as function of the applied potential, during three CV cycles from -1.25 V to +1.25 V, starting at +0.10 V. (b) The averaged PL counts between 505 and 520 nm from the spectrum shown in (a). (c) Differential absorbance as a function of the applied potential of the same measurement as shown in (a).

Appendix 5.8

n-Doping - Electrodes

As mentioned in Appendix 5.7, the PL quench observed when scanning to negative potentials is attributed to Pb^{2+} reduction, as initially reported by Samu *et al.*[46] Figure A5.10 shows a similar image as shown by Samu *et al.*, where a film that is scanned to positive potentials shows little to no change to the initial film. The film that is scanned to negative potentials however, shows a dark layer of metallic lead for the part of the film that was submerged in the electrolyte (Figure A5.10). It can furthermore be seen that the charge injection in the NCs is uniform, as the whole submerged electrode part is reduced evenly.

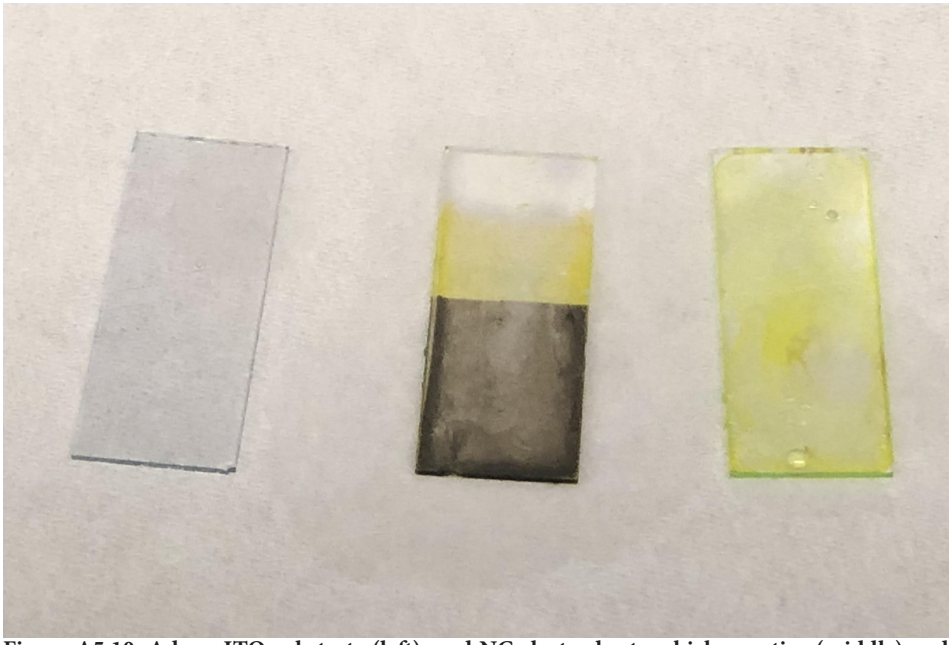


Figure A5.10. A bare ITO substrate (left), and NC electrodes to which negative (middle) and positive (right) potentials have been applied for respective attempts to n-dope and p-dope.

Appendix 5.9

n-Doping - XRD

To prove that the formed dark material shown in Figure A5.10 is indeed metallic lead, XRD was performed on the film. In Figure A5.11, which compares a pristine $CsPbBr_3$ film with an identical film after application of negative potentials, it can be seen that the signal related to the perovskite is no longer present in the latter case. Instead, a sharp peak corresponding to metallic lead (ICSD 96501) has appeared.

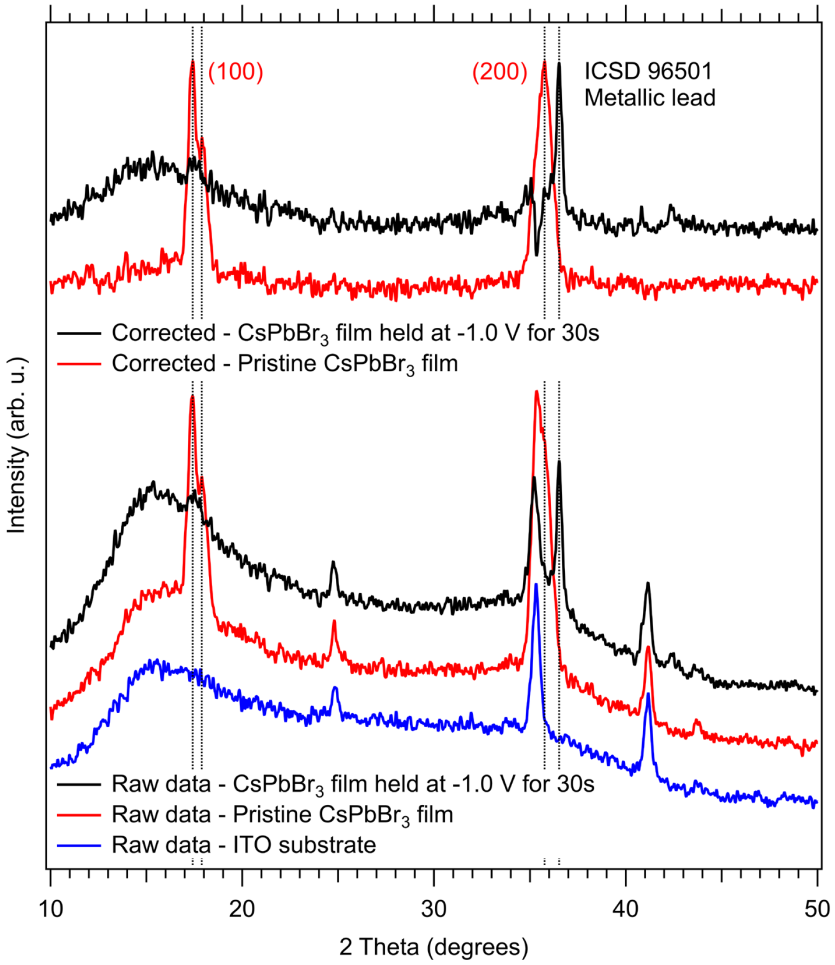


Figure A5.11. (bottom) Raw XRD patterns of a clean ITO substrate, a pristine $CsPbBr_3$ film on ITO and a negatively scanned $CsPbBr_3$ NC film on ITO (top). Corrected XRD patterns where the ITO pattern has been subtracted. It can be seen that both XRD peaks related to $CsPbBr_3$ are present in the pristine sample, but they are no longer present in the used film. A new peak has appeared that can directly be correlated to metallic lead. We can therefore conclude that the $CsPbBr_3$ NCs have completely deteriorated and only reduced lead remained.

Appendix 5.10

XPS Analysis on NC Films

To add additional proof that n-doping is unstable due to the formation of metallic lead, whereas p-doping is more stable, XPS measurements were performed on a new film (immersed in the electrolyte solution for 1 minute) and films to which a potential of -1.46 V, +0.84 V and +1.54 V *vs.* NHE were applied for 1 minute. In Figure A5.12 it can be seen that when a negative potential is applied, the signal for Pb^{2+} 4f reduces in intensity, and a new peak arises at the location of Pb^0 4f. This is additional proof that the lead ions are reduced to metallic lead. When positive potentials are applied, no shift is observed for the Pb 4f (indicating the Pb^{2+} does not get oxidized to Pb^{4+}), however a shift for the Br 3d towards higher binding energies indicates that the Br^- does get oxidized. The limiting factor when applying positive potentials is therefore the bromide oxidation, and not the lead oxidation.

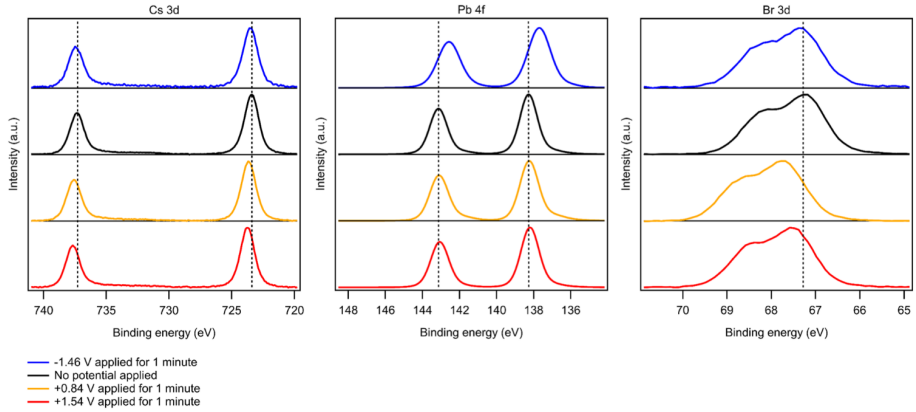


Figure A5.12. XPS measurements on a new film (immersed in the electrolyte solution for 1 minute) and films to which a potential of -1.46 V, +0.84 V and +1.54 V *vs.* NHE were applied for 1 minute. A large shift for the Pb 4f signal is observed when a negative potential is applied to the NC electrode, corresponding with the reduction of Pb^{2+} ions to metallic Pb^0, whereas no shift is observed when applying positive potentials. For the Br 3d signal however, applying positive potentials induces a shift to higher binding energies, corresponding with bromide oxidation.

Appendix 5.10

XPS Analysis on NC Films

From the XPS results, furthermore the elemental ratio of the NC films was determined (Table A5.1). It can be seen that the elemental ratio does not significantly change when positive potentials are applied to the NC electrode. However, when a negative potential is applied, a large fraction of the Cs^+ and Br^- ions is lost in comparison to the amount of lead. This is in line with our analysis that, when lead ions get reduced, the other ions of the perovskite NC move into the solvent and hence cannot form back.

Table A5.1. Elemental ratio of Cs, Pb and Br of the measured NC films.

Sample	Cs	Pb	Br (Br_3)
-1.46 V applied	0.6	1	2.0 (0.7)
No potential applied	1.3	1	4.1 (1.4)
+0.84 V applied	1.3	1	3.8 (1.3)
+1.54 V applied	1.0	1	4.2 (1.4)

Appendix 5.11

Synthesis Method of Protesescu *et al.* – Spectro-Electrochemical Measurements

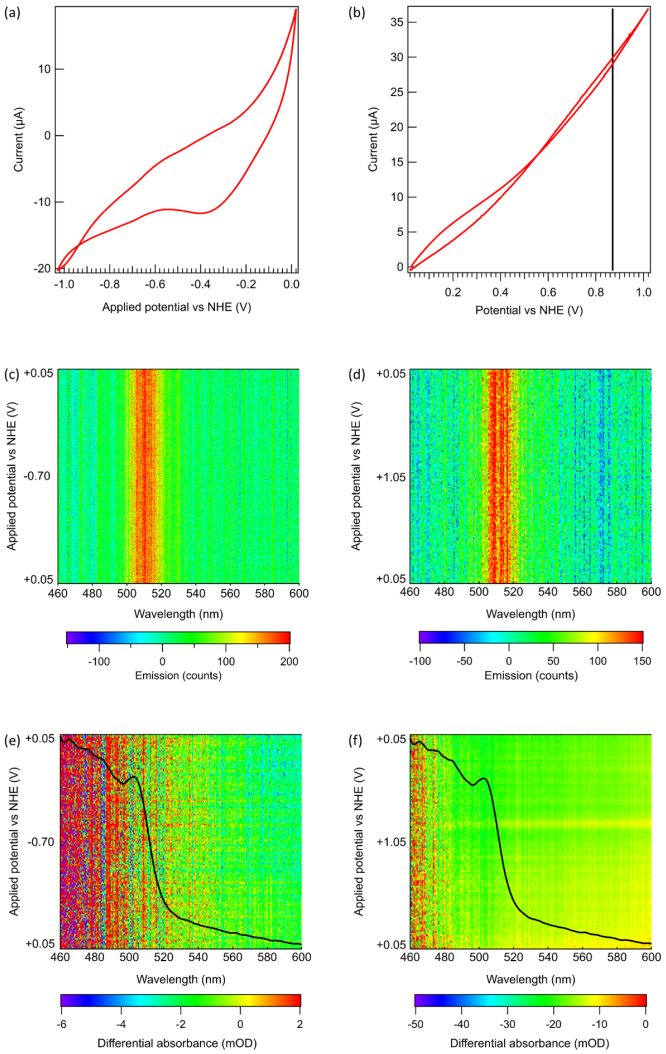


Figure A5.13. (a, b) CVs, (c, d) PL and (e, f) differential absorbance as function of the applied potential for NC electrodes made with NCs synthesized by the method of Protesescu *et al.*[49] It can be seen that the amount of current flowing is on the same order of magnitude as for the NC electrodes made with NCs synthesized following Imran *et al.*[48] Both attempts on n-doping (a, c and e) and p-doping (b, d and f) did not show the trends reported in the main article. It has to be noted that the initial PL count is very low. It is therefore assumed that these NCs are less stable in the electrolyte used, and we can therefore conclude that the different synthesis method had a large influence on the obtained results.

Appendix 5.12

Synthesis Method of Protesescu *et al.* – Electrodes

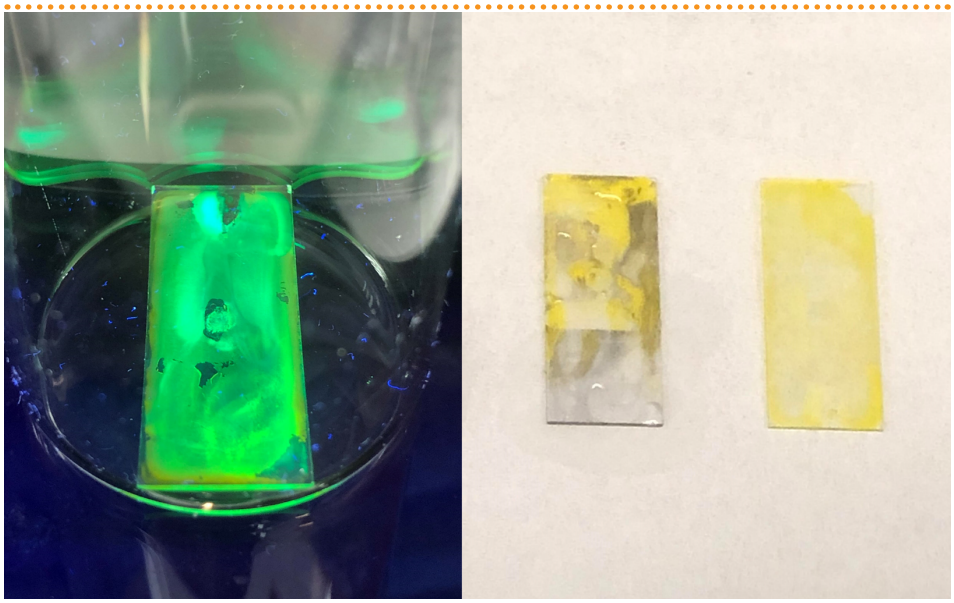


Figure A5.14. NC electrodes prepared with NCs synthesized by the method of Protesescu *et al.*[49] It can be seen that the electrodes are less consistent in PL intensity (left). Furthermore, the charge injection is not uniform, as the negatively scanned NC electrode (middle) only reduced in parts of the film. This is in contrast to the NC electrodes we used in Chapter 5 (as can be seen in Figures A5.2 and A5.10). The newly made NC electrodes (right) do not differ much in appearance, compared to the ones used in the main article.

Appendix 5.13

Cyclic Voltammetry Determination of the Formal Potentials of Pb^{2+} and Sn^{2+} Reduction and Oxidation, and Br^- Oxidation in Propylene Carbonate

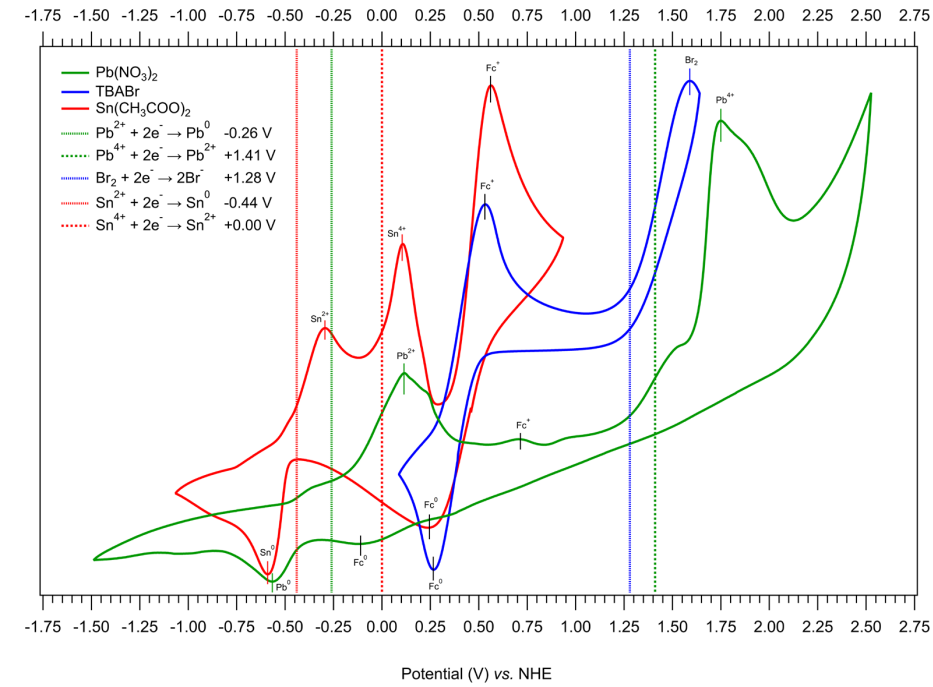


Figure A5.15. CV measurements of $Pb(NO_3)_2$ (green), TBABr (blue) and $Sn(CH_3COO)_2$ (red) dissolved in propylene carbonate. The exact applied potential is determined by ferrocene (Fc) (+0.4 V *vs.* NHE) which was added in each measurement. The midway potential of the reduction and oxidation peaks determines the formal potential. For cases where no reduction peak was observed, the peak to peak separation of the Pb^0/Pb^{2+} (for Pb^{2+}/Pb^{4+}), Fc^0/Fc^+ (for Br^-/Br_2), or Sn^0/Sn^{2+} (for Sn^{2+}/Sn^{4+}) was used.

Appendix 5.14

Thermodynamic Discussion of Cathodic and Anodic Decomposition Reactions

The cathodic decomposition of (bulk) $CsPbBr_3$ takes place *via*:

$$CsPbBr_3 + 2e^- \rightleftarrows Pb^0 + Cs^+ + 3Br^- \quad \text{(A5.3)}$$

The corresponding equilibrium potential of that reaction is given by the Nernst equation:

$$E_{eq} = E^{0'}_{CsPbBr_3/Pb} + \frac{RT}{2F} \ln\left(\frac{1}{[Cs^+][Br^-]^3}\right) \quad \text{(A5.4)}$$

This reaction can also be viewed as the dissolution of $CsPbBr_3$, followed by the reduction of the lead ions:

$$CsPbBr_3 \rightleftarrows Pb^{2+} + Cs^+ + 3Br^- \quad \text{(A5.5)}$$

$$Pb^{2+} + 2e^- \rightleftarrows Pb^0 \quad \text{(A5.6)}$$

Since the end products of (A5.3) and (A5.4) + (A5.5) are the same, they describe the same equilibrium and their equilibrium potentials must match. The dissolution reaction (A5.5) is described by the following solubility product:

$$K_{sp} = [Cs^+][Pb^{2+}][Br^-]^3 \quad \text{(A5.7)}$$

Thus, we can write the Nernst potential of (A5.6) as:

$$E_{eq} = E^{0'}_{Pb^{2+}/Pb} + \frac{RT}{2F} \ln [Pb^{2+}] \quad \text{(A5.8a)}$$

$$E_{eq} = E^{0'}_{Pb^{2+}/Pb} + \frac{RT}{2F} \ln\left(\frac{K_{sp}}{[Cs^+][Br^-]^3}\right) \quad \text{(A5.8b)}$$

$$E_{eq} = E^{0'}_{Pb^{2+}/Pb} + \frac{RT}{2F} \ln K_{sp} + \frac{RT}{2F} \ln\left(\frac{1}{[Cs^+][Br^-]^3}\right) \quad \text{(A5.8c)}$$

Equating (A5.8c) and (A5.4) we see that

$$E^{0'}_{CsPbBr_3/Pb} = E^{0'}_{Pb^{2+}/Pb} + \frac{RT}{2F} \ln K_{sp} \quad \text{(A5.9)}$$

This shows that in solvents wherein $CsPbBr_3$ is poorly soluble, and K_{sp} is smaller than 1, the cathodic dissolution will occur at more negative potential than the reduction of free Pb^{2+} ions. For instance, the reported value of K_{sp} for $CsPbBr_3$ in a mixture of GBL and DMSO is ~10^{-3} mol^5/L^5,[63] corresponding to a stabilization of ~89 mV. The propylene carbonate solvent used in the electrochemical experiments in the current paper was chosen because the $CsPbBr_3$ NC films do not readily dissolve in it (unlike in *e.g.* DMF or DMSO) and hence the expected solubility product is much lower, and the expected stabilization is

greater, than in GBL/DMSO.

We can also consider the likely anodic decomposition reactions:

$$CsPbBr_3 \rightleftarrows Pb^{2+} + Cs^{+} + \tfrac{3}{2}Br_2 + 3e^{-} \quad \text{(A5.10)}$$

$$CsPbBr_3 \rightleftarrows Pb^{4+} + Cs^{+} + 3Br^{-} + 2e^{-} \quad \text{(A5.11)}$$

And derive in a similar way that

$$E^{0'}_{Br_2/CsPbBr_3} = E^{0'}_{Br_2/Br^-} + \frac{RT}{3F} \ln K_{sp} \quad \text{(A5.12)}$$

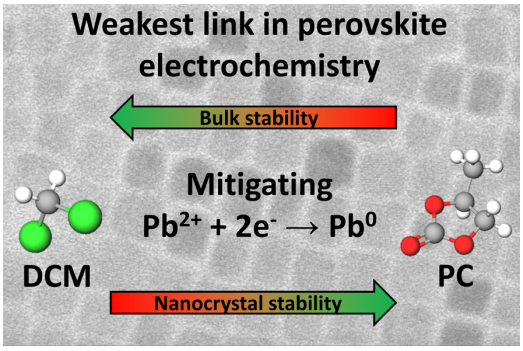
$$E^{0'}_{Pb^{4+}/CsPbBr_3} = E^{0'}_{Pb^{4+}/Pb^{2+}} + \frac{RT}{2F} \ln K_{sp} \quad \text{(A5.13)}$$

In general all cathodic and anodic dissolution reactions are stabilized by $RT/nF \cdot \ln(K_{sp})$, where n is the number of electrons involved in the reaction, compared to the reduction or oxidation of the free ions. Clearly the initial electrochemical reactions on the surface of $CsPbBr_3$ NCs will occur at sites that are undercoordinated compared to the bulk, and hence the standard reduction potential of these will be less negative for surface reduction and less positive for surface oxidation, compared to the bulk standard potentials.

6

Chapter 6

Orthogonal Electrochemical Stability of Bulk and Surface in Lead Halide Perovskite Nanocrystals



Lead halide perovskite materials have attracted widespread attention for application in various optoelectronic devices, such as LEDs and solar cells. A ubiquitous element in these applications is that charging of the perovskite is involved. This can, however, lead to electrochemical degradation reactions that deteriorate the device's performance. Understanding the electrochemical degradation reactions in perovskites has, however, remained challenging.

For bulk semiconductors, it is known that the electrochemical decomposition potentials depend on the stabilization of the atoms in the lattice, which is a function of the solubility product of the material in the electrolyte. For perovskite nanocrystals (NCs), however, the energetics of electrochemical surface reactions are strongly affected by passivating ligands, for which the binding equilibrium depends on the solvation forces in the electrolyte.

Here, we report a systematic spectro-electrochemical study on $CsPbBr_3$ NCs and bulk thin films in contact with different electrolytes to understand and control cathodic degradation reactions. These measurements reveal that the cathodic decomposition of $CsPbBr_3$ NCs is dominated by the solubility of surface ligands, which is high in low-polarity solvents and *vice versa*.

Unfortunately, for NCs, the solubility and stability of surface ligands and the bulk $CsPbBr_3$ lattice are orthogonal, such that no solvent was found where both are sufficiently electrochemically stable. This poses inherent complications for electrochemical measurements and applications: the non-faradaic potential window of the $CsPbBr_3$ NC electrodes is bound by the reduction potential of Pb^{2+} complexes in solution, and the cathodic decomposition of $CsPbBr_3$ occurs well before the conduction band can be populated with electrons. Our results offer guidelines to improve the electrochemical stability of perovskite NCs through a tailored combination of surface passivation and electrolyte selection.

This chapter is based on: Jence T. Mulder, Julius O.V. Monchen, Yan B. Vogel, Cheng Tai Lin, Filippo Drago, Valentina Caselli, Niranjan Saikumar, Tom J. Savenije, Liberato Manna and Arjan J. Houtepen. In preparation.

6.1 Introduction

Lead halide perovskite materials have become a major area of research for optoelectronic applications due to their strong absorbance and defect tolerance.[1–9] Perovskite nanocrystals (NCs) additionally offer enhanced optical properties and tunability through quantum size-effects.[10–13] All-inorganic cesium lead halide perovskite ($CsPbX_3$, X = Cl^-, Br^-, I^-) NCs exhibit a bright photoluminescence (PL) that is characterized by narrow emission linewidths, which forms an essential attribute for high color purity lighting and wide color gamut displays.[10,11,14] Another advantage of these NCs is their facile synthesis, flexible surface chemistry and solution-processability.[10,11,15,16] As such, $CsPbX_3$ NCs are promising optoelectronic materials for application in *e.g.* light emitting diodes (LEDs),[17] low-threshold lasers,[17] light emitting electrochemical cells (LECs)[18,19] and solar cells.[20]

A ubiquitous element in all these applications is that charging of the NCs is involved, either through charge injection, intentional electronic doping, or photoexcitation followed by charge separation.[14-16] Charging of these NCs can however lead to electrochemical degradation reactions that deteriorate the device performance.[14,16,17] For $CsPbX_3$ NCs, reduction of Pb^{2+} and oxidation of X^- ions can occur, resulting in cathodic and anodic decomposition respectively.[18,19] The positions of the standard electrochemical potentials of these reactions relative to the conduction band (CB) and valence band (VB) determine the limit for stable charging by electrons and holes.[17]

Recently a number of scientific publications have addressed the electrochemical characterization of perovskite bulk and NC films.[21–25] These measurements can provide information about material properties, such as the location and nature of trap states and the energy levels of the conduction CB and/or VB.[21,22,26] Additionally, insight can be gained on the material stability in the presence of additional charges, which consequently may have a significant impact on its use as *e.g.* a photocatalyst[27–33] or in light emitting devices[18,34–36].

Electrochemistry on perovskites, in our case $CsPbBr_3$, is complicated by the high solubility of these perovskite materials in most electrolyte solvents.[37] This has two important consequences: (i) it results in dissolved Pb^{2+} and Br^- complexes that may undergo reduction and oxidation reactions, respectively. Additionally, for NCs, the NC surface is coated with ligand complexes like Pb^{2+} oleate (Pb-OA), which may also dissolve and reduce. (ii) It results in easy cathodic (as well as anodic) decomposition, following:

$$CsPbBr_3 + 2e^- \rightleftarrows Pb^0 + Cs^+ + 3Br^- \qquad (6.1)$$

For a large $CsPbBr_3$ solubility product (K_{sp}), this reaction is characterized by a relatively positive formal potential for cathodic decomposition, $E^{0'}_{CsPbBr_3/Pb}$, *via* Equation 6.2:[38,39]

$$E^{0'}_{CsPbBr_3/Pb} = E^{0'}_{Pb^{2+}/Pb} + \frac{RT}{2F} \ln K_{sp} \qquad (6.2)$$

where $E^{0'}_{Pb^{2+}/Pb}$ is the formal potential for the reduction of free Pb^{2+} in the same solvent and the other parameters have their common meanings.

It is thus clear that understanding the solubility of both the $CsPbBr_3$ lattice and Pb-OA surface ligands is essential to understand electrochemical measurements on $CsPbBr_3$ NCs, as well as their stability. The various reactions of dissolved Pb^{2+} and Br^- complexes and the $CsPbBr_3$ lattice itself results in cyclic voltammograms (CVs) that depend strongly on the

chosen solvent, and that contain many features that are not easily assigned correctly.[21,22,24,37] In this work we systematically study the cathodic decomposition of $CsPbBr_3$ NCs and thin films in a wide range of solvents. We perform spectro-electrochemical experiments, which combine CV with measurements of the optical density (OD) and PL spectra. These measurements are compared to measurements on solutions of Pb^{2+} salts and $Pb(OA)_2$ to identify observed features in the CVs. In addition we measured the solubility of $CsPbBr_3$ in 25 solvents, as well as CsOA and $Pb(OA)_2$ in the five most interesting solvents, in order to explain observed trends in the electrochemical response. As the surface ligand composition is comparable, but not identical to $Pb(OA)_2$, throughout the text we refer to surface ligand Pb oleate as Pb-OA, and use $Pb(OA)_2$ solely to indicate Pb oleate as isolatable compound.

The results show that $CsPbBr_3$ is highly soluble in polar solvents like propylene carbonate (PC, $K_{sp} = 10^{-12}$ mol^5/L^5), but sparingly soluble in lower polarity solvents like dichloromethane (DCM, $K_{sp} \leq 10^{-37}$ mol^5/L^5). The solubility of the surface ligands is orthogonal: $Pb(OA)_2$ is most soluble in DCM and only sparingly soluble in PC.
In line with these solubilities we find that for bulk thin films without ligands the cathodic decomposition potential depends on the K_{sp} of the ions, and stable measurements are possible in DCM, in principle only limited by the cathodic decomposition at -1.7 V *vs.* Fc/Fc^+. In contrast, the electrochemical response on NC films always shows significant cathodic features around -1.2 V *vs.* Fc/Fc^+ in all solvents. We attribute these cathodic features to the reduction of dissolved Pb^{2+} complexes in solution. The orthogonal solubility of bulk $CsPbBr_3$ and surface Pb-OA implies that in all solvents a significant amount of dissolved Pb^{2+} complexes are present.
Ex situ XRD and XPS measurements, combined with *in situ* spectro-electrochemical measurements are used to verify the assignment of the different electrochemical features. These results show that the cathodic feature at -1.7 V results in the rapid dissolution of $CsPbBr_3$ and is hence the cathodic decomposition. The cathodic features around -1.2 V predominantly leads to increased scattering from metallic Pb^0, due to reduction of Pb^{2+} complexes in solution. However, there is also noticeable dissolution of the $CsPbBr_3$ NCs associated with this feature. This observation suggests that a correlation exists between the reduction of Pb^{2+} complexes in solution and the dissolution of the $CsPbBr_3$, perhaps by influencing the dissolution equilibrium.
In line with this observation we observe strong changes in the PL intensity of $CsPbBr_3$ that are correlated with the reduction of Pb^{2+} complexes in solution. The PL intensity increases when the potential is moved negative of the reduction potential of the Pb^{2+} complexes. This effect is visible in all solvents, but positively correlates with the solubility of $Pb(OA)_2$ in the solvent. Beyond the cathodic decomposition potential the PL drops rapidly and irreversibly. The drop is again fastest for solvents with high solubility of $Pb(OA)_2$.
Overall our results show that the solubility of Pb-OA surface ligands clearly limits the electrochemical stability of $CsPbBr_3$ NCs. While electrochemical measurements in PC, with low $Pb(OA)_2$ solubility but high $CsPbBr_3$ solubility, are relatively stable and reversible, measurements in DCM are highly irreversible and lead to rapid cathodic decomposition. Our work offers guidelines to improve the electrochemical stability of $CsPbBr_3$ NCs through a tailored combination of surface passivation and electrolyte selection. This is especially relevant for applications that involve a $CsPbBr_3$ NC electrode-electrolyte

interface, such as LECs,[18,19] and photoelectrodes,[40] although the insights have a broader significance for charging of $CsPbBr_3$ NCs in devices in general.

6.2 Measurement Setup

In this work, the electrochemical stability is investigated for $CsPbBr_3$ NC films and bulk films, both deposited on transparent and conductive ITO substrates. The NCs were synthesized following a protocol of Imran *et al.*,[12] and NC electrodes were made following our previously reported protocol.[38] The $CsPbBr_3$ bulk films were made using a layer-by-layer thermal evaporation method, following Xie *et al.*[41] The optical properties of the NC dispersion, NC film and bulk film are shown in Figure 6.1a, and additional information is provided in Appendices 6.1 and 6.2. For electrochemical measurements an important difference between both films is their microstructure. Electrolyte ions cannot easily diffuse into the bulk film (Figure 6.1b), while the space between the NCs does allow ion permeation (Figure 6.1c). It is thus expected that bulk films behave as 2D electrodes, while NC films behave as 3D porous electrodes.

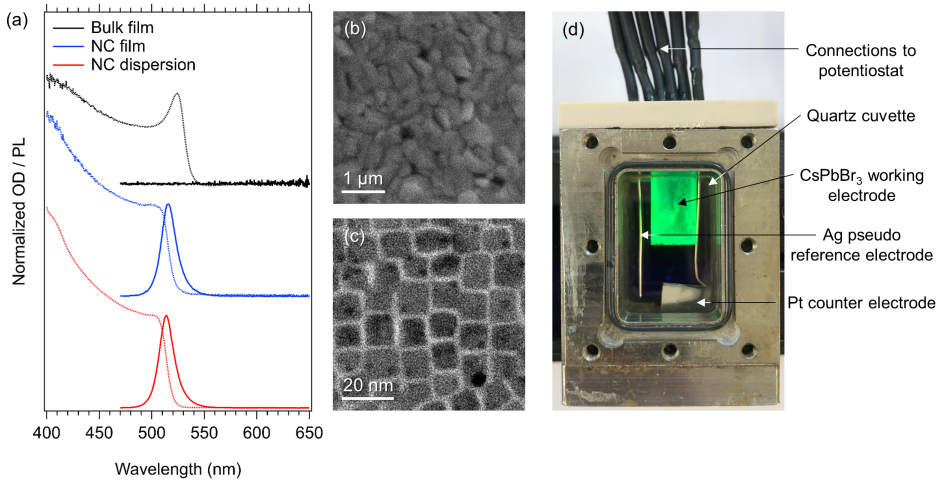


Figure 6.1. (a) The optical density (OD) and photoluminescence (PL) spectra of a $CsPbBr_3$ bulk film, a NC film, and a NC dispersion that are used in this work. (b) A scanning electron microscopy (SEM) image showing that the grains of the thermally evaporated bulk film are significantly larger than (c) the typical colloidal NCs observed in a transmission electron microscope (TEM). (d) The electrochemical cell used in this work, including a $CsPbBr_3$ NC electrode.

6.3 Electrochemical Signatures of $CsPbBr_3$

The electrodes were mounted in an electrochemical cell (Figure 6.1d), and CV measurement were performed in an electrolyte solution of 0.1 M tetrabutylammonium hexafluorophosphate ($TBAPF_6$) in either PC or DCM. The resulting CVs are shown in Figure 6.2. Potentials were applied starting from the open circuit potential (V_{OC}, indicated by the green triangle), down to ~-2.0 V *vs.* Fc/Fc^+ and back to V_{OC}. All cycles were repeated thrice to distinguish between reversible and irreversible electrochemical waves. The estimated conduction band (CB) potential is indicated by a dashed line. This is determined based on the valence band (VB) potential *vs.* Fc/Fc^+, at +0.5 V *vs.* Fc/Fc^+ as

determined in our previous work,[21] from which we subtracted the optical bandgap. The observed electrochemical features in the CV that are discussed below thus all occur within the $CsPbBr_3$ bandgap.

As displayed in Figure 6.2, CV measurements using NC electrodes show similarities but also clear differences between using PC (Figure 6.2a) or DCM (Figure 6.2b) as electrolyte solvent. Several observations can be made:

(1) Both the CV in PC and DCM contain a first cathodic peak (labelled I_A) at around -1.2 to -1.25 V *vs.* Fc/Fc^+ in the first cycle, which appears at less negative potentials in subsequent CV cycles (labelled I_B).

(2) A 2nd cathodic wave (II) starts at ~-1.7 V *vs.* Fc/Fc^+ and keeps increasing within the scanned potential window.

(3) On the reverse scan various anodic waves, labelled $III_{A,B,C}$ are observed, starting around -1.0 to -1.1 V *vs.* Fc/Fc^+.

(4) Both the CV in PC and in DCM are chemically irreversible, *i.e.* the integrated cathodic current is larger than the integrated anodic current. However the irreversibility is much more pronounced in DCM (for the NCs: Q_{out}/Q_{in} = 0.028) than in PC (for the NCs: Q_{out}/Q_{in} = 0.331).

To understand the nature of the observed features in the CV we performed identical CV measurements on an undersaturated solution of Cs^+, Pb^{2+} and Br^- ions in PC with an empty ITO working electrode. The resulting CV, shown in Figure 6.2c, shows striking similarities with the NC-based CV from Figure 6.2a: waves $I_{A,B}$ and $III_{A,B,C}$ are observed at virtually the same potentials, including the noticeable difference in potential of wave I between the first and subsequent cycles.
The only clear difference is the absence of wave II for the dissolved ions. We therefore tentatively attribute wave II to the cathodic decomposition reaction of the NCs, *via* reaction (6.1), as discussed in detail below.

As Cs^+ reduction occurs only at very negative potentials, the reduction waves observed in Figure 6.2c are attributed to electrochemical Pb^{2+} reduction. This is confirmed by the observation of metallic Pb^0 in XRD and XPS as shown in Appendices 6.3 and 6.4. In addition the electrodes visibly show the formation of a black metallic layer (*vide infra*).

The delayed charge injection in the first cycle is observed for both CVs, thus this is not due to Pb^{2+} reduction on or in the perovskite. In accordance to literature and chronoamperometry measurements (Appendix 6.3), we attribute the delayed charge injection in the first cycle to a nucleation overpotential for the formation of Pb^0 nuclei.[42,43] Since not all formed Pb^0 is oxidized in the reverse scan (Q_{out}/Q_{in} = 0.333) some Pb^0 domains are present in the subsequent cycles, so that this overpotential only occurs in the first cycle.

The three oxidation peaks $III_{A,B,C}$ present in both Figures 6.2a and 6.2c are again unrelated to the perovskite itself, hence we assign these to the oxidation of Pb^0 that formed during

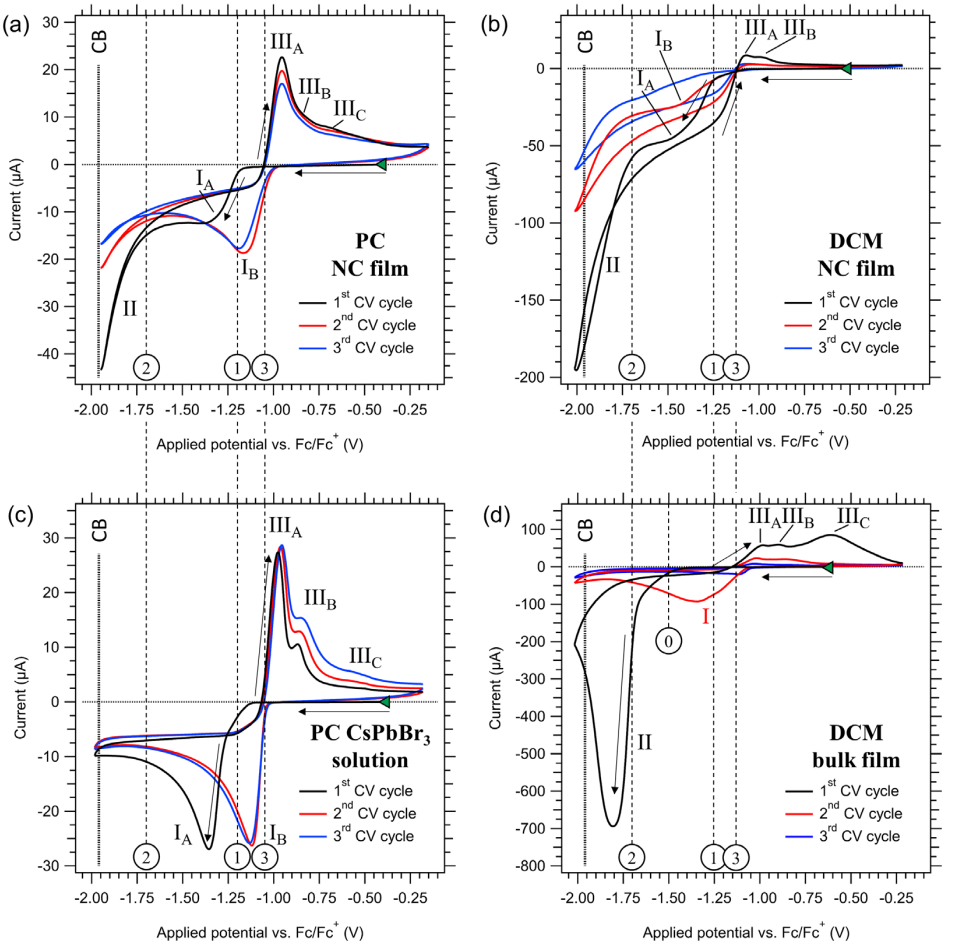


Figure 6.2. (a) The first three CV cycles of a $CsPbBr_3$ NC electrode in PC and (b) DCM, as well as (c) dissolved Cs^+, Pb^{2+} and Br^- in PC and (d) a bulk $CsPbBr_3$ film in DCM. For all figures, the expected location of the conduction band (CB) is indicated by the dotted line at -1.96 V. The scan direction is indicated by the black arrows and the Roman numerals indicate the corresponding electrochemical reactions mentioned in the text. All CVs start at the V_{OC}, indicated by a green triangle, in the negative scan direction with a scan speed of 10 mV/s. The used electrolyte salt is 0.1M $TBAPF_6$ in all cases. The circles numbers will be used for the discussion of the optical effects (*vide infra*).

the cathodic first part of the CV, as Br^- oxidation occurs at more positive potentials (see Figure A6.6). Specifically, as it is known that Pb^{2+} salts from strong complexes with halogen ions in most solvents[44,45] we suggest that the anodic peaks $III_{A,B,C}$ are due to the following reactions:

$$Pb^0 + n\,Br^- \rightarrow [PbBr_n]^{2-n} \qquad \text{where } n_A > n_B > n_C \tag{6.3}$$

Similarly this implies that the cathodic waves I_A and I_B in PC are most likely the reduction of $[PbBr_n]^{2-n}$ rather than free Pb^{2+}. As we will discuss in detail below it is expected that

the concentration of Pb^{2+} complexes is much lower in low-polarity solvents like DCM than in the much more polar PC. Hence it is at first sight surprising that wave I is also observed in DCM, Figure 6.2b, with a 2.5 fold higher current than in PC. We consider that surface Pb-OA ligands could play a role here. Indeed, CV measurements on $Pb(OA)_2$ show a strong cathodic peak at -1.4 V *vs.* Fc/Fc^+ (See Figure A6.7).

To investigate the electrochemical response of $CsPbBr_3$ in the absence of Pb-OA ligands, we performed identical CV measurements on thermally evaporated bulk $CsPbBr_3$ films. These films readily dissolved in PC, indicating a high bulk K_{sp} for $CsPbBr_3$ in the absence of surface ligands, but do not dissolve in DCM. The resulting CV in DCM is shown in Figure 6.2d. Similar to the CV measurement on the NC film in Figure 6.2b, the bulk film shows a large current at ~-1.7 V *vs.* Fc/Fc^+, *i.e.* wave II. As wave II is present in all CVs involving $CsPbBr_3$, but not in the ionic solution, this strengthens our assignment of wave II as the cathodic dissolution reaction. The current is 3.5 times larger than for the NC film in DCM and ~17 times larger than for the NC film in PC. This indicates that rapid cathodic dissolution takes place. Indeed the current is much lower in the second cycle and nearly vanished in the 3rd, as the film has completely decomposed.

An important difference between the bulk and NC films is that wave I is absent in the first CV cycle of the bulk film. The absence of wave I for the bulk film is a clear indication that this wave is related to dissolved Pb^{2+} complexes, as dissolved $CsPbBr_3$ in PC, and as dissolved $Pb(OA)_2$ in DCM.

6.4 Measuring the K_{sp} of $CsPbBr_3$ in Various Electrolyte Solvents

To quantify the solubility of $CsPbBr_3$ and $Pb(OA)_2$, we performed ionic coupled plasma optical emission spectroscopy (ICP-OES) measurements to determine the K_{sp} of $CsPbBr_3$ and $Pb(OA)_2$ in PC and DCM, as well a large number of other common organic electrolyte solvents. A full overview of the solubility of $CsPbBr_3$ in 26 solvents, and $Pb(OA)_2$ and CsOA in 5 different solvents, can be found in Appendices 6.7 – 6.11. Here we focus on the representative solvents PC, DCM, acetonitrile (MeCN), benzonitrile (PhCN) and tetrahydrofuran (THF).

Figure 6.3a shows the saturation Pb^{2+} concentration of $CsPbBr_3$ and $Pb(OA)_2$ obtained from the measured Pb concentration (see Experimental Methods for measurement details). Following Equation 6.2 the expected electrochemical stabilization for $CsPbBr_3$, a function of the K_{sp}, is displayed in Figure 6.3b. This equation indicates that the cathodic decomposition reaction can be shifted to more negative potentials if K_{sp} is lowered.

Figure 6.3 shows that $CsPbBr_3$ is highly soluble in PC compared to DCM. The solubility in DCM is so low that no Pb signal could be recorded above the background signal (<50 ppb). The measured K_{sp} for DCM of 10^{-37} mol^5/L^5 therefore corresponds to an upper limit. The solubility product of $CsPbBr_3$ in PC is ~10^{-12} mol^5/L^5, corresponding to a ~105 times higher molar solubility, and an expected difference of ≥0.75 V in the cathodic decomposition potential according to Equation 6.2. By and large, the solubility of $CsPbBr_3$ increases with the relative permittivity of the solvents, as may be expected for ionic compounds. The fact that THF and DCM, with similar relative permittivities, show widely varying solubility might be related to the mild Lewis basicity of THF, allowing it to coordinate to Pb^{2+} and Cs^+ ions in solution.

The opposite trend is observed for the solubility of $Pb(OA)_2$ in the same solvents (open circles in Figure 6.3a). $Pb(OA)_2$ is highly soluble in DCM (33 mM) and only sparingly

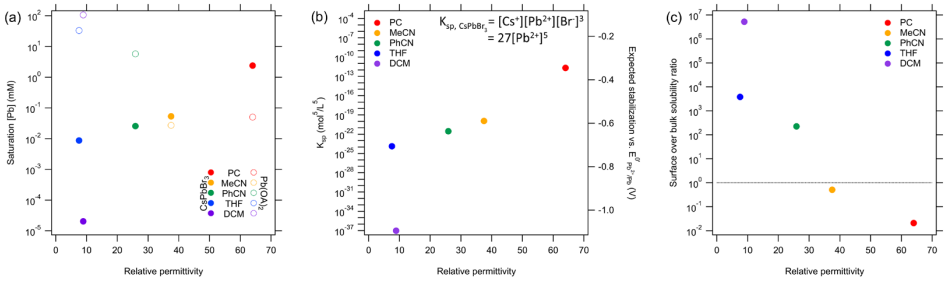


Figure 6.3. (a) The by ICP-OES measured [Pb] in saturated solutions of $CsPbBr_3$ and $Pb(OA)_2$ in propylene carbonate (PC), acetonitrile (MeCN), benzonitrile (PhCN), tetrahydrofuran (THF) and dichloromethane (DCM). (b) The calculated K_{sp} values of bulk $CsPbBr_3$ using the [Pb] from (a). The right axis shows the expected electrochemical stabilization from the K_{sp}, using Equation 6.2. (c) The surface over bulk solubility ratio, obtained by dividing the measured concentration of $Pb(OA)_2$ by that of bulk $CsPbBr_3$, indicating in which solvent $CsPbBr_3$ NCs are stabilized by their surface ligands (<1) or by the bulk solubility (>1).

soluble in PC (50 µM), and in general the $Pb(OA)_2$ solubility decreases with increasing relative permittivity of the solvent, most likely as a result of the non-polar character of the OA ligands. Thus the solubility of bulk Pb^{2+} and surface Pb-OA is orthogonal. This trend is summarized in Figure 6.3c which plots the ratio of the molar solubilities of Pb^{2+} and $Pb(OA)_2$ in the five studied solvents.

This figure shows the limitations of using ligand-covered NCs for these electrochemical measurements. Using solvents with a low bulk solubility (*e.g.* DCM) result in the dissolution of Pb-OA-based complexes, introducing dissolved Pb^{2+} complexes in the system. Using solvents with a high bulk solubility (*e.g.* PC) result in the dissolution of the $CsPbBr_3$ lattice. While this dissolution is strongly slowed down by the presence of insoluble surface ligands (allowing films of $CsPbBr_3$ NCs in PC to be fairly stable, while bulk films dissolve rapidly), we consider that the surface ligands are a dynamically bound, allowing the underlying $CsPbBr_3$ to slowly dissolve, releasing Pb^{2+} complexes into the solution. Our observations together explain why wave I, related to dissolved Pb^{2+} complexes, is present in both NC CVs and absent for the bulk film in DCM.

The above comparison of CVs on $CsPbBr_3$ NC films, the bulk film and the undersaturated solution allows to disentangle most of the electrochemical features in the CV. It does, however, not allow to identify if the reduction of Pb^{2+} complexes in solution affects the properties of the $CsPbBr_3$ films, for instance *via* influencing the dissolution equilibrium, or *via* the precipitation of Pb^0 on the perovskite surface. To this end we recorded the optical density (OD) and photoluminescence (PL) spectra of the films during electrochemical cycling. Below we discuss the results in PC and DCM, *i.e.* the two extremes in terms of the solubility of the bulk and surface. Similar experiments were performed in MeCN, PhCN and THF, and are reported in Appendices 6.12 – 6.14.

6.5 Spectro-Electrochemical Observations

Figure 6.4 shows false-color images of the change to the OD (Figure 6.4a-c) and PL (Figure 6.4e and f) as function of the applied potential during the three CV cycles shown in Figure 6.2. The detailed potential dependence of the OD and PL will be discussed below, but the

overview in Figure 6.4 already clearly shows various important differences.
The bulk $CsPbBr_3$ film shows a dramatic change to the optical density: a strong increase of the OD in the bandgap (>550 nm), attributed to reflection and scattering of the Pb^0 that forms and deposits on the working electrode, as shown in Figure 6.4d, and a strong decrease of the OD above the bandgap as the $CsPbBr_3$ undergoes cathodic decomposition. The full dissolution is complete after 3 cycles and the OD spectrum becomes constant. The same effects are seen for the NC film in DCM. The absolute changes are smaller, as the film is thinner, but similar to the bulk film the OD spectrum shows no evidence of $CsPbBr_3$ absorption after the 3rd cycle (see Appendix 6.15). This is in contrast to the changes observed for the NC film in PC: here the OD changes are smaller and partially reversible. The bandgap absorption has decreased by only 20% after 3 cycles, indicating much slower cathodic dissolution.
The spectro-electrochemical PL spectra are shown in Figure 6.4e and f. As no PL is observed from the bulk film, we only show the PL spectra for the NCs. The NC film in DCM (Figure 6.4e) shows a strong initial increase in PL intensity, followed by a blueshift of the PL peak and subsequently a collapse of the PL intensity. After the first cathodic

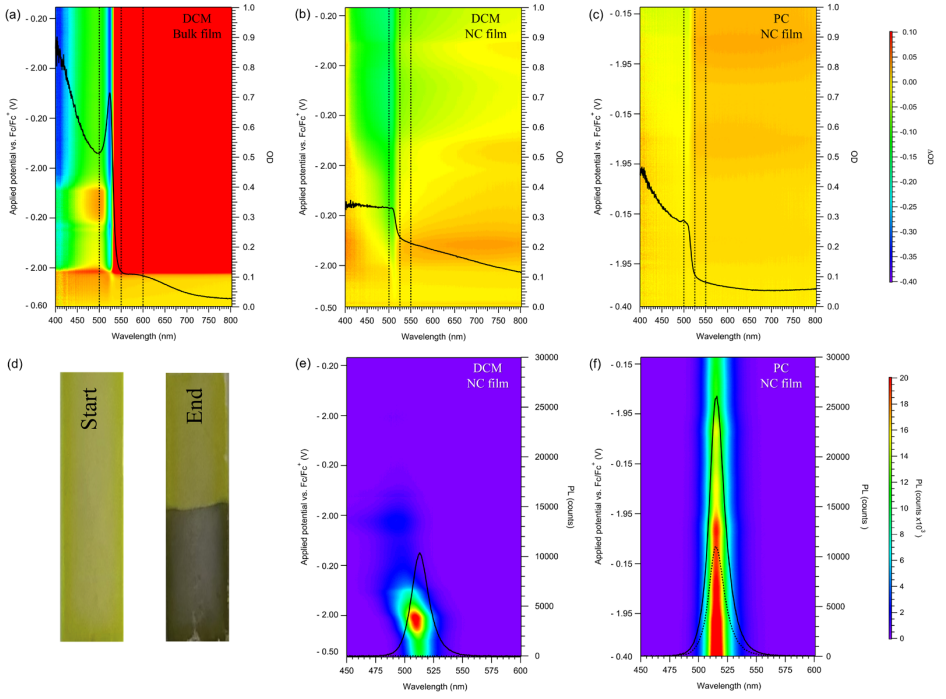


Figure 6.4. (a) False-color image of the change to the OD of a bulk $CsPbBr_3$ film and (b) a NC film in DCM, and (c) a NC film in PC during the three CV cycles shown in Figure 6.2. Plotted over each figure is the initial OD spectrum, as well as the wavelength regions where perovskite band edge and the sub-bandgap changes were averaged, used in Figure 6.5. (d) Photographs of a $CsPbBr_3$ NC film before and after the CV measurement in DCM, showcasing the formed Pb^0 as a dark gray area. (e) False-color image of the change to the PL spectrum of the NC film in DCM and (f) PC. Plotted on top of each figure is the initial and final PL spectrum.

cycle, almost no PL is observed indicating that the NCs are disintegrated. The PL for the NCs in PC (Figure 6.4f) shows a more gradual behavior than in DCM. An initial PL increase, as observed in DCM, is only present in the second and third cycle, and to a much smaller extent. Furthermore no blueshift is observed and PL intensity is clearly visible at the end of the CV measurement. These results show that the NC film in PC is by far the most electrochemically stable, suggesting that the surface passivation by Pb-OA is more important than the bulk solubility of the $CsPbBr_3$.

6.6 The Point of Cathodic Dissolution

Below we analyze the potential dependent changes to the OD and PL in detail. We start by discussing the bulk $CsPbBr_3$ films, since this shows the simplest electrochemical response without dissolved Pb^{2+} complexes in the first cycle.

Until the potential of the cathodic decomposition reaction (or the CB potential), no changes to the absorbance of the perovskite are expected. The most reliable information is therefore obtained from analyzing the OD spectra, as the PL can be influenced by a number of factors that are not related to decomposition of the perovskite (*e.g.* electrochemical trap state formation and filling).

However, this analysis gets complicated due to increased scattering of electrochemically formed Pb^0. We therefore correct the measured changes to the OD at the perovskite band edge (indicated in Figure 6.4a-c) by subtracting the measured sub-bandgap changes to the OD, resulting in a corrected OD of the perovskite only (Appendix 6.16). Here we work under the assumption that the scattering intensity from Pb^0 is similar at the perovskite bandgap and at wavelength just below the bandgap. Further, since we want to compare the changes in the OD to the current measured in the CVs, we plot the derivate dOD/dV as a function of potential. The rationale is that the change in absorption of the $CsPbBr_3$ films should scale with the injected charge Q, as each injected electron causes the dissolution of the same amount of $CsPbBr_3$: $\Delta OD \propto Q$. Since $I = dQ/dt = 1/v \cdot dQ/dV$, this implies that I should have the same potential dependence as dOD/dV. This is shown in Figure 6.5.

Figure 6.5a shows dOD/dV *vs.* V for the bandgap absorption of the bulk $CsPbBr_3$ film in DCM as the black solid line, overlaid with the CV in red. From this figure it is clear that until potential (0) no changes to the bulk perovskite OD occur, indicating that applying a potential where dissolved Pb^{2+} complexes in solution reduce ((1)) indeed does not affect the bulk perovskite. From (0) (-1.5 V *vs.* Fc/Fc^+) onwards, the CV shows a charge injection and at the same time the perovskite OD decreases. From potential (2) onwards, the bulk cathodic decomposition reaction results in a swift degradation of the entire perovskite film. As discussed before we attribute (2) to the cathodic decomposition of the bulk $CsPbBr_3$. The fact that some cathodic dissolution start at (0) could be related to the reduction of undercoordinated $CsPbBr_3$ at grain boundaries.

Interestingly, the current and dOD/dV show almost identical behavior, indicating that all charges injected are directly used for the decomposition of the bulk perovskite. This implies that no side reactions occur before cathodic decomposition takes place and confirms the assignment of wave II. The reverse scan shows an increase in $CsPbBr_3$ above bandgap absorption (dOD/dV turns positive at -0.75 V). This suggests that anodic formation of

$CsPbBr_3$ from deposited Pb^0 and dissolved Cs^+ and Br^- takes place. However, the amount of $CsPbBr_3$ formed is much smaller than the amount that dissolved in the cathodic scan. Both NC systems, in DCM (Figure 6.5b) and PC (Figure 6.5c), show similar behavior but also important differences. For both systems, even at the V_{OC}, a steady reduction of the OD is observed ($dOD/dV \neq 0$). This indicates that without any applied potential, NCs slowly dissolve in both electrolyte solvents. For DCM and PC, the reduction of Pb^{2+} complexes in solution (① at -1.25 V; ① at -1.2 V) already results in increased dissolution of the perovskite. This is true in both DCM and PC, although the effect is significantly stronger in DCM. When the cathodic decomposition potential ② is reached the dissolution speeds up much more.

This observation, that the reduction of Pb^{2+} complexes in solution results in increased dissolution of the perovskite, is unexpected. There does not appear to be a one-to-one relation between the current and dOD/dV as is the case for the cathodic dissolution of the bulk $CsPbBr_3$, *i.e.* dOD/dV decreases less than the current between potential ① and ②, but there is dissolution nonetheless. This suggests that there is a complicated interplay between the reduction of Pb^{2+} complexes in solution and the dissolution of the perovskite NC films. The release of OA^- or Br^- ions from this reaction may result in a change of the dissolution equilibrium, favoring the dissolution of the NCs themselves. This remains a speculation at present. It is however clear that the reduction of Pb^{2+} complexes in solution affects the decomposition of the $CsPbBr_3$ NCs. Spectro-electrochemical PL measurements, discussed next, indicate that this is accompanied with changes of the surface which result in a change in PL quantum yield.

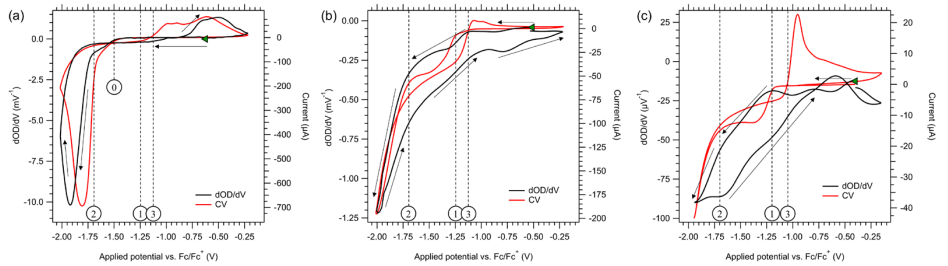


Figure 6.5. (a) The dOD/dV spectrum (in black) for the first CV scan (added in red) of a $CsPbBr_3$ bulk film and (b) NC film in DCM, and (c) a NC film in PC. Indicated in each figure is the V_{OC} as starting point (green triangle), the scan direction (black arrows) and the in the text discussed potentials.

6.7 Observations in the Photoluminescence Spectra

Figure 6.6a shows PL spectra at different potentials for the $CsPbBr_3$ NC film in DCM. At potential ③, the midway potential where a minute fraction of the dissolved Pb^{2+} complexes reduces, the PL initially increases significantly and at the same time shows a blueshift (Figure 6.6a). Once the cathodic decomposition potential ② is reached, after an initial continuation of the PL increase, a rapid and continuous decrease of the PL intensity is observed. The observed blueshift is a strong hint that the NCs are etched during the measurement. The decreasing NC size results in a blueshift through quantum confinement. The PL peak also broadens (inset Figure 6.6a) as the sample becomes more

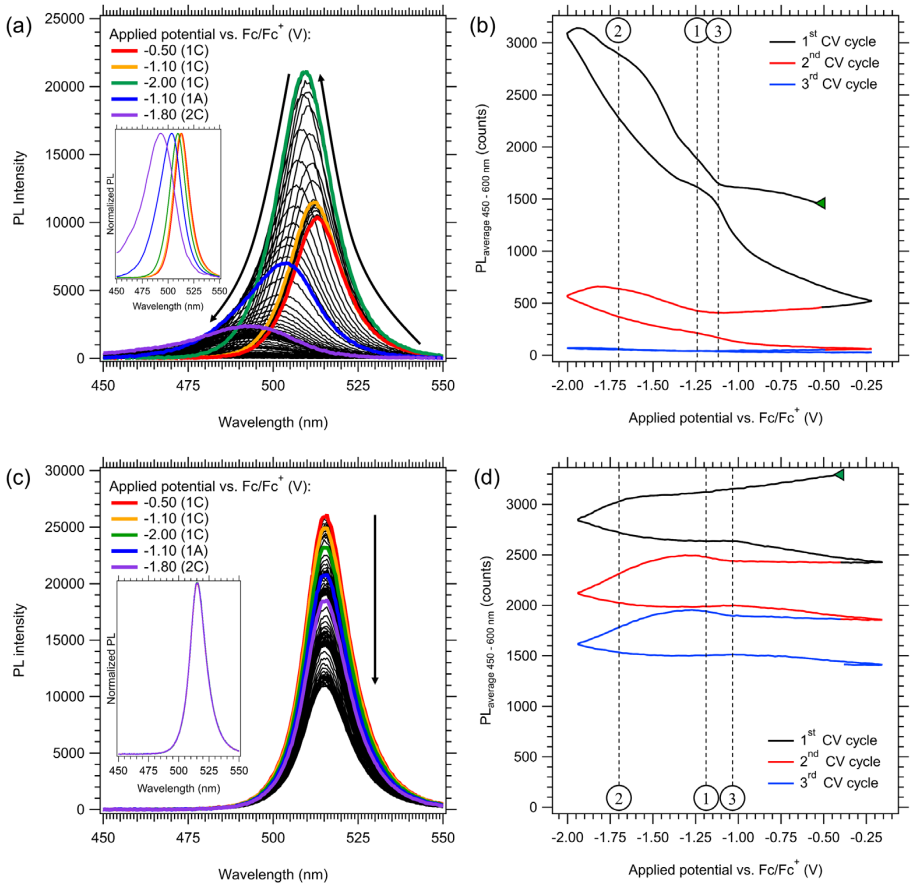


Figure 6.6. (a) The PL spectrum of a NC film in DCM during the CV measurement. The spectrum shows an increase of the PL intensity and at the same time a blueshift of the PL peak due to quantum confinement. Indicated with colors are the PL spectra at given potentials during the 1st cathodic (1C) cycle, as well as the 1st anodic cycle (1A) and the 2nd cathodic cycle (2C). The inset shows broadening of the PL spectrum due to an increase of polydispersity. (b) The average PL counts of the NC film in DCM between 450 and 600 nm as function of the applied potential. The potentials discussed in the text are indicated by the circled numbers. (c) The PL spectrum of the NC film in PC during the three CV cycles, showcasing a decrease of the PL intensity over time, but no blueshift or broadening (inset) as observed in (a). (d) The average PL counts of the NC film in PC between 450 and 600 nm as function of the applied potential. The potentials discussed in the text are indicated by the circled numbers.

polydisperse. Figure 6.6b shows the potential dependence of the spectrally integrated PL intensity. The most remarkable observation is the doubling of the PL intensity when the potential is scanned negative of ③. Such an increase in PL intensity with potential has been reported previously for various systems. In CdTe QDs for example, a strong increase of the PL quantum yield at negative potentials has been shown, which was attributed to the filling of trap states formed by undercoordinated Te surface atoms.[46,47] Brovelli *et al.* have previously observed a PL increase in films of $CsPbBr_3$ NCs and attributed it similarly to

the filling of electron traps at negative potentials.[14] While we cannot rule out that such trap filling occurs it is clear from our current work that the surface of $CsPbBr_3$ bulk and NC films undergoes several structural rearrangements during electrochemical measurements. Further, the correlation of the PL increase with the reduction of Pb^{2+} complexes in solution makes the scenario of filling static traps without strong changes to the surface composition appear too simple. Rather, we consider that the formation of metallic Pb^0 domains on the surface, or perhaps changing ligand concentrations on the NC surface due to the freeing of Br^- or OA^- could influence the electronic structure, removing traps states from the bandgap.

For the NCs in PC, the effects on the PL are vastly different. As shown in Figure 6.6c, the PL intensity reduces over time, but the shape of the spectrum is not affected at all. As shown in Figure 6.6d we observe a gradual decrease of the PL intensity, which we relate to slow dissolution of the NCs, irrespective of the potential. For the NCs in PC we consider that their bulk solubility is so high, that the removal of part of their protective Pb-OA ligands will result in their swift and complete dissolution. Hence NCs are either intact or dissolved, and no gradual blueshift due to etching is observed.

Figure 6.6d additionally shows an increased rate of PL reduction when potentials more negative than (2) are applied, once more confirming that wave II is the cathodic decomposition reaction. As a significant proportion of the initial PL is still present after 3 cycles, we conclude that the NCs in PC are, although also affected by gradual dissolution (see Appendix 6.19), much more stable. We note that the strong increase of the PL, as observed in DCM, is not seen in the first CV cycle in PC. However in the second cycle a small increase in the PL does occur at potential (3). This suggests that in the presence of sufficient Pb-OA surface passivation (in PC), decreasing the potential below (3) does not result in improved surface passivation, while in the absence of Pb-OA (in DCM) it does.

We note that similar results were obtained in MeCN, PhCN, and THF, as shown in Appendices 6.12 – 6.14. In all cases a PL increase can be observed around the midway potential where the slightest reduction of Pb complexes in solution occurs, although in MeCN the PL does not increase in the first cycle, and only by a few percent in the second scan, making it similar to PC. In general we observe that the extent of PL increase at this potential correlates positively with the solubility of $Pb(OA)_2$ in the solvent, suggesting that it is related to the density of Pb-OA on the NC surface.

The orthogonal solubility of $CsPbBr_3$ and $Pb(OA)_2$ prohibits stable electrochemical measurements or applications. An open question is whether an electrolyte solvent can be found wherein both $CsPbBr_3$ and $Pb(OA)_2$ have a low solubility. A potential candidate, shown in literature is the class of hydrofluoroethers.[25,48] Although we have measured that the solubility of the bulk can be compared to that in DCM (Appendix 6.9), we did not manage to perform electrochemical measurements without very large overpotentials (Appendix 6.20). This shows the 3rd requirement of a suitable electrolyte solvent, namely that it can dissolve electrolyte ions to achieve a sufficiently small solution resistivity. A more promising method to allow stable electrochemical applications would be to engineer NCs with different ligands, which show a much lower solubility in low-polarity solvents like DCM. Alternatively, core-shell $CsPbBr_3$ with an insoluble shell would be an interesting avenue.

6.8 Conclusions

The results presented in this work show that the electrochemical response of $CsPbBr_3$ NC films is dominated by the reduction and oxidation of Pb^{2+} complexes in solution, either as $[PbBr_n]^{2-n}$ or Pb-OA. ICP measurements show that this is due to the orthogonal solubility of $CsPbBr_3$ and the $Pb(OA)_2$-based surface ligands. Only bulk $CsPbBr_3$ films in the low-polarity solvent DCM show the absence of such electrochemical features. However, even in that case electrochemical decomposition occurs well before the conduction band can be reached.

While some solubility of Pb^{2+} complexes is thus inevitable for Pb-OA capped $CsPbBr_3$ NCs, the results clearly show that the solubility of Pb-OA is the dominant factor in determining the electrochemical stability of these films. High-polarity solvents like PC, wherein $Pb(OA)_2$ is least soluble, show the smallest irreversible change in absorption and PL of the $CsPbBr_3$ NC films.

Experimental Methods

Materials

6

Nanocrystal Synthesis and Film Preparation

Lead acetate trihydrate ($Pb(CH_3COO)_2{\cdot}3H_2O$, 99.999% trace metal basis), benzoyl bromide (97%), 1-octadecene (ODE, technical grade, 90%), toluene (anhydrous, 99.8%), methyl acetate (anhydrous, 99.5%), mercaptopropionic acid (≥99.0%), 1,8-octane dithiol (8DT, ≥97%) were purchased from Sigma-Aldrich. Oleic acid (extra pure) was purchased from Fisher Scientific. Cesium carbonate (Cs_2CO_3, Puratronic, 99.994%) was purchased from Alfa Aesar. Oleylamine (OLA, 80–90% C18, ≥96.0% (primary amine)) was purchased from Acros Organics. Methanol (anhydrous, max 0.003% H_2O, Seccosolv) was purchased from VWR international. ITO conductive substrates (20 Ohms/sq) were purchased from PGO GmbH.

Bulk Film

Cesium bromide (CsBr, 99.999% perovskite grade) and lead bromide ($PbBr_2$, 98+%) were purchased from Sigma-Aldrich. ITO conductive substrates (20 Ohms/sq) were purchased from PGO GmbH.

Electrochemistry

Propylenecarbonate (PC, anhydrous, 99.7%), dichloromethane (DCM, anhydrous, ≥99.8%), tetrahydrofuran (THF, anhydrous, ≥99.9%), acetonitrile (MeCN, anhydrous, 99.8%), benzonitrile (PhCN, anhydrous, ≥99%), tetrabutylammonium hexafluorophosphate ($TBAPF_6$, for electrochemical analysis, ≥99.0%), tetrabutylammonium bromide (TBABr, ≥98.0%) and ferrocene (98%) were purchased from Sigma-Aldrich.

ICP Measurements

Propylene carbonate (PC, anhydrous, 99.7%), dichloromethane (DCM, anhydrous, ≥99.8%), tetrahydrofuran (THF, anhydrous, ≥99.9%), acetonitrile (MeCN, anhydrous, 99.8%), benzonitrile (PhCN, anhydrous, ≥99%), N,N-dimethylformamide (DMF,

anhydrous, 99.8%), methyl acetate (anhydrous, 99.5%), ethylene carbonate (EC, anhydrous, 99%), chloroform (anhydrous, 99%), tetrachloroethene (TCE, anhydrous, ≥99.0%), methoxy perfluorobutane (HFE 7100, 99%, mixture of n- and iso-butyl isomers), dimethylsulfoxide (DMSO, anhydrous, ≥99.9%), 1-methylpyrrolidone (NMP, anhydrous, ≥99.5%), isopropanol (IPA, anhydrous, 99.5%), chlorobenzene (anhydrous, 99.8%), 1,2-dichlorobenzene (anhydrous, 99%), benzene (anhydrous, 99.8%), ethyl acetate (anhydrous, 99.8%), pyridine (anhydrous, 99.8%) diethyl carboante (DEC, anhydrous, 99%), Cesium bromide (CsBr, 99.999% perovskite grade) and lead bromide ($PbBr_2$, 98+%) were purchased from Sigma-Aldrich. Milli-Q water was obtained from a Milli-Q Advantage A10 system (Merck Millipore, 18.2 MΩ·cm, 2 ppb TOC). Methanol (anhydrous, max 0.003% H_2O, Seccosolv) was purchased from VWR international. Toluene (anhydrous, ≥99.8%), acetone (anhydrous, ≥99.8%) and ethanol (anhydrous, ≥99.8%) were purchased from VWR Chemicals. Hexane (anhydrous, >96.0%) was purchased from TCI.

Lead Oleate Synthesis

Lead(II) oxide (PbO, 99.999%), acetonitrile (MeCN, ≥99.9% Chromasolv), isopropanol (≥99.5%), triethylamine (≥99% for synthesis) and methanol (≥99.8%) were purchased from Sigma-Aldrich. Oleic acid (extra pure), trifluoroacetic acid (HTFA, ≥99.0%, for HPLC), trifluoroacetic anhydride (TFAA, ≥99.0%) were purchased from Fisher Scientific.

Cesium Oleate Synthesis

Cesium carbonate (Cs_2CO_3, Puratronic, 99.994%) was purchased from Alfa Aesar. Oleic acid (extra pure) was purchased from Fisher Scientific. Methanol (≥99.8%) was purchased from Sigma-Aldrich.

Methods

Nanocrystal Precursor Preparation

A large-scaled batch of metal precursors was prepared by combining 760 mg of $Pb(CH_3COO)_2{\cdot}3H_2O$ and 160 mg Cs_2CO_3 together with 50 mL ODE, 10 mL OLA and 3 mL OA. This mixture was attached to a Schlenk line and flushed 3 times with dry nitrogen. Whilst stirring, the mixture was then heated to 120 °C for one hour under a vacuum pressure of <0.2 mbar, to remove any water, oxygen and other volatile chemical species from the reaction mixture. The precursor was subsequently cooled down to room temperature, collected in nitrogen filled vials and stored in a nitrogen filled glovebox.

Nanocrystal Synthesis Method

The following synthesis protocol has been adapted from Imran *et al.*[12]

6.3 mL of the metal/ligand precursor solution was added to a nitrogen filled 25 mL three necked flask with a thermocouple insert, attached to a Schlenk line. Subsequently, the mixture was quickly heated to 185 °C and under vigorous stirring, 71 µL of benzoyl bromide diluted in 500 µL degassed ODE was injected into the metal precursor mixture. The mixture directly turned yellow and after exactly 10 seconds, the heating mantle was removed and the flask was quickly cooled down using an air gun. Once the mixture was at room temperature, 2 mL of anhydrous toluene was added to the reaction mixture, and

subsequently, the contents were transferred to nitrogen filled vials. The crude mixture was centrifuged at 3800 rpm for 10 minutes to get the NCs out of solution. After centrifugation, the supernatant was discarded in a glove box, and the solid pellet was redispersed in 2 mL of anhydrous toluene.
To remove most of the residual excess precursors and solvents, the NC solution was purified by the addition of 2 mL of methyl acetate to destabilize the dispersion. The cloudy solution was centrifuged at 6000 rpm for 10 minutes and after discarding the supernatant, the NC pellet was finally redispersed in 4 mL of anhydrous toluene.
An overview of the obtained sample characteristics can be found in Appendix 6.1.

Lead Oleate Synthesis Method

Lead oleate was synthesized following a procedure of Hendricks *et al.*[49]

In short, 10 grams of lead(II) oxide and 20 mL of acetonitrile are added to a 100 mL flask, which is cooled in an ice bath. Then, 0.7 mL trifluoroacetic acid and 6.2 mL trifluoroacetic anhydride are added and the mixture is stirred until all solids are completely dissolved. This solution is added to a 500 mL Erlenmeyer flask containing a mixture of 25 grams of oleic acid, 180 mL isopropanol and 10 grams of triethylamine, resulting in the formation of a white precipitate. This precipitate is completely dissolved by heating up to the point the solution refluxes slowly. Once the solution is clear, the heating is turned off and the solution is left to cool back to room temperature over time. Subsequently, the solution is stored in the freezer for a day to crystallize the lead oleate out of solution.
The formed lead oleate is then washed 3 times over a glass filter with 300 mL of methanol whilst stirring the slurry with a glass rod to remove any side products and unreacted precursors. The solids are then dried under vacuum for a day in order to remove all volatile solvents and subsequently stored in a nitrogen filled glovebox.

Cesium Oleate Synthesis Method

Cesium oleate was synthesized following a procedure of Bohn *et al.*[50]

In short, 33 mg of Cs_2CO_3 and 10 mL of oleic acid are added to a 25 mL three necked flask. The contents are then heated to 100 °C and kept at this temperature until all Cs_2CO_3 is fully reacted away. The solution is subsequently cooled down to room temperature and then centrifuged to collect all the precipitated cesium oleate. The liquid fraction is then decanted and the solids are washed 3 times with 50 mL of methanol and subsequently centrifuged again in order to remove all side products and unreacted precursors. The solids are then dried under vacuum for a day in order to remove all solvents, and stored in a nitrogen filled glovebox.

Nanocrystal Thin Film Preparation

ITO conductive substrates were cleaned by rinsing them thoroughly with isopropanol. Subsequently, the substrates were added to a methanolic solution of 1 $_{vol}$% MPA, to functionalize the oxide layer with surface thiol groups. After a day in the MPA solution, the substrates were submerged in clean methanol to remove excess MPA. On the functionalized, dry substrates 50 µL of NC solution was drop-cast and the toluene was

evaporated over time without application of a vacuum or heating. To cross-link the NCs, the dry films were submerged in a 0.1 M 8DT solution in methyl acetate. Subsequently, the film was dipped in clean methyl acetate to remove residual ligands. To counter NC degradation, the films were directly put under vacuum, to remove any residual solvents. The films were thereafter stored in a nitrogen-filled glovebox until use.
For the preparation of NC films on interdigitated gold electrodes, the electrodes were cleaned with technical grade acetone and subsequently, in a glove box, the films were drop casted by adding 100 µL of NC solution on the substrate. After all the solvent evaporated, a second 100 µL of NC solution was drop casted. Once all solvent evaporated, the NC film was cross-linked in the same manner as the ITO-based electrode films.

Bulk Film Preparation

ITO conductive substrates were cleaned by rinsing them thoroughly with isopropanol. Subsequently, the substrates were mounted inside an AJA ATC Orion 4 thermal evaporator. Layer by layer, 50 Å CsBr (source heated to 394 °C) and 44 Å $PbBr_2$ (source heated to 272 °C) were alternately deposited at an evaporation rate of 0.3 Å/s. After a total of 100 cycles (50 cycles per material), the evaporation was stopped and the films were brought into a nitrogen filled glovebox. Here, the films were thermally annealed on a hot plate at 100 °C for 1 hour.
An overview of the obtained sample characteristics can be found in Appendix 6.2.

Spectro-Electrochemical Measurements

All electrochemical and spectro-electrochemical measurements were performed in a nitrogen-filled glovebox with H_2O and O_2 levels of respectively ≤0.5 ppm and ≤0.1 ppm. All measurements were performed with an Autolab PGSTAT128N potentiostat with a bipotentiostat BA module. The electrochemical cell consisted of a cuvette, containing an electrolyte (0.1 M $TBAPF_6$ in PC) in which the NC working electrode (WE), a Ag pseudo-reference electrode (RE) and a Pt sheet as a counter electrode (CE) were submerged. In general, the CVs were repeated three times with a scan speed of 10 mV/s. Directly after measurements using the Ag pseudo-reference electrode, the reference electrode was calibrated with a ferrocene couple.

The absorbance and photoluminescence (PL) changes in the spectro-electrochemical measurements were measured as a function of the applied electrochemical potential with a fibre-based UV–vis spectrometer (Ocean Optics USB2000) using an Ocean Optics DH 2000 lamp as a light source.

Optical Characterization

Optical characterization was performed by using gastight 1 cm quartz cuvettes loaded in a N_2-filled glovebox. Absorption spectra were recorded on a PerkinElmer Lambda 365.

Emission spectra were obtained using an Edinburgh Instruments FLS980 spectrometer. A Xenon arc lamp from XBO was used as the excitation source.

Elemental Analysis for K_{sp} Determination Using ICP-OES

ICP-OES was performed on a Prodigy 7 spectrometer (LEEMAN LABORATORIES Ltd.). The samples were digested overnight in aqua regia prior to the ICP measurements. All chemical analyses performed by ICP-OES were affected by a systematic error of about 5%. The ratio of HCl to HNO_3 was 3:1 (v/v).

The analysis of the samples is based on the spectral lines at 217 nm and 220 nm (for Pb) and 455 nm and 672 nm (for Cs). The measured elemental concentrations based on the individual spectral lines were found to be in reasonable agreement with each other.

The ICP-OES instrument was calibrated for elemental Pb concentrations of 0.005-20 ppm and Cs concentrations of 20-200 ppm. Based on blank control sample experiments and the relative standard deviation of the measurements, the practical detection limits for Pb and Cs were taken as 0.05 ppm and 20 ppm respectively.

Structural Characterization

TEM images were acquired using a JEOL JEM1400 transmission electron microscope operating at 120 kV, equipped with an SSD-EDX detector for spot (>75 nm) analysis.

SEM images were acquired using a JEOL JSM-6010 scanning electron microscope. To prevent charging of the thin films, the ITO coated glass substrate was contacted with carbon tape on the sample holder. Secondary electron images were acquired at 8 kV.

XRD measurements were performed using a Bruckner D8 ADVANCE diffractometer (Cu Kα, λ = 0.15406 nm). The NC samples were dropcasted on zero diffraction (911) silicon substrates.

XPS measurements were performed using a Thermo Scientific K-Alpha system, equipped with an Al Ka source (1487 eV). The elemental surface composition of NC thin film electrodes was analyzed using a spot size of 400 µm. A flood gun was used to prevent charging of the sample during measurement. XPS depth-profiles were measured by etching the thin films with an Ar^+ ion beam, at a rate of 0.2 nm/s (*versus* a Ta_2O_5 reference).

References

1. Al Ghaithi, A. O.; Aravindh, S. A.; Hedhili, M. N.; Ng, T. K.; Ooi, B. S.; Najar, A. Optical Properties and First-Principles Study of $CH_3NH_3PbBr_3$ Perovskite Structures. ACS Omega 2020, 5 (21), 12313–12319.
2. Zhao, S.; Wu, J.; Chi, X.; Sui, N.; Kang, Z.; Zhou, Q.; Zhang, H.; Zhao, B.; Wang, Y. Optical Properties of Inorganic Halide Perovskite Nanorods: Role of Anisotropy, Temperature, Pressure, and Nonlinearity. J. Phys. Chem. C 2022, 126 (4), 2003–2012.
3. Yokoyama, M.; Sato, R.; Enomoto, J.; Oshita, N.; Kimura, T.; Kikuchi, K.; Asakura, S.; Umemoto, K.; Masuhara, A. Water-Assisted Perovskite Quantum Dots with High Optical Properties. Technologies 2022, 10 (1), 11.
4. Guan, X.; Lei, Z.; Yu, X.; Lin, C.; Huang, J.; Huang, C.; Hu, L.; Li, F.; Vinu, A.;

Yi, J.; Wu, T. Low-Dimensional Metal-Halide Perovskites as High-Performance Materials for Memory Applications. Small 2022, 18 (38), 2203311.

5. Ren, X.; Zhang, X.; Xie, H.; Cai, J.; Wang, C.; Chen, E.; Xu, S.; Ye, Y.; Sun, J.; Yan, Q.; Guo, T. Perovskite Quantum Dots for Emerging Displays: Recent Progress and Perspectives. Nanomaterials 2022, 12 (13), 2243.
6. Umemoto, K.; Yokoyama, M.; Kikuchi, K.; Kimura, T.; Oshita, N.; Sato, R.; Asakura, S.; Masuhara, A. Continuous-Flow Synthesis of Ultrahigh Luminescent Perovskite Nanocrystals Using Forced Thin Film Reactor and Application for Light-Emitting Diodes. Appl. Phys. Express 2022, 15 (2), 025503.
7. Lee, Y. J.; Han, J. S.; Lee, D. E.; Lee, T. H.; Kim, J. Y.; Suh, J. M.; Lee, J. H.; Im, I. H.; Kim, S. J.; Kwak, K. J.; Jang, H. W. High Hole Mobility Inorganic Halide Perovskite Field-Effect Transistors with Enhanced Phase Stability and Interfacial Defect Tolerance. Adv. Electron. Mater. 2022, 8 (1), 2100624.
8. Zhang, X.; Turiansky, M. E.; Van de Walle, C. G. Correctly Assessing Defect Tolerance in Halide Perovskites. J. Phys. Chem. C 2020, 124 (11), 6022–6027.
9. du Fossé, I.; Mulder, J. T.; Almeida, G.; Spruit, A. G. M.; Infante, I.; Grozema, F. C.; Houtepen, A. J. Limits of Defect Tolerance in Perovskite Nanocrystals: Effect of Local Electrostatic Potential on Trap States. J. Am. Chem. Soc. 2022, 144 (25), 11059–11063.
10. Protesescu, L.; Yakunin, S.; Bodnarchuk, M. I.; Krieg, F.; Caputo, R.; Hendon, C. H.; Yang, R. X.; Walsh, A.; Kovalenko, M. V. Nanocrystals of Cesium Lead Halide Perovskites ($CsPbX_3$, X = Cl, Br, and I): Novel Optoelectronic Materials Showing Bright Emission with Wide Color Gamut. Nano Lett. 2015, 15 (6), 3692–3696.
11. Kovalenko, M. V.; Protesescu, L.; Bodnarchuk, M. I. Properties and Potential Optoelectronic Applications of Lead Halide Perovskite Nanocrystals. Science 2017, 358 (6364), 745–750.
12. Imran, M.; Caligiuri, V.; Wang, M.; Goldoni, L.; Prato, M.; Krahne, R.; De Trizio, L.; Manna, L. Benzoyl Halides as Alternative Precursors for the Colloidal Synthesis of Lead-Based Halide Perovskite Nanocrystals. J. Am. Chem. Soc. 2018, 140 (7), 2656–2664.
13. Akkerman, Q. A.; Nguyen, T. P. T.; Boehme, S. C.; Montanarella, F.; Dirin, D. N.; Wechsler, P.; Beiglböck, F.; Rainò, G.; Erni, R.; Katan, C.; Even, J.; Kovalenko, M. V. Controlling the Nucleation and Growth Kinetics of Lead Halide Perovskite Quantum Dots. Science 2022, 377 (6613), 1406–1412.
14. Lorenzon, M.; Sortino, L.; Akkerman, Q.; Accornero, S.; Pedrini, J.; Prato, M.; Pinchetti, V.; Meinardi, F.; Manna, L.; Brovelli, S. Role of Nonradiative Defects and Environmental Oxygen on Exciton Recombination Processes in $CsPbBr_3$ Perovskite Nanocrystals. Nano Lett. 2017, 17 (6), 3844–3853.
15. Imran, M.; Ijaz, P.; Goldoni, L.; Maggioni, D.; Petralanda, U.; Prato, M.; Almeida, G.; Infante, I.; Manna, L. Simultaneous Cationic and Anionic Ligand Exchange for Colloidally Stable $CsPbBr_3$ Nanocrystals. ACS Energy Lett. 2019, 4 (4), 819–824.
16. Zaccaria, F.; Zhang, B.; Goldoni, L.; Imran, M.; Zito, J.; Van Beek, B.; Lauciello, S.; De Trizio, L.; Manna, L.; Infante, I. The Reactivity of $CsPbBr_3$Nanocrystals toward Acid/Base Ligands. ACS Nano 2022, 16 (1), 1444–1455.
17. Yan, F.; Tan, S. T.; Li, X.; Demir, H. V. Light Generation in Lead Halide Perovskite Nanocrystals: LEDs, Color Converters, Lasers, and Other Applications. Small

2019, 15 (47), 1–15.
18. Alahbakhshi, M.; Mishra, A.; Haroldson, R.; Ishteev, A.; Moon, J.; Gu, Q.; Slinker, J. D.; Zakhidov, A. A. Bright and Effectual Perovskite Light-Emitting Electrochemical Cells Leveraging Ionic Additives. ACS Energy Lett. 2019, 4 (12), 2922–2928.
19. Liu, Y.; Tang, S.; Fan, J.; Gracia-Espino, E.; Yang, J.; Liu, X.; Kera, S.; Fahlman, M.; Larsen, C.; Wågberg, T.; Edman, L.; Wang, J. Highly Soluble $CsPbBr_3$ Perovskite Quantum Dots for Solution-Processed Light-Emission Devices. ACS Appl. Nano Mater. 2021, 4 (2), 1162–1174.
20. Zhang, C.; Wang, S.; Li, X.; Yuan, M.; Turyanska, L.; Yang, X. Core/Shell Perovskite Nanocrystals: Synthesis of Highly Efficient and Environmentally Stable $FAPbBr_3$/$CsPbBr_3$ for LED Applications. Adv. Funct. Mater. 2020, 30 (31), 1910582.
21. Mulder, J. T.; du Fossé, I.; Alimoradi Jazi, M.; Manna, L.; Houtepen, A. J. Electrochemical P-Doping of $CsPbBr_3$ Perovskite Nanocrystals. ACS Energy Lett. 2021, 6 (7), 2519–2525.
22. Heo, S.; Roh, K.; Zhang, F.; Tignor, S. E.; Bocarsly, A. B.; Kahn, A.; Rand, B. P. Electrochemically N-Doped $CsPbBr_3$ Nanocrystal Thin Films. ACS Energy Lett. 2022, 7 (1), 211–216.
23. Jeong, H. W.; Zsigmond, T. S.; Samu, G. F.; Janáky, C. Sacrificial Agent Gone Rogue : Electron-Acceptor-Induced Degradation of $CsPbBr_3$ Photocathodes. ACS Energy Lett. 2022, 7 (1), 417–424.
24. Samu, G. F.; Scheidt, R. A.; Kamat, P. V.; Janáky, C. Electrochemistry and Spectroelectrochemistry of Lead Halide Perovskite Films: Materials Science Aspects and Boundary Conditions. Chem. Mater. 2018, 30 (3), 561–569.
25. Jha, S.; Hasan, M.; Khakurel, N.; Ryan, C. A.; McMullen, R.; Mishra, A.; Malko, A. V.; Zakhidov, A. A.; Slinker, J. D. Electrochemical Characterization of Halide Perovskites: Stability & Doping. Mater. Today Adv. 2022, 13, 100213.
26. Ravi, V. K.; Markad, G. B.; Nag, A. Band Edge Energies and Excitonic Transition Probabilities of Colloidal $CsPbX_3$ (X = Cl, Br, I) Perovskite Nanocrystals. ACS Energy Lett. 2016, 1 (4), 665–671.
27. Xu, Y. F.; Yang, M. Z.; Chen, B. X.; Wang, X. D.; Chen, H. Y.; Kuang, D. Bin; Su, C. Y. A $CsPbBr_3$ Perovskite Quantum Dot/Graphene Oxide Composite for Photocatalytic CO_2 Reduction. J. Am. Chem. Soc. 2017, 139 (16), 5660–5663.
28. Wang, Q.; Tao, L.; Jiang, X.; Wang, M.; Shen, Y. Graphene Oxide Wrapped $CH_3NH_3PbBr_3$ Perovskite Quantum Dots Hybrid for Photoelectrochemical CO_2 Reduction in Organic Solvents. Appl. Surf. Sci. 2019, 465 (August 2018), 607–613.
29. Li, L.; Gan, L.; Zhang, Z. Encapsulation Strategy on All Inorganic Perovskites for Stable and Efficient Photoelectrocatalytic Water Splitting. Adv. Mater. Interfaces 2021, 8 (13).
30. Wang, X. D.; Huang, Y. H.; Liao, J. F.; Wei, Z. F.; Li, W. G.; Xu, Y. F.; Chen, H. Y.; Kuang, D. Bin. Surface Passivated Halide Perovskite Single-Crystal for Efficient Photoelectrochemical Synthesis of Dimethoxydihydrofuran. Nat. Commun. 2021, 12 (1), 1–9.
31. Qian, X.; Chen, Z.; Yang, X.; Zhao, W.; Liu, C.; Sun, T.; Zhou, D.; Yang, Q.; Wei, G.; Fan, M. Perovskite Cesium Lead Bromide Quantum Dots: A New Efficient Photocatalyst for Degrading Antibiotic Residues in Organic System. J. Clean.

Prod. 2020, 249, 119335.
32. Chen, K.; Qi, K.; Zhou, T.; Yang, T.; Zhang, Y.; Guo, Z.; Lim, C. K.; Zhang, J.; Žutic, I.; Zhang, H.; Prasad, P. N. Water-Dispersible $CsPbBr_3$ Perovskite Nanocrystals with Ultra-Stability and Its Application in Electrochemical CO2 Reduction. Nano-Micro Lett. 2021, 13 (1), 1–13.
33. Gualdrón-Reyes, A. F.; Mesa, C. A.; Giménez, S.; Mora-Seró, I. Application of Halide Perovskite Nanocrystals in Solar-Driven Photo(Electro)Catalysis. Sol. RRL 2022, 6 (7), 2200012.
34. Kang, W.; Tsai, Y.; Ji, Y.; Yi, R.; Wang, Y.; Shen, H.; Chen, X.; Hsu, Y.; Lu, C.; Yang, Z.; Su, H. Perovskite Light-Emitting Electrochemical Cells Employing Electron Injection/Transport Layers of Ionic Transition Metal Complexes. Chem. – A Eur. J. 2021, 27 (71), 17785–17793.
35. Dong, Q.; Lei, L.; Mendes, J.; So, F. Operational Stability of Perovskite Light Emitting Diodes. JPhys Mater. 2020, 3 (1).
36. Yuan, Y.; Wang, Q.; Shao, Y.; Lu, H.; Li, T.; Gruverman, A.; Huang, J. Electric-Field-Driven Reversible Conversion Between Methylammonium Lead Triiodide Perovskites and Lead Iodide at Elevated Temperatures. Adv. Energy Mater. 2016, 6 (2), 1501803.
37. Kavan, L. Electrochemistry and Perovskite Photovoltaics. Curr. Opin. Electrochem. 2018, 11, 122–129.
38. Mulder, J. T.; du Fossé, I.; Jazi, M. A.; Manna, L.; Houtepen, A. J. Supporting Information for Electrochemical P-Doping of $CsPbBr_3$ Perovskite Nanocrystals. ACS Energy Lett. 2021, 6 (7), 2519–2525.
39. Bard, A. J.; Faulkner, L. R. Electrochemical Methods: Fundamentals and Applications, Second edi.; Wiley, 2000.
40. Bergamini, L.; Sangiorgi, N.; Gondolini, A.; Sanson, A. $CsPbBr_3$ for Photoelectrochemical Cells. Sol. Energy 2020, 212 (October), 62–72.
41. Xie, S.; Osherov, A.; Bulović, V. All-Vacuum-Deposited Inorganic Cesium Lead Halide Perovskite Light-Emitting Diodes. APL Mater. 2020, 8 (5), 1–6.
42. Guo, L.; Searson, P. C. On the Influence of the Nucleation Overpotential on Island Growth in Electrodeposition. Electrochim. Acta 2010, 55 (13), 4086–4091.
43. Pei, A.; Zheng, G.; Shi, F.; Li, Y.; Cui, Y. Nanoscale Nucleation and Growth of Electrodeposited Lithium Metal. Nano Lett. 2017, 17 (2), 1132–1139.
44. Clever, H. L.; Johnston, F. J. The Solubility of Some Sparingly Soluble Lead Salts: An Evaluation of the Solubility in Water and Aqueous Electrolyte Solution. J. Phys. Chem. Ref. Data 1980, 9 (3), 751–784.
45. Chin, S.-H.; Choi, J. W.; Hu, Z.; Mardegan, L.; Sessolo, M.; Bolink, H. J. Tunable Luminescent Lead Bromide Complexes. J. Mater. Chem. C 2020, 8 (45), 15996–16000.
46. Boehme, S. C.; Azpiroz, J. M.; Aulin, Y. V.; Grozema, F. C.; Vanmaekelbergh, D.; Siebbeles, L. D. A.; Infante, I.; Houtepen, A. J. Density of Trap States and Auger-Mediated Electron Trapping in CdTe Quantum-Dot Solids. Nano Lett. 2015, 15 (5), 3056–3066.
47. van der Stam, W.; du Fossé, I.; Grimaldi, G.; Monchen, J. O. V.; Kirkwood, N.; Houtepen, A. J. Spectroelectrochemical Signatures of Surface Trap Passivation on CdTe Nanocrystals. Chem. Mater. 2018, 30 (21), 8052–8061.

48. Hasan, M.; Venkatesan, S.; Lyashenko, D.; Slinker, J. D.; Zakhidov, A. Solvent Toolkit for Electrochemical Characterization of Hybrid Perovskite Films. Anal. Chem. 2017, 89 (18), 9649–9653.
49. Hendricks, M. P.; Campos, M. P.; Cleveland, G. T.; Jen-La Plante, I.; Owen, J. S. A Tunable Library of Substituted Thiourea Precursors to Metal Sulfide Nanocrystals. Science 2015, 348 (6240), 1226–1230.
50. Bohn, B. J.; Tong, Y.; Gramlich, M.; Lai, M. L.; Döblinger, M.; Wang, K.; Hoye, R. L. Z.; Müller-Buschbaum, P.; Stranks, S. D.; Urban, A. S.; Polavarapu, L.; Feldmann, J. Boosting Tunable Blue Luminescence of Halide Perovskite Nanoplatelets through Postsynthetic Surface Trap Repair. Nano Lett. 2018, 18 (8), 5231–5238.

Appendix 6.1

$CsPbBr_3$ Nanocrystal Characteristics

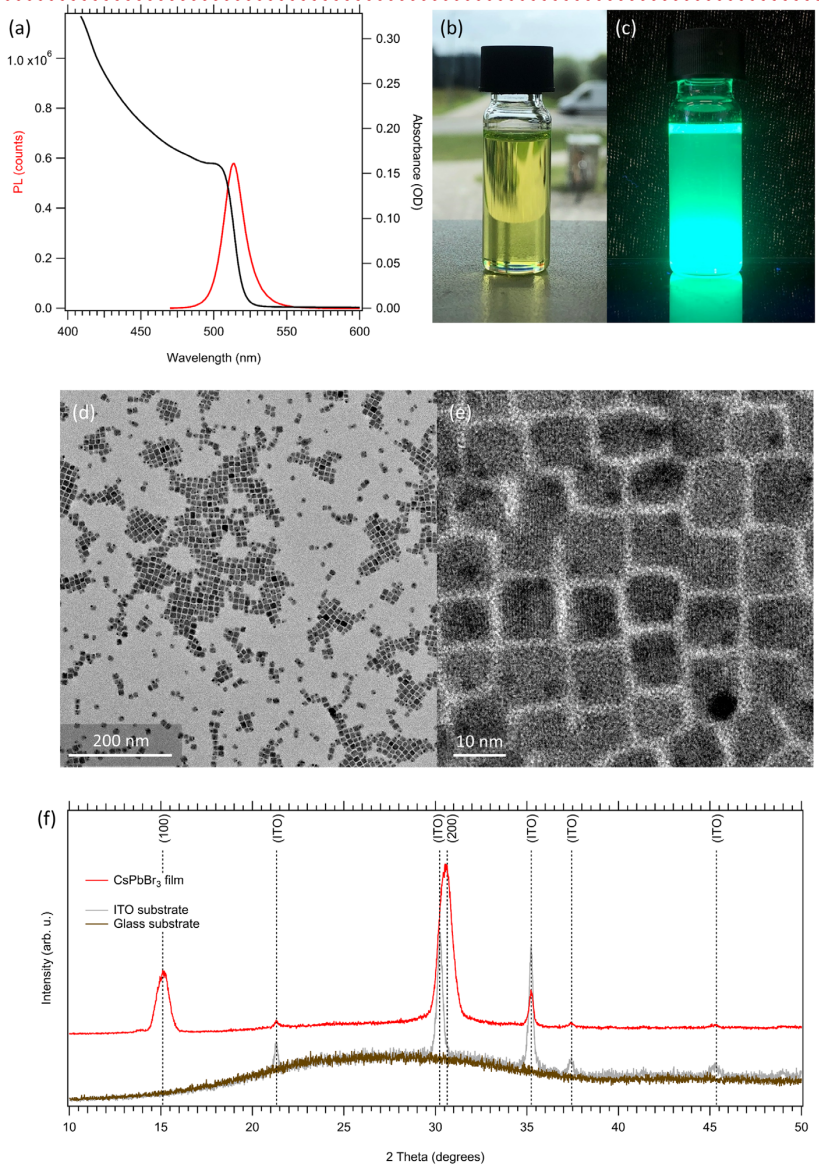


Figure A6.1. (a) Absorbance and emission spectra of $CsPbBr_3$ nanocrystals. (b) Photographs of a $CsPbBr_3$ nanocrystal sample under ambient and (c) UV illumination. (d) Large area and (e) small area TEM images of the $CsPbBr_3$ nanocrystals, showcasing the uniformity and crystallinity of the material. (f) An XRD of a cubic $CsPbBr_3$ nanocrystal film, indicating a phase-pure sample, unaffected by the film formation procedure.

Appendix 6.2

$CsPbBr_3$ Bulk Film Characteristics

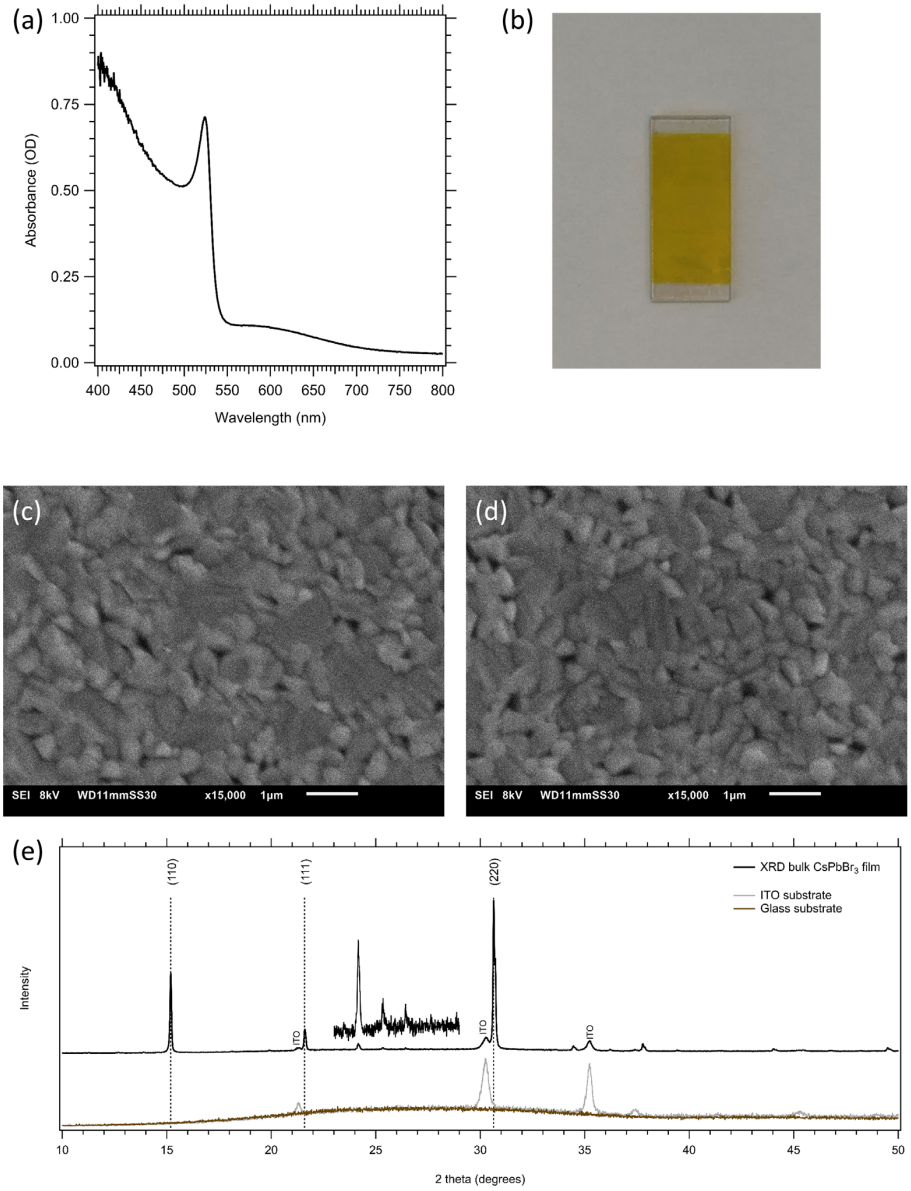


Figure A6.2. (a) Absorbance spectrum of an evaporated $CsPbBr_3$ bulk film, pictured in (b). (c, d) SEM images of an evaporated $CsPbBr_3$ film, showcasing the large $CsPbBr_3$ grains. (e) An XRD diffractogram, showing that the material evaporated is orthorhombic $CsPbBr_3$, best identified through the additional reflections between 24 and 28 degrees (see inset).

Appendix 6.3

Chronoamperometry and XPS – $CsPbBr_3$ Nanocrystals - PC

Figure A6.3 shows the chronoamperograms, and Figure A6.4 the XPS depth-profiles of four different $CsPbBr_3$ nanocrystal thin films after applying a specific potential for 120 seconds. From the depth-profiles of the films held at -0.95 V, -1.30 V and -1.80 V, it can be seen that the amount of reduced lead ions depends on the potential, and increases with more negative potentials. The chronoamperograms show largely different behavior for the charge injection in the three films. The film held at -0.95 V shows a relatively late maximum of injected charge compared to the film held at -1.30 V. For the film held at -0.95 V, the nucleation of Pb^0 clusters is more difficult. The larger nucleation overpotential results in a postponed maximum of the injected charge. When a more negative -1.80 V is applied to the electrode, the lack of an overpotential results in a large amount of injected charge. When holding a film that is scanned thrice (between -1.80 V and 0 V) at 0 V for 120 seconds, the injected positive charge is small and lead metal remains clearly visible through XPS. This indicates that the lead metal clusters are not fully re-oxidized (even after 120 seconds), explaining why the charge injection for the second and following CV scans using PC start at the same potential as free lead reduction. There is namely no more nucleation overpotental.

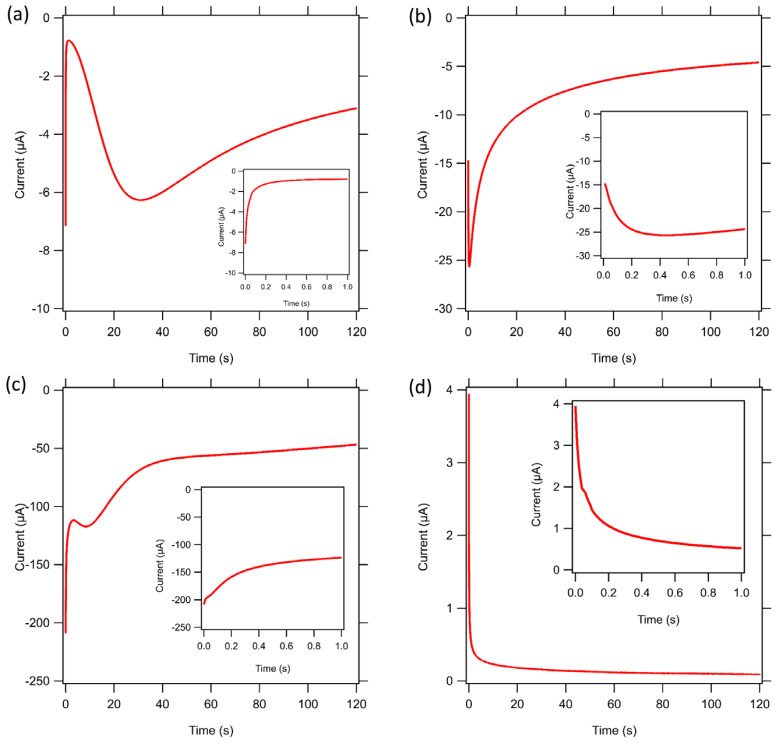


Figure A6.3. Chronoamperograms NC films held for 120 seconds at (a) -0.95 V, (b) -1.30 V, (c) -1.80 V and (d) after three CV cycles at 0 V.

Appendix 6.3

Chronoamperometry and XPS – $CsPbBr_3$ Nanocrystals - PC

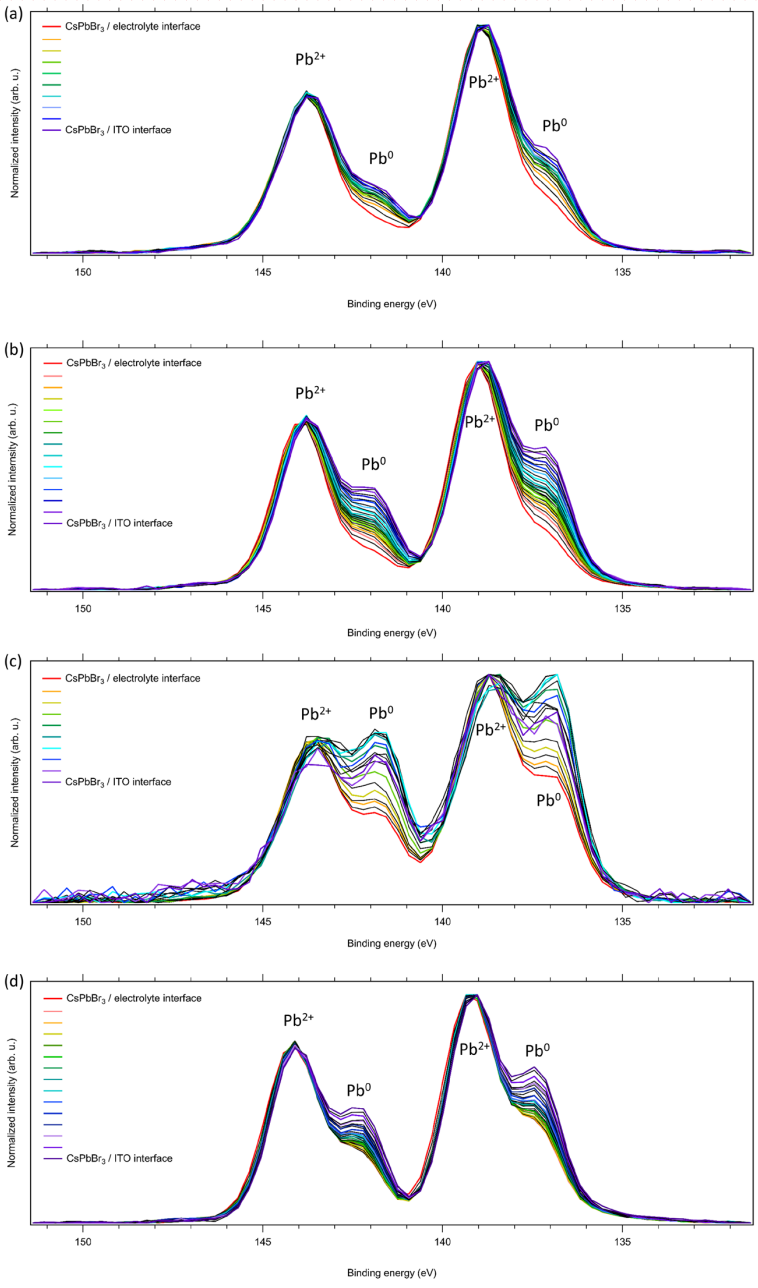


Figure A6.4. XPS depth-profiles of NC films held for 120 seconds at (a) -0.95 V, (b) -1.30 V, (c) -1.80 V and (d) after three CV cycles at 0 V.

Appendix 6.4

XRD on XPS Samples

The formation of Pb^0 metal clusters is difficult to detect through XRD, as XRD measurements taken on the same films that were used for the XPS and chronoamperometry measurements do not show significant changes (Figure A6.5). Compared to a pristine film that has been soaked in the electrolyte for the best comparison (red), practically no differences can be observed. Only for the film held at -1.30 V, a small signal of metallic lead is observed. The XPS and Chronoamperometry measurements are therefore more indicative.

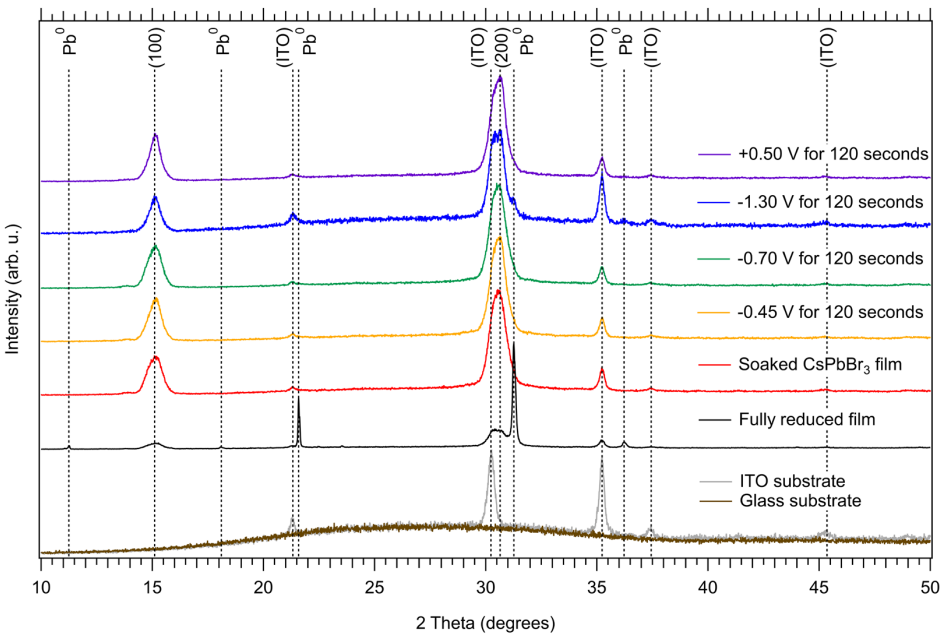


Figure A6.5. XRD diffractograms of the films used for XPS measurements (Appendix 6.3). This figure shows that observing Pb^0 by means of XRD is difficult, and only possible for significantly reduced films.

Appendix 6.5

Electrochemistry – $PbBr_2$ - PC

I: $Pb^{2+} + 2e^- \rightarrow Pb^0$ (as free ions, or dissolved Br^- complexes)

III: $Pb^0 + nBr^- \rightarrow [PbBr_n]^{(2-n)} + 2e^-$ ($n_A > n_B > n_C > n_D$)

IV: $PbBr_2 + 2e^- \rightarrow Pb^0 + 2\ Br^-$

V: $2\ Br^- \rightarrow Br_2 + 2e^-$

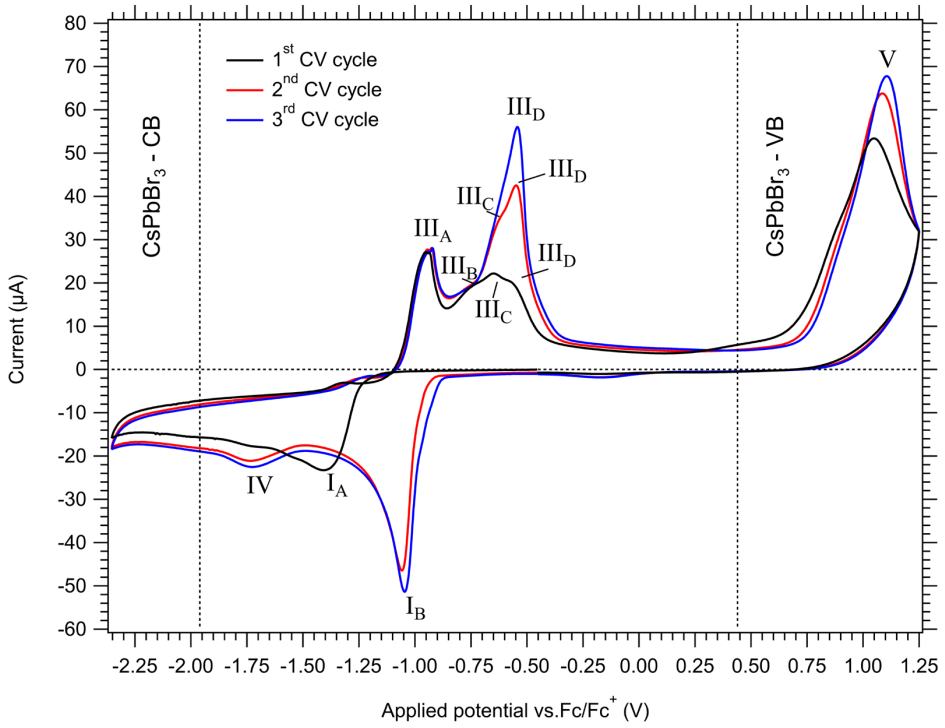


Figure A6.6. A CV of a saturated solution of $PbBr_2$ in PC. Most CV features have been assigned according to Figure 6.2 of the main text. As no $CsPbBr_3$ is present, reduction signal comes from a similar reaction, in this case the electrochemical decomposition of $PbBr_2$ (reaction IV). Additionally, the bromide oxidation reaction is observed at V, as mentioned in the main text, this reaction takes place at more positive potentials than the location of the valence band (VB) of $CsPbBr_3$.

Appendix 6.6

Electrochemistry – $Pb(OA)_2$ - DCM

From the reduction potential of free $Pb(OA)_2$ in DCM, we could conclude that indeed, the species to reduce first in the electrochemical measurements using DCM is free Pb^{2+} in solution, in this case bound to oleate ligands in order to facilitate its dissolution in DCM. Interestingly, and left unexplained, CV measurements on a solution of $Pb(OA)_2$ in DCM do not only show a reduction peak in the negative scan direction, but also one in the positive scan direction. This effect is not related to the initial formation of Pb^0 metal clusters or the decomposition of $Pb(OA)_2$, as in the second (and following) CV scan(s), the same behavior is observed.

I: $Pb^{2+} + 2e^- \rightarrow Pb^0$

VI: $Pb^0 + 2\ OA^- \rightarrow Pb(OA)_2 + 2e^-$

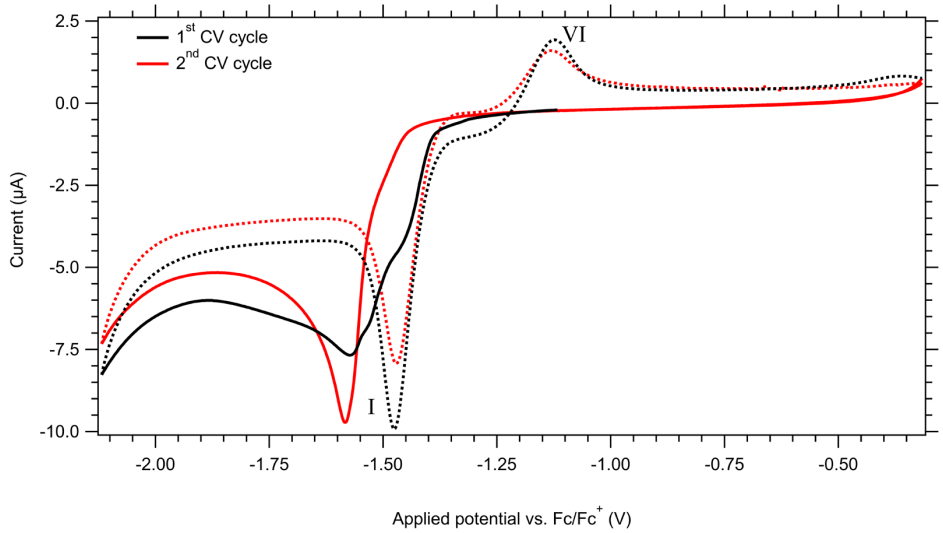


Figure A6.7. A CV of $Pb(OA)_2$ in DCM, with a scan speed of 10 mV/s and $TBAPF_6$ as electrolyte salt.

Appendix 6.7

ICP $CsPbBr_3$ Bulk - Samples



Figure A6.8. Photographs of all samples used for the determination of the bulk K_{sp}. The orange color indicates the formation of $CsPbBr_3$ from the white precursors (CsBr and $PbBr_2$).

Appendix 6.8

ICP $CsPbBr_3$ Bulk - XRD

In order to confirm that indeed $CsPbBr_3$ is the most stable crystal phase, XRD was performed on the formed solids of some of the orange samples (acetonitrile, methylacetate, HFE and hexane), as well as two samples that remained white (water and pyridine).
As can be seen in Figure A6.9, all four orange samples measured show identical diffraction patterns, corresponding with practically phase-pure orthorhombic $CsPbBr_3$. This strengthens the conclusion that what we measured is indeed the bulk solubility product of $CsPbBr_3$ in the given solvent. The white samples in water and pyridine show XRD reflections that do not correspond to CsBr and $PbBr_2$, indicating that another crystal phase has the lowest solubility, resulting in a different Cs:Pb ratio in solution. Interestingly, when the water is evaporated from the white sample, orange $CsPbBr_3$ appears, as shown in Figure A6.10b. From these observations, we conclude that, as long as the precipitate wetted by the solvent is orange, we measure the bulk solubility product of $CsPbBr_3$.

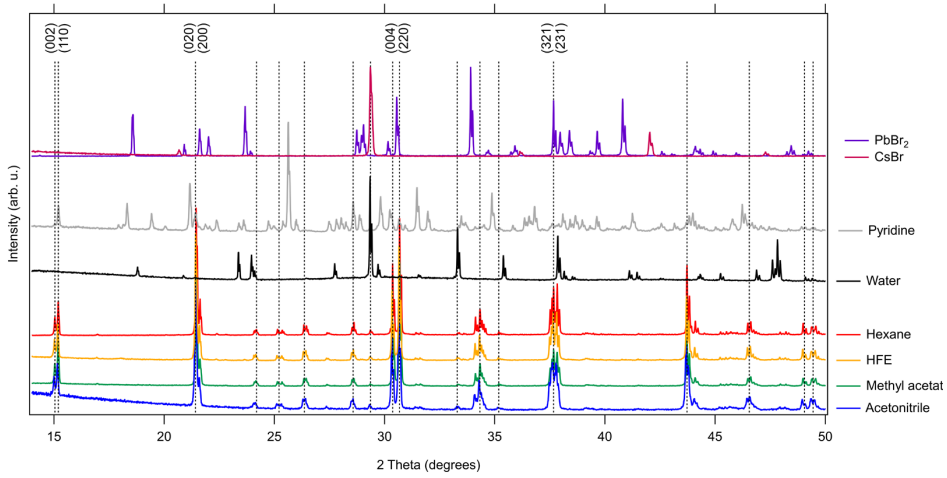


Figure A6.9. XRD diffractograms of samples shown in Figure A6.8, showcasing that the orange precipitates correspond to phase-pure orthorhombic $CsPbBr_3$. The white precipitates are neither $CsPbBr_3$, nor directly related to the precursors used.

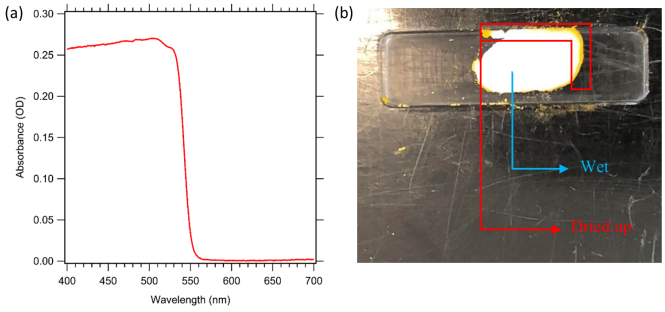


Figure A6.10. (a) The absorbance spectrum of the orange $CsPbBr_3$ powder, obtained from adding equimolar amounts of CsBr and $PbBr_2$ to hexane. (b) A picture of the white sample originating from water, showcasing the formation of orange $CsPbBr_3$ once the water evaporates from the solids.

Appendix 6.9

ICP $CsPbBr_3$ Bulk – Graphs

Figure A6.11 shows the K_{sp} and expected stabilization of $CsPbBr_3$ in the solvents mentioned in Table A6.1 (Appendix 6.10). From here it is clear that the best solvents are, in general, the less polar ones. In most of the non-polar solvents, no Pb was detected within the measurement error. Solvents generally used to dissolve perovskite precursors (9: DMF, 15: DMSO and 16: NMP) show the understandably highest solubility and hence the lowest stabilization.

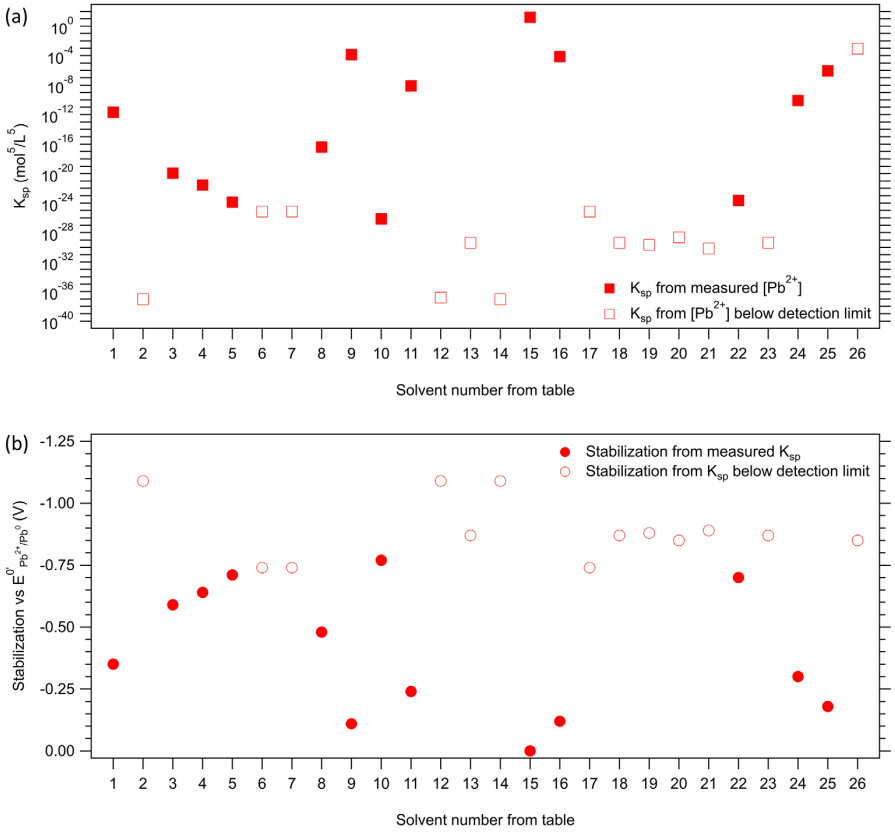


Figure A6.11. (a) The obtained K_{sp} values for bulk $CsPbBr_3$ in the solvents mentioned in Table A6.1. All Pb concentrations measured above the detection limit are shown with filled squares. The empty squares resemble K_{sp} values that are equal or lower than the indicated value, as the measured Pb concentration was below the detection limit. (b) The expected electrochemical stabilization *versus* free Pb^{2+} in solution, obtained from the K_{sp} values for bulk $CsPbBr_3$ in the solvents mentioned in Table A6.1. The stabilization from measured K_{sp} values are shown as filled circles. K_{sp} values from measurements below the detection limit are shown as empty circles. Note, the stabilization in those solvents is equal to, or larger than the indicated value.

Appendix 6.10

ICP $CsPbBr_3$ Bulk – Values

Table A6.1. The saturation concentration of $CsPbBr_3$ in a number of solvents, measured through Pb ICP-OES (and Cs ICP-OES, not used due to a higher detection limit than that of Pb). With these values, the K_{sp} of $CsPbBr_3$ was determined, and with that number, the expected electrochemical stabilization was determined. All samples not indicated in bold had a lead or Cs concentration below the detection limit. Therefore, the K_{sp} should be lower, and the stabilization larger than the reported values.

Table A6.1-I. List of all samples used in the figures displayed in this article.

	Solvent	Volume used (mL)	[Pb] from ICP (ppm)	Saturation [Pb] (mM)	Calculated K_{sp} (mol^5/L^5)	Expected stabilization *vs.* $E^{0'}_{Pb^{2+}/Pb}$ (V)	[Cs] from ICP (ppm)	Saturation [Cs] (mM)
1	Propylene carbonate	1.99	49.075	2.38E+00	2.07E-12	0.35	≤20.000	≤1.51E+00
2	Dichloro-methane	238.12	≤0.050	≤2.03E-05	≤9.23E-38	≥1.09	≤20.000	≤1.26E-02
3	Acetonitrile	24.61	13.504	5.30E-02	1.13E-20	0.59	21.979	1.34E-01
4	Benzonitrile	19.75	5.193	2.54E-02	2.84E-22	0.64	≤20.000	≤1.52E-01
5	Tetrahydro-furan	29.96	2.690	8.67E-03	1.32E-24	0.71	≤20.000	≤1.00E-01
6	Methanol	1.00	≤0.050	≤4.83E-03	≤7.07E-26	≥0.74	≤20.000	≤3.01E+01
7	Ethanol	1.00	≤0.050	≤4.83E-03	≤7.07E-26	≥0.74	≤20.000	≤3.01E+00
8	Acetone	1.00	2.833	2.73E-01	4.13E-17	0.48	≤20.000	≤3.01E+00
9	Dimethyl-formamide	0.05	45.332	8.75E+01	1.39E-04	0.11	≤20.000	≤6.02E+01
10	Methyl acetate	7.00	0.222	3.07E-03	7.32E-27	0.77	≤20.000	≤4.30E-01
11	Ethylene carbonate	0.10	12.924	1.25E+01	8.16E-09	0.24	≤20.000	≤3.01E+01
12	Chloroform	215.16	≤0.050	≤2.24E-05	≤1.53E-37	≥1.09	≤20.000	≤1.40E-02
13	Tetra-chloroethene	7.00	≤0.050	≤6.89E-04	≤4.21E-30	≥0.87	≤20.000	≤4.30E-01
14	HFE 7100	238.19	≤0.050	≤2.03E-05	≤9.22E-38	≥1.09	≤20.000	≤1.26E-02
15	Dimethyl-sulfoxide	0.05	467.02	9.02E+02	1.61E+01	-	53.029	1.60E+02
16	n-Methyl-pyrrolidone	0.05	40.043	7.73E+01	7.45E-05	0.12	≤20.000	≤6.02E+01
17	Isopropanol	1.00	≤0.050	≤4.83E-03	≤7.07E-26	≥0.74	≤20.000	≤3.01E+00
18	Chloro-benzene	7.00	≤0.050	≤6.89E-04	≤4.21E-30	≥0.87	≤20.000	≤4.30E-01
19	Dichloro-benzene	8.00	≤0.050	≤6.03E-04	≤2.16E-30	≥0.88	≤20.000	≤3.76E-01
20	Hexane	5.00	≤0.050	≤9.65E-04	≤2.29E-29	≥0.85	≤20.000	≤6.02E-01

Appendix 6.10

ICP $CsPbBr_3$ Bulk – Values

Table A6.1-II. List of all samples used in the figures displayed in this article.

	Solvent	Volume used (mL)	[Pb] from ICP (ppm)	Saturation [Pb] (mM)	Calculated K_{sp} (mol^5/L^5)	Expected stabilization *vs.* $E^{0'}_{Pb^{2+}/Pb}$ (V)	[Cs] from ICP (ppm)	Saturation [Cs] (mM)
21	Benzene	10.00	≤0.050	≤4.83E-04	≤7.07E-31	≥0.89	≤20.000	≤3.01E-01
22	Ethyl acetate	6.50	0.644	9.57E-03	2.17E-24	0.70	≤20.000	≤4.63E-01
23	Toluene	7.00	≤0.050	≤6.89E-04	≤4.21E-30	≥0.87	≤20.000	≤4.30E-01
24*	Water	1.00	51.751	4.99E+00	8.37E-11	0.30	49.203	7.40E+00
25*	Pyridine	0.05	16.458	3.18E+01	8.74E-07	0.18	≤20.000	≤6.02E+01
26*	Diethyl carbonate	5.50	≤0.050	≤8.78E-04	≤1.40E-29	≥0.85	≤20.000	≤5.47E-01

**The precipitate in these solvents did not become orange, indicating that $CsPbBr_3$ is not the most stable crystal phase. Therefore, these solvents will not result in stable electrochemistry on $CsPbBr_3$ due to an expected phase change.*

Appendix 6.11

ICP Nanocrystal Ligands - Values

Table A6.2. The saturation concentration of $Pb(OA)_2$ in the five solvents used throughout this work, measured through Pb ICP-OES. With these values, the K_{sp} of the nanocrystal surface was approximated. All samples were measured above the detection limit. Therefore, the [Pb] is the true value for $Pb(OA)_2$ in the corresponding solvent.

Solvent	Volume used (mL)	[Pb] from ICP (ppm)	Saturation [Pb] (mM)
Propylene carbonate	10.00	10.298	5.00E-02
Dichloromethane	1.00	684.432	3.30E+01
Acetonitrile	10.00	5.518	2.70E-02
Benzonitrile	1.00	118.038	5.70E+00
Tetrahydrofuran	0.80	1751.026	1.06E+02

Table A6.3. The saturation concentration of CsOA in the five solvents used throughout this work, measured through Cs ICP-OES, which is not used due to a higher detection limit than that of Pb. The values show a similar trend as that of the $Pb(OA)_2$ measurements. The samples in acetonitrile and benzonitrile had a Cs concentration below the detection limit. Therefore, the [Cs] should be equal or lower than the reported values.

Solvent	Volume used (mL)	[Cs] from ICP (ppm)	Saturation [Cs] (mM)
Propylene carbonate	10.00	28.736	2.87E-01
Dichloromethane	0.10	64.961	6.50E-01
Acetonitrile	19.00	≤20.000	≤2.51E+00
Benzonitrile	0.60	≤20.000	≤1.50E-01
Tetrahydrofuran	10.00	52.190	5.22E-01

Appendix 6.12

$CsPbBr_3$ Nanocrystal Electrochemistry - MeCN

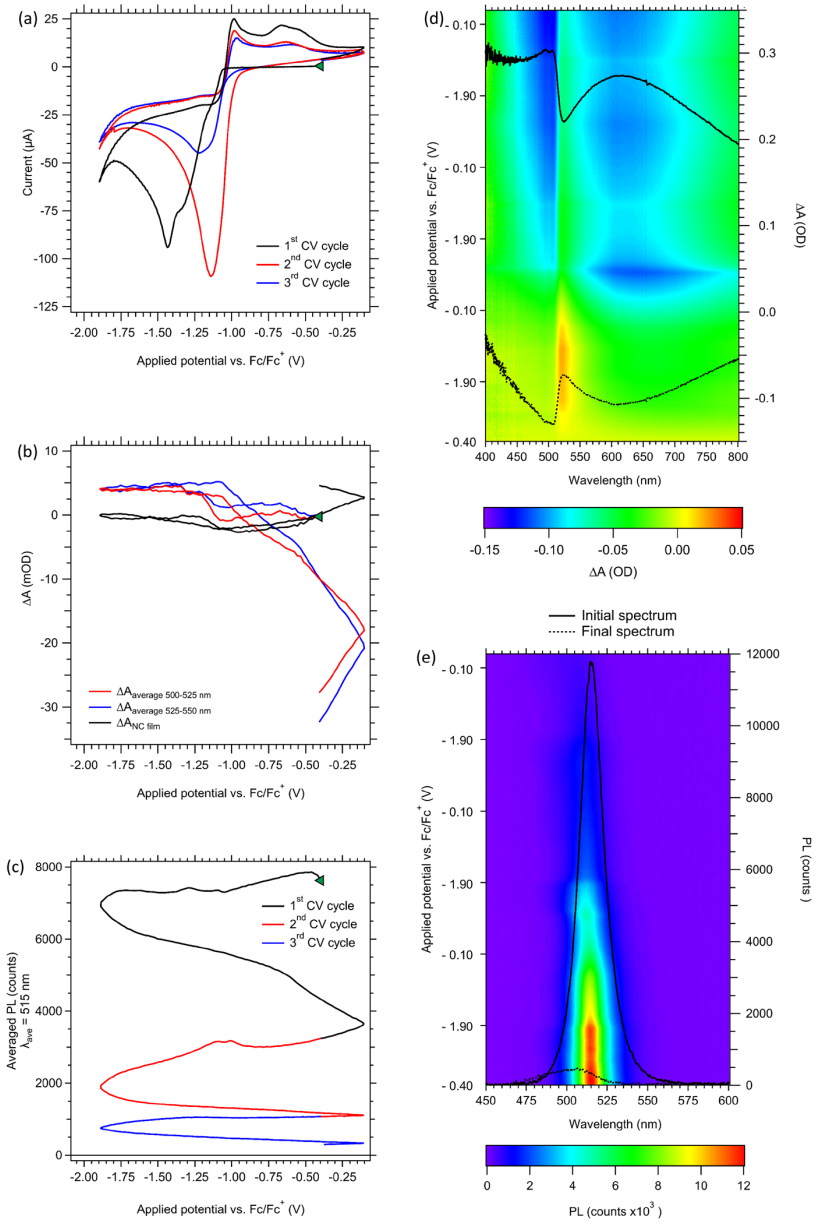


Figure A6.12. Spectro-electrochemical dataset of a measurement on a $CsPbBr_3$ NC thin film in acetonitrile with 0.1 M $TBAPF_6$ and a scan speed of 10 mV/s. (a) The CV, (b) the change of absorbance in the first CV cycle, (c) the PL intensity during the three CV cycles, and (d) the 2D spectra of the absorbance and (e) the PL.

Appendix 6.13

$CsPbBr_3$ Nanocrystal Electrochemistry - PhCN

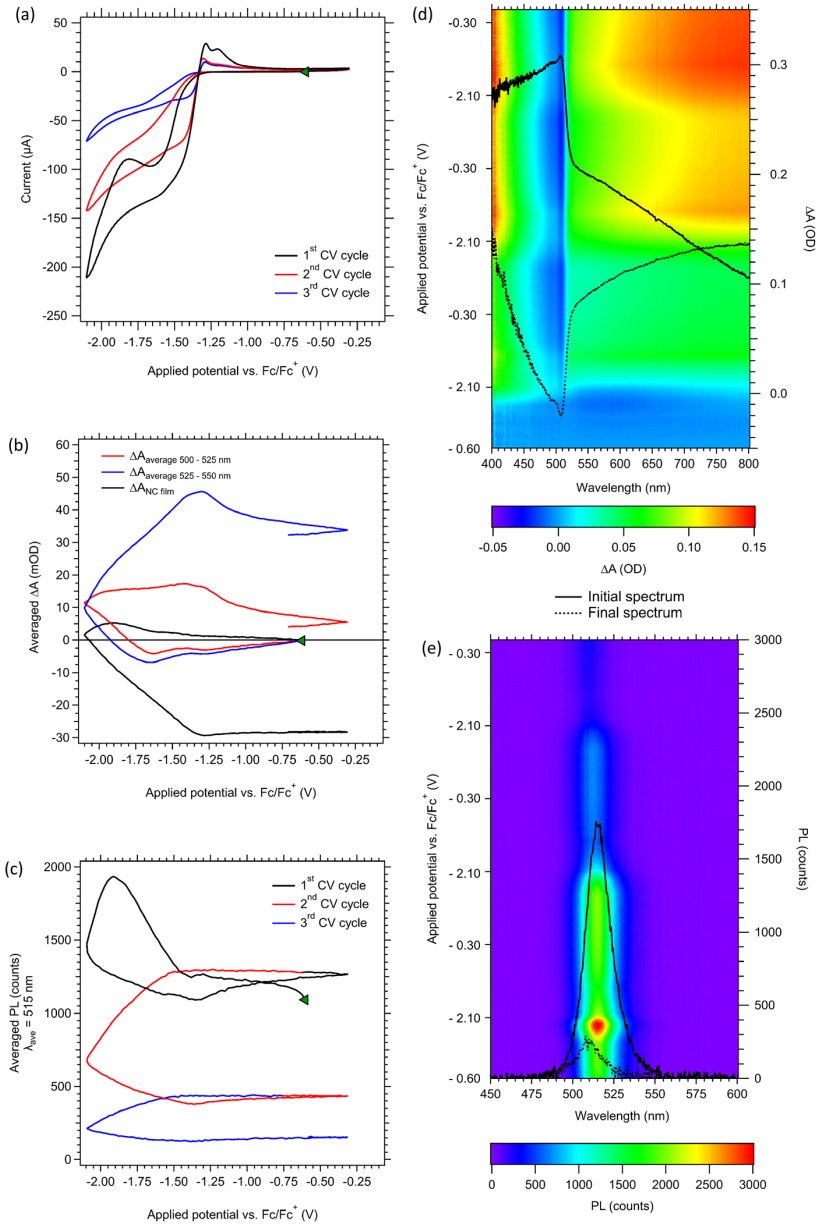


Figure A6.13. Spectro-electrochemical dataset of a measurement on a $CsPbBr_3$ NC thin film in benzonitrile with 0.1 M $TBAPF_6$ and a scan speed of 10 mV/s. (a) The CV, (b) the change of absorbance in the first CV cycle, (c) the PL intensity during the three CV cycles, and (d) the 2D spectra of the absorbance and (e) the PL.

Appendix 6.14

$CsPbBr_3$ Nanocrystal Electrochemistry - THF

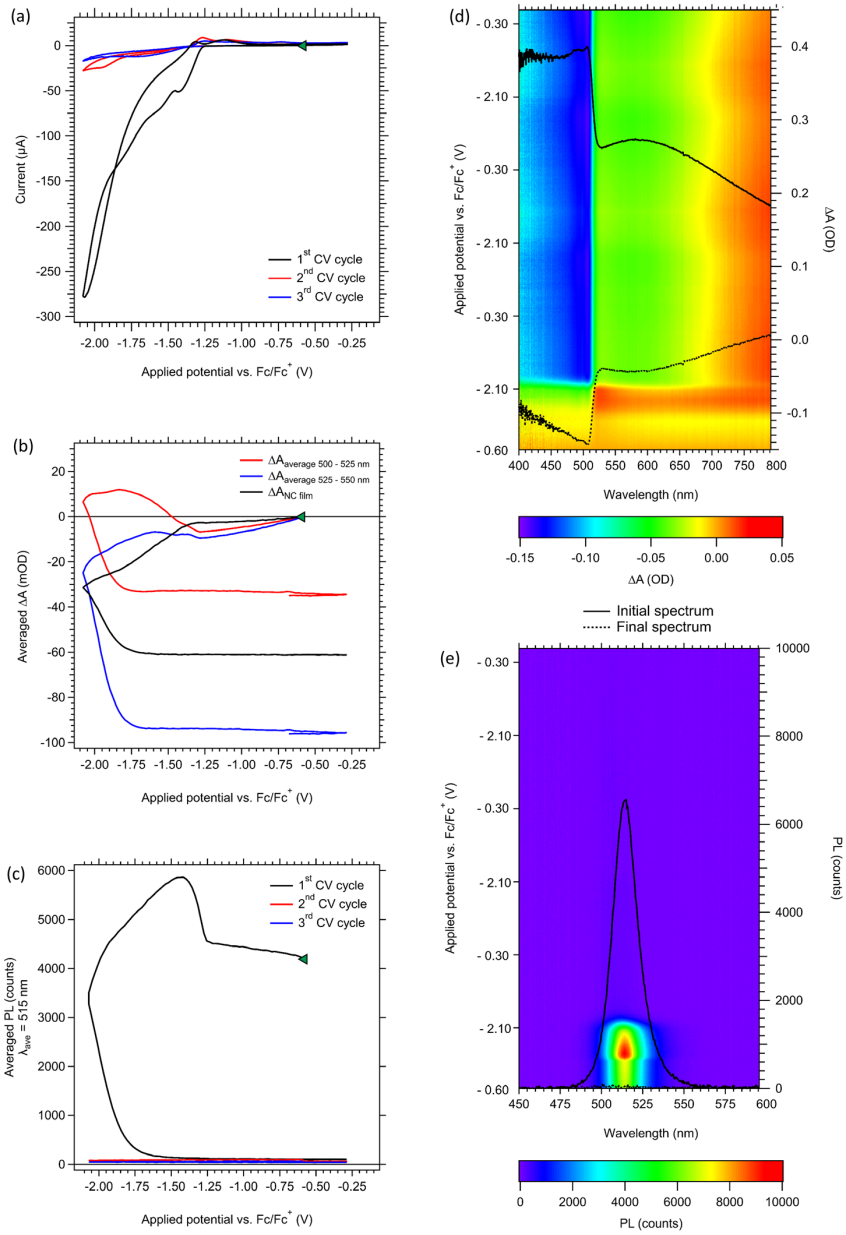


Figure A6.14. Spectro-electrochemical dataset of a measurement on a $CsPbBr_3$ NC thin film in tetrahydrofuran with 0.1 M $TBAPF_6$ and a scan speed of 10 mV/s. (a) The CV, (b) the change of absorbance in the first CV cycle, (c) the PL intensity during the three CV cycles, and (d) the 2D spectra of the absorbance and (e) the PL.

Appendix 6.15

OD and ΔOD Spectra Before and After CV Measurements

Figure A6.15 shows the OD and ΔOD spectra of the $CsPbBr_3$ films before and after the three CV cycles. The dashed lines indicate the wavelength regions over which is averaged, to correct ΔOD for the increased scattering, as worked out in Figure A6.16.

Figure A6.15a shows that the general shape of the initial perovskite OD (red) of the bulk film in DCM has completely disappeared after the CV measurement, as shown by the black spectrum in Figure A6.15a. The increase in OD at all wavelengths is due to the formation of metallic Pb^0. A similar set of spectra is obtained for the NC film in DCM (Figure 6.15b).

For the NC film in PC however, significantly different behavior is observed, as shown in Figure 6.15c. In PC, the OD spectra before and after the CV measurement still has the same shape, indicating that $CsPbBr_3$ is still present on the film. The figure shows that the OD spectrum after the measurement has decrease in overall intensity due to partial dissolution of the film, and furthermore an increase of the background due to the reduction of dissolved Pb^{2+} complexes.

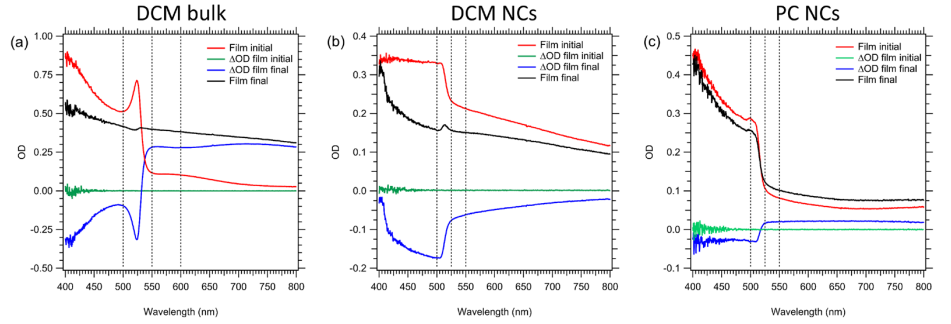


Figure A6.15. (a) OD and ΔOD spectra before and after the CV measurements were performed on a bulk and (b) NC film in DCM, and (c) a NC film in PC. This figure shows the full degradation of both films in DCM, and only a minor change to the film in PC.

Appendix 6.16

Scattering Correction for ΔOD Spectra

As explained in the main text, the data presented in Figure 6.5 is obtained by subtracting the ΔOD of the sub-bandgap region (indicated in Figure 6.4 and Figure A6.15) from that of the band edge absorbance region. By doing so, a correction is applied for the increased scattering of the Pb^0 film, resulting in the change of the perovskite ΔOD. In Figure A6.16, we do not only show the ΔOD for the perovskite (as shown in Figure 6.5), but also the original changes to the spectra.

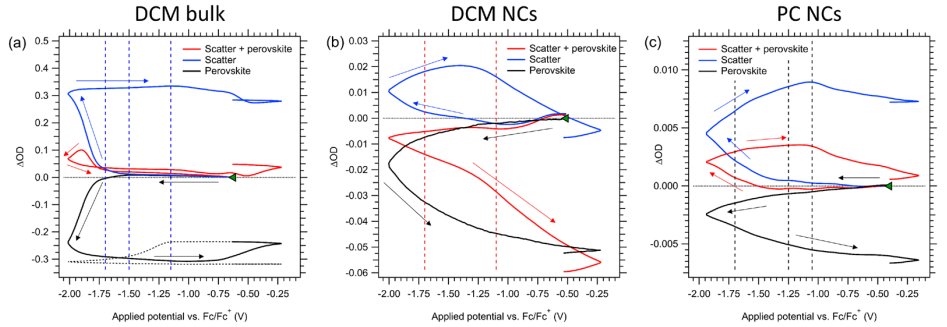


Figure A6.16. (a) the ΔOD of the perovskite (as shown in Figure 6.5), obtained by subtracting the sub-bandgap scatter (blue) from the band edge absorbance region (red), for the bulk finm and (b) NC film in DCM, and (c) a NC film in PC.

Appendix 6.17

Correlation of Injected Charge to Change of OD for NC Samples

As explained in the main text, the changes to the NC films in DCM and PC are significantly different. In Figure A6.17a, we show that for DCM, most of the injected charges in the first CV cycle result in a change of the perovskite OD (hence are used for the cathodic dissolution reaction). In Figure A6.17b, we show that in PC, the OD is more affected by gradual dissolution, as charge extraction results in a roughly identical degree of decrease of the perovskite OD as charge injection.

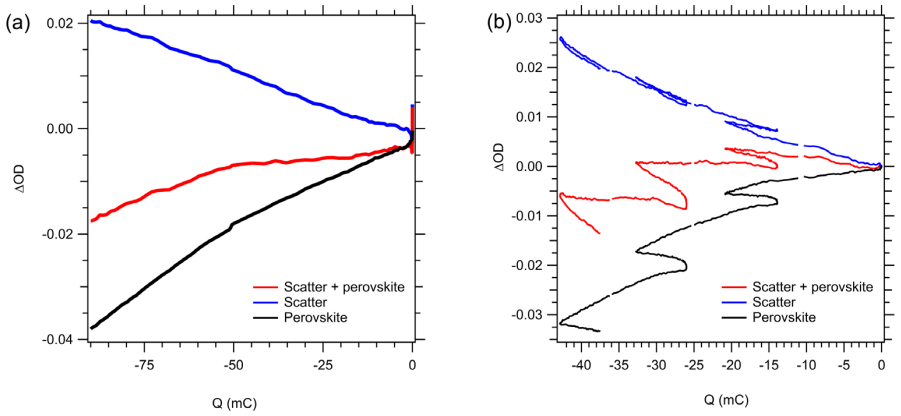


Figure A6.17. (a) the dOD of the perovskite NCs as function of the injected charge (Q) for the first CV cycle in DCM, and (b) for all three CV cycles in PC.

Appendix 6.18

Correlation of PL Peak Position with the Applied Potential and Time

Figure 6.6a shows a blueshift of the PL peak position of $CsPbBr_3$ NCs during the CV measurement in DCM. Figure A6.18 shows the change of PL peak-position as function of applied potential and time. This figure shows that at potentials below the Pb^{2+} reduction potential, the blueshift occurs faster. However, even at the most positive potentials, a decrease of the position is observed, showcasing dissolution of the NC film over time.

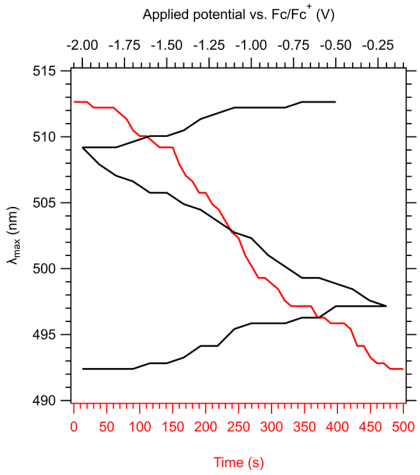


Figure A6.18. The PL peak position of the NC film in DCM as function of the applied potential and the time. t_0 = the start of the CV measurement.

Appendix 6.19

Stability $CsPbBr_3$ Nanocrystal Thin Films - PC

As mentioned in the main text, the nanocrystal thin films are not entirely stable in propylene carbonate. However, due to the very insoluble ligand shell, the nanocrystals degrade much slower than is expected for bulk $CsPbBr_3$. As shown in Figure A6.19, 75% of the film is still left after 1800 seconds when no potential is applied.

When TBABr is added to the solution, the solubility of the nanocrystals increases as more Pb^{2+} polybromide complexes form, which are more soluble than the intrinsic perovskite. As shown in Figure A6.19, the stability decreases as the TBABr concentration increases. For a solution containing 100 mM $TBAPF_6$ and 1000 mM TBABr, the film instantly dissolved completely.

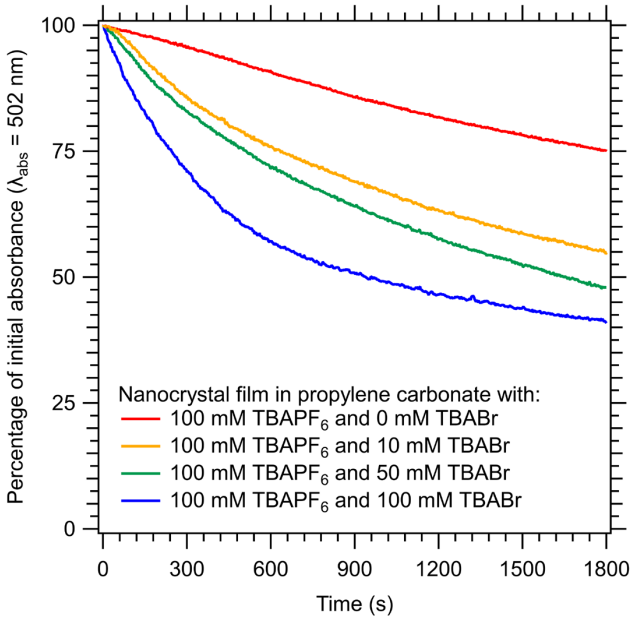


Figure A6.19. The stability of the $CsPbBr_3$ nanocrystal thin films in propylene carbonate with 100 mM $TBAPF_6$ and a specific TBABr concentration added. All trends are made by recording the absorbance at 502 nm, and measuring the decrease of the initial absorbance.

Appendix 6.20

$CsPbBr_3$ Nanocrystal Electrochemistry - HFE

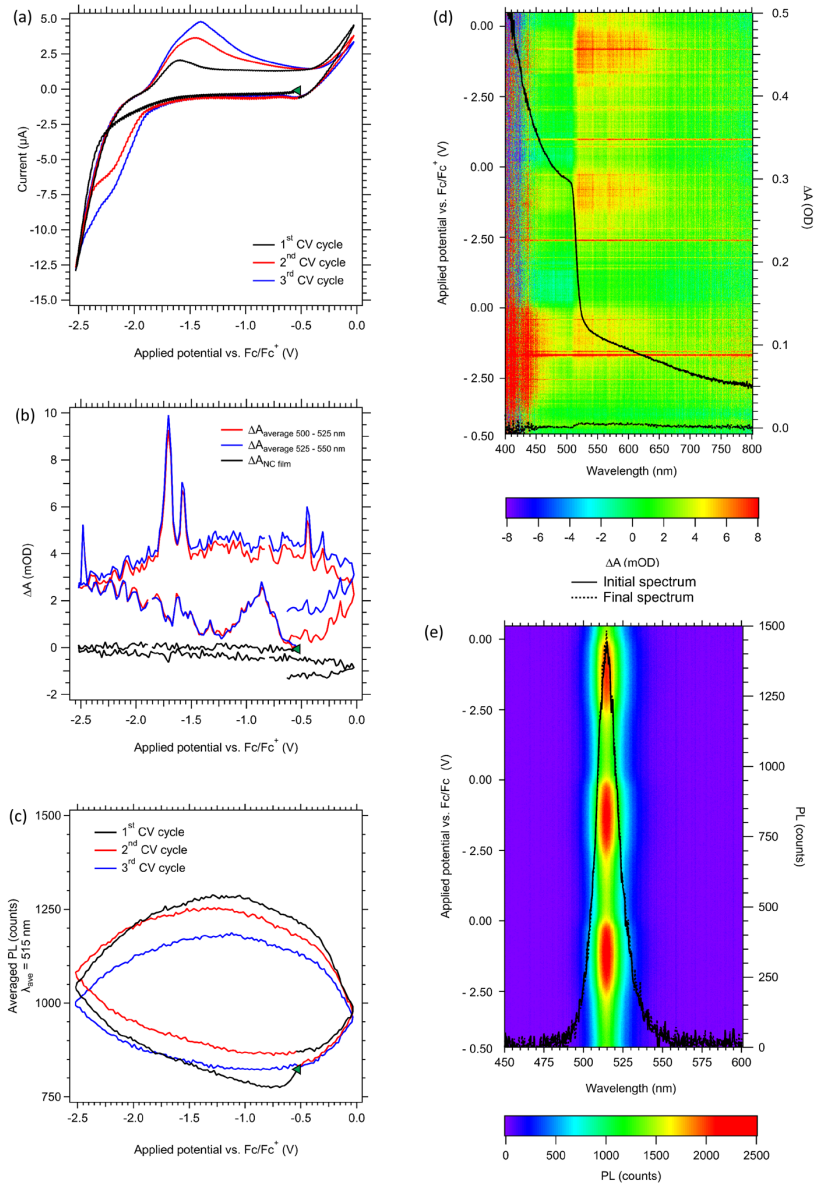


Figure A6.20. Spectro-electrochemical dataset of a measurement on a $CsPbBr_3$ NC thin film in 97 $_{vol}$% methoxyperfluorobutane (HFE) with 0.1 M LiTFSI (including 3 $_{vol}$% diethylcarbonate) and a scan speed of 10 mV/s. (a) The CV, (b) the change of absorbance in the first CV cycle, (c) the PL intensity during the three CV cycles, and (d) the 2D spectra of the absorbance and (e) the PL.

Summary

For this thesis, we have studied the synthesis, material characteristics and optical properties of a variety of optically active nanomaterials. These materials can be used, for example, to convert energy into light and *vice versa*. Downscaling well-understood bulk materials to a nanoscaled size significantly increases their applicability on nonuniform surfaces, in biological applications and for quantum mechanical studies, such as quantum collapse studies. However, when scaling down the size of a material, the properties can change due to quantum confinement (for semiconductor materials) and the large increase of the surface to volume ratio. Although this expands the applicability of the nanomaterials further it also introduces detrimental effects, like significantly increased surface related quenching, that have to be tackled before the optically active nanomaterials can be applied in any studies, and further down the road, for their use in general customer products.
There is no single storyline in this thesis that connects each chapter to the next. However, in this thesis we show the broad variety of optically active nanomaterials that exist. We do this by discussing the differences and similarities in their synthesis methods, their material properties and issues, and furthermore their applicability in scientific studies and products.

In **Chapter 1**, we introduce the background concepts, necessary to understand the scientific chapters of this thesis. Starting from bulk material concepts, we move towards the changes in properties when scaling down the size of a material and elaborate on the size-related problems. It is the investigation of these problems that form the core of the thesis.
Chapter 2 shows the synthesis stages of lithium yttrium fluoride ($LiYF_4$) nanocrystals, an optically inactive host material. We show that, in this one-pot synthesis, different growth stages of the nanocrystals are observed. After thermal cracking of the precursor, inducing the release of free fluoride monomers, amorphous $LiYF_4$ nanospheres nucleate at first. These spheres grow *via* Ostwald ripening, until they crystallize into bipyramidal nanocrystals. By keeping the nanocrystals at the synthesis conditions for a day, instead of recovering them, we show that the $LiYF_4$ nanocrystals have dissolved and LiF recrystallized. From there, we conclude that the $LiYF_4$ nanocrystals are in a metastable phase at the synthesis conditions. $LiYF_4$ thus forms due to the initial formation of the amorphous nanospheres, due to a much higher activation energy for the nucleation of LiF.
In **Chapter 3**, the $LiYF_4$ (or YLF) nanocrystals are doped with optically active ytterbium (Yb^{3+}) ions that act as point emitters. Here we observe that the optical efficiency, called the photoluminescence quantum yield (PLQY), is significantly different for bulk Yb:YLF (100% PLQY) than for nanocrystals. In this chapter we identify the main photoluminescence (PL) quenching routes, and subsequently attempt to remove all quenching routes to obtain unity PLQY. We show that we can chemically remove all traces of water during the synthesis, avoiding the inclusion of PL quenching hydroxide ions in the nanocrystals. Therefore, energy transfer of excited states to the nanocrystal surface is the only remaining

quenching pathway. We show that, as expected, energy transfer to the nanocrystal surface is facilitated by higher Yb^{3+} doping densities due to the formation of a larger energy transfer network to the nanocrystal surface. We show that up to 20% Yb^{3+} doping, the Yb:YLF nanocrystals have high PLQYs. However, due to efficient energy transfer, doping densities above 20% show a sharp decrease of the PLQY. By growing an undoped YLF shell around the Yb:YLF nanocrystal core, we remove the possibility of energy transfer of excited states to the nanocrystal surface. In this chapter we show that even for a full $LiYbF_4$ nanocrystal core, with 2% PLQY for the core nanocrystal, the PLQY can be increased to near-unity solely by growing an undoped YLF shell. Additionally, in this chapter, we elaborate on how to measure the PLQY accurately, which is not straightforward for this poor-absorbing dopant. We show and confirm that using the average PL lifetime of the Yb^{3+} ions mitigates the measurement errors introduced by the poor absorbance, which results in a more accurate determination of the PLQY.

Chapter 4 shows similar issues with respect to the reduced PLQY for nanocrystals. However, in this case not for a point emitter-based nanomaterial, but for a semiconductor nanomaterial. This chapter focuses on indium phosphide (InP), which shows quantum confinement as an additional property. Due to the very small size of InP nanocrystals, the wavefunction of an exciton can no longer freely move inside the nanomaterial, resulting in a size-specific emission. Therefore, we generally refer to these materials as quantum dots. In contrast to the point-emitter based nanocrystals, where optically active ions are surrounded by an insulating host material, the wavefunction of the exciton of semiconductor nanomaterials is delocalized over the entire nanocrystal. Therefore, growing an additional "shell" of InP around the core InP quantum dot does not result in surface passivation and concomitant increase of the PLQY, but solely in a redshifted emission due to the increase of the quantum dot size. In this chapter, we build on existing work where InP quantum dots are passivated by higher bandgap, type-I semiconductor shell materials such as zinc selenide (ZnSe). The lattice parameter of InP is large, and hence a suitable shell material that can passivate the InP core without creating interfacial surface states is not easily found. As we found the lattice mismatch between InP and ZnSe to be too large, and the band alignment insufficiently type-I to completely confine the exciton in the InP core, we attempted to grow an alloy of ZnSe with magnesium ($Zn_xMg_{x-1}Se$), denoted as ZnMgSe. This material, with a high fraction of Mg, has an expected perfect lattice match with InP and furthermore has a larger bandgap, likely improving the preferred type-I band alignment. Attempts to grow ZnMgSe around InP quantum dots through the most common methods, using metal carboxylates, did not result in the growth of ZnMgSe shells. Therefore, we used much more reactive, organometallic precursors for the shell growth. With this method, we were able to grow ZnMgSe shells on InP quantum dots, albeit with a significantly lower incorporation of Mg than the precursor feed fraction. We did not observe a relative increase of the PLQY, all values remained similar, but a much more color pure emission was found for core shell samples with higher fractions of Mg. This led to the conclusion that the inclusion of Mg, and concomitant increase of the bandgap energy of the shell material, likely reduces trap state emission and the delocalization of the exciton from the core into the shell, resulting in the observed improvement of the color purity.

In **Chapter 5**, we show our attempts to electrochemically dope a cesium lead bromide ($CsPbBr_3$) perovskite nanocrystal based thin film electrode. In contrast to InP, $CsPbBr_3$

nanocrystals are not (strongly) quantum confined and furthermore no suitable shell material has been found yet. Nonetheless, due to their defect tolerance, their PLQY is relatively high. An outstanding challenge for $CsPbBr_3$ nanocrystals is to control the density of electrons and holes *via* doping. In this chapter we study electrochemical p-doping of films of $CsPbBr_3$ nanocrystals. By applying a positive charge to the nanocrystal electrode, we inject holes into the valence band of the nanocrystals, electrochemically p-doping the material. By analysing the induced effects on the absorbance, emission and conductivity due to applying positive potentials to the electrode, we conclude that we electrochemically p-doped the nanocrystals. However, from the cyclic voltammogram we learn that the injected holes were not stable in the system and reacted away, most likely by oxidizing the bromide component of the perovskite. With density functional theory simulations, we confirm that $CsPbBr_3$ nanocrystals can be p-doped in a stable way, while n-doping leads to lead ion reduction.

Chapter 6 digs deeper into understanding the (in)stability of electrochemical n-doping of $CsPbBr_3$ nanocrystals. In this chapter we report a systematic spectro-electrochemical study on $CsPbBr_3$ nanocrystals and bulk thin films in contact with different electrolytes to understand and control cathodic degradation reactions. These measurements reveal that the cathodic decomposition of $CsPbBr_3$ nanocrystals is dominated by the solubility of surface ligands, which is high in low-polarity solvents and *vice versa*. For nanocrystals, the solubility and stability of surface ligands and the bulk $CsPbBr_3$ lattice are orthogonal, such that no solvent was found where both are sufficiently electrochemically stable. This poses inherent complications for electrochemical measurements and applications: the non-faradaic potential window of the $CsPbBr_3$ nanocrystal electrodes is bound by the reduction potential of Pb^{2+} complexes in solution, and the cathodic decomposition of $CsPbBr_3$ occurs well before the conduction band can be populated with electrons. This chapter offers guidelines to improve the electrochemical stability of perovskite nanocrystals through a tailored combination of surface passivation and electrolyte selection.

Throughout these chapters, we conclude that the main problems with the nanomaterials investigated in this thesis occur at the surface of the materials. This effect is significantly larger for nanomaterials than for bulk materials due to their extreme surface to volume ratio. As we find, the most efficient method to remove these problems is by passivating the nanomaterials with an inorganic shell. But we also show that with materials for which no inorganic shell exists (yet), improvement of scientific understanding can be made.

Samenvatting

Voor dit proefschrift hebben we de synthese, materiaalkarakteristieken en optische eigenschappen van verschillende optisch actieve nanomaterialen bestudeerd. Deze materialen kunnen bijvoorbeeld worden gebruikt om energie om te zetten in licht en *vice versa*. Door goed begrepen bulkmaterialen te verkleinen naar een grootte op nanoschaal, wordt hun toepasbaarheid aanzienlijk vergroot op ongelijkmatige oppervlakken, in biologische toepassingen en voor kwantummechanische studies, zoals kwantuminstortingsstudies. Bij het verkleinen van een materiaal kunnen de eigenschappen echter veranderen als gevolg van kwantumopsluiting (voor halfgeleidermaterialen) en de grote toename van de verhouding tussen oppervlak en volume. Hoewel dit de toepasbaarheid van de nanomaterialen verder uitbreidt, introduceert het ook nadelige effecten, zoals aanzienlijk meer oppervlaktegerelateerde uitdoving, die moeten worden aangepakt voordat de optisch actieve nanomaterialen kunnen worden toegepast in studies, en verder in het verschiet, voor het gebruik in algemene gebruiksvoorwerpen. Er is geen hoofdverhaallijn in dit proefschrift die elk hoofdstuk met het volgende verbindt. In dit proefschrift laten we echter de grote verscheidenheid aan optisch actieve nanomaterialen zien die er bestaan. Dit doen we door het bespreken van de verschillen en overeenkomsten in hun synthesemethoden, hun materiaaleigenschappen en problemen, en verder hun toepasbaarheid in wetenschappelijke studies en producten.

In **Hoofdstuk 1** introduceren we de achtergrondconcepten die nodig zijn om de wetenschappelijke hoofdstukken van dit proefschrift te begrijpen. Beginnend vanaf bulkmateriaalconcepten, bewegen we naar de veranderingen van eigenschappen bij het verkleinen van een materiaal en gaan we dieper in op de problemen met betrekking tot de grootte. Het is het onderzoek naar deze problemen die de kern van het proefschrift vormen.
Hoofdstuk 2 toont de synthesestadia van lithiumyttriumfluoride ($LiYF_4$) nanokristallen, een optisch inactief gastheermateriaal. We laten zien dat in deze één-pots-synthese verschillende groeistadia van de nanokristallen worden waargenomen. Na het thermisch kraken van de voorlopermolecule, waardoor vrije fluoridemonomeren vrijkomen, kiemen eerst amorfe $LiYF_4$ nanosferen. Deze sferen groeien *via* Ostwald-rijping, totdat ze kristalliseren tot bipiramidale nanokristallen. Door de nanokristallen een dag bij de synthesecondities te houden, in plaats van ze te oogsten, laten we zien dat de $LiYF_4$ nanokristallen zijn opgelost en LiF herkristalliseerd. Van daaruit concluderen we dat de $LiYF_4$ nanokristallen zich in een metastabiele fase bevinden bij de syntheseomstandigheden. $LiYF_4$ vormt dus vanwege de initiële vorming van de amorfe nanosferen, vanwege een veel hogere activeringsenergie voor de nucleatie van LiF.
In **Hoofdstuk 3** worden de $LiYF_4$ (of YLF) nanokristallen gedoteerd met optisch actieve ytterbium (Yb^{3+}) ionen die fungeren als puntstralers. Hier zien we dat de optische efficiëntie, de fotoluminescentiekwantumopbrengst (FLKO) genoemd, significant verschilt voor bulk Yb:YLF (100% FLKO) dan voor nanokristallen. In dit hoofdstuk identificeren

we de belangrijkste fotoluminescentie (FL) uitdovingsroutes en proberen vervolgens alle uitdovingsroutes te verwijderen om eenheid FLKO te verkrijgen. We laten zien dat we tijdens de synthese alle sporen van water chemisch kunnen verwijderen, waarbij de opname van PL-uitdovende hydroxide ionen in de nanokristallen wordt vermeden. Daarom is de energieoverdracht van aangeslagen toestanden naar het nanokristaloppervlak de enige overgebleven uitdovingsroute. We laten zien dat, zoals verwacht, energieoverdracht naar het nanokristaloppervlak wordt vergemakkelijkt door hogere Yb^{3+}-doteringsdichtheden als gevolg van de vorming van een groter energieoverdrachtsnetwerk naar het nanokristaloppervlak. We laten zien dat tot 20% Yb^{3+}-dotering, de Yb:YLF nanokristallen hoge FLKO's hebben. Dopingdichtheden boven de 20% laten echter door een efficiënte energieoverdracht een scherpe daling van de FLKO zien. Door een ongedoteerde YLF schil rond de Yb:YLF nanokristalkern te laten groeien, verwijderen we de mogelijkheid van energieoverdracht van aangeslagen toestanden naar het nanokristaloppervlak. In dit hoofdstuk laten we zien dat zelfs voor een volledige $LiYbF_4$ nanokristalkern, met 2% PLQY voor het kernnanokristal, de FLKO kan worden verhoogd tot bijna één alleen door een ongedoteerde YLF schil te groeien. Daarnaast gaan we in dit hoofdstuk dieper in op het nauwkeurig meten van de FLKO, wat niet eenvoudig is voor deze slecht absorberende doteerstof. We laten zien en bevestigen dat het gebruiken van de gemiddelde FL-levensduur van de Yb^{3+} ionen de meetfouten die geïntroduceerd wordt door door de slechte absorptie worden ontweken, wat resulteert in een accuratere bepaling van de FLKO.

Hoofdstuk 4 laat soortgelijke problemen zien met betrekking tot de gereduceerde FLKO voor nanokristallen. In dit geval echter niet voor een op een puntstraler gebaseerd nanomateriaal, maar voor een halfgeleider nanomateriaal. Hoofdstuk 4 concentreert zich op indiumfosfide (InP), dat kwantumopsluiting als extra eigenschap laat zien. Vanwege de zeer kleine omvang van InP nanokristallen kan de golffunctie van een exciton niet langer vrij bewegen in het nanomateriaal, wat resulteert in een groottespecifieke emissie. Daarom noemen we deze materialen over het algemeen kwantumstippen. In tegenstelling tot de op puntstraler gebaseerde nanokristallen, waar optisch actieve ionen worden omgeven door een isolerend gastheermateriaal, is de golffunctie van de exciton van halfgeleider nanomaterialen gedelokaliseerd over het gehele nanokristal. Daarom resulteert een extra "schil" van InP rond de InP kwantumstipkern niet in oppervlaktepassivering en daarmee gepaard gaande toename van de FLKO, maar alleen in een roodverschoven emissie als gevolg van de toename van de kwantumstip-grootte. In dit hoofdstuk bouwen we voort op bestaand werk waarin InP kwantumstippen worden gepassiveerd door type-I halfgeleiderschilmaterialen met hogere bandkloof, zoals zinkselenide (ZnSe). De roosterconstante van InP is groot, en daarom is het niet gemakkelijk om een geschikt schaalmateriaal te vinden dat de InP-kern kan passiveren zonder oppervlaktetoestanden te creëren. Omdat we vonden dat het roosterverschil tussen InP en ZnSe te groot was, en de banduitlijning onvoldoende type-I om de exciton volledig in de InP-kern te beperken, hebben we geprobeerd om een legering van ZnSe met magnesium ($Zn_xMg_{x-1}Se$) te laten groeien, aangeduid als ZnMgSe. Dit materiaal, met een hoge Mg-fractie, heeft een verwachte perfecte roosterovereenkomst met InP en heeft bovendien een grotere bandafstand, waardoor waarschijnlijk de geprefereerde type-I banduitlijning wordt verbeterd. Pogingen om ZnMgSe rond InP kwantumstippen te laten groeien via de meest gebruikelijke methoden, met behulp van metaalcarboxylaten, resulteerden niet in de groei van ZnMgSe schillen. Daarom gebruikten we veel meer reactieve,

organometallische voorlopermoleculen voor de schilgroei. Met deze methode konden we ZnMgSe schillen op InP kwantumstippen laten groeien, zij het met een aanzienlijk lagere opname van Mg dan de fractie van de voorlopermolecuulvoeding. We hebben geen relatieve toename van de FLKO waargenomen, alle waarden bleven vergelijkbaar, maar er werd een veel kleurzuiverdere emissie gevonden voor kern-schilmonsters met hogere fracties Mg. Dit leidde tot de conclusie dat de opname van Mg, en de daarmee gepaard gaande toename van de bandkloofenergie van het schilmateriaal, waarschijnlijk de emissie van de valtoestanden en de delokalisatie van het exciton van de kern naar de schil vermindert, resulterend in de waargenomen verbetering van de kleurzuiverheid.
In **Hoofdstuk 5** laten we onze pogingen zien om een op cesiumloodbromide ($CsPbBr_3$) perovskiet nanokristal-gebaseerde dunnefilmelektrode elektrochemisch te doteren. In tegenstelling tot InP zijn $CsPbBr_3$ nanokristallen niet (sterk) kwantumbegrensd en bovendien is er nog geen geschikt schilmateriaal gevonden. Desalniettemin is hun FLKO vanwege hun valtoestandtolerantie relatief hoog. Een open uitdaging voor $CsPbBr_3$ nanokristallen is het beheersen van de dichtheid van elektronen en gaten *via* doping. In dit hoofdstuk bestuderen we elektrochemische p-dotering van films van $CsPbBr_3$ nanokristallen. Door een positieve lading op de nanokristalelektrode aan te brengen, injecteren we gaten in de valentieband van de nanokristallen, waarbij we het materiaal elektrochemisch p-doteren. Door de geïnduceerde effecten op de absorptie, emissie en geleidbaarheid als gevolg van het toepassen van positieve potentialen op de elektrode te analyseren, concluderen we dat we de nanokristallen elektrochemisch p-gedoteerd hebben. Uit het cyclische voltammogram leren we echter dat de geïnjecteerde gaten niet stabiel in het systeem waren en wegreageerden, hoogstwaarschijnlijk door oxidatie van de bromidecomponent van het perovskiet. Met dichtheidsfunctionaaltheoriesimulaties bevestigen we dat $CsPbBr_3$ nanokristallen op een stabiele manier p-gedoteerd kunnen worden, terwijl n-dotering leidt tot reductie van loodionen.
Hoofdstuk 6 gaat dieper in op het begrijpen van de (in)stabiliteit van elektrochemische n-dotering van $CsPbBr_3$ nanokristallen. In dit hoofdstuk rapporteren we een systematische spectro-elektrochemische studie van $CsPbBr_3$ nanokristalfilms en dunne bulkfilms in contact met verschillende elektrolyten om kathodische degradatiereacties te begrijpen en te beheersen. Deze metingen laten zien dat de kathodische ontleding van $CsPbBr_3$ nanokristallen wordt gedomineerd door de oplosbaarheid van oppervlakteliganden, die hoog is in oplosmiddelen met lage polariteit en *vice versa*. Voor nanokristallen zijn de oplosbaarheid en stabiliteit van oppervlakteliganden en het bulk $CsPbBr_3$-rooster orthogonaal, zodat er geen oplosmiddel werd gevonden waar beide voldoende elektrochemisch stabiel zijn. Dit brengt inherente complicaties met zich mee voor elektrochemische metingen en toepassingen: het niet-faradaïsche potentiaalvenster van de $CsPbBr_3$ nanokristalelektroden wordt begrensd door het reductiepotentieel van Pb^{2+} complexen in oplossing, en de kathodische ontleding van $CsPbBr_3$ vindt plaats lang voordat de geleidingsband gevuld kan worden met elektronen . Dit hoofdstuk biedt richtlijnen om de elektrochemische stabiliteit van perovskietnanokristallen te verbeteren door een op maat gemaakte combinatie van oppervlaktepassivering en elektrolytselectie.

In deze hoofdstukken concluderen we dat de belangrijkste problemen met de nanomaterialen die in dit proefschrift zijn onderzocht zich voordoen aan het oppervlak van de materialen. Dit effect is aanzienlijk groter voor nanomaterialen dan voor

bulkmaterialen vanwege hun extreme verhouding tussen oppervlak en volume. Zoals we ontdekken, is de meest efficiënte methode om deze problemen op te lossen, door de nanomaterialen te passiveren met een anorganische schil. Maar we laten ook zien dat met materialen waarvoor (nog) geen anorganische schil bestaat, verbetering van het wetenschappelijk inzicht mogelijk is.

Acknowledgements

I often question how I have become who I am today. More and more, I realize that this journey started long before I began my 10-year rollercoaster at university. The professional and personal growth during my PhD years can be attributed to all the people that have had a positive influence on my life at some point since that stormy Sunday, mid-November 1993. Therefore, to ensure this section would not be thicker than a scientific chapter of my thesis, I promised to myself to keep it short and strictly to the point. And as usual, I somewhat failed doing that. However, I am sure that I missed to mention many people that brought me up to the point where I am now. Everyone that I handed one of these books may certainly consider themselves part of my life and part of this journey. To all of you, my honest thanks for helping me reaching the (for me) unimaginable. To all of you who read this without getting this book in some way from me, interesting, you reached the acknowledgements section of a stranger. Thank you too for the potential interest in my work. If at any point you want to become part of the first group of people, reach out to me, feel free to ask questions and ensure that all the work from the past, present and future keeps on being used, made and improved. Having that said, let me increase the thickness of this thesis a bit more by thanking some people without whom I would have likely not completed this particular journey.

In the first place, I want to thank **Arjan** for continuously believing in me. Up to this day, I have no idea what you saw in me during my master thesis project, but the opportunity you gave me has changed my life in many good ways. Your guidance through the large variety of projects, the possibility of unbiased scientific as well as personal conversations and the way you trusted me with my work have not just resulted in this thesis, written on paper, but also in a large amount of experience and memories for me and for all the students that I guided. I feel honored that I could do all my work under your direct guidance.

Libero, I wish I could have met you more often, but COVID changed the plans quite a bit. However, especially during those uncertain times, you could reassure me that things go as they do, progress will be made and that in the end the result will be there. Your sharpness and wisdom have significantly improved my work and mentality.

It will not surprise anyone that next on the list is the person that could very well be me (but then the updated, much smarter version from 1995), at least according to quite a few of the OM employees… **Indy**, the fact we are so different and yet very similar has always made me feel able to be who I am, and to say what I think, at any point. Not without judgement, but with pure honesty, your answers always helped me further. When we met at the start of our masters, almost seven years ago, I met a timid but very smart person that I knew I could build on (and gosh I did). You have allowed me to build on your knowledge, seemingly at the cost of your mental sanity. And now, after we have bothered everyone with our office singing (from Ludwig van Beethoven to Minnie Riperton), code words (I'll

better refer to your thesis) and the occasional "*list the 100 most recorded classical composers game*" on Sporcle (it took me ages to correctly write Leoncavallo and Buxtehude, let alone remember it…), we may now conclude that we are two broccolis, ready to continue our lives. I hope that we will always stay in touch and please know I'm very grateful for all the years where you dragged me out of tough moments, just by being you. Oh, and my apologies for all the snoring when we had to share rooms in (well, never really in…) Veldhoven, Berlin and Genoa…

Maarten, you've had the misfortune of starting at the same time COVID decided to. Therefore, your initial trainings (as well as your job application tour) were handled by me. If anything goes wrong in the coming year, you're certainly allowed to blame it on me. Jokes aside, you have always shown strong scientific potential combined with an amazing, helpful personality. In the last year, whenever in need I knew I could always rely on you. Thank you so much for the great times and all the help you generously offered.

I almost feel like I need to continue with an apology. **Michael**, you haven't had the easiest time. After choosing to go to the Erasmus College in Zoetermeer (I mean, the Alfrink College was the place to be), preferring Leiden University over TU Delft for your bachelors, masters and PhD, you finally made the right decision to come to TU Delft to work on a project focusing on hypomanganate that I once attempted with my student Cathleen, and deemed far too difficult due to its intrinsic instability (perovskite electrochemistry was the way to go). The moment you arrived, you have taken over many lab duties, improved work for all of your colleagues and students, and helped everyone before even thinking about yourself. Writing this, maybe I should've gone to the Erasmus, or chosen Leiden University, because that route made you someone to whom I look up to. But I am very glad that we met, albeit in the end, at TU Delft. Your work and support, the talks we had and your strong scientific insights have helped me to an extreme extent.

Tom, my respect towards you has grown over the years to a very high level. If I think of what academia should look like, in my eyes, you are the perfect example. You do not seem to care about all the managerial drama, you do science. Literally. Talking to you also made me understand much better how to do science. I praise your attitude towards science and research, because it is thát attitude that made me confident. You taught me to not just do the work, but to talk and ask, inside and outside the research group.

I honestly cannot thank **Valentina**, practically my "second mother", enough. I've seen you grow as a scientist, and as an increasingly strong mother to Hayden and Ian. Next to your boys you decided to adopted me, ensuring I would eat sufficiently. Whenever I needed something, especially some advice, I could always go to you. A small chat with you solves problems, it gets things done and the end result cannot be better. Valentina, thank you so much for always caring and always thinking ahead. I will promise you that I'll keep eating!

Jasmeen, I've only met a few women as strong as you. You have not just taken over the duties from Valentina for being a mother figure at the OM group, early on in your PhD you already dare to tell everyone what's the way to go. And you make the much more experienced people realize that you are generally correct. You have taught me more than

you know, scientifically and personally. Please, stay who you are, and educate the OM group for as long as you can.

Ferdinand, I am surprised you have tolerated all the noises coming from the office next to yours. All the singing and whistling, and later on the many office discussions with Maryam and Michael must have hurt your eardrums. I have furthermore appreciated every time you walked into my office to have a chat, to let off some steam, or just to prepare before online meetings and lectures continued. The many chats and lunch breaks, often with Tom, have made my time at TU Delft much more enjoyable and made the COVID situations more than acceptable.

Zimu, you are one of the most brilliant allrounders I've ever met. You have shown me that syntheses that I have difficulty with reproducing, or even doing, can be "easily" done. You are a magician with both theory and experimental work. Discussing science with you has always been a great pleasure for me.

Laurens, although our work has not overlapped much, you have shown to care about everyone, and take every request seriously. I want to thank you especially for helping Niranjan to prepare for an interview. It showed me that your limits of academia are not bound to our field of engineering, but that you are open to help anyone who asks. I have very much felt the same positive attitude from **Susan**, who's been an amazing office mate. There have only been few moments where I felt happier in the office, than when Susan was around.

Deepika, I am going to miss bothering you, because every chat helped me to get back on track. It has always been a pleasure talking to you, as conversations with you never get boring. Your open mindset has helped me through the last stages of my PhD carreer, and I hope I have been able to repay you that favor.

Never a silent moment in the office. **Maryam**, as no other you have taught me what academic life really is. You understood the ups, but were especially able to help me with the downs. Straightforward, unfiltered comments and advise. And always useful. Thank you so much for educating me about being happy, it worked!

Jaco, I will likely never meet someone that should be in the academic world more than you. I envy your never-ending optimism, combined with knowledge about, well, everything. However, it doesn't stop with knowledge. You showed me how theory becomes practice, translating in (for me) above-expected results.

A good and enjoyable thesis project really depends on a great supervisor. **Nick**, when I started my master thesis I could not have wished for a better supervisor than you. You are the reason why I enjoyed making indium phosphide quantum dots and why I wanted to continue making them (for a while). You have shown a part of academia to me that I missed before that. Thank you, for indirectly shaping the last five years of my life in a beautiful way.

Wiel, you were the foundation of the opto-electronic materials group. No matter what we broke, within five minutes you had not just fixed it, but generally improved it such that we wouldn't break it again no matter how hard we tried. Insights, ideas, you had already finished them before we even thought about it. In my opinion, you are one of our faculty's most valuable assets. Thank you so much for all the help and talks.

Running all of the OM labs, teaching students, knowing every person in the faculty and seemingly having had tea or dinner with at least ten percent of the national and international celebrities. **Ruben**, every day since your retirement, I have missed you around. All the amazing chats, the numerous bus rides and especially all the help on the synthesis lab. I cherish every memory. My sincere thanks, as master student, and as PhD candidate. You have changed many lives in a positive manner.

Wil, **Adinda**, to me you have so many things in common. Helping me out with questions I did not know where to ask, shipping a large number of packages over the years, keeping an eye out for everyone in the OM group. And, at points where I had to travel back home late after a PhD defense, both of you have offered me rides back to Zoetermeer. The amount of very welcome help and support has made my life at TU Delft so much easier during my five years at the OM group. Thank you both, for always being a ray of sunshine, no matter how cloudy the day was!

I have thankfully shown my gratitude before, but I wish I could do it at least once more. **Tonny**, the department felt safe because of you. No matter what question I had, no matter the chemicals that I wanted to use, you always had a well-founded answer. You even came by to talk about my (and other's) experimental ideas, and told me how I could do things best. I can only wish that, wherever the future brings me, safety will be handled in the best way. Your way.

Putting your health and safety at risk on a daily basis, and seemingly overlooked by most employees in the faculty. **Nayyar**, **Joyce**, both of you have not just facilitated my work, every single time we met there was always a positive, personal and certainly not rushed moment of acknowledgement, often resulting in a nice small chat. The faculty and all its employees thrive because of your excellent work.

Vidya, **Snigdha**, **Harshini**, all of you impressed me with knowledge, skills and attitude. Seeing each of you grow, getting and extending confidence in your work and person was beautiful. Indian women are powerful and independent, they know what they want. You have shown that to me, in a strong yet very pleasant manner. I hope I'll be able to meet you again in the future. And please know, you are ridiculously strong. You'll get exactly where you want, that I'm sure of!

Georgy, I think nobody knows how much of a support you have been to me. Whatever I want to say, I can say it to you. Literally, everything seems to be less than odd to your ears, and you seemingly have a proper response to everyone who is smart enough to keep listening. Please, stay who you are. The world is boring enough already.

Jos, without your work, practical help and scientific support, lots of my thesis work would not have been possible. Additionally, talking to you always resulted in nice, personal conversations. Strength is not shown by those who feel the need to open their mouths at all times, it is shown by those who know how to do their job. You are a brilliant mind. You are much more than "just" a technician!

I wish I needed more XPS for my work. **Bart**, I thankfully also met you early on when teaching the practical computational chemistry. You are always friendly, supportive and helpful, to anyone who needs help. I very well remember that, during busy COVID-times, I needed help with an XPS measurement for a rebuttal within practically one week. Two days later, the results were with me, accompanied with an email with an elaborate overview and additional help offered at any point. I am going to miss you in many ways, and want to thank you for all the good times and generous help.

Especially after the onset of COVID, there was little difference between my office mates and people that came by my office to have, honestly, amazing conversations. Every OM member has been great to me, and helped me to further develop, or even find myself. However, during the first months of my PhD, I remember being warmly welcomed by **Aditya**, **Prashant** and **Hamit**, who taught me very well how to handle a PhD without drowning in all the expectations. More life lessons came later, when **Sólrún** joined my office. You have shown me much better than anyone before than which directions were the smartest to go. **Reinout**, later you brought some rest back into the office. Always up for a chat, but never bothered by the many sighs and random chats that went around in the office. **Yan**, although only residing in our office for a short time, I learned a lot from you about electrochemistry. You have helped me as well as Julius a lot, to ensure we would both write a great thesis story. **Hua**, as being the last person to join my office, you may have mostly seen me grumpy. No matter how tensed I was, your continuously positive attitude has helped me a lot in the finishing stages. Obviously, every OM member counted, and taught me things from opening up, to scientific understanding. Of course, including getting somewhat used to the way how PhD defenses are conducted. Therefore, I certainly don't want to forget to thank **Cansel**, **Damla**, **Davide**, **Dengyang**, **Eline**, **Frank**, **Gianluca**, **Goutam**, **Guilherme**, **Jannika**, **Jiashang**, **Jin**, **Kevin**, **Lara**, **Lennart**, **Magnus**, **María**, **Michele**, **Nisha**, **Ryan**, **Silke**, **Sourav**, **Sudeep** and **Ward**.

Without laboratory support, I would not have been able to perform the amount of work that is now shown in my thesis. Maintaining labs, reducing risks and supplying me with all the materials and programs I needed. **Nick**, **Bahiya** and **John**, all of you have ensured that not just me, but every lab user could do their work without difficulties and frustrations.

My PhD thesis would have been nothing without the help of external advisors and collaborators. It is easy to ask help when you know what you need. But it has been so powerful to get to hear about different directions, insights and measurement methods that you haven't even thought of. In the first place, I wish to thank Sara Bals and her group at EMAT Antwerp for the amazing electron microscopy work that has been featured in three of my chapters. **Sara**, **Chen** and **Kellie**, without your willingness to both help and push further than a trial measurement, my chapters would have missed important puzzle

pieces. By supplying these pieces, you turned my chapters into pieces of art of which I am honestly very proud.

For the numerous honest and informative advises and all the helpful discussions, I would like to thank Andries Meijerink and Freddy Rabouw from Utrecht University. **Andries**, **Freddy**, because of your continuous feedback, generally through Arjan, we were really able to understand the materials that we were working on.

It was great to not only ask for answers and help, but furthermore for input and feedback on the materials that I made. I was amazing to see that the particles I made were not just used for my thesis chapters in an aim to improve understanding in the nanocrystal field, but also for, in my opinion, much more hardcore and complex quantum collapse studies at University College London in the group of Peter Barker. **Peter**, **Markus** and **Jonathan**, not only have you given me a reason to keep pushing, you have shown me that the work I did can really be useful for many more things than I could have imaged. Discussing science, both the synthesis of the YLF particles as well as the measurements conducted at UCL taught me how to communicate and ask for feedback to and from scientists in different fields of expertise.

Whenever I lost faith in the academic world, I would think of Elizabeth von Hauff and Simon Boehme, whom I met when they were both part of the Vrije Universiteit Amsterdam. Being part of my first collaborative project, making perovskite nanocrystals for my internship in Genoa, you both have allowed me to enter the academic world in a positive way. **Elizabeth**, **Simon**, seeing both of you continuously grow in the academic world really has made me feel happy and positive about a working environment that I have often questioned.

A few words can change a lot when said in the right way. Sometimes, without even knowing. I really wish to thank **Brandi** Cossairt, **Jonathan** Owen and **Fabien** Delpech. During roughly the most insecure times of my PhD, while presenting a poster at NanoGe in Berlin on my first paper (well, at that time during the most frustrating rebuttal), you all showed honest interest in my work. This was the first time I realized that, apart from my direct research group, my work was also interesting to others in our scientific community. Your kind words and honest interest gave me the confidence to continue fighting, now with the confirmation that it was worth fighting for.

The Istituto Italiano di Tecnologia and a large number of its employees have shaped my scientific career. **Luca**, what can't you do. Honestly, you have an answer to practically everything and you know how to help many people out at once. And that, always with an amazingly positive attitude. I've looked up to you during my internship. Now, after my PhD phase, I admire all your input and qualities even more. **Quinten**, by teaching me how to make perovskite nanocrystals, and **Beatriz**, by allowing me to use your well-maintained fumehood and showing me all the important tricks of proper lab work, you both have ensured I survived my internship and could continue my PhD with confidence. **Filippo**, the magic you have performed with all the ICP measurements has helped Julius and myself a lot by composing the most complex chapter of this thesis. **Mirko**, whenever I

needed answers quickly, you were the one supplying them. Your XPS magic took away a lot of my stress, by filling in the last needed puzzle pieces of multiple chapters.

Obviously, a large amount of thanks goes out for each of the students I was allowed to guide through their thesis projects. **Cathleen**, before I even started my PhD, it was already decided that together we would dig into a project with the start-up company Physee on the synthesis and stabilization of hypomanganate doped phosphors. A difficult project, initially because neither of us had any experience in this type of phosphor and the preparation thereof. Once we got started and you made beautiful blue solutions, we knew we were on the right path. But the stability of the hypomanganate ion made it tough. You battled yourself through your project and showed your strengths throughout your thesis. Verbally strong, excellent in giving presentations and, no matter how hard things were, never giving up. All that, you had to do with a supervisor that had zero experience in supervising. Your master thesis work in the end resulted in a continuation of the hypomanganate project, where since then Michael has shown that this project is much more difficult than we all imagined when we started it. During the final stages of your thesis, I thought it would be a smart idea to get some additional help on other projects that I had started. **Tai**, I found a real hard-working power in you when you accepted a master thesis project on electrochemical n-doping of $CsPbBr_3$. Little did we know that, once again, this project was much harder than we anticipated. Nonetheless, you did an amazing amount of work in the lab, which helped me to further understand the electrochemical (in)stability of $CsPbBr_3$. With that basis, I could in the end compose two chapters on electrochemistry of this material. At the same time as Tai, **Jasper** started on a master thesis project regarding the synthesis of optically refrigerating $Yb:LiYF_4$ nanocrystals. I dare to acknowledge that at that time, you started to understand the project better than I did. You excelled, made many samples and ensured that I could focus on the more important points once you graduated. Because of your work, I could compose a very nice story (Chapter 3 of this thesis) that I am very proud of. After your graduation, you decided to go along the same lines as I did, starting a PhD position at the reactor institute Delft. And Jasper, I have seen that you are doing a great job there too! Even before the graduation of Tai and Jasper, a matter of days before the COVID-lockdowns began, together with Guilherme I decided to guide one more master student on a project synthesizing $CsYbI_3$ perovskite nanocrystals. Due to the lockdowns, we never got to the point of making these nanocrystals together with **Anne**. At the start of your master thesis project we had to change the topic as the labs closed for an unknown amount of time and go into a completely different direction, roughly doing a 180 degree turn from synthesis to DFT. Therefore, Indy took over as the main supervisor, but I was happy that you kept me closely involved on the project. What you then did amazed me. You performed work I could never have done. You performed computer simulations, not at all the practical synthesis work you wanted, and you did it very well. It was not always easy, but you pulled through with very good end results. I will never forget your defense, where you confidently told us exactly what you had done and defended it as if you had always wanted to work on such a project. Performing a master thesis, fully in COVID-times, and with results far above expectations. I am very proud of your achievements, as well as your strong personal and scientific growth! And Anne was not the only student that I co-supervised. Roughly at the time that I should not have taken another student anymore, but just focus on finishing writing my thesis, I had an idea and

managed to talk Arjan and Maarten into it. **Colin**, you were the only bachelor student I supervised during my PhD, working on the synthesis and electrochemistry of ZnSe/ZnS quantum dots. Looking back on your project, I am happy no accidents have happened. Not because you were a danger on the lab, on the contrary, but because the synthesis protocol we gave you was, let's say, risky. Your swift scientific growth and eagerness to learn resulted in a nice thesis and perfect presentation and defense. Your personality and skills will bring you far, and I hope to hear from you once you are ready to defend your master thesis for the Chemical Engineering masters. And then I kept one student, who started between Anne and Colin for the last. I remember that, at the time Arjan asked if anyone wanted to guide anymore students, I really wanted to focus on finishing my own work. Hence my answer was no. Until I saw the list with candidates… Seeing the name Julius Monchen was enough for me to say, and I don't like admitting this, "Okay, if I may guide Julius I will take one more student". Thank god you accepted the master thesis project that seemingly was easy, although we now know much better. **Julius**, since I met you in the first year of my bachelors, I knew you were smart and strong. And you had already more than proven this during your bachelor thesis where you worked with my master thesis supervisor Nick. Julius, you have done a lot of work on the synthesis lab and you have understood more than your supervisor. You did not give up when the results did not make sense anymore. On the contrary, you prolonged your thesis work and showed me science in the most extensive ways. You came with answers to questions we hadn't thought of. Your thesis work represents you in every positive way. I admire your strong working attitude, and hope that it will bring you very far. I would not be surprised if you end up doing a PhD, and if you would, I am sure we are going to hear from you. You, and your work, are almost too good to be true. Julius, thank you for saving me from so much trouble by helping my thesis work so much further!

Taking a step back from my PhD, I want to acknowledge some people who ensured I graduated in the first place. The support, and answers to homework exercises, I have obtained from **Arjan**, **Brian**, **Charlie**, **Dennis** and **Lennart** during my high school time have been significant. You guys have helped me with some hash moments, knowingly or unknowingly. You were, and still are there for me if I need you. The same is true for **Daniël** and **Jurriaan**, who made my bachelor time much better. Before and after surgery, I have been able to lean on you guys whenever I got lost in one of the many courses. During my master phase, apart from my seemingly identical twin Indy, the same support was very generously offered by **Lois**, **Soraya** and **Vincent**. Discussing homework, science and especially frustrations with you very much helped me to cope with some of the moments I encountered during my PhD time.

No matter for how long you share a faculty building, there is always sufficient time to ignore all the wonderful people that work in the same concrete block. And sometimes, unexpectedly, your paths cross in an entirely different way. All the wonderful PDEngs that I met outside of TU Delft have been of great support, in dragging me out of the daily struggles, but especially by teaching me how to relax and set work aside for a bit. All of you, especially **Albert**, **Diogo**, **Miguel**, and **Roman** have ensured I would finish and have furthermore prepared me for the next steps in life.

Chris, **Diego**, **Gonçalo**, **João** and **Richard**. You are the strongest safety nets I have encountered. No matter what, I could always rely and fall back on you guys. You are as close as it gets to family. Mentally, you have kept me sane in the worst of times, without ever asking anything in return.

The entire **Mulder** and **Mugge** families (don't blame me for not writing three pages of names) have supported me from an early age onwards. Stories about explosions in the backyard, bedrooms on fire and lots of smoke intrigued me, and later on made me decide to study chemistry. Your support, to who I am and what I do, has been of great help. I am bringing a load of good memories with me, wherever I may go, and praise myself that my family is awesome and at points just perfectly retarded.

Irna, **Simon**, or better, ma en pa, I have not met any people that are stronger than you. Raising a child, continuing life and at points having to act as if everything is fine when your other child has just died is something impossible. Yet, you have managed to raise a son that, against the expectations of some, got to this point in life. I see so much of you in myself. The power and ignorance to push when knowing that stopping is easier (and maybe better), but managing to get to the finish line. I look up to both of you in many ways, and hope to make you smile many more times.

Niranjan, without you and your continuous support I would have quit. That's for sure. I have no idea how you have been able to handle me all these years, with ups and downs through my PhD time. But I'm very glad you did. You are the main support I needed, a person with PhD experience, a person that listens and always gives good advice. You dragged a (somewhat) grown up man out of a timid person. I owe you, big time.

Daphne, I cannot other than conclude that this thesis would possibly not even have been here without you. In my mind the memories stick, good and bad. Whenever it really got dark, the thoughts of you kept me going. Until the end of times, I will keep you with me, and I will ensure to make you proud. I wish you were here to see it all, as I know you would have loved it.

Posters and Presentations

Posters

Lattice Matched Epitaxial Shell Growth on InZnP Quantum Dots

Physics@Veldhoven, January 2019

Developing Lattice Matched ZnMgSe Shells on InZnP Quantum Dots for Phosphor Applications

NanoGE Berlin, November 2019

CHAINS, December 2019

Physics@Veldhoven, January 2020

Electrochemical p-Doping of $CsPbBr_3$ Perovskite Nanocrystals

GRC Les Diablerets, July 2022

Presentations

Electrochemical p-Doping of $CsPbBr_3$ Perovskite Nanocrystals

CHAINS, December 2021

Supervised Thesis Projects

It has been a great please to see all of the students I supervised learn, grow and eventually graduate. With passion and perseverance, each and every one has shown to be a strong scientist, ready for the academic and industrial life. I feel honored that I have been part of all of your great works!

Cathleen Scheepers – Master thesis: Synthesis and stabilisation of $Mn^{V}O_4^{3-}$ doped phosphors – in collaboration with the start-up company Physee with Joe Kao and Ana Jung

Cheng-Tai Lin – Master thesis: Spectro-electrochemistry of $CsPbBr_3$ NCs

Jasper van Blaaderen – Master thesis: Synthesis and Optical Analysis of Ytterbium Doped Yttrium Lithium Tetrafluoride Nanocrystals - Towards Laser Cooling in Nanocrystals – in collaboration with University College London with Jonathan Gosling and Peter Barker

Anne Spruit – Master thesis: Tolerance to surface vacancies in halide perovskite nanocrystals – co-supervision, with Indy du Fossé and Guilherme Almeida

Colin van der Made – Bachelor thesis: Synthesis and analysis of high quality ZnSe core and ZnSe/ZnS core/shell quantum dots for blue phosphor applications – co-supervision, with Maarten Stam

Julius Monchen – Master thesis: On the Electrochemical Stability of $CsPbBr_3$ Nanocrystals: Finding the Weakest Link with Regard to Cathodic Decomposition

List of Publications

Jence T. Mulder, Michael S. Meijer, J. Jasper van Blaaderen, Indy du Fossé, Kellie Jenkinson, Sara Bals, Liberato Manna, Arjan J. Houtepen, Understanding and Preventing Photoluminescence Quenching to Achieve Unity Photoluminescence Quantum Yield in Yb:YLF Nanocrystals, *ACS Appl. Mater. Interfaces* 2023, 15, 2, 3274–3286

Yan B. Vogel, Maarten Stam, **Jence T. Mulder** and Arjan J. Houtepen, Long-range charge transport via redox ligands in quantum dot assemblies, *ACS Nano* 2022, 16, 12, 21216–21224

Markus Rademacher, Jonathan Gosling, Antonio Pontin, Marko Toroš, **Jence T. Mulder**, Arjan J. Houtepen and Peter F. Barker, Measurement of single nanoparticle anisotropy by laser induced optical alignment and Rayleigh scattering for determining particle morphology, *Appl. Phys. Lett.* 2022, 121, 221102

Indy du Fossé, **Jence T. Mulder**, Guilherme Almeida, Anne G. M. Spruit, Ivan Infante, Ferdinand C. Grozema and Arjan J. Houtepen, Limits of Defect Tolerance in Perovskite Nanocrystals: Effect of Local Electrostatic Potential on Trap States, *J. Am. Chem. Soc.* 2022, 144, 25, 11059–11063

Jence T. Mulder, Indy du Fossé, Maryam Alimoradi Jazi, Liberato Manna and Arjan J. Houtepen, Electrochemical p-Doping of $CsPbBr_3$ Perovskite Nanocrystals, *ACS Energy Lett.* 2021, 6, 7, 2519–2525

Jence T. Mulder, Nicholas Kirkwood, Luca De Trizio, Chen Li, Sara Bals, Liberato Manna and Arjan J. Houtepen, Developing Lattice Matched ZnMgSe Shells on InZnP Quantum Dots for Phosphor Applications, *ACS Appl. Nano Mater.* 2020, 3, 4, 3859–3867

Nicholas Kirkwood, Annick De Backer, Thomas Altantzis, Naomi Winckelmans, Alessandro Longo, Felipe V. Antolinez, Freddy T. Rabouw, Luca De Trizio, Jaco J. Geuchies, **Jence T. Mulder**, Nicolas Renaud, Sara Bals, Liberato Manna and Arjan J. Houtepen, Locating and Controlling the Zn Content in In(Zn)P Quantum Dots, *Chem. Mater.* 2020, 32, 1, 557–565

Curriculum Vitae



Jence Theodorus Mulder was born on the 14th of November 1993 in Zoetermeer, the Netherlands. He completed a bachelor in Molecular Science and Technology, a joint degree between Leiden University and Delft University of Technology, with a thesis project entitled "The conjugation of lactoferrin to maleimido-terminated PBd-b-PEO polymersomes and biodegradable PEG-b-PCl micelles" at the Radiation and Isotopes for Health group of the Reactor Institute Delft, under the supervision of Dr. ir. Robin de Kruijff and Dr. Antonia Denkova. Subsequently, he started a masters in Chemical Engineering at Delft University of Technology, which he completed with a master thesis project entitled "Lattice matched epitaxial shell growth on InZnP quantum dots - Towards a fully passivated surface" under the supervision of Dr. Nicholas Kirkwood and Prof. dr. Arjan Houtepen. He then finished his masters with a scientific internship on "The synthesis of highly luminescent cesium lead halide perovskite nanocrystals and photon upconverting ytterbium doped yttrium lithium fluoride particles" at the Italian Institute of Technology in Genoa, under the supervision of Dr. Luca de Trizio and Prof. dr. Liberato Manna. On the 1st of July 2018, he started his PhD in the opto-electronic materials group at Delft University of Technology, under the guidance of Prof. dr. Arjan Houtepen and Prof. dr. Liberato Manna. His main focus here is on the synthesis and characterization of a broader variety of optically active nanomaterials. He furthermore acted as interim lab manager of the nanocrystal synthesis lab, assisted with bachelor practicals and master courses and (co-)supervised one bachelor and five master students.

Apart from chemical syntheses, Jence likes to play the oboe and English horn. For many years, he was the first oboist and group leader of the woodwind section of the Viotta Youth Orchestra. In attempts to fully dissociate from any stress, he can furthermore be found on the other side of the musical spectrum, attending techno festivals.

